

***National Nanotechnology Infrastructure Network  
Research Experience for Undergraduates Program***

**2008 Research  
Accomplishments**

# Synthesis of a BioMEMS Device for Direct Delivery of Cancer Drugs

Andrew U. Abreu

Materials Science and Engineering, Rensselaer Polytechnic Institute

**NNIN REU Site: Howard Nanoscale Science and Engineering Facility, Howard University, Washington, DC**

*NNIN REU Principal Investigator(s): Dr. Gary Harris, Howard Nanofabrication Facility, Howard University*

*NNIN REU Mentor(s): Nefertiti Patrick-Boardley, Applied Physics, University of Michigan*

*Contact: abreu@rpi.edu, gharris@msrce.howard.edu, boardley@umich.edu*

## Abstract:

This project focused on optimizing the fabrication process of a biological microelectromechanical systems (bioMEMS) device for direct delivery of cancer drugs. A photolithographic process was used to fabricate  $50 \times 50 \mu\text{m}$  "step" groove patterns on aluminum substrates, which were then used to make a metal mold for device synthesis with the inclusion of grooves. Heat was incorporated during PDMS curing to drastically reduce production time.

## Introduction:

Direct delivery of cancer drugs is a topic of increasing importance, as current methods of cancer treatment are expensive and inefficient. High concentrations and large dosages are required for chemotherapy drugs and other substances to have a significant effect in treating cancer, driving up treatment costs as chemotherapy drugs are expensive to make. Direct delivery of cancer drugs increases the efficiency of treatment, lowers the costs as less drugs and lower concentrations are required, and reduces the severity of side-effects.

One method for implementing direct delivery is to implant a biocompatible device made of polydimethylsiloxane (PDMS) containing cancer drugs into sites of recently removed tumors. The drugs are dispensed from a hydrogel inside the device, using a hyperthermia coil to supply heat for activating the gel's contraction mechanism, with micro-channels acting as delivery pathways for drug flow.

This project focuses on the inclusion of microgrooves onto the device surface for cell attachment, fostering biocompatibility with the human body. The grooves can be tailored to the average size of the specific cancer cell type for optimum cell adhesion.

## Procedure:

SU-8 50 microgrooves were made on  $0.5 \text{ in} \times 0.5 \text{ in}$  aluminum 5052 alloy substrates of thickness 0.3 mm, following the procedures outlined by MicroChem for  $50 \mu\text{m}$  films [1]. It should be noted that: the final ramp-up spin speed was  $\sim 2180 \text{ RPM}$ ; all bakes were done in convection ovens, so heating times were 50% longer than outlined in procedures; and a hard-bake of 2 hrs minimum was carried out on the aluminum substrates. After making four substrates, a mold was assembled so that the bottom had a cylindrical piece of metal with diameter of 0.6-0.7 cm and height of 0.9 cm, and

the interior length and width (on the inside of the mold) was 1 cm each, with the height at 1.1 cm. Under a fume hood, the mold was placed on a Petri dish with a few drops of silanizing agent. The dish was placed into a vacuum desiccator and was left in chamber for 1 hr under a pressure of 12.5 psi.

Two pieces of aluminum foil were molded onto the bottoms of 250 ml and 150 ml beakers. Using materials from a 184 Sylgard kit, PDMS was prepared by mixing at a weight ratio of 10:1 monomer to curing agent on a chemistry boat. Once the mixture became cloudy due to bubbles, the boat was degassed in vacuum at 12.5 psi for 45 min. Afterwards, any remaining bubbles were removed and the mold was placed on large foil boat. Next, the mixture was poured into a mold and small foil boat and re-degassed at 12.5 psi for a minimum of 1 hr, with pressure throttled every 20 min to assist with bubble removal. The boat was then placed on a hot plate, set to  $125^\circ\text{C}$ , for 20 min until the PDMS cured. After air cooling,

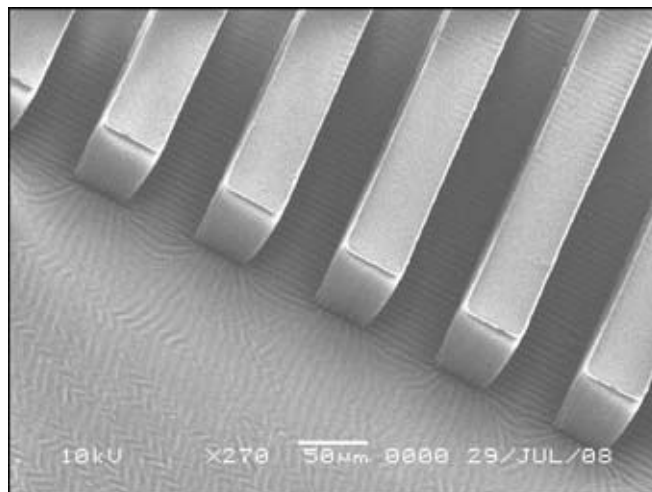


Figure 1: SEM of PDMS replica of microgroove pattern.

the mold was disassembled, using a razor to remove excess PDMS and foil from the small boat while carefully removing the substrates from casing. Using a micropipette to drop a small amount of curing agent on the side of the casing with a hole, the thin piece of PDMS from the small foil boat was cured onto a PDMS casing at 125°C for 20 min. After an air cool, the excess PDMS was removed using a razor.

### Results and Discussion:

Using scanning electron microscopy (SEM) images of PDMS replicas such as in Figure 1, we confirmed the process conditions for good resolution replica molding of SU-8 microgrooves, and then fabricated the casing mold with the substrates. The original processing time, without the addition of heat, was dramatically reduced from 48 hours to 45 minutes with the inclusion of heat during PDMS curing. Figure 2 shows the completed device casing, and Figure 3 demonstrates the successful microgroove pattern replication onto the device surface. A preliminary experiment monitoring the cell attachment to microgrooves was conducted, and initial results showed that cells were in fact attached to the microgroove walls, as shown in Figure 4.

### Conclusion:

In conclusion, the process and conditions used were successful in the fabrication of microgrooves on the bioMEMS device surface, potentially allowing the device to integrate with the human body without rejection. Along with the reduction in production time, our findings increase the viability of the device as an alternative to current cancer therapy methods.

### Future Work:

For future work, long term studies of cell adhesion to device microgrooves will be conducted, flow-rate measurements of drug delivery via the hydrogel will be obtained, and efficacy of iron-oxide nanoparticles as a potential therapy in conjunction with the device will be determined.

### Acknowledgments:

Thanks in part to: Prof. Wole Soboyejo and research group, Princeton University; James Griffin, HNF site coordinator; Nefertiti Patrick, Mentor; Dr. Gary Harris, HNF PI; All HNF staff and faculty; National Nanotechnology Infrastructure Network Research Experience for Undergraduates Program; National Science Foundation.

### References:

- [1] MicroChem, NANO™ SU-8 Negative Tone Photoresist Formulations 50-100.

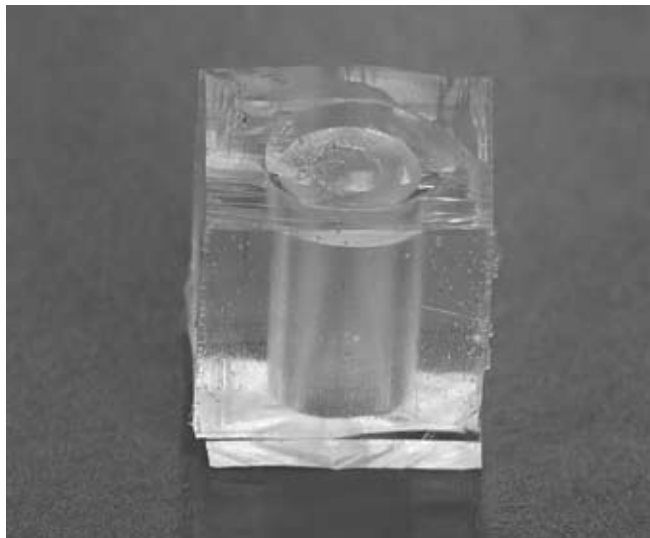


Figure 2: Photo of finished device casing.

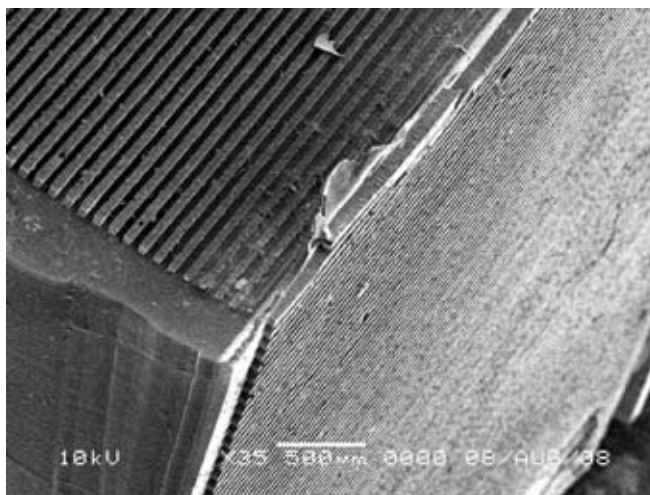


Figure 3: SEM micrograph of a corner of PDMS casing.

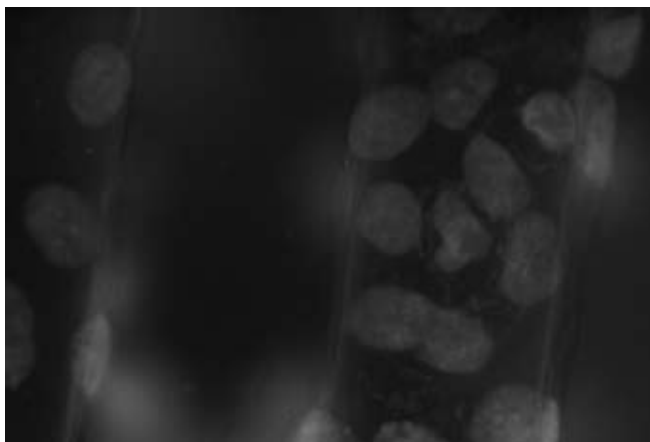


Figure 4: Photo of nuclear-stained cancer cells attached to microgrooves.

# Optimizing the Direct Fabrication of Nanoparticles for Cancer Diagnostics

Sophia M. Allaf

Applied Health, Azusa Pacific University

**NNIN REU Site: Stanford Nanofabrication Facility, Stanford University, Stanford, CA**

*NNIN REU Principal Investigator(s): Dr. Mary Tang, Professor Yi Cui, Material Science and Engr, Stanford University*

*NNIN REU Mentor(s): Ching-Mei Hsu, Stephen Connor, Material Science and Engr, and Chemistry, Stanford University*

*Contact: sophiaallaf2@apu.edu, mtang@stanford.edu; chingmei@stanford.edu*

## Abstract:

Nanoparticles with specific ordered structure and composition can produce unique optical or electromagnetic signatures. These nanoparticles are finding new uses such as biomarker scaffolds in cancer diagnostics. This work involved optimizing the process of direct fabrication using nanoimprint and other techniques common to device manufacturing in order to produce these nanoparticles. In particular, our work focused on creating nanoimprint templates and optimizing their use in thermal nanoimprinting. In order to optimize the direct fabrication process, solution phase synthesis and various characterizations, such as scanning electron microscopy (SEM) of metal nano-structures were used [1]. Nanosphere lithography (NSL) of wafer-scale arrays was achieved through Langmuir-Blodgetry (LB) and careful reactive ion etching as shown in Figure 1. We utilized LB in order to bypass many of the limitations of the current fabrication methods and still be able to create close-packed nanoparticle arrays over large scales.

This is unique in the field of NSL and originates primarily in the use of nanoparticles of silica as a direct mask for etching. The motivation behind this research was to develop an optimized method of fabricating magnetic nanoparticles for highly selective and sensitive cancer bioassays.

## Introduction:

Magnetic nanoparticles were first developed approximately 35 years ago [1]. These nanoparticles have shown remarkable potential for curing the cancer disease and have brought new dimensions to cancer research. Our group has previously demonstrated the use of the Langmuir-Blodgett (LB) method to produce stamps, and used those stamps for to produce templates for synthetic antiferromagnetic (SAF) nanoparticle fabrication. However, the complete process to use these stamps and templates to produce the SAF nanoparticles has not yet been done. We fabricated stamps which will be utilized in this process so that the SAF nanoparticles can be fabricated and investigated as bioassays for cancer.

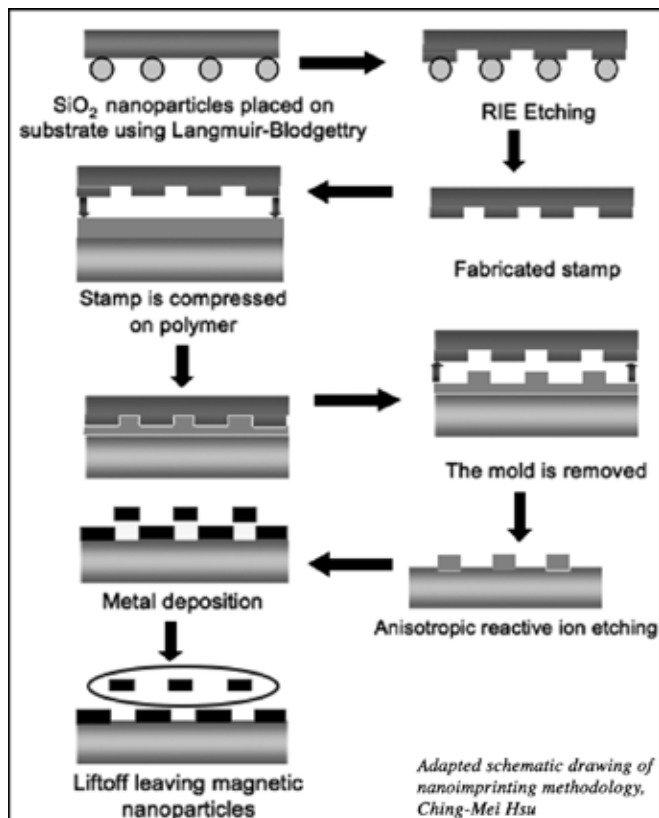


Figure 1: Fabrication of the magnetic nanoparticles.

In order to enhance the process of direct fabrication, we needed to make high-density arrays of the SAF nanoparticles, which are typically made using either electron beam lithography or photolithography methods. However we utilized the LB method, which is relatively fast, inexpensive and uses only small amounts of raw material, whereas lithography is expensive, time consuming and uses large amounts of raw material. The LB method utilizes the LB trough.

In brief the LB trough, as shown in Figure 2, is an instrument that is used to study the properties of a monolayer of amphiphilic molecules. Among other applications, the instrument can compress the monolayer to deposit LB films on a solid substrate, such as silicon.

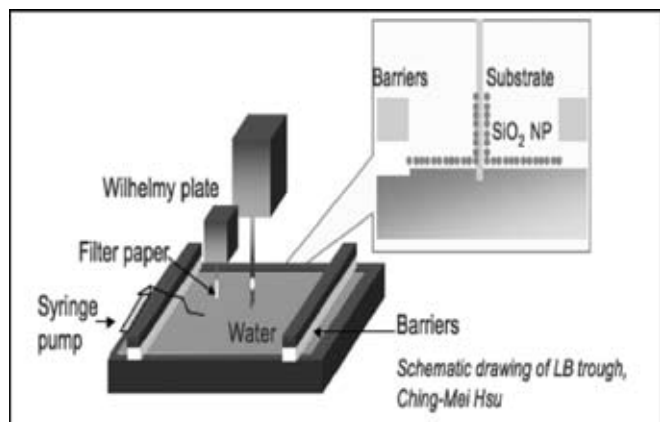


Figure 2: Langmuir-Blodgett trough and deposition.

Utilizing this method we hoped to accomplish our objectives of enhancing the process of direct fabrication using nanoimprint and other techniques, such as the LB trough for deposition, in order to produce uniform arrays of silicon nanopillars across the substrates surface, create many nanoimprint templates in a short amount of time and improve their use in thermal nanoimprinting. Finally we hoped to employ an optimized method of fabricating magnetic nanoparticles for use in highly selective and sensitive cancer bioassays. Our particular research area concentrated on placing the  $\text{SiO}_2$  nanoparticles on the Si substrate to be used as etch masks to create silicon nanopillars for nanoimprint templates.

### Experimental Procedure:

**Functionalization of  $\text{SiO}_2$ .** Two mL of the cleaned silica nanoparticles solution was diluted into 14 mL absolute ethanol 1 mL water, and 100  $\mu\text{L}$  3-aminopropyl (diethoxymethylsilane). 97% (APDES) is added with vigorous stirring. The sample was stirred overnight and then heated at  $100^\circ\text{C}$  for one hour while being covered in aluminum foil. Cleaning was then performed on the functionalized sample by centrifugation into ethanol and methanol, in 15-minute intervals for a total of five intervals. The solution-based sample was then taken for deposition, with final dispersion into the spreading solvent desired for LB.

**Langmuir-Blodgett Deposition.** The functionalized samples of silica nanoparticles were injected onto the water subphase by means of a syringe pump. The film was then compressed until a sharp rise was observed in the surface pressure, indicating the formation of a monolayer. Dip-coating depositions were usually performed on oxygen plasma cleaned silicon substrates with the substrate perpendicular to the water surface. The substrate was dipped through the monolayer at 40 mm/min, followed by raising the substrate at 5 mm/min to collect an even film. The surface pressure for optimal deposition was strongly dependent on the size of the nanoparticles, with larger silica samples commonly reaching pressures of  $5 \text{ mN/m}^2$ .

### Results and Conclusions:

It is clearly seen in the SEM image shown in Figure 3 that uniform arrays of masked nanoparticles are evenly formed across the silicon wafer. (See T. Sengupta's report, page 28, for etching the Si using this mask, and producing the stamp.) Thus, the Langmuir-Blodgett method bypassed many of the limitations of the current fabrication methods on the nanoscale. Additionally, we produced close packed arrays of  $\text{SiO}_2$  nanoparticles by LB deposition. Using this process and subsequent etching, a stamp for the fabrication of magnetic nanoparticles was produced.

### Future Work:

In the further experimentation of the LB process, we hope to investigate the limitations of the current functionalization method, such as defects, incomplete coverage and imperfect hydrophilicity that occurs in certain regions of the substrate after deposition. Also, we hope to utilize these stamps to produce magnetic nanoparticles for cancer bioassays.

### Acknowledgments:

I would like to thank my mentors Ching-Mei Hsu and Stephen Connor, my PI's Professor Yi Cui and Dr. Mary Tang, our site coordinator Dr. Michael Deal, James Conway, Ben Weil, Maureen Baran and all the SNF processing staff. I would especially like to thank the National Nanotechnology Infrastructure Network Research Experience for Undergraduates Program, Stanford Nanofabrication Facility, National Science Foundation and the Center of Cancer Nanotechnology Excellence for their financial support.

### References:

- [1] Hsu, C. and S. Connor, Nanosphere Lithography. 2-8 (2007).

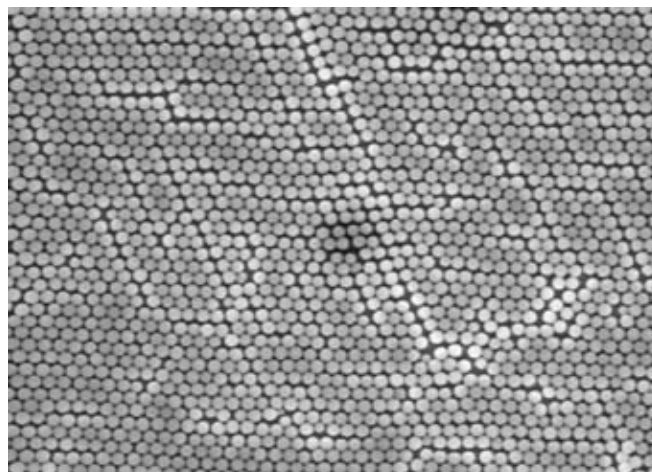


Figure 3: Uniform nanoparticles are formed across the silicon wafer. SEM taken at 25000x.



1%, 2% and 5% (w/v) polymer solutions of PVA were made by heating distilled (DI) water to 85°C and adding PVA one gram at a time until all was dissolved. The solution was brought up to its correct volume, sealed and left to stir overnight. The next day, the solution was vacuum filtered. To test viscosity, 5 mL of the solution was pipetted into a Canon-Fenske Routine glass viscometer. The solution was timed moving from marks A to B giving the viscosity. Prior to spin-coating, 4 inch silicon wafers were cleaned in a 30 minute piranha solution, a 10 minute buffered oxide etch (BOE) and spun dry for 3.5 minutes. Approximately 650  $\mu\text{L}$  of BARC was spun on a wafer at 2500 RPM for 25 seconds and post baked at 180°C for 1 minute. The wafer was then allowed to sit for  $\sim$  20-30 minutes to allow the BARC coating to dry and the wafer to cool.

Approximately 5,000  $\mu\text{L}$  polyvinyl alcohol solution (PVA) was dispensed onto the center of the wafer. The wafer was allowed to sit for one minute and was then spun for 60 seconds on variable speeds. 1%, 2% and 5% (w/v) polymer solutions were used at speeds of 1000 RPM, 2000 RPM, 3000 RPM and 4000 RPM. Afterwards, BARC and PVA film thicknesses were measured using a Cauchy model with a J. A. Woollam M-3000 ellipsometer.

### Results/Conclusion:

As the weight/volume percent (w/v%) of the polymer, PVA 31,000, in the solution increased, the viscosity and refractive index increased proportionally. Higher percent polymer solutions yielded higher average thicknesses at all speeds. An exponential trend was found when examining increasing spin speeds and thicknesses as shown in Figure 4. The 5% PVA polymer had the thickest layers; however, the high viscosity of the solution caused a large amount of air bubbles to form causing multiple imperfections in the substrate. The 1% polymer had such a low viscosity that its average thickness always ranged from 250 to 300  $\text{\AA}$  regardless of spin speed. Although the substrate was consistently the most uniform and had the least imperfections, the PVA layer was too thin so that particles, when imprinted on the wafer, may still adhere to the BARC. The 2% solution had more imperfections in the substrate than the 1% solution, but its thickness was high enough at speeds of 1000 to 2000 RPM to create a uniform, reproducible substrate. Thus, the 2% polymer was found to be the most ideal concentration to use, while 2000 RPM was found to be the best spin speed to create the least number of imperfections.

### Future Work/ Acknowledgments:

In the future, this imprinting substrate will help produce uniform, reproducible imprints, maximizing the number of particles created. I would like to acknowledge the National Nanotechnology Infrastructure Network Research Experience for Research Program and National Science Foundation for funding, and UT Austin, Microelectronics Center, Mary Calderera-Moore, and my PI, Dr. Krishnendu Roy, for their assistance in completing this project.

### References:

- [1] Glangchai, L.C., Calderera-Moore, M., Shi, L. and Roy, K. Journal of Controlled Release 125, 263-272 (2008).

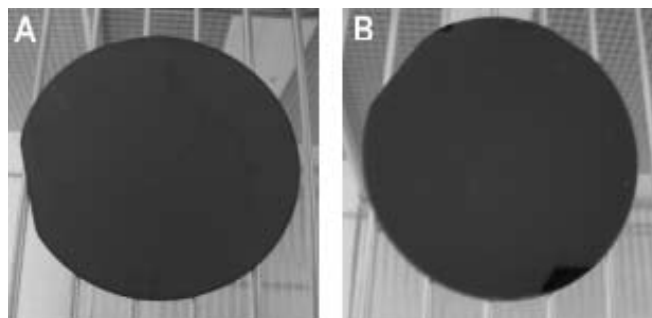


Figure 2: A. BARC coated wafer; B. PVA coated wafer.

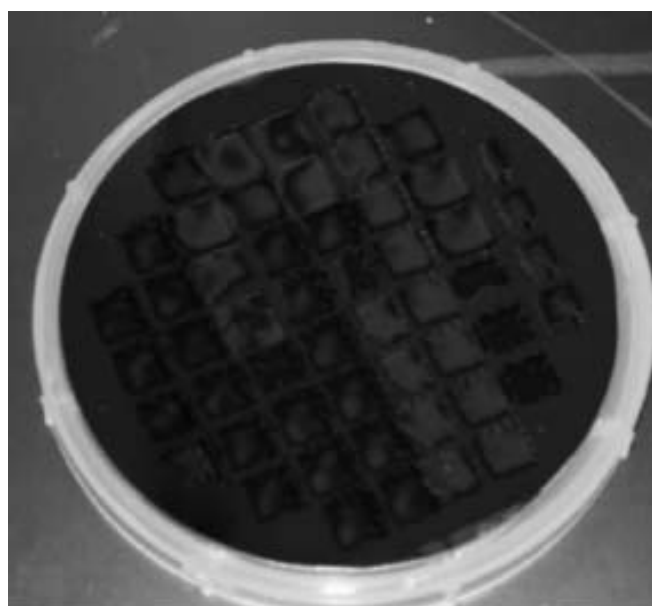


Figure 3: A wafer that has been fully imprinted on. Areas with various coloring show imperfections in the substrate.

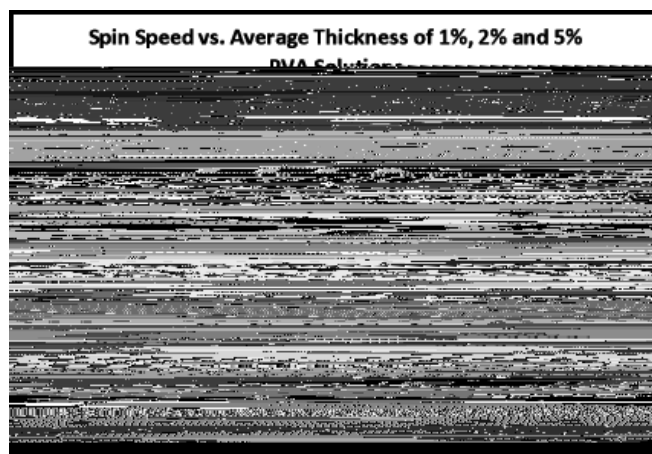


Figure 4: Graph of spin speed vs. average thickness of various percentages of PVA solutions: 5% showed an exponential trend while 2% and 1% polymer solutions had nearly linear trends in thickness.

# Optimization and Microfabrication of an Electrosonic Ejector Microarray for Intracellular Nanomaterial Delivery

Allison Connolly

Biomedical Engineering, Johns Hopkins University

**NNIN REU Site: Microelectronics Research Center, Georgia Institute of Technology, Atlanta, GA**

NNIN REU Principal Investigator(s): Dr. Andrei G. Fedorov, Mechanical Engineering, Georgia Institute of Technology

NNIN REU Mentor(s): Dr. J. Mark Meacham, Mechanical Engineering, Georgia Institute of Technology

Contact: aconnol2@jhu.edu, andrei.fedorov@me.gatech.edu, jmarkmeacham@gmail.com

## Abstract:

This REU project focused on optimization of the electrosonic ejector microarray (EEM) to enable efficient intracellular nanomaterial delivery. The EEM ejects biological cells through microscopic nozzles with incorporated electroporation electrodes, thereby opening pores in the cell membrane for uptake of drugs and/or genes/nucleic acids. The device assembly consists of a piezoelectric transducer for ultrasound generation, a polydimethylsiloxane (PDMS) chamber for holding the biomolecule and cell solution, and a  $20 \times 20$  array of pyramidal-shaped nozzles etched in silicon and coated with gold. The piezoelectric transducer drives the sono/mechanoporation of the cells, while the gold-coated nozzles are used to generate an electric field, which allows for electroporation. The PDMS serves as both a fluid reservoir and a microfluidic device. The water in the reservoir transfers the generated acoustic waves from the piezoelectric to the cell mixture, and fluidic channels that are cast into the PDMS allow separate groups of nozzles to be accessed for simultaneous ejection of multiple samples.

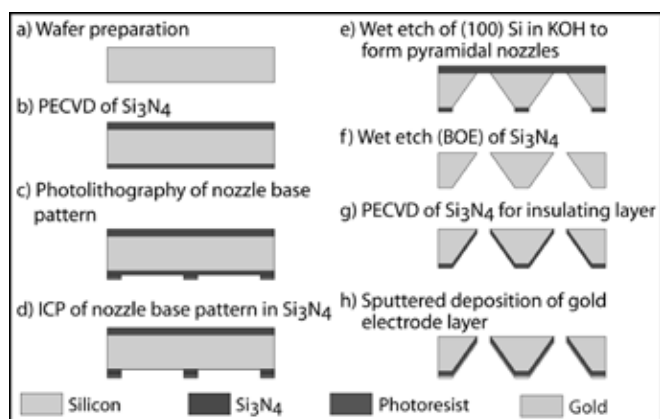


Figure 1: Electrosonic ejector microarray fabrication process.

## Device Fabrication:

The fabrication process for the EEM is shown in Figure 1. An array of square openings for the nozzle bases was patterned in Microposit SC 1827 photoresist. This pattern was then transferred into a silicon nitride ( $\text{Si}_3\text{N}_4$ ) layer on the backside of a [100]-oriented silicon wafer using inductively coupled plasma (ICP) etching. The pyramidal nozzles were formed by wet etching through the silicon wafer in a potassium hydroxide (KOH) solution (see Figure 1e). The KOH solution etched the [100] orientation (normal to the wafer face) significantly faster than the [111] orientation ( $54.74^\circ$  to the wafer face). The size of the nozzle apertures was controlled by varying the etch time. Following the KOH etch, a 500 nm silicon nitride

layer was deposited to insulate the silicon nozzles from the gold electrode layer. For better adhesion, a titanium seed layer was sputtered onto the nitride before depositing the gold.

PDMS was selected for its mechanical properties (e.g., high flexibility and compressibility), biocompatibility, and low cost. The PDMS spacer separates the disposable EEM from the remainder of the assembly, maintaining a sterile environment for the cell mixture. The fluidic channels are designed to isolate small groups of nozzles, minimizing sample volumes while maximizing throughput. A mold for the channels is patterned in SU-8 10 on a silicon wafer [1].

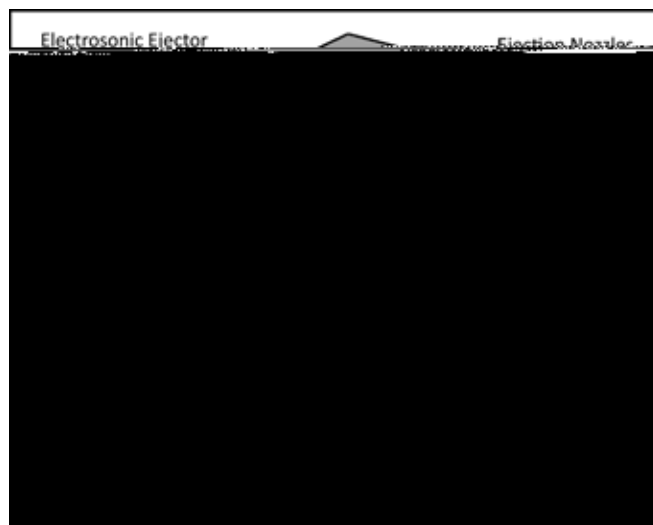


Figure 2: Expanded device assembly.



# Nano-Scale Fluidics for Ultra-Compact Lab-On-A-Chip Device Applications

Ryan Edwards

Biomedical Engineering, University of Oklahoma

**NNIN REU Site: Microelectronics Research Center, Georgia Institute of Technology, Atlanta, GA**

NNIN REU Principal Investigator(s): Dr. Ali Adibi, Electrical and Computer Engineering, Georgia Institute of Technology

NNIN REU Mentor(s): Dr. Siva Yegnanarayanan, Electrical and Computer Engineering, Georgia Institute of Technology

Contact: ryan.h.edwards-1@ou.edu, ali.adibi@ece.gatech.edu, sivay@ece.gatech.edu

## Abstract:

Ultra-high quality factor ( $Q$ ) chip-scale silicon nitride (SiN) optical microresonators are very attractive for lab-on-a-chip biological sensing. Two key challenges in developing multiplexed sensor arrays are fluidic sample delivery and surface coating of the sensor surface. This project focused on designing, fabricating, and testing various SU8 microfluidic channels tightly integrated on the top of an array of SiN microresonators. Each resonator was functionalized with a specific surface coating for a particular analyte, using a large-angle surface patterning tool and the Nano eNabler™ System from BioForce Nanosciences, Inc. Fluidic channels were sealed by a polydimethylsiloxane (PDMS) or glass cover slip and inlet/outlet ports were provided for the sample injection through external syringe. Preliminary experimental results, obtained by flowing a set of Brix fluids in the microfluidic channel with different refractive index units (RIU), showed that the sensor bulk refractive index sensitivity was  $\sim 1$  nm/RIU.

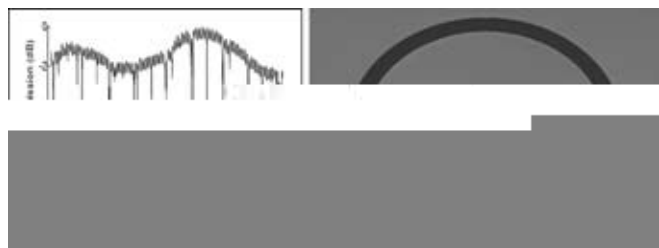


Figure 1: (a) Measured spectral response for an SiN resonator. (b) SEM picture of resonator. The resonator had a diameter of 40  $\mu\text{m}$ .

## Introduction:

Our goal is a compact, handheld, lab-on-a-chip device for

In a multiplexed sensor array, each sensor surface has a unique surface coating for sensing a specific biomolecule. In this work, we have developed techniques to solve the two major challenges in developing such a multiplexed sensor. The first involves the development of optimal microfluidic channels fabricated directly on the top of the SiN resonators that enable dramatic reduction in the diffusion time for the biomolecules thereby enabling assay time to be dominated mostly by the binding kinetics on the sensor surface. The second task in this research involves the development of surface patterning techniques that could enable highly-specific surface coatings to be applied to the sensor surface following the fabrication of the fluidic channels.

## Experimental Procedure:

SiN resonator chips were fabricated using electron beam lithography. They were operated in the visible wavelength range to overlap with the low optical absorption loss region for water. SU-8 (MicroChem) was spin-coated on the SiN resonators to a thickness of 15  $\mu\text{m}$  and patterned to define microfluidic channels pre-aligned to the resonators (see Figure 2a).

A large-angle surface patterning tool and the Nano eNabler™ System was used to print sub-femtoliter volumes directly on the surface of the resonators within the microfluidic channels. We repeatedly approached  $< 1 \mu\text{m}$  protein buffer spots on the top of the SiN resonator, by optimizing the approach velocity and dwell times for the surface patterning tool. We could also achieve a good alignment between the spot and the peak in the electromagnetic mode in the resonator (see Figure 2b).

Finally, we explored several different fluidic channel sealing techniques. One approach was to use a rectangular piece of PDMS (Sylgard 184), treated in oxygen plasma and then attached on the top of the SU-8 microfluidic channel. Another approach that we adopted was direct SU-8 to SU-8 bonding using a SU-8 coated glass cover slip. Prebaking conditions were optimized to enable good bonding. A blanket UV-exposure was used to cure and finally seal the cover slip to the fluidic channel. More optimization of this process is required in order to get a repeatable tight fluidic seal and to avoid fluid leaks.

A prototype sensor consisting of a SiN resonator with a SU-8 microfluidic channel and a PDMS lid was used to evaluate

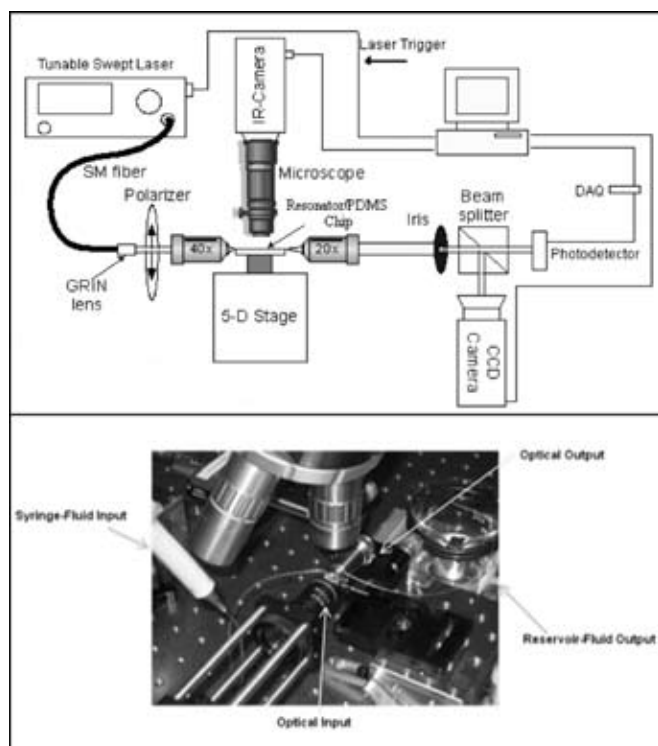


Figure 3: (a) Schematic of optical test setup. (b) Picture showing prototype sensor test using a syringe for fluid injection.

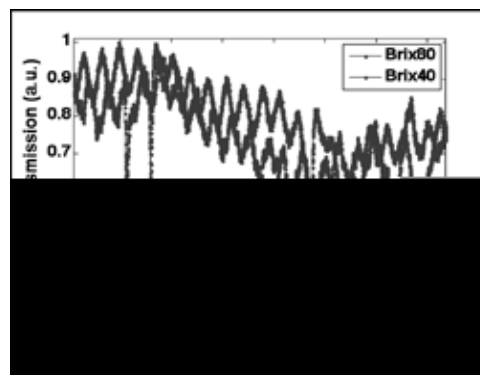


Figure 4: Spectral response of microdisk resonator. Bulk refractive index sensitivity of  $\sim 1 \text{ nm/RIU}$  was experimentally obtained.

initial sensor bulk refractive index sensitivity using Brix fluids injected into the microfluidic channel (Figure 3b). Following fluid injection, the resonance wavelength was obtained by a swept-wavelength test using a tunable laser (New Focus Velocity 650-660 nm) (Figure 3a). We obtained a bulk refractive index sensitivity of  $\sim 1 \text{ nm/RIU}$  (Figure 4). Leaking was observed from the PDMS fluidic seal with prolonged fluid flow and resulted in incomplete removal of fluid and even fluid mixing in the sensor. We anticipate that with a more stable fluidic sealing, fluidic mixing could be eliminated and the sensor sensitivity could be improved.

## Results and Conclusions:

SU-8 microfluidic channels were fabricated directly overlapping SiN microresonators. A technique suitable for fabricating multiplex-sensor arrays was developed by depositing sub-femtoliter volumes of surface coating ligands directly onto the resonator surface within the microfluidic channel. Due to ease of fabrication, PDMS to SU-8 seal using oxygen plasma was adopted in this project for the first sensor prototypes. Bulk refractive index sensitivity of  $\sim 1 \text{ nm/RIU}$  was experimentally obtained. Better fluidic sealing is required in order to prevent leaks and fluid mixing in the sensor.

## Future Work:

One way to improve the fluidic seal would be to use a cover slip. An initial process for such a sealing has been developed by using SU-8 coated glass cover slip and exploiting the SU-8 to SU-8 bonding process to directly seal the SU-8 fluidic channel with the glass cover slip.

## Acknowledgements:

I would like to express my appreciation to the NSF, NNIN REU Program, and Georgia Tech for their funding and facilities. I would like to express my gratitude towards the site coordinator, Jennifer Tatham Root, for providing the interns with all necessities and a productive research environment. I would like to give a special thanks to Dr. Siva Yegnanarayanan, Dr. Ali Adibi, and the members of the Photonics Research Group for their guidance, time, and supplies.

# Flow Cytometry with a Soft Elastomer-on-Silicon Nano Photonic Device for High-Speed Fluorescence Multi-Spectrum Acquisition

Jose Guevarra

Mechanical Engineering, University of California, Santa Barbara

**NNIN REU Site: Lurie Nanofabrication Facility, University of Michigan, Ann Arbor, MI**

NNIN REU Principal Investigator(s): Dr. Katsuo Kurabayashi, Mechanical Engineering, University of Michigan

NNIN REU Mentor(s): Steven Truxal, Mechanical Engineering, University of Michigan

Contact: joseg@engineering.ucsb.edu, katsuo@umich.edu, trux@umich.edu

## Abstract:

Flow cytometry is an invaluable tool in separating and analyzing biological samples. Applications of this technology include medicine, biology, and Homeland Security. This project fabricated a microfluidics flow cell of polydimethylsiloxane (PDMS) to demonstrate on-chip flow cytometry. The fabricated device allowed for detection of fluorescent beads and discrimination of their relative sizes as they passed the interrogation zone. The use of this flow cell in conjunction with a nano photonic microelectromechanical systems (MEMS) device will lead to real-time measurement of fluorescence spectra.

## Introduction:

Traditional multispectral flow cytometry measurements use multiple photomultiplier tubes (PMT) to detect photons of varying wavelengths from fluorescent samples. This approach is costly, requiring complex, bulky optics. Steven Truxal, Yi-Chung Tung, and Dr. Katsuo Kurabayashi have developed a novel MEMS device that uses polydimethylsiloxane (PDMS) as a transparent, flexible nano-grating for diffracting multispectrum light and directing it onto a single photomultiplier tube. Coupled with a well-designed microfluidic flow chamber, the device can be used to realize an on-chip multispectral flow cytometry system.

The object of this project was to fabricate a flow cytometer to generate emission light from fluorescent beads passing through flow cell microchannels as part of our aimed system. This will show whether emission intensities are strong enough for fluorescence spectra measurements.

## Fabrication:

The flow cell consisted of a PDMS slab with micro patterns that acted as inflow, outflow, and microchannels. To make the flow cell mold a 20  $\mu\text{m}$  photoresist layer of SU-8 10 was spun onto a 4 inch silicon wafer. The wafer was then exposed at 11  $\text{mW}/\text{cm}^2$  for 20 seconds with 365 nm light under a pre-existing lithography mask. The wafer was then developed in SU-8 developer until the high aspect ration "hills" were revealed (see step 2 in Figure 1).

Next, PDMS was mixed using the Sylgard 184 silicone elastomer kit (Dow Corning Corporation, 10:1 base-curing agent ratio). The viscous PDMS was placed in a vacuum for 30 minutes to remove any bubbles. The mold was placed in a handmade, aluminum foil cup; PDMS was poured over the

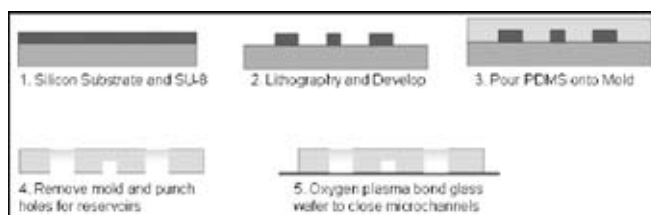


Figure 1: Microfluidics flow cell fabrication.

mold, and then cured at 150°C for 10 minutes. The solidified PDMS was then peeled from the mold. The PDMS now had 20  $\mu\text{m}$  deep patterns that act as microfluidics channels.

The mold consisted of several different patterned microfluidic devices. Each was cut from the PDMS to create individual cytometers. Using a 2 mm biopsy punch, holes were punched through the PDMS to create inflow and outflow openings. The PDMS devices were then treated with a  $\text{O}_2$  plasma along with a thin glass wafer (250 mT, 80 W, 45 seconds, 17%  $\text{O}_2$ , March Asher), then bonded. The flow openings and microchannels were sealed by the glass, leaving openings at the top of the device for inflow and outflow tubing (see Figure 2). Flow cells with channels of 340  $\mu\text{m}$  in width, and 20  $\mu\text{m}$  and 70  $\mu\text{m}$  in depth were fabricated.

## Experiment Setup:

The performance of the fabricated microfluidic flow chamber was characterized by observing individual fluorescent beads passing through its microchannel. By measuring the emission light intensity of fluorescent beads, their relative size can be distinguished. Fluorescent beads of diameters 6.5, 31, and



Figure 2: Flow cell excited on microscope stage.

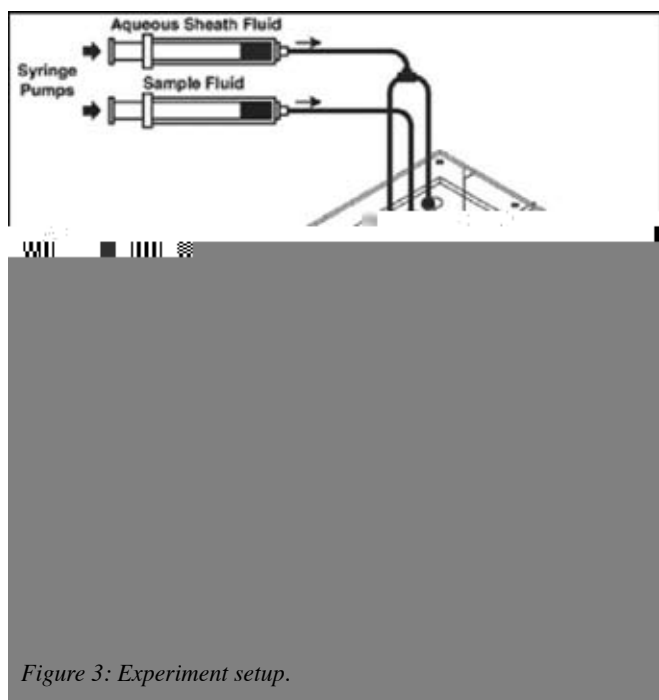


Figure 3: Experiment setup.

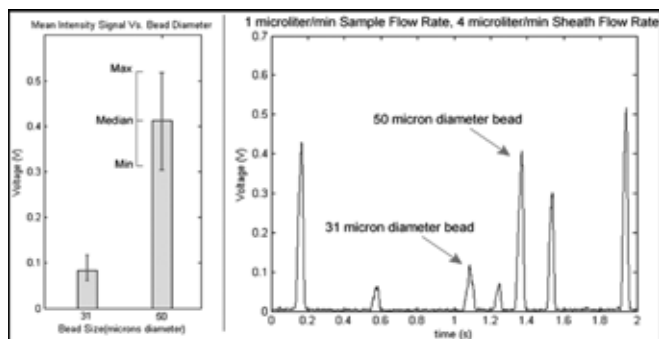


Figure 4: Flow observations.

50  $\mu\text{m}$  were driven through the microchannels. As the beads flowed through the microchannel, they could be observed optically via microscope or the emission light could be directed by fiber optic cable to the PMT for data acquisition (see Figure 3).

## Results and Discussion:

The measured intensities provided information on several characteristics of the bead samples and flow cell. The emission intensities could be compared, as in Figure 3, and their relative sizes of the beads could be determined. The mean intensities for 31  $\mu\text{m}$  beads were about 0.9 V and 0.4 V for 50  $\mu\text{m}$  beads. We also determined that 6.5  $\mu\text{m}$  beads require an oil emersion lens to be detected out of the ambient noise in our system.

## Conclusion:

We demonstrated simple flow cytometry analysis can be done using MEMS technology. The size of different particles can be determined by their emission light intensity. The measurement error may be reduced by using a two dimensional sheathing flow to direct fluorescent particles closer to the objective lens. Emission light intensity passing through the nano photonic device may be reduced to 10%. Experiments show the emission light intensities are high enough for fluorescence spectroscopy measurements.

## Acknowledgements:

National Nanotechnology Infrastructure Network Research Experience for Undergraduates (NNIN REU) Program, the National Science Foundation, and Lurie Nanofabrication Laboratory. I would like to thank Dr. Katsuo Kurabayashi and Steven Truxal for their guidance and help with my project. Thanks to Sandrine Martin and Trasa Burkhardt for their motivation and making the summer a great experience.

## References:

- [1] Yi-Chung Tung, Katsuo Kurabayashi "PDMS-based opto-fluidic micro flow cytometer with two-color, multi-angle fluorescence detection capability using PIN photodiodes"; Sensors and Actuators B 98 (2004) p 356.
- [2] Steven C. Truxal, Yi-Chung Tung, and Katsuo Kurabayashi "High-speed deformation of soft lithographic nanograting patterns for ultrasensitive optical spectroscopy"; Applied Physics Letters; Issue 92, 051116 (2008).

# Incorporating Nanocrystals into the Bilayer of Phospholipid Vesicles

Angela L. Holmberg

Chemical Engineering and Chemistry, University of Minnesota-Twin Cities

**NNIN REU Site: Microelectronics Research Center, University of Texas, Austin, TX**

NNIN REU Principal Investigator(s): Brian A. Korgel, Chemical Engineering, The University of Texas at Austin

NNIN REU Mentor(s): Michael R. Rasch, Chemical Engineering, The University of Texas at Austin

Contact: holmb108@umn.edu, korgel@che.utexas.edu, mr8729@che.utexas.edu

## Introduction:

Phospholipid vesicles are useful tools in biotechnology and medicine because of their subcellular size and ability to encapsulate diagnostic and therapeutic molecules. Hydrophobic nanocrystals with useful optical or magnetic properties embedded in the vesicle's lipid membrane could provide a way to control externally the chemical state or the trans-membrane transport rate of molecules trapped inside the vesicle for controlled release of medicine [1], to enhance resolution in magnetic resonance imaging (MRI) [2], or to permit the tracking of vesicles and medicine within the body.

In this project, varying amounts of 1.5-5 nm gold nanocrystals were mixed with lipid and dialyzed to determine the nanocrystals' influence on vesicle formation. Cryo-transmission electron microscopy (cryo-TEM) and TEM images of the vesicle suspensions revealed that gold nanocrystals smaller than the bilayer thickness were primarily embedded within the vesicle membranes, while larger nanoparticles were primarily centered inside lipid micelles. The size-dependence of the incorporation of the nanocrystals into the vesicle lipid bilayer is important to note as vesicle-embedded nanocrystals are investigated further for drug transport, imaging, and controlled release applications.

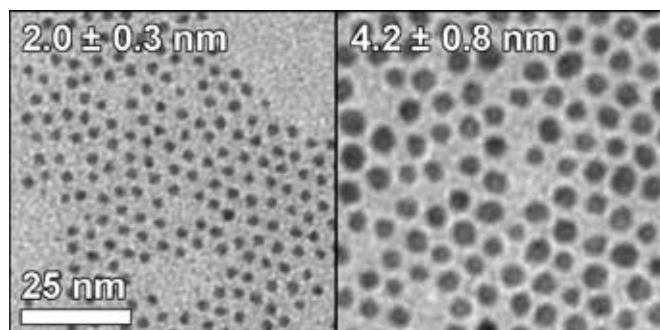


Figure 1: TEM images of separated Au nanocrystals.

## Experimental Procedure:

Hydrophobic gold nanocrystals (Figure 1) were prepared as described by Brust [3] by combining a solution of hydrogen tetrachloroaurate in water (0.03 M, 14.4 mL) to a solution of tetraoctylammonium bromide in toluene

(0.2 M, 9.8 mL) and stirring for one hour. Neat 1-dodecanethiol (5 mmols, 1.2 mL) and an ice-cold aqueous sodium borohydride solution (0.4 M, 12 mL) were sequentially added to the organic layer and stirred for an additional hour. Larger Au nanocrystals were synthesized by a similar procedure except the initial solution was reduced by  $\text{NaBH}_4$  and stirred for four hours before 1-dodecanethiol was added to the organic phase. The resultant Au nanocrystals were centrifuge-washed with methanol at 8000 rpm for five minutes, resuspended in chloroform, and separated by size-selection.

Phospholipid vesicles were synthesized by detergent dialysis for strong membrane integrity and vesicle monodispersity [4]. Egg lecithin (phosphatidylcholine, 0.03 mmols, 0.02 g) and various concentrations and sizes of gold were combined in chloroform and dried under reduced pressure at 40°C. These films were rehydrated with 1 mL of a sodium chloride (0.05 M) and sodium cholate (0.04 M) solution, and equilibrated over two hours with occasional swirling. The lipid solutions were then transferred to wetted dialysis bags and suspended in aqueous NaCl solutions (0.05 M, 0.1 L). The water was changed approximately every four hours over 24 to 28 hours, or whenever possible. Resultant vesicle solutions appeared opalescent or tinted purple or brown depending on the size and concentrations of gold. Carbon-coated copper TEM grids of diluted samples were dried and later stained with uranyl acetate for imaging.

## Results and Discussion:

High contrast spots visible in the TEM images (Figure 2) of samples prepared with Au measuring  $2.0 \pm 0.3$  nm in diameter indicate that nanocrystals were incorporated into the vesicles. Unfortunately, due to the dark contrast of the uranyl acetate stain, the small size of the nanocrystals, and the ability of the stain to leak under the edges of the vesicles, it was often difficult to distinguish spots of gold from the stained background. The lipid membrane itself was not stained and therefore not visible either, which made it difficult to determine where exactly the nanocrystals were located relative to the lipid bilayer. As such,

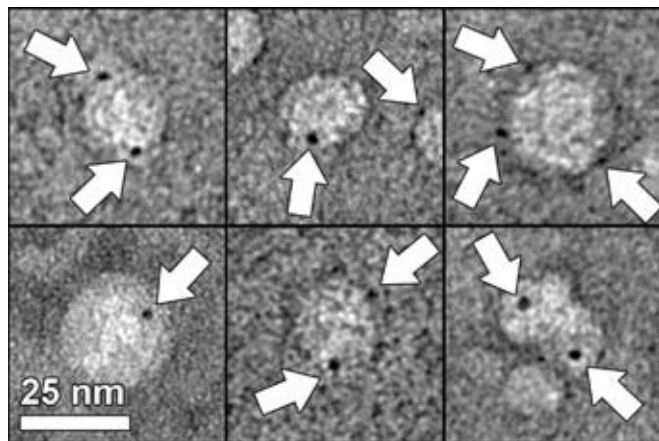


Figure 2: TEM images of stained vesicles with arrows pointing to "small" Au particles.

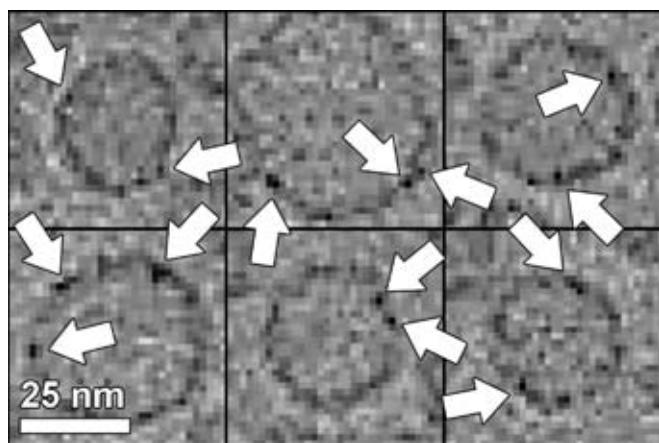


Figure 3: Cryo-TEM images of vesicles with arrows pointing to "small" Au particles.

cryo-TEM (Figure 3) was necessary to better understand how the nanocrystals affected the vesicles. The cryo-TEM images reveal many high contrast spots clearly visible inside the lipid bilayer walls of the vesicles, confirming that the  $2.0 \pm 0.3$  nm Au nanocrystals added at a concentration of 0.3 mg/mL were in fact embedded within the vesicle walls. Nanocrystals were found to aggregate and precipitate out of solution at higher concentrations, and consequently were not analyzed under cryo-TEM. In these cases, there were not enough lipid molecules to completely encapsulate the particles and prevent them from coming in contact with water.

Larger Au nanocrystals measuring  $4.2 \pm 0.8$  nm in diameter behaved somewhat differently. While TEM micrographs (Figure 4) showed that some of the nanocrystals were embedded in the presumed bilayer membrane of vesicles, other nanocrystals appeared trapped in the center of micelle structures. Presumably, nanocrystal-induced bulges in the lipid bilayer equilibrate toward micelles, and crowded lipid molecules in the micelles favor incorporation into the vesicles.

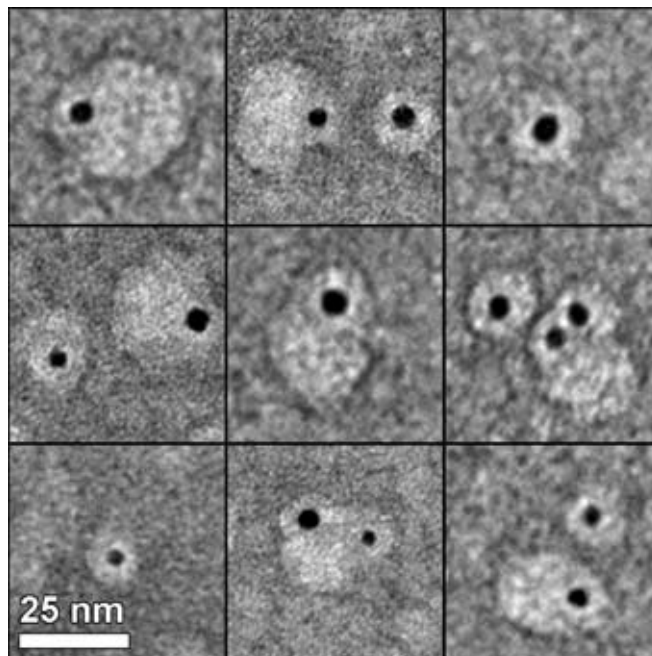


Figure 4: TEM images of a stained vesicle sample with "large" Au nanocrystals.

#### Future Work:

To further investigate the effect of nanocrystals on vesicle formation, fresh vesicle samples prepared with "large" nanocrystals will need to be synthesized for cryo-TEM analysis. Other future endeavors include incorporating iron oxide nanocrystals into the vesicle walls, and attempting to separate out micelles from vesicles via size-exclusion chromatography.

#### Acknowledgements:

Much thanks to Dr. Brian Korgel for this opportunity, Michael Rasch for his guidance and support, Jordi Arbiol and his research group at the University of Barcelona for their cryo-TEM images, Jean Toll for her hospitality, and both the National Nanotechnology Infrastructure Network Research Experience for Undergraduates (NNIN REU) Program for funding.

#### References:

- [1] Paasonen, L.; Laaksonen, T.; Johans, C.; Yliperttula, M.; Kontturi, K.; Urtti, A.; "Gold Nanoparticles Enable Selective Light-Induced Contents Release from Liposomes"; *J. Cont. Release*, 122, 86-98 (2007).
- [2] Pankhurst, Q. A.; Connolly, J.; Jones, S. K.; Dobson, J.; "Applications of Magnetic Nanoparticles in Biomedicine"; *J. Phys. D: Appl. Phys.*, 36, R167-R181 (2003).
- [3] Brust, M.; Walker, M.; Bethell, D.; Schiffrin, D. J.; Whyman, R.; "Synthesis of Thiol-derivatised Au Nanoparticles in a 2-phase Liquid-Liquid System"; *J. Chem. Soc., Chem. Commun.*, 7, 801-802 (1994).
- [4] Korgel, B. A.; Van Zanten, J. H.; Monbouquette, H. G.; "Vesicle Size Distributions Measured by Flow Field-Flow Fractionation Coupled with Multiangle Light Scattering"; *Biophys. J.*, 74, 3264-3272 (1998).

# Glass-Frit Bonding for Selective Functionalization and Packaging of Biosensors

Pradeep Hothur

Department of Electrical Engineering, San Jose State University

**NNIN REU Site: Microelectronics Research Center, Georgia Institute of Technology, Atlanta, GA**

NNIN REU Principal Investigator(s): Dr. Oliver Brand, Electrical and Computer Engineering, Georgia Tech

NNIN REU Mentor(s): Luke A. Beardslee, Electrical and Computer Engineering, Georgia Institute of Technology

Contact: bauerstatus@gmail.com, oliver.brand@ece.gatech.edu, luke.beardslee@gatech.edu

## Abstract:

In an effort to enhance diagnostic techniques for diseases, the development of microelectromechanical system (MEMS) biosensors offers a novel approach towards mass producing inexpensive reliable sensors. The objective of this project is to effectively package a biosensor through a glass-frit bonding process using a screen printer. In particular, the process outlined here is meant to work with mass sensitive biosensors; these sensors work by inducing a change in resonant frequency based on the change in mass due to analyte attaching to the sensor, i.e. protein binding. Upon completion of the research, packaging wafers have been successfully micromachined and etch rates and etch rate selectivity for the required silicon etching was established. Furthermore the glass-frit material was successfully screen-printed onto a packaging wafer, which was then bonded to a test wafer. Future work will include bonding a packaging wafer to a wafer with actual sensors.

## Introduction:

As a means to test our biosensors, we initially resorted to individually assembling them using die-level packaging; the process involved placing a plastic ring onto the resonator chip to form a sample fluid cavity. This however proved to be ineffective for three reasons. To begin with, it was time consuming to place the plastic rings. Second, the resonators and wire bonds could easily break as a result of inserting the plastic rings by hand. Finally, an exact amount of epoxy had to be placed to glue the rings: too much destroyed the resonators and too little resulted in an insufficient seal. The glass-frit bonding process alleviates these problems utilizing wafer-level packaging. The screen-printing process allows to package many resonator dies at once and greatly diminishes the chances of breaking the resonators. Furthermore, the glass-frit bonding is of interest since it is cost effective process, provides a hermetic seal, and can tolerate the surface roughness on the wafer being bonded.

## Fabrication:

Fabrication started by depositing  $2\ \mu\text{m}$  and  $4\ \mu\text{m}$  of oxide on the top and backside of the packaging wafer, respectively. Following standard photolithographic protocols, proximity photolithography and etching in an inductively coupled plasma (ICP) tool were used to pattern the oxide film on the top of the packaging wafer (step 3 in Figure 1). Once we confirmed that the oxide was etched down to the silicon using optical microscopy, we patterned the backside oxide film using a double-side mask aligner (step 4 in Figure 1).

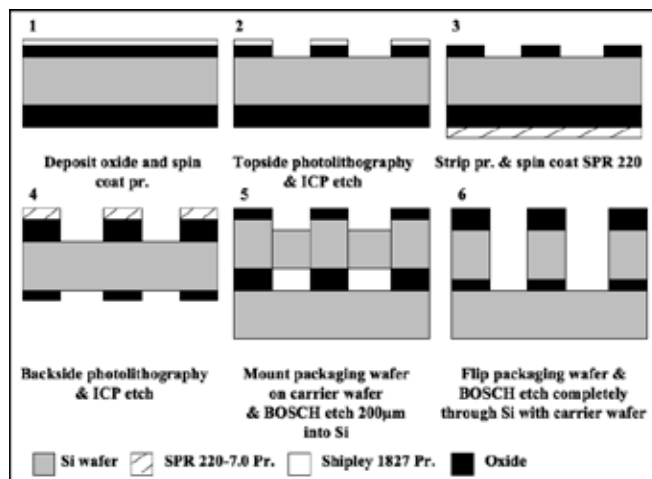


Figure 1: Diagram of fabrication process.

Using the BOSCH process, we then etched  $200\ \mu\text{m}$  into the silicon wafer from the topside and then etched completely through the wafer from the backside. This process allowed us to wedge the resonators in the windowed areas on the packaging wafer. Continuing the fabrication, we screen-printed the glass-frit material (DIEMAT, Byfield, MA) onto the packaging wafer (Figure 2). In order to eliminate the organic binder in the glass-frit material, we then went through an organic burnout process. This process step glazed the glass-frit material to the substrate, an initial step towards completing the bonding process. The fabrication was then completed by bonding the packaging wafer to a test wafer.

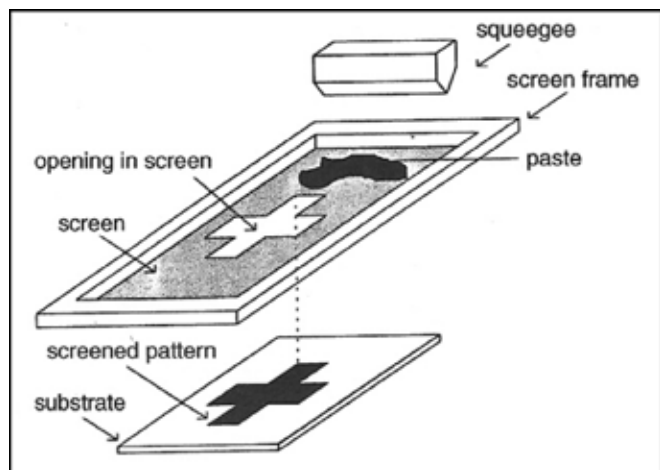


Figure 2: Diagram of screen printer.

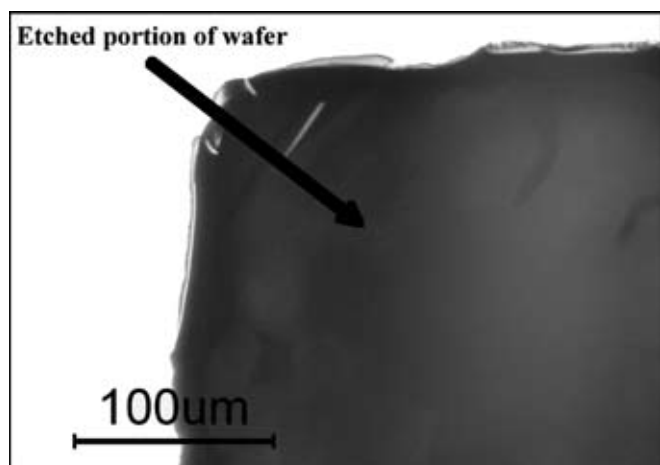


Figure 3: Micrograph of windowed area on packaging wafer after through-wafer etch.

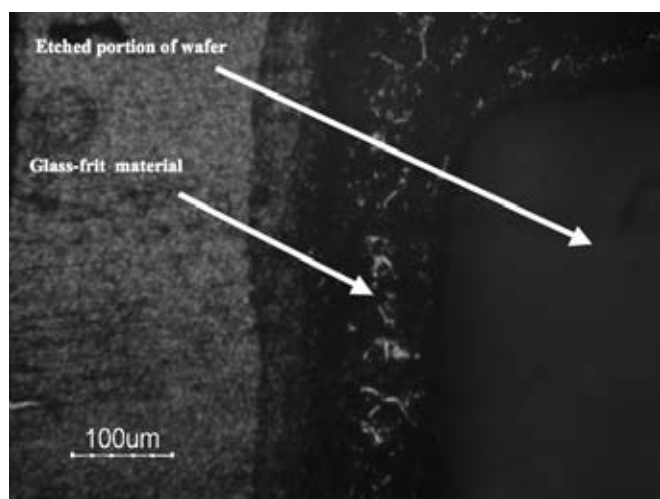


Figure 4: Micrograph of windowed area on packaging wafer after organic burnout and glazing.

## Results:

The packaging wafer was successfully fabricated and the fabrication steps were carefully characterized. For the silicon etching with the Bosch process, we acquired an etch rate of  $800\text{\AA}/\text{cycle}$  and an etch rate selectivity to  $\text{SiO}_2$  of 178 to 1. Shipley 1827 photoresist was used for the topside photolithography, while Megaposit SPR 220-7.0 photoresist was used for the backside photolithography, due to the difference in oxide thickness. The thickness of the screen-printed glass-frit ranged from  $30\text{-}50\ \mu\text{m}$ . In order to confirm whether this thickness will suffice, the packaging wafer has to be bonded to the device wafer. In the present research, we were able to successfully bond the packaging wafer to the rough side of a prime wafer.

## Future Work:

We hope to completely characterize the glass-frit bonding process and to bond the packaging wafer to a device wafer with resonant microstructures to acquire fully packaged biosensors.

## Acknowledgements:

I would like to sincerely thank my mentor Luke Beardslee, my principal investigator Dr. Oliver Brand, and my site coordinator Jennifer Root. I would also like to thank Dr. James Meindl, the staff of the Microelectronic Research Center, the National Nanotechnology Infrastructure Network Research Experience for Undergraduates (NNIN REU) Program, and the NSF without which this research would not have been possible.

## References:

- [1] Madou, Marc J. Fundamentals of Microfabrication: The Science of Miniaturization. Boca Raton: CRC Press, 2002.
- [2] Hyeong, Jae, and Oliver Brand. "High Q-factor In-Plane-Mode Resonant Microsensor Platform for Gaseous/Liquid Environment." Journal of Microelectromechanical Systems 17 (2008): 483-93.

# Synthesis and Characterization of Multifunctional Magnetic Nanoparticles for Treatment of Cystic Fibrosis

Adam Jakus

Materials Science and Engineering, Georgia Institute of Technology

**NNIN REU Site: Nanoscience @ UNM, University of New Mexico, Albuquerque, NM**

NNIN REU Principal Investigator(s): Marek Osinski, Electrical and Computer Engineering, Computer Science, Physics and Astronomy, University of New Mexico

NNIN REU Mentor(s): Tosifa Memon, Biochemistry, University of New Mexico; Krishnaprasad Sankar, Electrical Engineering, University of New Mexico

Contact: adamjakus@gatech.edu, osinski@chtm.unm.edu, tmemon@unm.edu, krishna@unm.edu

## Introduction:

Cystic fibrosis is an inborn genetic disorder that results in a defective transmembrane regulator protein. As a result, the salt concentration within the body's various systems cannot be adequately controlled, producing excess sweat as well as excess viscous mucus in the pancreas, liver, intestines, and lungs that cannot be expelled through by the body's usual processes. Current treatments for infections of the lungs resulting from the stagnant environment are not effective. As a consequence, most individuals with cystic fibrosis die from infections of *Pneumonia aeruginosa* that could normally be treated using antibiotics, but because of the thick mucus barriers, these drugs cannot be efficiently delivered to the sites of infection.

A new method is required to facilitate the transport of antibiotics through the thick mucus. One potential method, and the subject of this work, is to conjugate antibiotic molecules to iron oxide nanoparticles that display superparamagnetic properties. These nanoparticles could then be directed through the lungs to the regions of infection by applying a direct magnetic field, while simultaneously applying a perpendicular, high frequency alternating magnetic field to induce vibrations causing localized heating, thereby easing the transport of the particles through the mucus. This work focuses on the synthesis of magnetic nanoparticles, their hydrophilization and multifunctionalization with ZnS, fluorescent CdSe quantum dots, and an additional layer of ZnS to allow for easy optical characterization of the dynamic properties of the particles under the influence of a magnetic field *in vitro*.

## Experimental Procedure:

The iron oxide nanoparticles were synthesized according to a procedure outlined in detail by Selvan, et al. [1], using a hyperthermal process under a nitrogen atmosphere resulting in hydrophobic particles. A solution of iron pentacarbonyl and oleic acid was refluxed at 290°C, contrary to the 200°C suggested in [1], until it turned black in color, upon which an oxidizer, trimethylamine N-oxide, was added.

The final solution was centrifuged to separate out the nanoparticles. These nanoparticles were suspended in hexane and tested using a small magnet to obtain a qualitative determination of their magnetic character. Hydrophilization of the iron oxide cores was attempted using a reduced form of lipoic acid.

A portion of the hydrophobic iron oxide particles were coated with ZnS/CdSe/ZnS following Du, et al. [2] and previous work completed in Dr. Marek Osinski's lab [3]. The particles were injected into a solution of trioctylphosphine oxide and hexadecyl amine under nitrogen prior to injection of zinc and sulfur precursors. Separate solutions of zinc and sulfur precursors were prepared and injected into the hot iron oxide solution in equal volume increments sequentially and allowed

to react. Additional zinc sulfide (ZnS) layers were added by performing more injections; typically three ZnS layers were used to cap the iron oxide particles.

A cadmium selenide (CdSe) layer was added to add optical functionality to the particles. This layer was synthesized by first producing a precursor solution of cadmium acetate and selenium in trioctylphosphine. This precursor solution was allowed to interact with the iron oxide/ZnS nanoparticles at elevated temperatures. Upon completion of the reaction, additional capping layers of ZnS were added on top of the CdSe, using the same procedure as previously described.

## Results and Discussion:

Iron oxide nanocrystals without (Figure 1) and with (Figure 2) ZnS coating were imaged using a transmission electron microscope. From the tunneling electron microscopy (TEM) images, it is apparent that the iron oxide nanoparticles are highly monodisperse at ~2-3 nm. These results were produced several times over, indicating reproducibility. Upon addition of the ZnS capping layers, the diameter of the particles increased

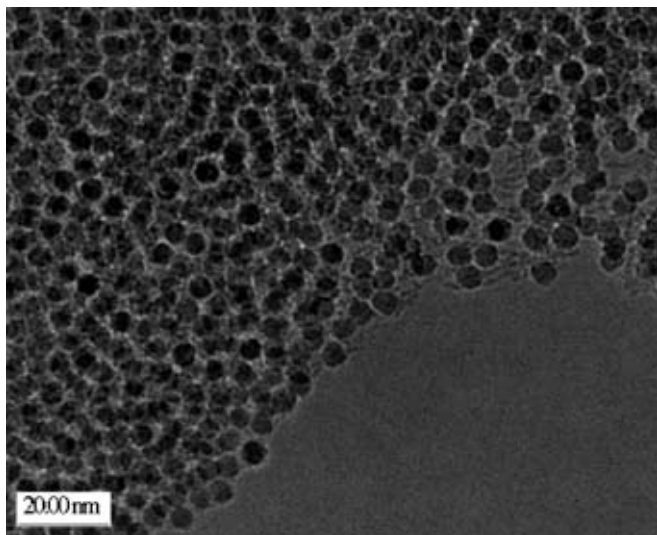


Figure 1: TEM image of iron oxide nanoparticles.

to ~ 10-12 nm. X-ray diffraction (Figure 3) indicates that the iron oxide particles are a mixture of maghemite and magnetite. Although the synthesis outlined by [1] was aimed at producing maghemite, the mixture of species has no negative impact on the magnetic character of the particles as both have inherent superparamagnetic properties at the nanoscale.

Synthesis of the multifunctional iron oxide/ZnS/CdSe/ZnS was unsuccessful. Their magnetic character was minimal, and their absorbance spectrum (Figure 4), indicates limited to no optical excitation, which would be present if the quantum dots were synthesized correctly. From TEM images (not shown), it appears that the CdSe particles were too large to fluoresce and effectively coat the smaller iron oxide/ZnS particles.

The success of the hydrophilization attempts of the iron oxide with reduced lipoic acid is unknown. The necessary equipment required to successfully centrifuge out the small quantity of altered nanocrystals was not present and not available in the time permitted for this research.

### Conclusions and Future Work:

Although the synthesis of multifunctional nanoparticles was unsuccessful, the reproducibility of highly monodisperse iron oxide cores is a big step in the right direction. These particles showed significant magnetic character, a necessary property for the proposed application. In addition to the success of the synthesis of the cores was their capping with ZnS.

The procedure for multifunctionalization will need to be modified and perfected before characterization can be done investigating the behavior of these particles within a direct and an alternating magnetic field. Additionally, hydrophilization techniques with lipoic acid, or possibly polyethylene glycol, will need to be perfected.

Figure 2: TEM image of ZnS capped iron oxide nanoparticles.

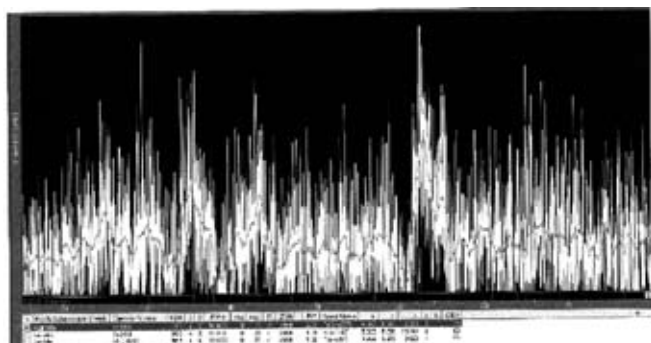


Figure 3: X-ray diffraction profile of iron oxide nanoparticles.

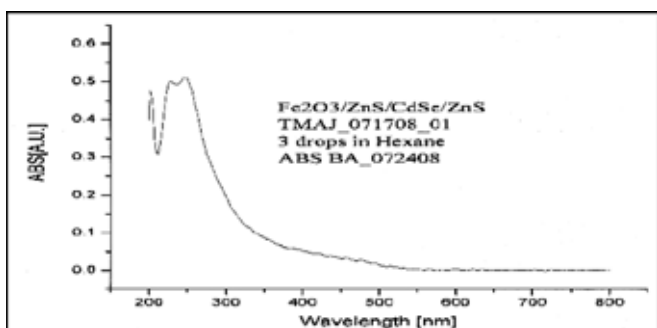


Figure 4: Absorption spectrum of iron oxide/ZnS/CdSe/ZnS.

### Acknowledgments:

I would like to thank Prof. Marek Osinski, Tosifa Memon, and Krishnaprasad Sankar for their guidance and support of this work. I would also like to thank Stefi Weisburd, Site Coordinator, for all her help.

This work was funded by the National Science Foundation through the National Nanotechnology Infrastructure Network Research Experience for Undergraduates Program at the University of New Mexico.

### References:

- [1] S.T. Selvan, P.K. Patra, C.Y. Ang, J.Y. Ying, "Synthesis of Silica-Coated Semiconductor and Magnetic Quantum Dots and Their Use in the Imaging of Live Cells," *Angew Chem. Int. Ed.*, vol. 46, no. 14, pp. 2448-2452, 2007.
- [2] G.H. Du, Z.L. Liu, Q.H. Lu, et al., "Fe<sub>3</sub>O<sub>4</sub>/CdSe/ZnS Magnetic Fluorescent Bifunctional Nanocomposites," *Nanotechnology*, vol. 17, no. 12, pp. 2850-2854, 2006.
- [3] Melisa Greenberg and Shin Bowers, "Procedure for CdSe Colloidal Nanocrystal with ZnS Coating Synthesis."

# Nano and Microfluidics for Single Molecule Biophysics Applications

Patrick Journey

Mechanical Engineering, University of Portland

**NNIN REU Site: Nanoscience @ UNM, University of New Mexico, Albuquerque, NM**

*NNIN REU Principal Investigator(s): Dr. Steven Koch, Center for High Technology Materials, University of New Mexico*

*NNIN REU Mentor(s): Lawrence Herskowitz, Center for High Technology Materials, University of New Mexico*

*Contact: journey09@up.edu, sjkoch@unm.edu, lherskow@unm.edu*

## Abstract:

The recently developed abilities to manipulate and visualize single deoxyribonucleic acid (DNA) molecules are making a significant impact on discoveries in cellular and molecular biology. Innovations in micro- and nanofluidics are an important enabler of single-molecule techniques. Two projects were pursued, one to develop microfluidic devices for optical tweezers applications and one to develop porous nanochannel devices for elongation of single DNA molecules. First, microchannel devices were fabricated using polydimethylsiloxane (PDMS) cured on microfabricated silicon templates for future use with optical tweezers in DNA unzipping applications. The ability to form single-molecule DNA-microsphere tethers was demonstrated. Second, porous-wall nanochannels were fabricated using interferometric lithography and silica nanoparticles for use in visualizing fluorescently labeled DNA molecules. The ability to elongate and visualize lambda phage DNA molecules was confirmed in nanochannels on both silicon and quartz substrates. Both of these achievements are an important foundation for future work in analysis of protein-DNA interactions, including a specific goal of analyzing single chromatin fibers isolated from living cells.

## Purpose:

With DNA tethers in microchannels, an optical tweezers apparatus can be used to “unzip” the DNA constructs and ultimately to map where nucleosomes occur on chromatin in living cells by comparing force profiles with thermodynamically predictable controls. While very powerful, the current method of Chromatin Immunoprecipitation (ChIP) and real-time polymerase chain reaction (PCR) has problems with sensitivity and other drawbacks. With mapping by single-molecule unzipping, the accuracy would be improved to approximately three base pairs compared to about 100 base pair accuracy with the current method and will reveal correlations on single molecules [1]. Mapping where nucleosomes occur on chromatin in living cells may also be achievable by labeling histones with either gold nanoparticles or quantum dots and elongating them in nanochannels.

## Experimental Procedure:

Photolithography techniques were employed for the fabrication of both the microchannels and the porous nanochannels. The microchannels were first designed using AutoCAD and a mask was printed using an inkjet printer (CAD/Art Services Inc, Bandon, OR). SU-8 2025 photoresist (Microchem Corp, Newton, MA) was then spin coated onto a silicon wafer, exposed, and developed. PDMS (Microchem Corp.) was then mixed with a curing agent and poured over the wafer to create the desired patterns. Finally the PDMS was cut from the template and attached to a glass cover-slide using plasma

surface activation. Fluid could then be pumped through the channels either by a syringe pump or, more crudely, syringes, in order to create the desired tethers.

Porous nanochannel fabrication involved bottom-up self-assembly and top-down pattern definition. An anti-reflective coating or ARC was spin coated onto a quartz or silicon substrate followed by photoresist. Interferometric lithography was then used to expose the chip in a periodic fashion, the exposed chip was then developed creating a template around which the silica nanoparticles were applied using several spin coatings (Figure 1). High temperature calcination was then used to remove the photoresist and enhance the structural stability of the nanoparticle assembly by strengthening the binding between adjacent particles [2]. Lambda DNA (New England BioLabs, Ipswich, MA) stained with YOYO-1 (Invitrogen, Carlsbad, CA) was then placed in the channels and visualized.

## Results:

We have familiarized two effective methods of enabling chromatin mapping and general single molecule biophysics research. DNA constructs were assembled in PDMS microchannels. The ability to form tethers was confirmed by observation of microspheres undergoing constrained Brownian motion. Lambda DNA stained with YOYO-1 was visualized in the porous nanochannels using both silicon and quartz substrates (Figure 2).

## Conclusions and Future Work:

This work has been an effective enabler of numerous biophysics applications. The most immediate work is attaching thinner PDMS segments to the glass cover-slides so that optical tweezing may be effectively performed without too much scattering. With respect to the nanochannels; attaching PDMS and automating the flow process so that single DNA molecules can be elongated and visualized in about thirty seconds would be a huge accomplishment. Labeling nucleosomes in chromatin extracted from yeast cells with gold nanoparticles or quantum dots and elongating them in these nanochannels is also a priority.

## Acknowledgements:

A special thank you is extended to Dr. Steve Koch, my mentor Larry Herskowitz, Anthony Salvagno and the entirety of the Koch Lab along with Deying Xia and the Brueck lab. I would also like to thank Nick Carroll and the Lopez lab for facilitating the use of the Keck Nanofluidics Laboratory, the Center for High Technology Materials, the University of New Mexico, the National Science Foundation, and the National Nanotechnology Infrastructure Network Research Experience for Undergraduates (NNIN REU) Program for their support of my summer in the land of enchantment.

## References:

- [1] Koch, S. J., A. Shundrovsky, B. C. Jantzen, and M. D. Wang. Probing protein-DNA interactions by unzipping a single DNA double helix. *Biophys J* 83:1098-1105 (2002).
- [2] Deying Xia, Thomas C. Gamble, Edgar A. Mendoza, Steven J. Koch, Xiang He, Gabriel P. Lopez, and S. R. J. Brueck. DNA Transport in Hierarchically-Structured Colloidal-Nanoparticle Porous-Wall Nanochannels (2008).

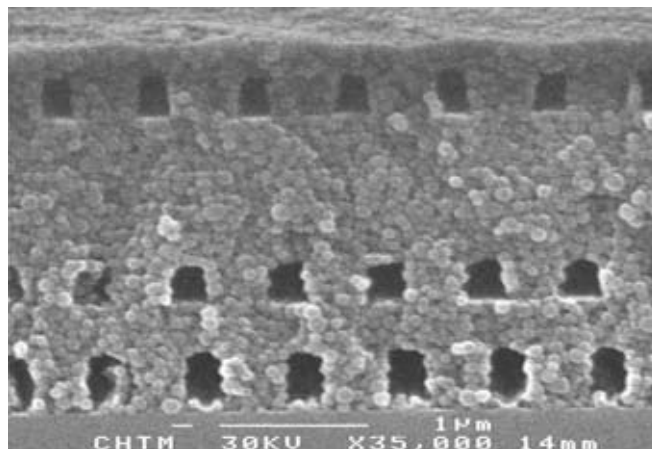


Figure 1: Edge on view of silica nanochannels after calcination demonstrating localized sintering and structural stability (1).

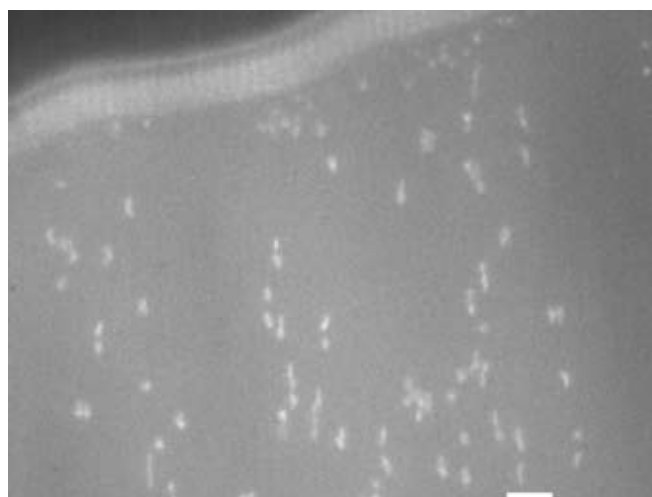


Figure 2: Lambda DNA (bright white streaks) elongated in nanochannels. Scale bar = 5 microns.

# Fluorescent Silver Nanoclusters Self-Assembled on DNA

Kishore Padmaraju

Physics, University of Rochester

**NNIN REU Site: Nanotech @ UCSB, University of California, Santa Barbara, CA**

NNIN REU Principal Investigator(s): Dr. Deborah Fygenon, Physics, University of California, Santa Barbara

NNIN REU Mentor(s): Patrick O'Neill, Physics, University of California, Santa Barbara

Contact: kishore.padmaraju@rochester.edu, deborah@physics.ucsb.edu, patrick@physics.ucsb.edu

## Introduction:

Fluorescent chemical groups, known as fluorophores, are essential to fields such as biology and medical imaging. Our group has been investigating a completely new class of fluorophores: silver nanoclusters self-assembled on deoxyribonucleic acid (DNA). These fluorophores are especially interesting because simple changes to their DNA sequence or structure can effectively tune their spectral properties. We are trying to resolve just how sequence and structure influence spectra by investigating and characterizing these fluorescent nanoclusters.

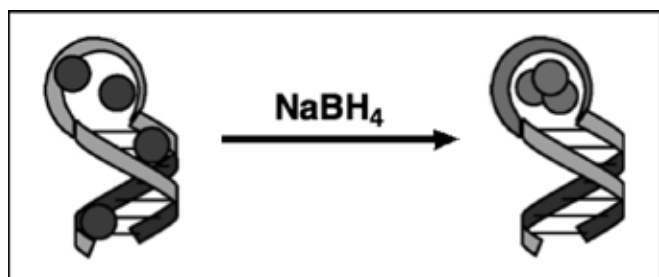


Figure 1: Synthesis of Ag nanocluster.

## Synthesis:

Fluorescent silver nanoclusters are hosted in loops comprised of a single strand of DNA bases, also known as hairpins. To synthesize the nanoclusters, we prepare 25  $\mu\text{M}$  of the DNA strand in a solution of 50-500  $\mu\text{M}$  free Ag ions. Adding 25-325  $\mu\text{M}$   $\text{NaBH}_4$ , a reducing agent, enables the formation of Ag clusters in the hairpins of the DNA (Figure 1).

The synthesis typically produces two or three species of fluorescent nanoclusters, differentiated by their excitation and emission wavelengths. The DNA strand determines which species of fluorescent nanoclusters are produced. Ag and  $\text{NaBH}_4$  concentrations, as well as the temperature and pH of the solution, determine the proportions of the different nanoclusters.

## Experimental Design:

We used fluorescence spectroscopy to characterize the fluorescence of the nanoclusters. Using a fluorimeter, we performed emission scans at incremented excitation wavelengths. From these emission scans we can identify the peak excitation and emission wavelengths of the fluorescent nanoclusters.

We also used mass spectrometry to determine the distribution of cluster sizes in the hairpins. In order to distinguish fluorescent clusters from non-fluorescent clusters at least two sets of data are needed. We identify the fluorescent clusters by correlating a shift in the relative intensity of emitters with a shift in the cluster distribution. To determine the size of the fluorescent clusters we vary the synthesis conditions, often the Ag concentration.

Hairpin loops composed of strictly cytosine bases are the most effective at generating fluorescent nanoclusters. Previous work in this group investigated the 9C hairpin (9C hairpin). The 9C hairpin hosts a green emitter and a red emitter with emission wavelengths 530 nm and 650 nm, respectively. Fluorescence spectroscopy and mass spectrometry identified the  $\text{Ag}_{11}$  cluster as the green emitter and the  $\text{Ag}_{13-15}$  clusters as red emitters.

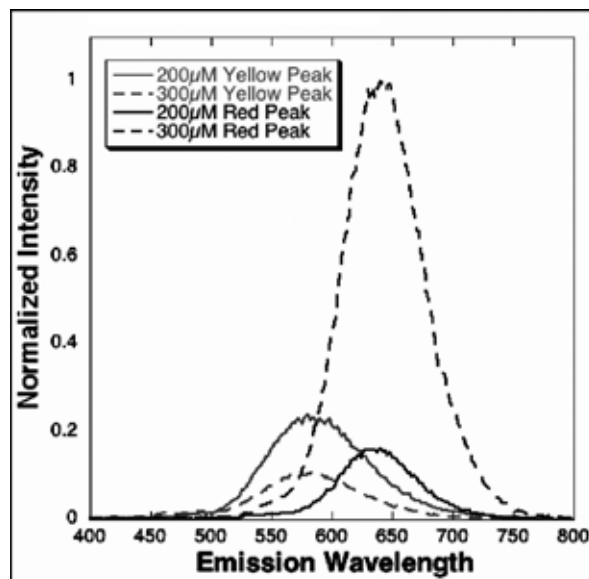


Figure 2: Emission scans of 12C hairpin.

Our research investigated nanoclusters hosted in 12C hairpins. The 12C hairpin hosts a yellow emitter with emission wavelength 580 nm and a red emitter with emission wavelength 650 nm. The red emitters of the 9C and 12C hairpins have the same excitation and emission wavelengths. Our goal was to determine whether the size of the 12C's red emitter was the same size as that of the 9C hairpin. Confirmation would support the hypothesis that the number of Ag atoms comprising the nanocluster is a major determinant of its spectral characteristics.

## Results and Conclusions:

With the 12C hairpin, we found that lower concentrations of Ag during synthesis favored the yellow emitter and that higher concentrations of Ag favored the red emitter. Figure 2 depicts normalized emission scans of the red and yellow fluorescence for Ag concentrations of 200  $\mu\text{M}$  and 300  $\mu\text{M}$ . Given the low concentration of emitters in these solutions, we expect a linear relationship between the fluorescence and the number of emitters. Increasing the Ag concentration from 200  $\mu\text{M}$  to 300  $\mu\text{M}$  decreases the number of yellow emitters by a factor of two and increases the number of red emitters by a factor of five.

The cluster size distribution in Figure 3 displays a broad shift in cluster sizes between samples. By contrast with previous work on the 9C hairpin, where specific clusters were identified as emitters, we can only establish ranges of 3-7 atom clusters for the yellow emitter and clusters of 13 atoms or more for the red emitter. We attempted to identify the emitter sizes using selective photobleaching, that is, exposing the sample to intense light that had been filtered to contain only the excitation light of one of the emitters. Due to the limited photostability of these fluorophores, we expected the excited emitter to stop fluorescing and the non-excited emitter to retain its fluorescence. We exposed the nanoclusters for 5 minutes to a mercury lamp filtered to excite only the red emitter. The fluorescence of the yellow emitter was preserved while the

fluorescence of the red emitter was diminished by a factor of three. However, the mass spec spectra of two samples showed no difference in distribution of cluster sizes, prohibiting the identification of fluorescent emitters and indicating that the cluster fluorescence is more strongly determined by factors other than cluster size.

Focusing on the yellow emitter of the 12C hairpin, we analyzed a different strand that hosted the same yellow emitter, the 6C dumbbell. The 6C dumbbell consists of a duplex with a 6C hairpin on both ends. Fluorescence of the 6C dumbbell has a temperature sensitivity that we were able to exploit. When a sample, originally synthesized in refrigerated conditions, was incubated for 15 hours at 35°C, the number of yellow emitters decreased by a factor of 1.5 and the number of red emitters increased by a factor of 5. Surprisingly though, the mass spec, shown in Figure 4, again indicates no change in the cluster distribution between samples.

The ranges of cluster sizes established for the emitters are consistent with the hypothesis that the number of Ag atoms determines nanocluster fluorescence. However, our photobleaching and incubation experiments suggest that cluster fluorescence is determined not only by the number of Ag atoms, but also by features such as cluster geometry, cluster charge, or specific Ag-DNA bonds as well. Our work has been instrumental in helping this group determine to redirect further research on these fluorophores towards such features.

## Acknowledgments:

I would like to thank my mentor Patrick O'Neill and Dr. Deborah Fygenon for the time and resources they dedicated throughout my research experience. I would also like to thank the Fygenon group for their input, as well as the National Nanotechnology Infrastructure Network Research Experience for Research Program and National Science Foundation.

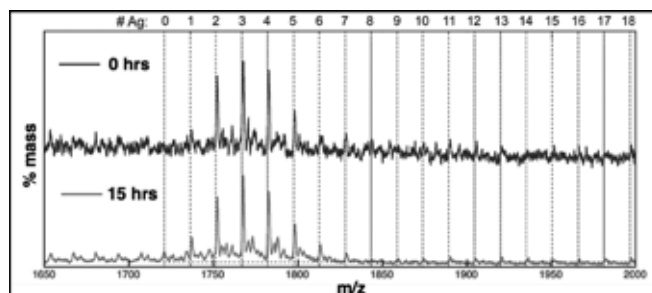
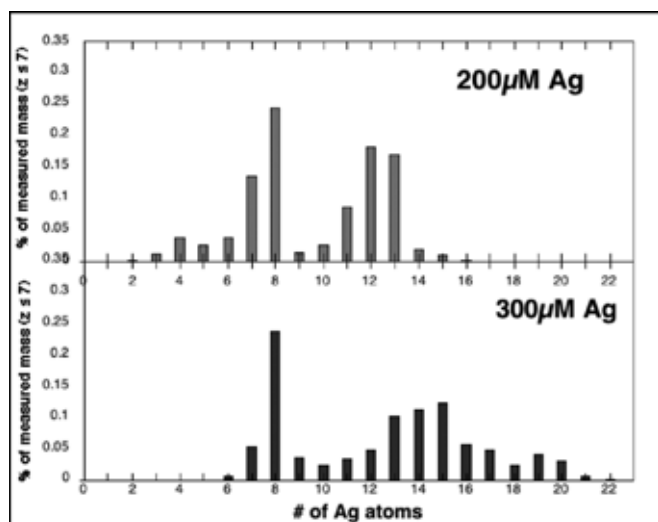


Figure 3, left: Cluster distribution of 12C hairpin.

Figure 4, above: Mass spec of 6C dumbbell.

# A Wireless Remote Biosensor for the Detection of Biological Agents

Taemee Pak

Chemical Biology, Stony Brook University

**NNIN REU Site: Cornell NanoScale Science and Technology Facility, Cornell University, Ithaca, NY**

*NNIN REU Principal Investigator(s): Dr. Carl Batt, Food Science, Cornell University*

*NNIN REU Mentor(s): Matthew Kennedy, Electrical and Computer Engineering, Cornell University*

*Other Contributors/Mentors: Scott Stelick, Clarissa Lui, Diego Rey; Cornell University*

*Contact: tpak@ic.sunysb.edu, cab10@cornell.edu, mjk67@cornell.edu*

## Abstract:

A biosensor capable of wireless data transfer has been designed, fabricated, and tested. The sensor uses aptamers immobilized to a pair of interdigitated electrodes to detect *Staphylococcus enterotoxin B* (SEB). We have designed a solvent-free method to fabricate sensor chips comprised of interdigitated gold electrodes (150 nm thickness) evaporated onto a silicon substrate. The electrodes are functionalized with thiol-modified aptamers that were chosen based upon their bioaffinity for the target analyte. Upon contact with SEB, discriminative binding between SEB and electrode-bound aptamers occurs thereby producing an observable change in the electrical properties of the electrodes. A minimum two-fold increase in capacitance resulted from sensor exposure to SEB in comparison to exposure to non-specific proteins, thereby demonstrating device sensitivity and selectivity for the target analyte. Ultimately, we envision that this device may be used for remote detection of biological agents, thereby limiting the exposure of humans to potential biological threats.

## Introduction:

A device with the ability to sensitively and selectively detect target molecules is a technology of interest because of its applications in military and public health sectors. Electronic biosensors may be manufactured at small dimensions with small features while necessitating very low power. They may also be connected to a system consisting of a data acquisition and a base station module that wirelessly transmits data from the sensor to a computer for analysis. Though electronic sensors have shown sensitivity, selectivity has been a persistent issue and has forced current biosensors to rely on optical methods such as surface plasmon resonance and molecular flow cytometry which require on-site illumination and power sources. An electronic biosensor with wireless capabilities will introduce a new generation of nanoscale biosensors.

## Experimental Procedure:

**Sensor Fabrication.** 2  $\mu\text{m}$  of Parylene C were vapor-deposited onto a 100 mm diameter silicon wafer. Two coats of photoresist were spun and soft-baked. Sensor electrodes were UV-patterned onto the wafer before post-exposure baking and development. Oxygen plasma reactive ion etching (RIE) was then employed as a parylene etchant. Electron gun

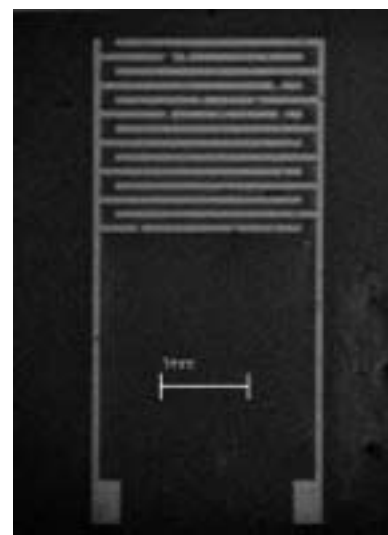


Figure 1: SEM of gold interdigitated electrodes with 100  $\mu\text{m}$  interdigital spacing.

evaporation was used to deposit 10 nm titanium and 150 nm gold on top of the parylene in unexposed areas and on top of Si in exposed areas, the titanium layer facilitating adhesion at the gold-silicon interface. Residual parylene was peeled from the wafer using tweezers. Wafer dicing yielded individual chips that were wire-bonded to copper breadboard circuits. In sensor functionalization, thiol-modified nucleic acid probes with an SEB bioaffinity (“spiegelmers”) were used because of their resistivity to natural enzymatic degradation. 20  $\mu\text{L}$  of 50 mM spiegelmer solution were pipetted onto the sensors and incubated for 8 hours at ambient temperatures to ensure spiegelmer immobilization onto the electrode surface via thiol chemistry (Figure 2).

**Electrical Characterization.** A wire-bonded sensor chip was connected to a capacitance meter before a baseline reading was taken with phosphate buffer. After 10 minutes of equilibration, the chip was exposed to SEB. Subsequently, the chip was rinsed three times with buffer. A post-wash reading was taken while the sensor was again exposed to buffer. Residual SEB-spiegelmer binding was expected to be reflected in capacitance. The chip was incubated with 20 mM sodium hydroxide (NaOH) for 5 minutes and washed three times with buffer before a final buffer reading was taken. If

the altered capacitance was due to SEB-spiegelmer binding, the post-NaOH reading should return to baseline. The sensor was kept in the dark during characterization because previous results indicated that the sensors are light-sensitive due to photoelectric effects.

## Results and Conclusions:

Preliminary electrical characterization showed sensor selectivity towards SEB, reporting nearly a two-fold increase in capacitance upon SEB addition to the sensor relative to the capacitance upon sensor exposure to bovine serum albumin (BSA). Water showed a  $(262 \pm 15)$ nF capacitance increase from baseline and a  $(109 \pm 15)$ nF disparity from the BSA control whereas phosphate buffer showed a  $(298 \pm 28)$ nF capacitance increase and a  $(188 \pm 48)$ nF disparity. Furthermore, a slightly-elevated capacitance was recorded after an initial wash which dropped back to baseline post-NaOH incubation (Figure 3). This re-occurring capacitance pattern is indicative of SEB-spiegelmer binding. These results were seen in both de-ionized water and  $10\text{-}\mu\text{M}$  phosphate buffer, although significant salt-shielding effects were detected as buffer concentration increased possibly because of interactions between salts and nucleic acids at higher concentrations.

Furthermore, upon addition of a protein cocktail containing BSA, green fluorescent protein (GFP), and SEB in water, there was an initial capacitance increase of  $(288.5 \pm 0.5)$ nF. Upon system stabilization, the capacitance settled at 237-nF whereas the control cocktail (BSA+GFP) showed a 61-nF increase from baseline, a 176-nF disparity (Figure 4). The capacitance returned to baseline post-NaOH incubation, demonstrating SEB selectivity during exposure to protein arrays and proving viability for practical sensing applications.

Voltaic characterization using a wireless system was performed as well; however, the data acquisition module was flawed in design. Nevertheless, the sensors were capable of successful wireless data transfer and preliminary voltaic results showed efficient SEB detection with the characteristically-elevated voltage readings indicative of SEB-spiegelmer binding.

## Future Work:

The next steps involve acquiring consistent electrical characterization results with phosphate buffers that have environmentally-relevant salt concentrations and conducting voltaic experiments using the wireless biodetection system upon re-designing of the data acquisition module.

## Acknowledgements:

I extend my sincere gratitude to Dr. Carl Batt and the Batt Research Group. I would also like to thank the Cornell NanoScale Science & Technology Facility (CNF), National Nanotechnology Infrastructure Network Research Experience for Undergraduates Program, National Science Foundation (NSF), NYS Center for Advanced Technology, and the Center for Life Sciences Enterprise for funding.

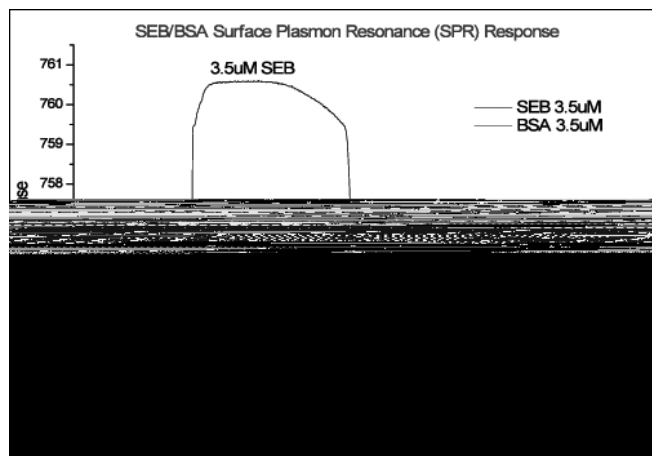


Figure 2: SPR confirmed effective functionalization of electrodes by spiegelmers and spiegelmer functionality.

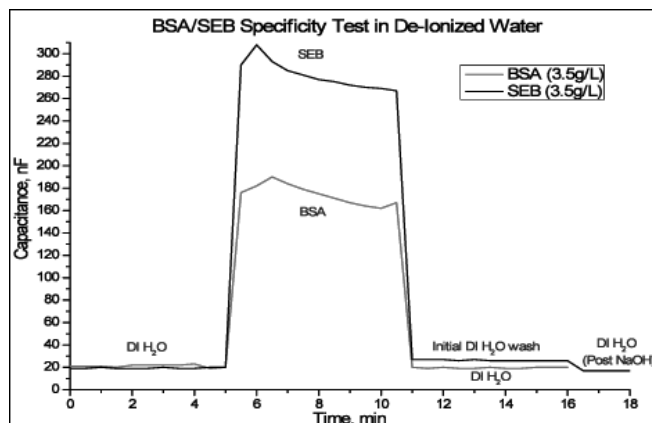


Figure 3: Specificity assays. There is a two-fold capacitance increase upon sensor exposure to SEB with elevated post-wash capacitance.

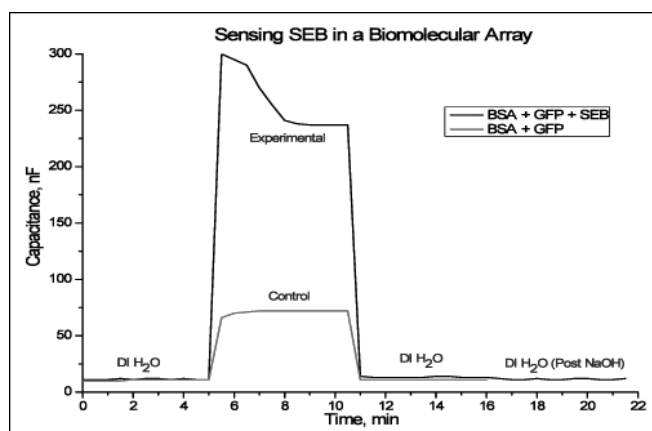


Figure 4: Selectivity assay. The BSA+GFP+SEB capacitance response was four times greater than the BSA+GFP capacitance response, demonstrating sensor selectivity for SEB.

## Nano Meets Micro: Synthesis of Proteins for the Organization of Nanostructures

Laurel Schmidt

Undeclared, Carleton College

**NNIN REU Site: Center for Nanotechnology, University of Washington, Seattle, WA**

NNIN REU Principal Investigator(s): Dr. Beth Traxler, Microbiology, University of Washington

NNIN REU Mentor(s): Ruth Hall, Microbiology, University of Washington

Contact: schmidt@carleton.edu, btraxler@u.washington.edu, rah7@u.washington.edu

### Abstract:

Manufacturing reliable nanoelectronics can be challenging, simply because of the scale on which these devices are built. In the future, it may be effective to find a way to direct their self-assembly. Certain proteins can be genetically engineered to assist in this process. Permissive sites, which allow for the insertion of short amino acid sequences without a loss of function, have been identified in two different proteins from the bacterium *Escherichia coli*, LacI and TraI. A short polypeptide sequence with a known affinity for silver particles was inserted into different permissive sites in each protein, and the resulting modified proteins were characterized. LacI derivatives successfully repressed expression of  $\beta$ -galactosidase, an enzyme whose transcription is controlled by LacI. TraI derivatives participated successfully in conjugation. An assay was attempted to measure the proteins' affinity for silver, but the results were inconclusive; a different assay will be needed in the future. The expected ability of these modified proteins to bind strongly to both deoxyribonucleic acid (DNA) and inorganic particles suggests they could play a key role in the organization of nanostructures by arranging silver particles in defined patterns along a DNA template.

### Introduction:

The broad goal of this project is to create a library of proteins that can bind to both DNA and inorganic particles. These proteins can be used to determine where in a cell a certain protein is most concentrated, or to organize nanoparticles along a DNA scaffold, perhaps leading to self-assembling structures with applications in nano-electronics and -photonics. Researchers have had success modifying proteins to bind to several inorganics; this work builds on their work by modifying two proteins to bind to silver.

Many proteins made by the bacterium *E. coli* naturally have the ability to bind to DNA. Researchers have already identified permissive sites in several of these, including LacI and TraI. LacI is a transcriptional repressor: when there is no lactose present in a cell, LacI binds to dsDNA at the operator sequence and prevents the transcription of the genes that follow. These genes encode the enzyme  $\beta$ -galactosidase which breaks down lactose. If lactose is present in the cell, LacI releases, and the genes are transcribed.

TraI is involved in F-plasmid conjugation, the process by which bacteria transfer DNA to one another. TraI binds to a double-stranded DNA plasmid in the donor bacterium and nicks it, and then helps it unwind so that one strand can be transferred to the recipient. Both bacteria then synthesize the complementary strand of DNA. While LacI binds only at its 30 base dsDNA operator sequence, TraI has the ability to bind non-specifically on both ds and ssDNA. Different applications in the future may require sequence-specific or

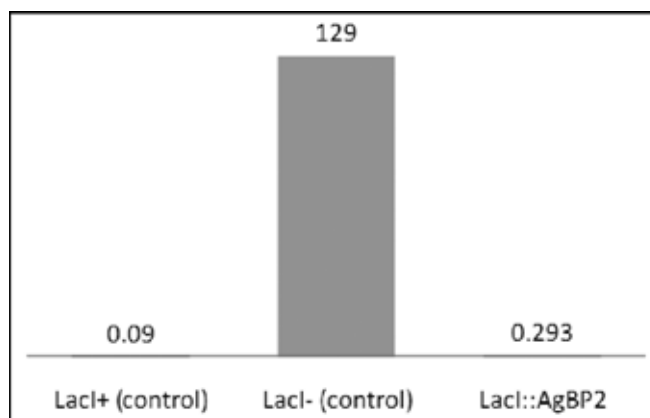


Figure 1: Level of  $\beta$ -galactosidase activity for cells carrying three different versions of LacI

sequence-independent binding, so both proteins were used.

Using a phage display system, researchers have identified a cysteine-constrained 12 amino acid peptide (EQLGVRKELRGV), known as AgBP2, with a high affinity for silver. This sequence was inserted into the permissive sites of LacI and TraI after the 317<sup>th</sup> and 369<sup>th</sup> amino acids, respectively, to produce LacI::AgBP2 and TraI::AgBP2. These derivatives were identified using polymerase chain reaction (PCR) screening, DNA sequencing, and expression samples, and then characterized for their affinities to DNA and silver.

### Characterizing DNA-Binding:

Since LacI represses synthesis of  $\beta$ -galactosidase, a high level of DNA binding by LacI::AgBP2 would be associated with a low level of  $\beta$ -galactosidase activity. Figure 1 shows the level of  $\beta$ -galactosidase activity for cells carrying three different versions of LacI; the units shown in the chart are proportional to the level of  $\beta$ -galactosidase activity per cell per unit time. The LacI::AgBP2 showed wild type-level  $\beta$ -galactosidase repression.

Because the ability of TraI to bind to DNA is necessary for conjugation, a mating assay was performed to characterize TraI::AgBP2 DNA-binding activity. TraI::AgBP2 had wild type-level mating activity.

### Characterizing Silver-Binding:

To determine the affinity of LacI::AgBP2 and TraI::AgBP2 for silver, clarified cell extracts were mixed with silver powder. After suspension and centrifugation, the supernatant was saved, and the powder was washed twice and then resuspended. Ideally, proteins exhibiting no binding would be found in the initial supernatant, those showing nonspecific binding would come off in one of the washes, and those with a strong affinity for silver would remain with the powder until the end. However, as shown in Figure 2, the affinity of modified proteins for silver was not demonstrated to be any stronger than that of the unmodified proteins. This particular method of measuring binding ability had sometimes been ineffective in the past, and the silver nanoparticles agglomerated into larger particles during the pre-test preparation phase, indicating that this test for Ag binding is not accurate. Future characterization will assess binding on Ag surfaces with purified proteins.

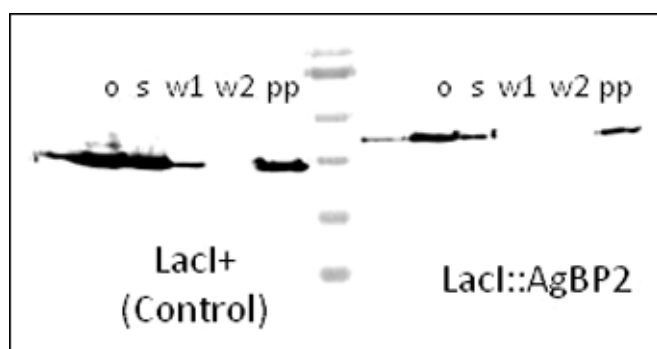


Figure 2: Results of silver binding assay. *o* = original amount of protein; *s* = supernatant; *w1* = wash 1; *w2* = wash 2; *pp* = powder pellet.

### Conclusions and Future Work:

Derivatives of LacI and TraI containing a silver-binding peptide have been synthesized successfully, and their sequences have been confirmed. LacI::AgBP2 shows wild type-level  $\beta$ -galactosidase repression, verifying its *in vivo* binding to DNA at the *lac* operator. TraI::AgBP2 exhibits wild type-level mating activity, indicating wild type-level DNA binding. The abilities of both derivatives to bind to silver have not been demonstrated. To further characterize these proteins, a more accurate and quantitative assay is needed. Surface plasmon resonance or quartz crystal microbalance will be used to characterize silver binding. Silver and DNA binding will be visualized via atomic force or electron microscopy. Such images could confirm ability of the proteins to bind to silver and DNA simultaneously, and perhaps demonstrate the expected sequence-specific binding of LacI derivatives and sequence-independent binding of TraI derivatives.

### Acknowledgements:

I would like to thank my PI, Dr. Beth Traxler, my mentor, Ruth Hall, my lab mates Eli Gachelet and Rembrandt Haft, and my site coordinator Ethan Allen for guidance and encouragement. I would like to thank the National Nanotechnology Infrastructure Network Research Experience for Undergraduates Program and the National Science Foundation for funding.

# Direct-Fabrication of Nanoparticles in Cancer Diagnostics

Trisha Sengupta

Biology, Emory University

**NNIN REU Site: Stanford Nanofabrication Facility, Stanford University, Stanford, CA**

*NNIN REU Principal Investigator(s): Dr. Yi Cui, Materials Science and Engineering, Stanford;*

*Dr. Mary Tang, Stanford Nanofabrication Facility, Stanford University*

*NNIN REU Mentor(s): Ching-Mei Hsu, MSE; Stephen Connor, Chemistry; Stanford University*

*Contact: tsengup@emory.edu, chingmei@stanford.edu, stconnor@stanford.edu,*

*yicui@stanford.edu, mtang@stanford.edu*

## Abstract:

Synthetic antiferromagnetic (SAF) nanoparticles possess unique tunable magnetic properties, which make them instrumental in developing highly selective, highly sensitive bioassays for tumor detection and surveillance. Through a combination of top-down and bottom-up approaches, we are able to fabricate these nanoparticles and bypass the disadvantages of following either single approach. Monodisperse SAF nanoparticles are fabricated by means of nanoimprint lithography (NIL), a top-down process. However, the method we used to construct the template of nanopillars for NIL mainly involved the bottom-up approach, which involved the following steps; synthesis of silica nanoparticles, surface functionalization, deposition by Langmuir Blodgett, and reactive ion etching. Scanning electron microscope (SEM) images after the etching step show that we were able to construct uniform arrays of nanopillars on a silicon wafer, thus resulting in a low-cost and production-worthy stamps for fabricating SAF nanoparticles.

## Introduction:

Magnetic nanoparticles show great promise in improving medical diagnostics, treatments, and therapies due to their relatively small size in comparison to biomolecules, and their externally controlled magnetization. Particularly, magnetic nanoparticles have made significant advances in bioanalysis. In our case, the ultimate goal was to improve the process of magnetic sorting for a multiplexed bioassay [1].

This process involves a deoxyribonucleic acid (DNA) probe, which is bound to a biosensor, to hybridize with a complementary strand which is attached to a magnetic nanoparticle. The biosensor is able to detect magnetization, and therefore quantify the amount of the target DNA [2].

Our objective was to fabricate stamps for nanoimprint lithography (NIL). The stamps were fabricated according to the following steps; synthesis of silica nanoparticles, surface functionalization, deposition by Langmuir Blodgett (LB), and reactive ion etching (RIE)—as depicted in Figure 1. Once the stamps were made, they were used in a top-down process, which involved a combination of nanoimprint lithography (NIL) and lift-off to produce SAF nanoparticles. Our group has previously demonstrated the use of LB to produce stamps and used those stamps to produce templates for SAF nanoparticle fabrication. However, the complete process to use these stamps and templates to produce the SAF nanoparticles has not yet been completed. Here, we were fabricating stamps which would be utilized in this process, so that the SAF nanoparticles could be fabricated and investigated as bioassays for cancer.

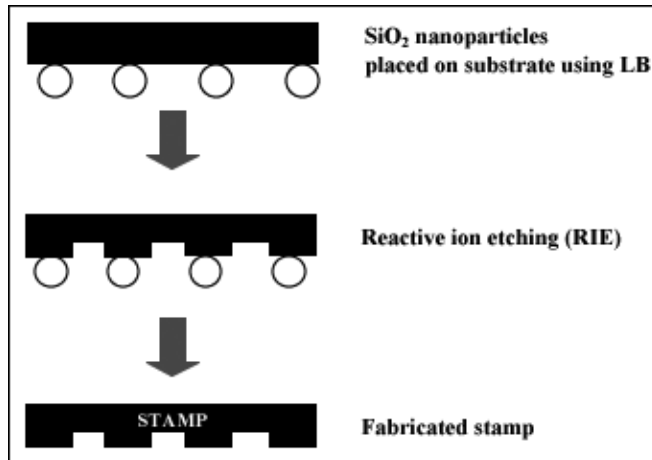


Figure 1: Fabrication of stamp for NIL and lift-off.

Herein, we report on the reactive ion etching (RIE) of the SiO<sub>2</sub> mask to produce stamps. The etching requires a two-step process; shrinking the SiO<sub>2</sub> nanoparticles, and anisotropic etching to form a stamp of uniformly distributed nanopillars.

## Experimental Procedure:

The LB method was applied to pattern an etch mask. Afterwards, a reactive ion etch (RIE) was performed on the etch mask in order to obtain a nanopillar array with straight sidewalls. By using an isotropic etch with a fluorine-based

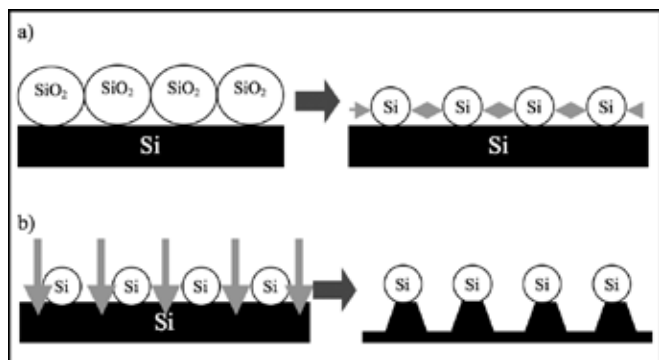


Figure 2: a) Isotropic etching of  $\text{SiO}_2$  mask with fluorine-based etchant; b) Anisotropic etching of Si with  $\text{O}_2/\text{Cl}_2/\text{HBr}$ .

etchant, we shrank the mask of  $\text{SiO}_2$  nanoparticles, and then we used a combination of  $\text{O}_2/\text{Cl}_2/\text{HBr}$  to achieve anisotropic etching as demonstrated in Figure 2. However, scattering caused the sidewalls to be slightly sloped. Additionally, mask erosion was caused by imperfect selectivity and physical etching. Scanning electron microscopy (SEM) was used to characterize the pillars.

## Results and Conclusion:

We obtained the expected result after RIE, which were sloped nanopillars. The slight sloping might be caused by scattering as shown in Figure 3. After plasma etching the 250 nm  $\text{SiO}_2$  nanoparticle mask, the resulting nanopillars were approximately 120 to 150 nm in diameter. Using Langmuir Blodgett, the uniformity of the size and distribution of the  $\text{SiO}_2$  nanoparticles allowed for the etching to be uniform. Conversely, the etch mask created using spin-coated latex-spheres possessed microdomains, and after RIE, the different etching rates in and out of those domains produced an unevenly distributed and sized nanopillar stamp. Therefore the template for SAF nanoparticle fabrication produced using this technique will also be uniform in distribution and size, while the latex-sphere technique has not been uniform.

Ultimately, the stamps were fabricated for a nanoimprinting process to produce SAF nanoparticles for cancer detection. We successfully utilized a two-step etch process to create the stamp.

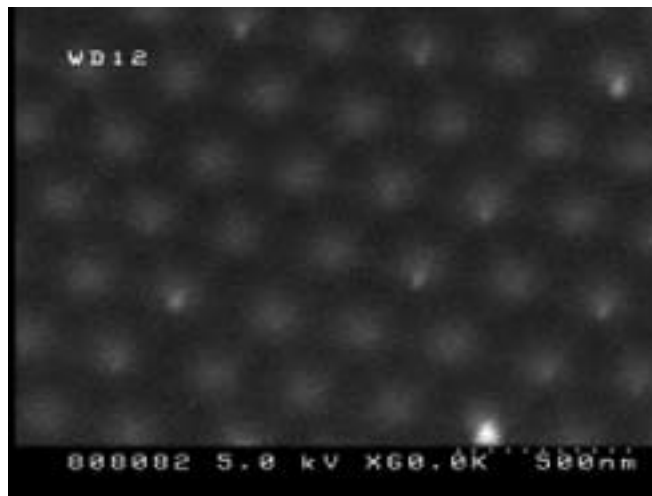


Figure 3: Planar SEM view of nanopillars of stamp.

## Future Work:

Our future plans involve ion milling the stamp to round out the pillars and ensure that the liftoff does not remove the magnetic material in the troughs. These stamps will then be used to produce SAF nanoparticles for cancer bioassay. Additionally, we can utilize the uniformity created by this general stamp fabrication technique for microfluidics and optics. The stamp may also be used as a template for other nanomaterial growth.

## Acknowledgments:

I would like to thank Dr. Michael Deal, Mingliang Zhang, Ben Weil, James Conway, SNF Process Staff, Mihir Tendulkar, and Maureen Baran for making my research possible. This work was supported by the Stanford Nanofabrication Facility, Centers of Cancer Nanotechnology Excellence, NSF, and the National Nanotechnology Infrastructure Network Research Experience for Undergraduates (NNIN REU) Program.

## References:

- [1] Wei Hu, Robert J. Wilson, AiLeen Koh, Aihua Fu, Anthony Z. Faranesh, Christopher M. Earhart, Sebastian J. Osterfeld, Shu-Jen Han, Liang Xu, Samira Guccione, Robert Sinclair, Shan X. Wang, High-Moment Antiferromagnetic Nanoparticles with Tunable Magnetic Properties, *Advanced Materials*, 20 (2008), pp. 1479-1483.
- [2] S.X. Wang, S.-Y. Bae, G. Li, S. Sun, R.L. White, J.T. Kemp and C.D. Webb, Towards a magnetic microarray for sensitive diagnostics, *J. Magn. Mater.* 293 (2005), pp. 731–736.

# Cellulose Fibril Patterning for Real Time Studies of Cellulase Kinetics

Rachel Simmons

Biological Engineering, Utah Sate University

**NNIN REU Site: Cornell NanoScale Science and Technology Facility, Cornell University, Ithaca, NY**

NNIN REU Principal Investigator(s): Larry Walker, Ph.D., Biological and Environmental Engineering, Cornell University;

Jose Moran-Mirabal, Ph.D., Biological and Environmental Engineering, Cornell University

Contact: rachel.simmons@aggiemail.usu.edu, lpw1@cornell.edu, jmm248@cornell.edu

## Abstract:

Cellulases are key enzymes in the breaking down of cellulose into fermentable sugars used for bioethanol production. Lignocellulose-based biofuels have shown to be a viable alternative to fossil fuels. However effective production of cellulosic bioethanol is dependent on understanding kinetic interactions between cellulases and cellulose. A technique for immobilizing cellulose fibrils on solid substrates using a polymer lift-off method that allows for real time imaging of cellulase-cellulose interactions has been developed.

Photolithographically patterned features on a thin polymer coating allow exposure of selected areas of the solid substrate to the cellulose fibrils. Incubation of the cellulose followed by drying, and subsequent polymer lift-off results in the immobilization of cellulose aggregates and yields specific morphologies depending on the pattern size used for the immobilization. The specific pattern attributes the various patterned features allow for imaging of immobilized cellulose mats, particles, or fibrils. Cellulose and *Thermobifida fusca* cellulases Cel6B and Cel9A can be fluorescently tagged and in combination with cellulose immobilization, can be imaged via fluorescence microscopy. This fluorescence-based system can be used to elucidate interactions between cellulose fibrils and the cellulases involved in depolymerization.

As part of this project, novel patterns containing registration and alignment marks were developed. These patterns can be used to identify specific cellulose features and image them in real time. Furthermore, the registration marks included in the novel patterns allow the tracking of specific cellulose features over prolonged time-lapsed experiments. Immobilization and identification through photolithographic patterning in combination with quantitative fluorescence microscopy techniques will result in a better understanding of cellulose-cellulase interactions. This can provide a more thorough understanding of the steps involved in the depolymerization of cellulose into fermentable sugars, which will aid the formulation of enzyme cocktails that improve the efficiency and reduce the cost of bioethanol.

## Introduction:

Cellulases are instrumental in the depolymerization of cellulose fibrils into fermentable sugars for bioethanol production. Development of the most effective cocktail of enzymes for the depolymerization of cellulose fibrils into fermentable sugars is dependent upon understanding the intrinsic molecular mechanisms of cellulases. In turn, the design and creation of effective cellulase cocktails will dramatically reduce the cost of bioethanol production from lignocellulosic biomass.

Techniques that would allow for the evaluation of enzyme performance on insoluble cellulose materials ranging from single fibrils to complex cellulose mats are important for observing on-off rates and processive behaviors of cellulases. Effective imaging of these behaviors mandates high spatial and temporal imaging resolution, and in order to achieve these parameters, cellulose fibrils must be immobilized on a solid substrate.

This project developed a polymer lift-off technique that allowed for cellulose immobilization on a solid substrate by photolithographically patterning an evaporated polymer coating on a glass substrate. The immobilization of cellulose fibrils was achieved by selectively exposing the underlying

glass surface and then removing the unpatterned cellulose by lifting off the polymer coating.

## Experimental Procedure:

Polymer lift-off surfaces with specific pattern designs for fibril immobilization were fabricated on 170  $\mu\text{m}$  thick fused-silica wafers ranging in diameter from 15 mm to 54 mm. The wafers were initially cleaned with three successive 10 minute baths in acetone, isopropanol and deionized water, followed by drying under a nitrogen stream. Further removal of organic contaminants was performed by 10 min of oxygen plasma cleaning (60 mTorr, 50 SCCM  $\text{O}_2$ , 150W, Oxford PlasmaLab 80+ RIE System). The back sides of the wafers were attached to adhesive tape to protect them from polymer deposition. A 1  $\mu\text{m}$  thick conformal coating of di-para-xylylene (Specialty Coating Systems) was evaporated onto the wafer surfaces, after which the adhesive tape was removed.

Shipley 1827 photoresist was spun over the polymer coating on the wafers to a thickness of 3.5  $\mu\text{m}$  and baked at 90°C for 1 minute. Photolithography was performed using an HTG System IIIHR Contact Aligner. The exposed photoresist was

developed in AZ300-MIF developer (Clariant Corp., AZ Electronic Materials) for 1 min, followed by a 1 min rinse in deionized water and dried under a nitrogen stream.

Exposed regions of the polymer layer were etched in a reactive oxygen ion plasma chamber (60 mTorr, 50 SCCM  $O_2$ , 150W, Oxford PlasmaLab 80+ RIE System). Residual photoresist was removed by successive 10 minute baths in acetone and isopropanol.

## Results and Conclusions:

The polymer lift-off technique was successful in immobilizing cellulose fibrils on solid substrates, and allowed for high resolution fluorescence imaging of cellulose-cellulase interactions. Different patterned features yielded varying cellulose aggregate sizes. 10  $\mu\text{m}$  features in width were most effective in immobilizing single cellulose fibrils and small fibril aggregates. 10  $\mu\text{m}$  diameter dots were successful in isolating single cellulose fibrils important for imaging. Features smaller than 10  $\mu\text{m}$  were not consistent in immobilizing cellulose fibrils, as most material was removed in the lift-off process and only small fibrils remained in patterned features. Patterns larger than 10  $\mu\text{m}$  in width yielded larger cellulose aggregates and cellulose mats. Pattern alignment schemes allowed for identification of specific pattern features and cellulose fibrils.

## Acknowledgments:

Photolithography was performed at the Cornell NanoScale Facility. The project was supported by the NSF via NNIN REU Program. The project was also supported by the departments of Biological and Environmental Engineering, and Applied Physics and Engineering at Cornell University.

## References:

- [1] Ilic, B. Topographical Patterning of Chemically Sensitive Biological Materials Using a Polymer-Based Dry Lift Off. *Biomedical Microdevices*. 2000 2:4, 317-322.
- [2] Moran-Mirabal, J. Controlling Microarray Spot Morphology with Polymer Lift-off Arrays. *Anal. Chem.* 2007, 79, 1109-1114.
- [3] Moran-Mirabal, J. Micrometer-Sized Supported Lipid Bilayer Arrays for Bacterial Toxin Binding Studies through Total Internal Reflection Fluorescence Microscopy. *Biophysical Journal*. 2006, 89, 296-305.

Figure 2, upper middle, right: Solid substrate pattern design with alignment scheme. Different feature sizes (ranging from 5  $\mu\text{m}$  to 500  $\mu\text{m}$  in width) were designed to immobilize various cellulose bundle sizes for imaging.

Figure 3, lower middle, right: 10  $\mu\text{m}$  diameter dots incubated with *Thermobifida fusca* cellulases allowed for imaging of cellulose-cellulase interactions. A) Cellulose incubated with AF488-Cel6B enzyme. B) Cellulose incubated with AF 647-Cel9A enzyme. C) Combined fluorescence of both Cel6B and Cel9A.

Figure 4, bottom: Surface patterning and cellulose immobilization through polymer lift-off. (a) Glass surface is coated with a thin polymer layer and photoresist is spun on and exposed through a mask. (b) Wafer is developed and exposed photoresist areas are washed away. (c) Exposed polymer is reactive ion etched with oxygen ion plasma, exposing the underlying glass surface. (d) Left over resist is removed. (e) Cellulose in aqueous solution is dried on the patterned surface. (f) Polymer is lifted-off leaving behind cellulose fibrils and fibril bundles in patterned areas.

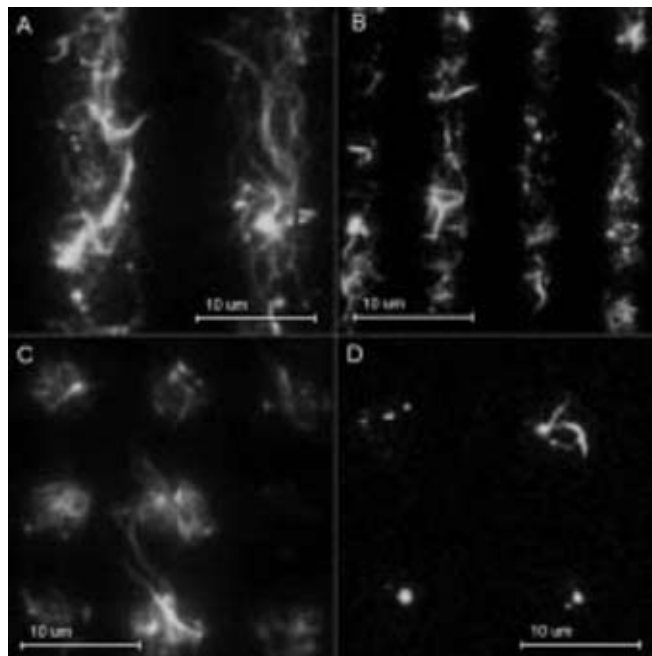
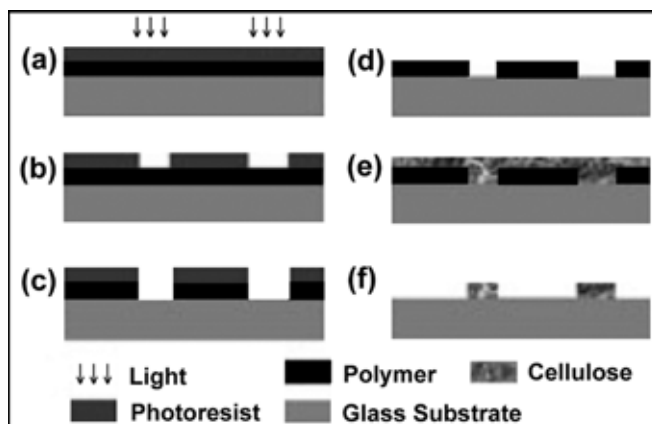
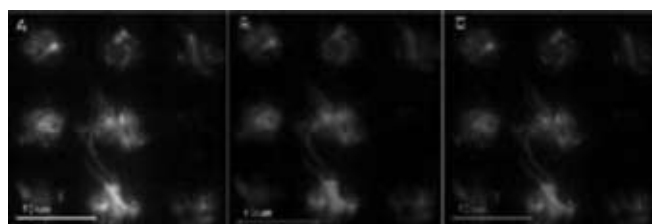
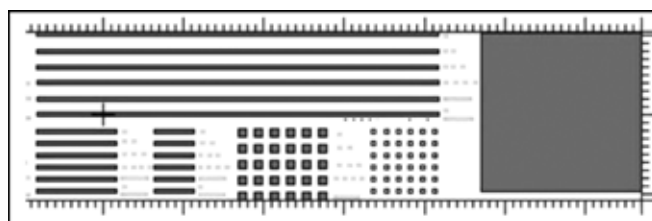


Figure 1: Imaging of immobilized cellulose particles on solid substrate. A) 10  $\mu\text{m}$  wide lines immobilized cellulose aggregates and cellulose bundles with some single fibrils. B) 5  $\mu\text{m}$  wide lines immobilized single cellulose fibrils and smaller cellulose bundles. C) 10  $\mu\text{m}$  dots immobilized single cellulose fibrils and cellulose bundles. D) 5  $\mu\text{m}$  diameter dots immobilized single fibrils and very few larger bundles.



# Fabrication and Optical Characterization of Nanoimprinted Plasmonic Constructs for Biosensor Applications



Isaias Tesfaslassie

Applied Physics, Appalachian State University

**NNIN REU Site: Lurie Nanofabrication Facility, University of Michigan, Ann Arbor, MI**

NNIN REU Principal Investigator(s): L. Jay Guo, Department of Electrical Engineering and Computer Science, University of Michigan, Ann Arbor, MI

NNIN REU Mentor(s): Brandon D. Lucas, Applied Physics, University of Michigan, Ann Arbor, MI

Contact: tesfaslassieim@appstate.edu, guo@eecs.umich.edu, bdlucas@umich.edu

## Abstract:

This work focuses on the fabrication of Au nanoparticle arrays using nanoimprint lithography (NIL), and their application as biosensor transduction elements. Noble metal nanoparticles such as gold (Au) are unique in that upon illumination by light of certain frequency, collective oscillations of the free electrons can be produced. This characteristic response is known as the localized surface plasmon resonance (LSPR). Optical characterization of the nanoparticle arrays show that the LSPR is not only sensitive to nanoparticle shape and size but it is also sensitive to the surrounding dielectric medium. Therefore, a biomolecular binding event on the particle surface causes the LSPR spectral line to shift. Specifically in this project, the LSPR of Au nanoparticles is used to transduce the interaction between two non-structural proteins responsible for viral genome replication, NS3 and NS5. This goal was accomplished by implementing an immobilization strategy for purified His-tagged NS3 proteins to the nanoparticle surface using a nickel-nitrilotriacetic acid (Ni-NTA) surface chemistry.

## Introduction:

Surface plasmons are collective electron-density oscillations generated on the surface of metallic films. As the resonant excitation of these plasmons is highly dependent on the dielectric function of the material on the metal surface, monitoring the resonance condition serves as a suitable method to transduce dielectric changes in the near-field of the metallic surface. Based on this principle, surface plasmon resonance (SPR) biosensors have been utilized extensively over the last decade to characterize various biomolecular systems. Most significant among the benefits of SPR is the ability to monitor biomolecular interactions in real-time without the need for various labels that can generate less robust signals and putative effects on the interaction of interest. An extension of this technique, known as localized surface plasmon resonance (LSPR), uses noble metal nanoparticles. LSPR is gaining interest in part due to the availability of more reliable fabrication methods, adaptability for use in commercially available spectroscopic systems and enhanced sensitivity. In this work, nanoimprint lithography (NIL) is utilized to produce plasmonic constructs that are optically characterized using microextinction spectroscopy. We subsequently utilize a surface-modified Au nanoparticle array to detect interactions between two non-structural proteins NS3 and NS5 which are found in a *Flavivirus replicase* complex.

## Fabrication Process:

Nanoimprint lithography (NIL), a mold-based fabrication

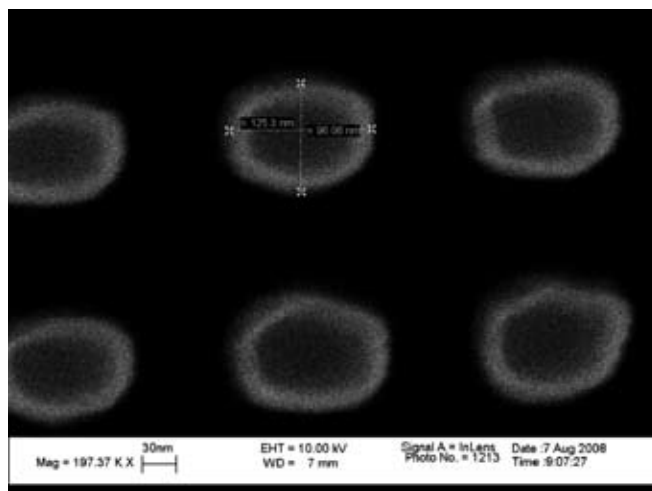


Figure 1: SEM of the nanoimprint mold.

method, was used to fabricate nanoscale patterns on glass. Glass substrates were cleaned in a 1:1 piranha solution of  $\text{H}_2\text{O}_2:\text{H}_2\text{SO}_4$  for 20 minutes followed by a rinse in deionized water solution and dried using  $\text{N}_2$ . Nanoimprint resist (MRi-8030) was spin-coated on the glass substrates to the appropriate thickness and then baked on a hot plate at  $140^\circ\text{C}$  for 5 minutes to remove residual solvent. A nanoimprinter (Nanonex, NJ) was used to imprint with a mold possessing an array of pillars with oval cross-sections ( $\sim 130$  nm by  $100$  nm) and gaps of  $\sim 90$  nm (Figure 1) directly onto the prepared glass substrates.

The glass substrates were heated above the glass transition temperature of the nanoimprint resist (180°C) and pressure (670 psi) is used to create a conformal contact with the mold. After imprinting, a thin layer (~ 5 nm) of Ni was deposited using a shadow evaporation technique to promote undercutting and enhance the subsequent lift-off process. Residual layer removal was accomplished using a suitable O<sub>2</sub> plasma dry etching process (20 sccm; 50W; 20 mTorr). Following the etching, Au was deposited to the desired thickness on the glass substrates using an electron beam evaporator. Lift-off was performed by immersing the glass substrates in a beaker of acetone, and sonication when necessary. The finished samples were rinsed with methanol and IPA and dried with N<sub>2</sub>. The resulting Au NP arrays were surface-modified with a Ni-nitrilotriacetic acid (Ni-NTA) surface chemistry in order to immobilize the purified His-tagged NS3 proteins onto the Au NPs. The surface modification technique was accomplished by the incubation of the Au NP substrates in solutions of cystamine, glutaraldehyde, N $\alpha$ ,N $\alpha$ -bis(carboxymethyl)-L-lysine hydrate (NTA), and nickel sulfate respectively.

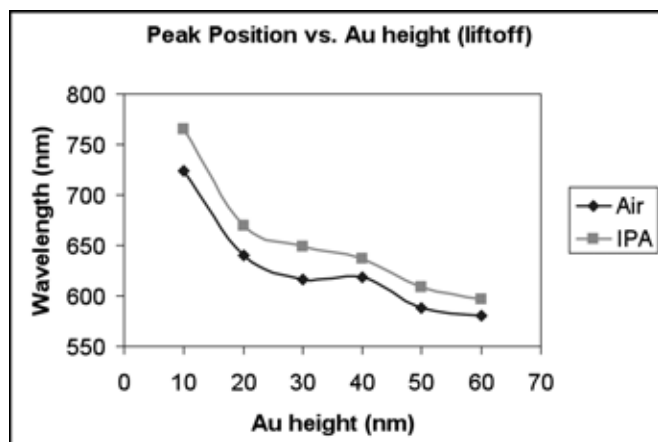


Figure 2: LSPR response of fabricated particle array (in air & IPA).

### Experimental / Results:

The optical properties of the nanoparticles arrays were determined by an optical extinction measurement. These measurements were conducted using a Nikon TE300 Eclipse inverted microscope (40x objective) with transmitted broadband light focused into an optical fiber which was coupled to spectrometer (Ocean Optics HR4000). The SpectraSuite software package was used for all data acquisition and analysis. The first test was conducted on a variety of samples that were differentiated only by the height (10-60 nm) of the Au NPs. As shown in Figure 2, with increasing nanoparticle height there is a consistent resonance peak shift in the LSPR to shorter wavelengths (blue-shift). In addition, dielectric sensitivity was measured on the different heights by monitoring the LSPR response of the nanoparticles as

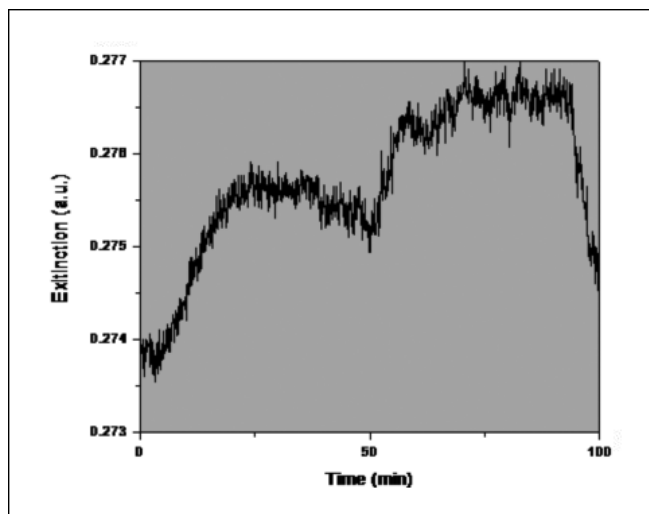


Figure 3: LSPR measurement of NS3 and NS5 interaction.

they interact with ambient air and isopropanol (IPA). Overall behavior shows an increase in wavelength (red-shift) with increasing refractive index. We observed that there is an optimal particle thickness (30 nm) that produces the highest environmental sensitivity.

Lastly, we tested the interaction of NS3 and NS5. A flow cell setup was used to flow NS3, NS3 buffer, NS5, and NS5 buffer respectively. As seen in Figure 3, the interactions of NS3 with the nanoparticle surface and with NS5 are clearly distinguishable based on the extinction vs. time graph (NS3 at ~ 0.0 min, NS3 buffer at ~ 25 min, NS5 at ~ 50 min, and NS5 buffer at ~ 75 min).

### Conclusions / Future Work:

We successfully fabricated Au nanoparticles using NIL and have characterized their plasmonic properties. We applied our nanoparticles to detect interactions between NS3 and NS5. Optimization of the surface chemistry used to bind His-tagged proteins is being addressed and should lead to improved biosensor performance.

### Acknowledgements:

I would like to thank Professor L. Jay Guo, Brandon Lucas, Dr. Sandrine Martin, Guo Nanogroup, Lurie Nanofabrication Facility, the National Science Foundation, Intel Foundation for funding, and the National Nanotechnology Infrastructure Network Research Experience for Undergraduates (NNIN REU) Program for all their help and support.

# Integration of Biological Observations and Theory into Computer Simulations of Bacterial Binding

Suron Woods

Bioengineering, Oregon State University

**NNIN REU Site: Center for Nanotechnology, University of Washington, Seattle, WA**

NNIN REU Principal Investigator: Wendy Thomas, Bioengineering, University of Washington

NNIN REU Mentor: Matt Whitfield, Bioengineering, University of Washington

Contact: suronwoods@gmail.com, wendyt@u.washington.edu, mjwhit16@u.washington.edu

## Abstract:

Some biological adhesive bonds, called catch bonds, are enhanced by tensile force which enables complex behaviors at the cellular level. For example, *Escherichia coli* bacteria, binding to mannosylated surfaces via a catch-bond forming protein called FimH, switch from transient to rolling to stationary adhesion as hydrodynamic shear stress is increased, and detach again if the flow is turned off. The behavior of the catch bond is also influenced by the mechanical structure of the bacteria.

Our lab currently uses adhesive dynamic simulations and computational analysis to examine the relationship between catch bonds under shear stress, the mechanical structure of the fimbriae, and the behavior of the bacteria in fluid flow. The goal of this project is to design and implement into the simulation the additional functionality of fimbrial uncoiling so that the affect of this behavior on the catch bonds as well as the behavior of the bacteria can be determined via computational analysis. We created a two-state Monte Carlo algorithm using the polymer Worm-Like-Chain equation to model the behavior of the fimbriae under shear force.

## Introduction:

The first step in successful colonization and infection of many bacteria is adhesion to host tissues. *Escherichia coli* adheres to mannosylated surfaces via a catch-bond forming protein called FimH, which is located at the tip of its fimbriae, which are long rods composed of more than 1000 coiled FimA protein subunits forming a helical structure anchored to the outer bacterial membrane. These fimbriae exhibit spring-like uncoiling behavior under shear force which mediate the forces at the FimH tip and enhances bacterial adhesion.

Mechanical measurements done on fimbriae using atomic force microscopes show that fimbriae readily extend under applied force, caused by the uncoiling of the FimA protein subunits [1]. This uncoiling produces a force plateau region in the force extension curve which is optimized to mediate the shear forces at the FimH tip and enhances the catch-bond lifetimes, which in turn enhances bacterial adhesion [2].

In order for our adhesive dynamic simulations to accurately model the behavior of bacterial in fluid flow, the uncoiling behavior of the fimbriae must be accurately modeled in our simulation. Once the modeling of fimbrial behavior is incorporated into the simulation, we can use the simulations to explore the dynamics of the FimH catch bonds and their role in the adhesion of bacteria.

## Procedure:

The behavior of fimbriae under shear force has previously been probed in atomic force microscope (AFM) experiments. The data from these experiments has been used to determine the structure and behavior of fimbriae under force, which can be modeled using the polymer Worm-Like-Chain equation. These experiments also produced force extension curve data that we can use to compare with our simulation data to determine the accuracy of our simulation model, as seen in Figure 1.

We created a two-state Monte Carlo algorithm to model the uncoiling behavior of fimbriae, and incorporated this into our simulation of bacterial behavior in fluid flow. Previous experiments have shown this type of algorithm best models the uncoiling behavior of fimbriae [3].

Our simulation models the fimbriae much like a two spring force scenario. Using the overall fimbrial extension and the number of subunits in each state (coiled and uncoiled), we set the two force equations equal to each other and solved for the total tensile force from the fimbriae using an iterative method. The algorithm then used that force to calculate the uncoiling of the FimA subunits based on the probability of uncoiling adjacent subunits. These fimbrial forces were then used to determine the behavior of the FimH catch bonds, and summed to determine the overall behavior of the bacteria in fluid flow.

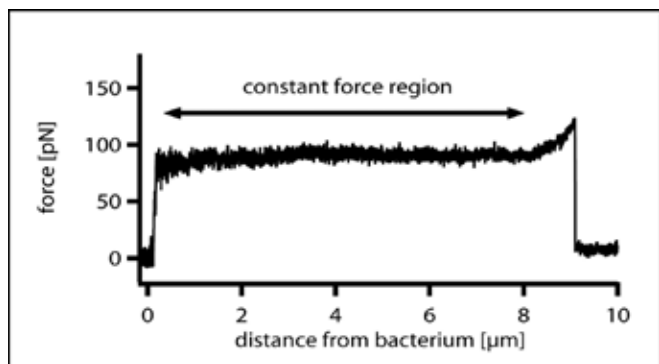


Figure 1: Force extension curve of uncoiling fimbriae from atomic force microscope experiments.

To determine the accuracy of our simulation, we ran the simulation using parameters to model a single fimbriae, and used the outputted simulation data to produce a force extension curve which we could compare to the data obtained from the AFM experiments.

### Results and Conclusion:

Our simulation, resulting from modeling a single fimbriae, produced a force extension curve that matched the data obtained from AFM experiments. This was evidence that our simulation correctly modeled the behavior of single fimbriae under shear force. Thus, the simulation can be used to accurately describe and predict the behavior of bacteria in fluid flow, based on multiple fimbrial-surface interactions.

### Future Work:

Our simulation can be used to run computational experiments to model the behavior of bacteria in fluid flow. Because these experiments are computational, we can alter parameters to explore the dynamics of fimbrial behavior, catch-bond interactions, and bacterial adhesion and behavior in fluid flow. In the future, this data may be used to fight bacterial disease or engineer adhesives that exhibit similar force dependant properties and behavior.

### Acknowledgements:

I would like to thank the following for their assistance and support with this project: Wendy Thomas, Matt Whitfield, University of Washington Bioengineering Department, The National Nanotechnology Infrastructure Network Research Experience for Undergraduates Program, and The National Science Foundation.

### References:

- [1] Miller, Garcia, Hultgren, and Oberhauser. "The Mechanical Properties of E. coli Type 1 Pili Measured by Atomic Force Microscopy Techniques." *Biophysical Journal* 91 (2006): 3848-3856.
- [2] Forero, Yakovenko, Sokurenko, Thomas, Vogel. "Uncoiling Mechanics of Escherichia coli Type I Fimbriae Are Optimized for Catch Bonds." *PLOS Biology* vol. 4 issue 9 e298 (2006): 1509-1516.
- [3] Bjornham, Andersson. "Modeling of the elongation and retraction of Escherichia coli P pili under strain by Monte Carlo simulations." *Eur. Biophysical Journal* 37 (2008): 381-391.

# Molecular Immobilization on a Gold Surface Using a Microfluidic Device

Justine Soo Yun Yoon

Biomedical Engineering, Rensselaer Polytechnic Institute

**NNIN REU Site: Minnesota Nanotechnology Cluster, University of Minnesota-Twin Cities, Minneapolis, MN**

*NNIN REU Principal Investigator(s): Professor Sang-Hyun Oh, Electrical and Computer Engr, University of Minnesota*

*NNIN REU Mentor(s): Hyungsoon Im, Electrical and Computer Engineering, University of Minnesota*

*Contact: yoonj4@rpi.edu, sang@umn.edu, imxxx019@umn.edu*

## Abstract/Introduction:

In this study, surface plasmon resonance (SPR) imaging and microfluidics were combined to immobilize single stranded deoxyribonucleic acid (DNA) on a patterned gold surface, detect DNA hybridization, and measure molecular binding kinetics in a real-time, label-free manner. Single-stranded thiolated DNA (T-DNA) was first immobilized on a gold surface; thereafter, the complementary DNA (cDNA) strand and the non-complementary DNA (ncDNA) strand were injected through a polydimethylsiloxane (PDMS) flow cell [1]. Because there are multiple channels in the PDMS flow cell, different solutions were injected through each channel, rendering a multi-array sensor—the PDMS flow cell reduced the volume of the sample solution needed (which increases the diffusion rate) and decreased the overall size of the biosensor. The hybridization was detected through an SPR imaging technique, comprised of a collinear system in which an incident light is shone underneath the sensor [2]. The sub-wavelength nanoholes can efficiently convert incident photons into collective oscillations of conduction electrons, known as surface plasmon (SP) waves at the gold surface. These surface plasmon waves propagate throughout the surface, and re-radiate as a sharp transmission of light at the other surface end. This transmission was detected by a couple charge device (CCD) camera and was shown as an intense transmission peak (peak position depends on the periodicity of the array and the refractive index surrounding the gold surface). If there were molecules present on the surface of the array, there would be a decrease in transmission intensity, resulting in a shift of the peak. Fluorescently tagged cDNA was used to verify the hybridization of DNA using a fluorescence array scanner. This technique can be used, in part, for gene mutation screenings as well as molecular interaction studies. The results showed that hybridization was possible through a microfluidic device and that a transmission peak could be detected through the biosensor.

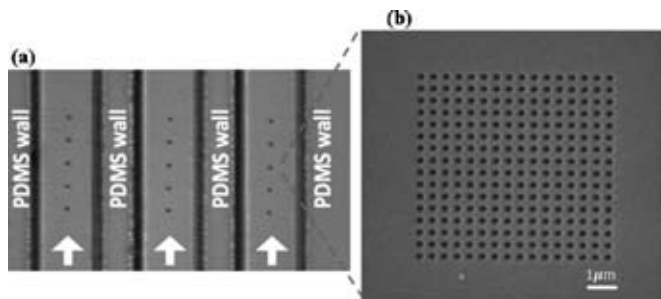


Figure 1: (a) Bright field image of a PDMS channel. (b) SEM image of nanohole array milled by a focus ion beam (200 nm diameter and 400 nm period).

## Experimental Procedure:

Using an electron beam evaporator, 5 nm of chromium, followed by 100 nm of gold, were deposited onto a clean glass slide, and placed in an ozone oven for ten minutes. Next, a  $3 \times 5$  array of  $16 \times 16$  nanoholes, (200 nm diameter and 400 nm periodicity), was milled onto the surface of the slide using a focused ion beam (Figure 1).

The fabricated microfluidic device used photolithography to construct three channels (each channel 100  $\mu\text{m}$  wide and

50  $\mu\text{m}$  deep) (Figure 2a) by spinning SU-8 photoresist onto a blank four inch silicon wafer at 2000 rpm for 30 seconds. The wafer was then prebaked, soft-baked, exposed to ultraviolet light under a patterned chrome mask, baked again, and developed [1]. Next, it was coated with a self-assembled monolayer of alkanethiols using a vacuum chamber. A 10:1 mixture of PDMS and curing agent was poured onto the wafer, and cured. Finally, six holes (1 mm diameter), were punctured into the inlets and outlets.

After preparing the reagents in Table 1, 30  $\mu\text{L}$  of T-DNA were pipetted onto the surface of the slide over the nanoholes, incubated in a 37°C humid chamber, and rinsed. The T-DNA area was then treated with 90  $\mu\text{L}$  of mercaptohexanol, incubated, and washed. The PDMS flow cell was coated with bovine serum albumin, incubated, and rinsed. A glass cover slide was placed over the PDMS and gold slide and secured by mechanical bonding, where tubes (0.05 inches in diameter and 3 inches long) were inserted into the inlets and outlets (Figure 2a and b). Finally, fluorescent/complementary-DNA (F/cDNA) was injected into the right channel, fluorescent/non-complementary-DNA (F/ncDNA) into the left channel, and the center channel was left empty. After a 24 hour incubation period in the humid chamber, the fluorescent labels were detected using a fluorescent microarray scanner.

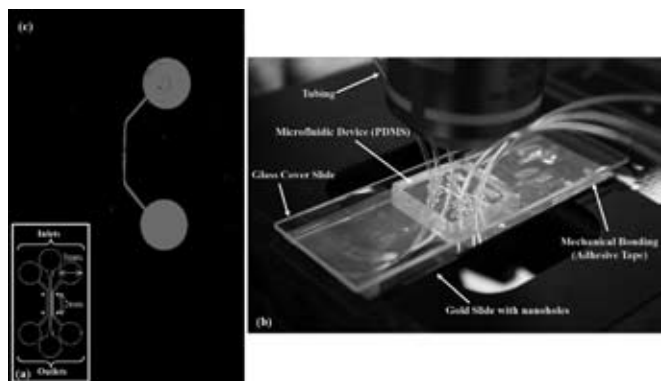


Figure 2: (a) Schematic of PDMS flow cell. (b) Complete SPR sensor. (c) Result from fluorescence array scanner. Right channel (F/cDNA), Left channel (F/ncDNA), Center channel (empty).

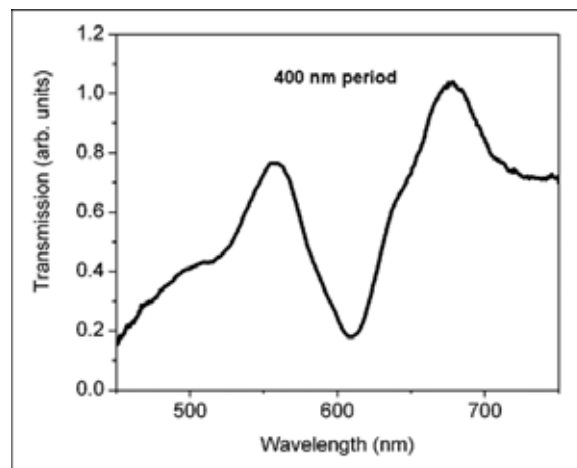


Figure 3: Transmission spectrum. The sharp peak shifts when DNA binds to the surface.

**Results and Conclusions:**

After several trials, DNA hybridization in a PDMS flow cell was successful. Figure 2c shows the fluorescence of the positive control channel. The main problem encountered for the first several trials revolved around the F/cDNA leaking out of its channels and into other channels; this error could be attributed to air bubbles or impurities between the PDMS flow cell and gold slide, or the flow rate of F/cDNA. Since DNA is hydrophilic, it is more prone to spread on the surface rather than stay within the channel walls. This leakage problem was corrected using a contact aligner to apply the flow cell to the gold surface—a uniform pressure over a wide area was applied onto the PDMS and the gold slide ensuring a tight seal. Figure 3 shows a transmission spectrum of the nanohole arrays without any molecules on the surface. The two peaks are due to the different periodicities between the adjacent hole, and the diagonal hole.

Future work would include the injection of DNA and complementary DNA through the flow cell while simultaneously measuring the transmission to see if the imaging system could detect the hybridization.

**Acknowledgments:**

The author would like to acknowledge Professor Sang-Hyun Oh, Hyungsoon Im, Nathan Lindquist, Antione Lesuffleur, Kwan Seop Lim and Si-Hoon Lee for the opportunity to work alongside them in their lab and for all their guidance. She would also like to thank the National Nanotechnology Infrastructure Network Research Experience for Undergraduates (NNIN REU) Program and NSF for funding this experiment.

**References:**

- [1] Sia, S.K., Whitesides, G.M.; "Microfluidic devices fabricated in Poly(dimethylsiloxane) for biological studies"; *Electrophoresis*, 24, 3563 – 3576 (2003).
- [2] Lesuffleur, A., Im, H., Lindquist, N. C., Lim, K. S., and Oh, S.; "Laser-illuminated nanohole arrays for multiplex plasmonic microarray sensing"; *Opt. Express*. 16, 219-224 (2008).

Stock solution	T-DNA	F/C-DNA	F/N-CDNA	DNA
100 mM Tris-HCl	12.5 mM	10 mM	10 mM	10 mM
10 mM EDTA	1.25 mM	1 mM	1 mM	1 mM
5 M NaCl	0	1M	1M	1M
10 mM TCEP	1.25 mM	0	0	0
20 μM T-DNA	1.25 mM	0	0	0
20 μM F/C-DNA	0	1 μM	0	0
20 μM F/NC-DNA	0	0	1 μM	0
20 μM DNA	0	0	0	1 μM
DNase I	*	*	*	*

Table 1: Reagents used \* Volume varies depending on total solution volume.

# Scanning Nanowire Waveguide for Molecular Imaging of Cancer Cells

Katherine Aristizabal

Chemistry, Universidad del Valle

**NNIN REU Site: Microelectronics Research Center, University of Texas, Austin, TX**

NNIN REU Principal Investigator(s): Prof. Li Shi, Mechanical Engineering, University of Texas at Austin

NNIN REU Mentor(s): Chad Baker, Dr. Yong Lee, Mechanical Engineering, University of Texas at Austin

Contact: karisti@clemson.edu, lishi@mail.utexas.edu, calbaker@mail.utexas.edu, yjlee@physics.utexas.edu

## Abstract:

A novel near field scanning optical microscopy (NSOM) method promises to achieve sub-50 nm spatial resolution along with enhancing signal to noise ratio (SNR) in optical imaging of single molecules and cell membranes. This technique proposes use of a zinc oxide (ZnO) nanowire plasmonic probe, synthesized by a chemical vapor transport and condensation (CVTC) system based on the vapor-liquid-solid (VLS) nanowire growth mechanism. In the present research, ZnO and graphite were used as source materials and the substrates were coated with 5 nm of thin film gold (Au) catalyst at a temperature of 1000°C and 700°C, respectively. Using scanning electron microscopy (SEM), it was found that the growth and the shape of nanowires were critically dependent on the temperature of the substrates, which is a function of position in furnace and temperature set point.

## Introduction:

Cancer research is pointing toward the development of technologies that allow the study of living cancer cells at a single molecule level, in order to achieve a better understanding of this disease. Biomarkers, as Au nanoparticles, have the ability to reveal neoplastic changes; these nanoparticles can be detected in live cells with optical techniques [1]. However, resolving the spatial distribution of individual molecules remains a challenging problem because of light diffraction [2]. NSOM has overcome this limitation, but with a low light transmission inducing a very weak signal [3]. Here, we are proposing a new NSOM method, which consists of a ZnO nanowire probe with an Au nanoparticle at the free end, where the nanowire works as a waveguide and the Au tip enhances the local electric field at tip-sample (Au biomarkers) gap at a single molecule level.

## Experimental Procedure:

The synthesis of ZnO nanowires was carried out by a CVTC system based on the VLS nanowire growth mechanism [4]. Single-crystalline silicon was used as a substrate for the ZnO nanowire growth. The substrates were coated with a layer of 5 nm Au thin film using a thermal evaporator under  $3 \times 10^{-5}$  Torr at 30 mA for 10 s. Then, the Au on the substrates was annealed at 1000°C for 20 min under argon atmosphere for the Au island formation. [place Figure 1]

Equal molar amounts of ZnO powder (99.9 %, Kurt J. Lesker Company) and graphite powder (Riedel-de Haën, Sigma-Aldrich lab) were mixed together, transferred to an alumina boat and then placed into a quartz tube (2.3 cm diameter and 118 cm length) in the upstream furnace of an argon flow (Figure 1). The Au-coated substrates were placed in the downstream furnace. The temperature of the upstream furnace was ramped

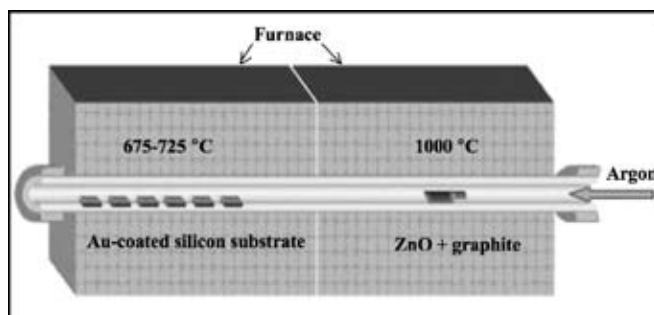
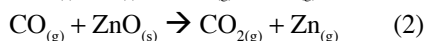
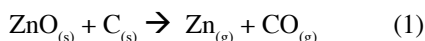


Figure 1: Schematic illustration of the ZnO nanowires growth by CVTC system.

to 1000°C and the downstream furnace was heated at 675°C - 725°C for 30 min under a constant flow of argon of 21 sccm.

The VLS growth mechanism of ZnO nanowires occurred in the following way: when the upstream furnace was heated at 1000°C, Zn, CO and CO<sub>2</sub> vapors were produced by the chemical reactions 1 and 2:



These vapors were transported by argon to the downstream furnace, which was at a lower temperature. Zn vapor was absorbed by Au to form an alloy droplet; then, the diffusion of Zn through the alloy occurred and when it became supersaturated, reactions 1 and 2 proceeded in the opposite direction with the formation of ZnO nanowires.

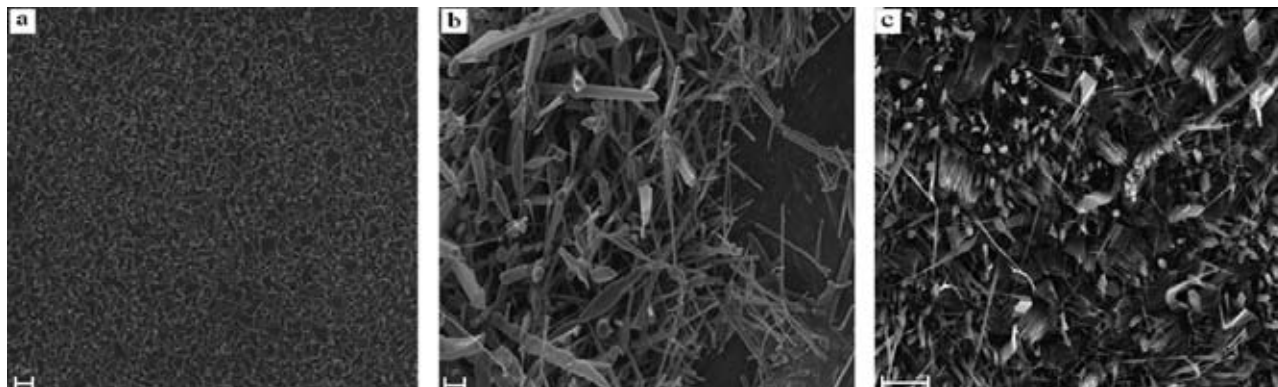


Figure 2: SEM images of ZnO nanowires grown at: a) 675°C, b) 700°C, c) 725°C.

After the furnace was cooled to room temperature, light gray material was found on the surface of the substrates, indicating the deposition of material.

Samples were characterized using SEM and x-ray diffraction (XRD).

### Results and Conclusions:

ZnO nanowire growth was analyzed at different substrate position in the downstream furnace and it was found that larger nanostructures were formed in regions located downstream. Nanowire growth was observed at the center of the furnace.

Experiments carried out at temperatures from 675°C to 725°C in the downstream furnace shown that at the low temperature (675°C), the Au catalyst nanoparticles were partially solid and therefore the nanowires were not formed (Figure 2a). At 700°C, adsorption, diffusion and crystallization occurred properly for the nanowire growth. Here, the dimensions of the nanowires ( $\sim 100$  nm width,  $\sim 2$   $\mu\text{m}$  length) and the presence of Au at the end indicated that these conditions were optimal for this research (Figure 2b). Higher temperatures (725°C) introduced significant crystal overgrowth and agglomeration (Figure 2c).

Control experiments without graphite did not form nanowires, which indicated that Zn vapor was generated only by a carbothermal reduction of ZnO in this furnace environment. Extensive growth was also found after annealing, due to the formation of Au droplets.

XRD was used to examine the crystallinity and composition of the nanowires. Samples gave similar XRD patterns, indicating high crystallinity of ZnO nanowires (Figure 3). Au peaks were also detected.

### Future Work:

After successful growth of the nanowires, the cantilever will be prepared and the ZnO nanowire growth with Au at the tip will be performed on the cantilever based on conditions previously found for optimum growth.

### Acknowledgments:

This work was supported by the National Nanotechnology Infrastructure Network Research Experience for Undergraduates (NNIN REU) Program of the National Science Foundation. Thanks to University of Texas at Austin, Mechanical Engineering Department, Dr. Li Shi, and my mentor Chad Baker.

### References:

- [1] Aaron, J., et al. *Opt. Express*. 2008, 16, 2153-2167.
- [2] Kusumi, A., et al. *Biophys. J.* 1993, 65, 2021-2040.
- [3] Betzig, E., et al. *Biophys. J.* 1986, 49, 269-279.
- [4] Yang, P., et al. *Adv. Funct. Mater.* 2002, 12, 323-331.

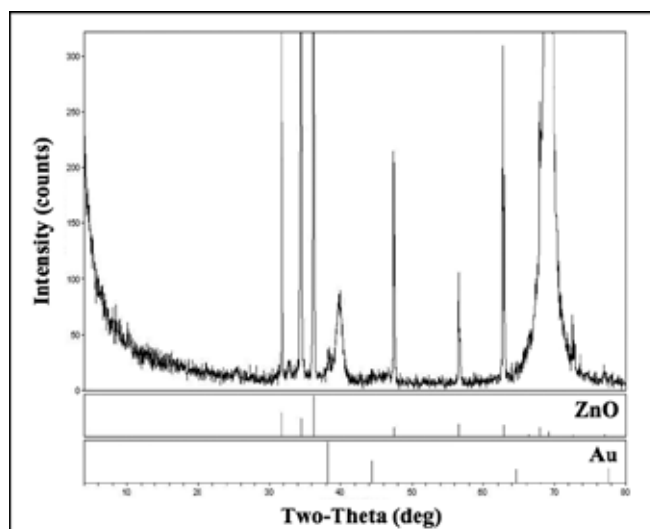


Figure 3: XRD of ZnO nanowires on silicon substrate.

# Low Field Dynamic Nuclear Polarization for Studying Soft Matter Systems

Alissa Cote

Materials Science and Engineering, University of Illinois at Urbana-Champaign

**NNIN REU Site: Nanotech @ UCSB, University of California, Santa Barbara, CA**

NNIN REU Principal Investigator(s): Prof. Songi Han, Chemistry and Biochemistry, University of California, Santa Barbara

NNIN REU Mentor(s): Mark Lingwood, Chemistry and Biochemistry, University of California, Santa Barbara

Contact: acote2@illinois.edu, songji@chem.ucsb.edu, mlingwood@chem.ucsb.edu

## Abstract:

Nuclear magnetic resonance (NMR) is a versatile technique for soft matter analysis. We can use NMR for imaging, as in the MRI of a brain, or to study the water dynamics in lipid membranes, the structure of proteins and their aggregates, and the aggregation of asphaltene, an element of crude oil. Although NMR is versatile, it also poses some challenges. NMR is an insensitive technique with low contrast. When studying large molecular assemblies, it is difficult to know if we see aggregation because of the insensitivity. In order to solve this problem, we can introduce a probe molecule, which in this case is a nitroxide radical, which gives localized information regarding the area of placement. We can either detect this probe molecule directly, through electron spin resonance (ESR), or transfer the information to the NMR signal of neighboring nuclei by using both ESR and NMR simultaneously; this is known as dynamic nuclear polarization (DNP).

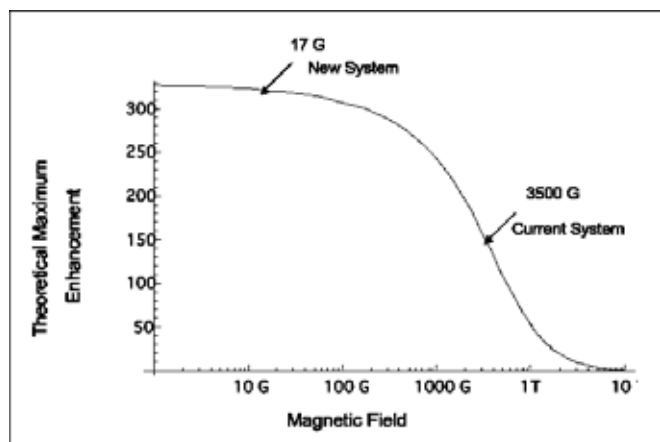


Figure 1; Plot of magnetic field vs. theoretical maximum enhancement

## Introduction:

DNP is a method to enhance NMR signal through polarization transfer from electron spins to nuclear spins, and can study water content and viscosity in lipid membranes. At 3500 G, which is the field of our current working DNP system, we have less-than-maximum or even no NMR signal enhancement at all. This project focuses on moving to a magnetic field of about 20 G since the theoretical maximum enhancement increases at a lower field (Figure 1). By moving to a low field, we will be able to both compare the DNP enhancement of samples at different fields and test samples in which no DNP enhancement was observed at 3500 G. We will focus on the design, construction, and testing of this new DNP system, and show some initial results.

In order to understand DNP, one must be able to understand NMR and ESR. When certain nuclei are placed in a magnetic field, the nuclear spin energy splits into different levels. This energy difference can be detected by applying radio frequency radiation to the nuclei. The small differences in the splitting of the energy levels give information on the molecule, seen in the NMR signal. Like NMR, ESR uses electromagnetic radiation to detect differences in energy levels. However, instead of detecting the nuclei, ESR detects the electron spin of free radicals or other paramagnetic species. This is only useful in systems which contain free electrons. Since the free electrons have a higher energy splitting than nuclei, ESR has greater signal sensitivity than NMR. When the free electrons are in close contact with the nuclei, NMR and ESR can be used simultaneously in a process known as DNP. Saturating the electrons with strong electromagnetic radiation perturbs the electron spins, which transfer the higher polarization to the nearby nuclei, and enhances the NMR signal.

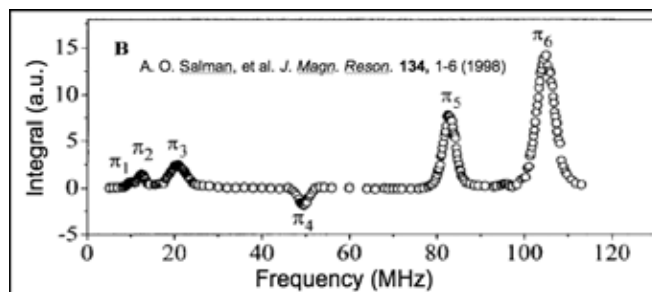


Figure 2: Example of an ESR spectrum at 15.3 G.

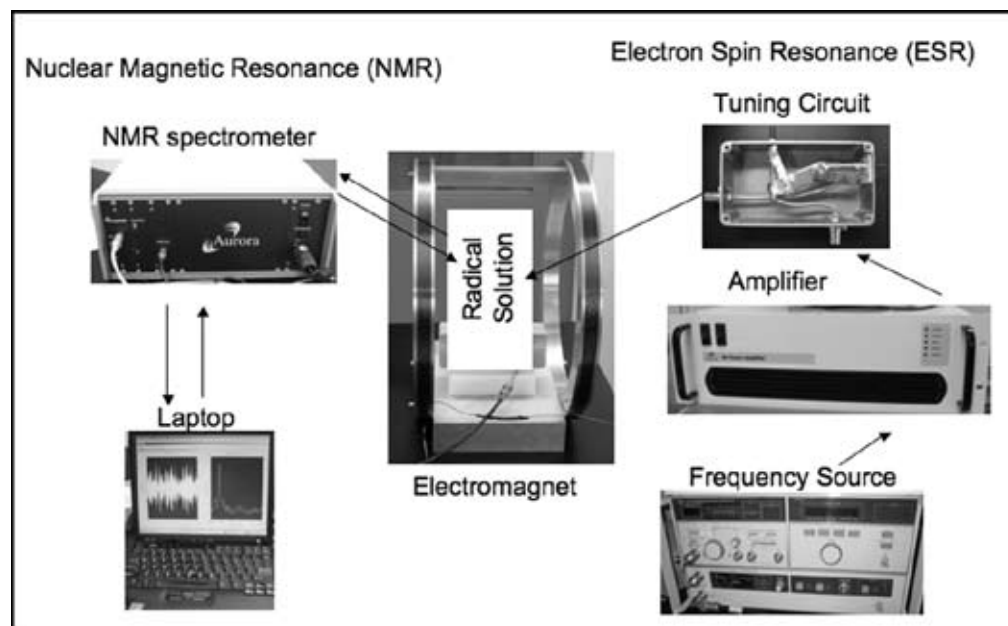
Moving to low fields has many advantages, but there are also some disadvantages. The ESR spectrum is much different at low fields than at high fields, and this spectrum can only be detected through DNP. At high fields, the applied magnetic field dominates the spectrum and we see three transitions, one for each spin state of the nitrogen nucleus in the nitroxide. However, at low fields, the applied field no longer dominates, but the nitrogen transitions dominate, and we see many more peaks in the ESR spectrum (Figure 2).

### Experimental Procedures:

Because DNP instruments are not commercially available, we built our own. First we built the electromagnet, a Helmholtz coil design, which consists of two coils placed on the same axis with the same current flowing through each one producing a homogeneous magnetic field. Our sample can be easily inserted or removed from the magnet.

The NMR system contains four parts: a laptop, an NMR spectrometer, the magnet, and a coil. The laptop first sends a signal to the spectrometer to send a radiofrequency pulse to the sample, which in our case is a 1 mM radical solution (4-amino-TEMPO). The spectrometer then sends the pulse to the sample, which in turn perturbs the nuclei from the water. This perturbation is then picked up by the NMR coil and sent back to the spectrometer, and the laptop collects information about the molecule.

For the ESR system, we have a frequency source, an amplifier, a tuning circuit, and a second coil. The frequency source sends a fixed frequency through the amplifier. From the amplifier, the frequency is sent to a tuned and matched circuit into the coil. This allows for the most power to get to the sample. A normal NMR experiment is conducted with the ESR saturation on in order to perform DNP. This setup is shown in Figure 3.



### Results and Conclusions:

In order to prove that our new low field DNP system worked, we reproduced previous results found in the literature. We successfully obtained a similar ESR spectrum through DNP (Figure 4). When using DNP, 117-fold enhancement with respect to the normal NMR signal was observed. Compare this to our current system of 3500 G with the same radical concentration in which the maximum enhancement is about 32-fold. This proves that the enhancement is greater at low fields.

### Future Work:

We can now use this low-field to test other systems, for example, studying the water dynamics in lipid membranes using this low field system compared with results with those taken at high fields. Also, we can now study crude oil in which no DNP enhancement was observed at high fields.

### Acknowledgements:

Thanks to Professor Songi Han, Mark Lingwood, and the Han group for all of their help with this project. Also thank you to the National Nanotechnology Infrastructure Network Research Experience for Undergraduates (NNIN REU) Program, the NSF and Angela Berenstein for opportunity to participate in this program at UCSB.

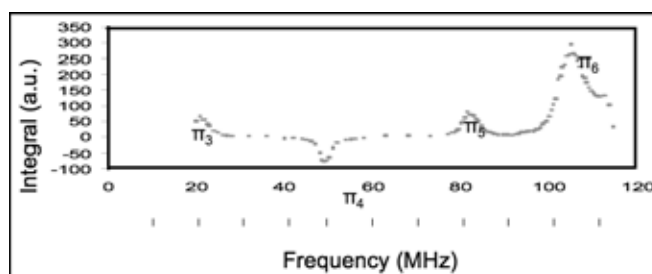


Figure 3, left: Experimental setup.

Figure 4, above: ESR spectrum at 15.3 G with our homebuilt system

# Investigation of the Reaction of Benzaldehyde on Titanium Dioxide

Christina Elias

Chemical Engineering, Ohio State University

**NNIN REU Site: Center for Nanoscale Systems, Harvard University, Cambridge, MA**

NNIN REU Principal Investigator(s): Professor Cynthia M. Friend, Chemistry and Biochemistry, Harvard University

NNIN REU Mentor(s): Dr. Lauren Benz, Dr. Jan Haubrich, Department of Chemistry and Biochemistry, Harvard University

Contact: christina.elias@gmail.com, cfriend@deas.harvard.edu, lbenz@fas.harvard.edu, haubrich@fas.harvard.edu

## Abstract/Introduction:

The interaction between oxide surfaces and organic compounds is of general industrial importance as many catalytic processes involve reactions between these species. Furthermore, volatile organic compounds are a class of environmental pollutants [1,2] and the interaction of such molecules with natural and engineered oxide surfaces is not well understood [3]. It is thought that processes such as adsorption, reaction, and/or decomposition over such oxides play a crucial role in the remediation of the pollutants. Additionally, organic compounds can alter the surface properties of oxide coatings, aerosols particles and catalysts significantly.

Therefore we have chosen to study the interaction of an organic molecule containing an aldehydic function with the surface an oxide using a simple model system: benzaldehyde on rutile titanium dioxide ( $\text{TiO}_2$ ) (110). Previously we observed carbon coupling reactions via loss of oxygen for such systems employing temperature programmed reaction spectroscopy (TPRS) [5]. Conversion of benzaldehyde to stilbene occurs for approximately 30 percent of the adhered benzaldehyde molecules. Previous studies attribute the reactivity to defects such as oxygen vacancies that leave active ensembles of reduced  $\text{Ti}^{3+}$  sites on the oxide substrate [6].

In the present study, scanning tunneling microscopy (STM) experiments were performed under ultra-high vacuum (UHV) conditions to identify the adsorption sites of benzaldehyde and search for reaction intermediates. Although benzaldehyde appeared mobile at room temperature, a preferred adsorption on five coordinated  $\text{Ti}^{4+}$  sites was observed; however, the movement of benzaldehyde molecules during the time scale of our experiment prevented a better resolution of the features. Future work will require cooling to low temperatures to immobilize the molecules, allowing for the precise identification of the active sites and possible reaction intermediates.

## Experimental Procedure:

A UHV Omicron STM set up (base pressure  $\sim 3 \times 10^{-10}$  torr) equipped with low energy electron diffraction (LEED), two mass spectrometers and an ion gun for argon sputtering, was used in this study. The sample surface was cleaned by a series of sputtering ( $10^{-6}$  mbar Ar, 1 keV, filament current 10 mA, 20 min.) and annealing ( $\sim 850$ - $900^\circ\text{K}$ , 5 min.) cycles prior to imaging. Temperatures were calibrated using a type K thermocouple. Benzaldehyde (Aldrich 99.5% plus purity) was further purified by freeze-pump-thaw cycles and dosed at room temperature exposures measured in Langmuir:  $1\text{L} = 1 \text{ torr}\cdot\mu\text{s} = 1.33 \cdot 10^{-6} \text{ mbar}\cdot\text{s}$ ) on the surface from a doser positioned 1 cm above the surface. Constant current images were taken with typical scanning parameters of 0.1-0.3 nA and 1-3 V. Both electrochemically etched and platinum/iridium (Pt/Ir) W tips were used while scanning.

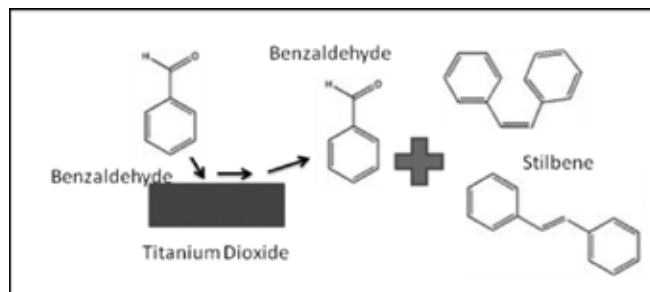
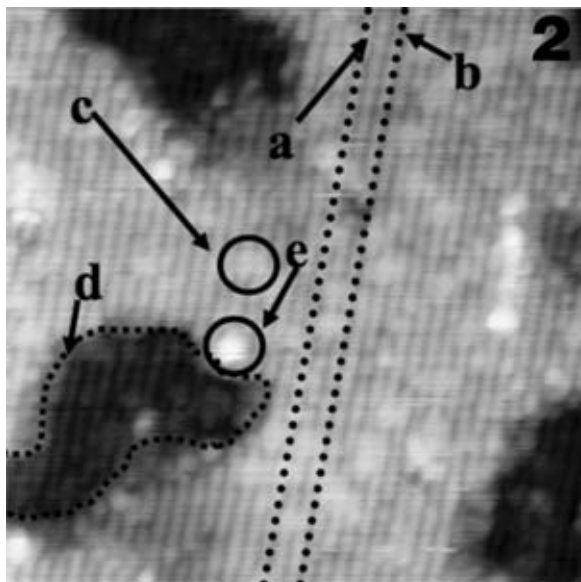


Figure 1: Reaction scheme developed after TPRS data analysis.

## Results:

Figure 2 shows the  $\text{TiO}_2$  (110) surface after cleaning. The spatial resolution achieved with STM clearly allows for the observation of  $\text{Ti}^{4+}$  (a, bright) and bridging oxygen (b, dark) rows. Inherent defects included bridging oxygen atom vacancies seen as bright breaks in the O rows (c), and step edges (d). These locations are regions of high interest for potential binding sites.

In Figure 3 one can see that the same area of the sample following dosing of ca 0.5 L benzaldehyde at room temperature. This coating is depicted clearly in the image and is represented by the bright round features which were observed bound to the titanium atom rows (g). Hence the preferred binding site of benzaldehyde must be over five coordinated  $\text{Ti}^{4+}$  ions. In contrast to our expectations, benzaldehyde did



not bind to bridging oxygen vacancies or step edges, which are usually strong adsorption sites.

Figure 4 that this is again the same region scanned after a five minute time elapse. This image illustrates how benzaldehyde molecules are mobile at room temperature. While some molecules remain in their original binding locations, others diffuse away to new locations. Still no accumulation at step edges occurs.

### Conclusions:

Points to take away from the work completed this summer include the following: benzaldehyde molecules bind weakly to five coordinated  $\text{Ti}^{4+}$  sites at room temperature. Notably they did not adsorb preferentially to oxygen vacancies or steps. At room temperature, they diffuse slowly across the surface. Future low temperature scanning to immobilize the molecules while investigating the reaction of benzaldehyde is required.

### Acknowledgments:

I would like to thank my principal investigator, Cynthia Friend, and mentors, Lauren Benz and Jan Haubrich, and organizations including National Science Foundation, National Nanotechnology Infrastructure Network Research Experience for Undergraduates Program, and the Harvard Center for Nanoscale Systems.

### References:

- [1] Usher, C.; Michel, A.; Grassian, V.; Chem. Rev. 2003, 103, 4883.
- [2] E.P.A, U. S. The original list of hazardous air pollutants, 2007.
- [3] Diebold, U. Surface Science Reports 2003, 48, 53.
- [4] Agency for Toxic Substances and Disease Registry, Toxicological Profile for Acrolein, Public Health Service, U.S. Department of Health and Human Services, Atlanta, GA, 1990.
- [5] Benz, L.; Haubrich, J.; Quiller, R. G.; " Reactions of Benzaldehyde and Acrolein on  $\text{TiO}_2(110)$  and the Influence of Defects and Coadsorbed Species", in preparation.
- [6] (a) Sherrill, A.B.; Idriss, H.; Barteau, M.A.; Chen, J.G. Catalysis Today 2003, 85, 321; (b) Idriss, H.; Pierce, K.G.; Barteau, M.A. Journal of the American Chemical Society 1994, 116, 3063.

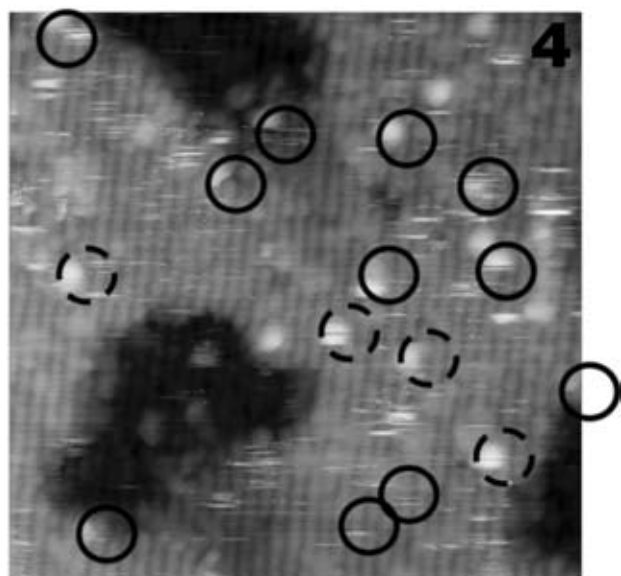
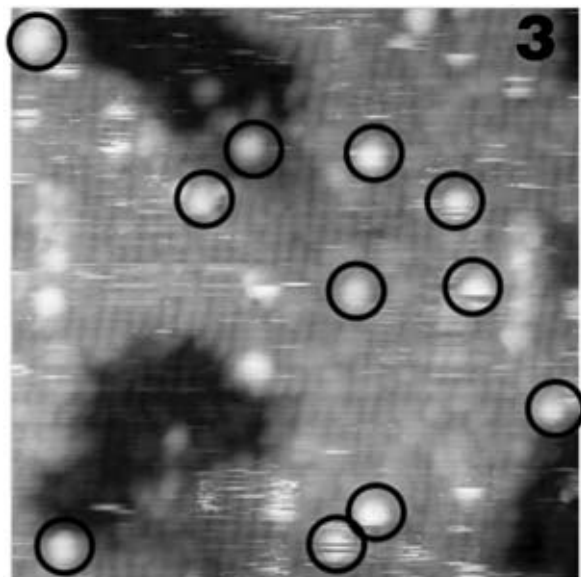


Figure 2, top: STM image of clean  $\text{TiO}_2$  surface (imaging parameters:  $30 \text{ nm} \times 30 \text{ nm}$ ,  $300\text{K}$ ). Features identified are (a) bright Ti atom rows; (b) dark O atom rows; (c) bridging O vacancy; (d) step edge; (e) unknown contaminant.

Figure 3, middle: STM image of  $\text{TiO}_2$  immediately after a  $0.5\text{L}$  benzaldehyde exposure (imaging parameters:  $30 \text{ nm} \times 30 \text{ nm}$ ,  $300\text{K}$ ).

Figure 4, bottom: STM image taken after 5 min. Filled circles are previous molecule locations, while new molecules are circled with hatched lines. (imaging parameters:  $30 \text{ nm} \times 30 \text{ nm}$ ,  $300\text{K}$ ).

# Synthesis of Nanostructured Iron Oxide Thin Films for Photocatalytic Hydrogen Production

Olaronke Latunde

Chemistry, University of Maryland Baltimore County

**NNIN REU Site: Nanotech @ UCSB, University of California, Santa Barbara, CA**

NNIN REU Principal Investigator(s): Prof. Eric McFarland, Department of Chemical Engineering, University of California

NNIN REU Mentor(s): Dr. Yong-Sheng Hu, Department of Chemical Engineering, University of California, Santa Barbara

Contact: latuola1@umbc.edu, mcfar@engineering.ucsb.edu, yshu@engineering.ucsb.edu

## Abstract:

Photocatalytic hydrogen production has the potential to provide an alternative source of energy. For this to occur, a suitable semiconductor with the right band gap is needed for maximum visible light absorption. The two main methods used for the synthesis were sol-gel for dip coating and electrodeposition. Iron chloride and ferric nitrate were used as iron precursors, and the substrates used included fluoride doped tin oxide (FTO) glass, and platinum coated on quartz. After synthesis using various combinations of precursors, substrates, methods and dopants, the samples are calcined at 550°C or 700°C for 4 hours depending on the substrate used. This is to ensure that the iron hydroxide is converted to iron oxide. So far samples calcined at 700°C show the best performance.

## Introduction:

Energy issue is a great challenge in the 21st century. The focus of the group is to create a cost effective and more efficient way to produce hydrogen using solar energy in a photoelectrochemical cell.

In the case of photoelectrochemical hydrogen production [1-3], a suitable semiconductor absorbs light causing electrons to be excited from the valence band to the conduction band. The excited electrons cause water reduction to form hydrogen, the holes left behind result in oxidation to yield oxygen as a byproduct.

Iron oxide has potential advantages [4] for photoelectrochemical hydrogen production. It is stable in aqueous solutions with pH above 3, it has a suitable band gap of 2-2.2eV that enables 40% sunlight absorption. It is also abundant and inexpensive. However iron oxide has limitations which hinder its photoelectrochemical performance such as its poor conductivity which often leads to a high recombination rate, its inappropriate conduction band for hydrogen evolution, its low kinetics for water oxidation and its low optical absorption. The focus was to address the limitations hindering its photoelectrochemical performance.

## Experimental Methods for Synthesis:

**Sol-Gel Method.** Sol-gel method is fast, simple and efficient. It can be done on a large scale. The mixture of 0.46M solution of the iron precursor in ethanol, 1.2 ml of propylene oxide and 30% F127 polymer forms a sol for the following dip-coating. The substrates are dipped in a sol solution using a linear motion stage at a rate of 100  $\mu\text{m}/\text{sec}$  for a downward displacement of 15 mm; the substrate stays in the solution

for 120 secs and is then displaced upwards at the same rate. Following the evaporation of the solvent by air the process is repeated twice to ensure the right amount of thickness of iron oxide film.

**Electrodeposition Method.** Electrodeposition enables good electronic contact, the microstructure of the samples can be controlled and it also enables large scale production. Three-electrode system was used for the electrodeposition. The counter electrode was platinum, the working electrode was the FTO or Pt and the reference electrode was Ag/AgCl. The applied voltage was between -0.49 and 0.41V for 5 cycles. The solution contained 5 mM  $\text{FeCl}_3$ , 5 mM KF, 0.1 M KCl and 1 M  $\text{H}_2\text{O}_2$  [5]. All samples were calcined at the same conditions as the sol-gel samples. Detailed PEC measurements are shown in Ref [5].

## Results and Discussion:

**Structure and Optical Properties.** Figure 1 shows the typical Raman spectra of iron oxide prepared by sol-gel and electrodeposition methods. All the peaks are belonging to  $\alpha\text{-Fe}_2\text{O}_3$ , indicating the Hematite structure. The UV-vis absorption curves and Tauc plots of undoped and 5% Ti doped iron oxide thin films are presented in the inset of Figure 1. It can be seen that both samples exhibit very similar bandgap around 2.2 eV, which is a typical value for  $\alpha\text{-Fe}_2\text{O}_3$ .

**Doping Effect:** In Figure 2, it can be seen that, among all the samples prepared by sol-gel method, 5% Ti doped sample shows the best photoelectrochemical performance. The samples are also quite stable as indicated by the negligible corrosive current in the dark. The  $\text{FeCl}_3$  iron precursor induced

sample displays slightly better performance than that of  $\text{Fe}(\text{NO}_3)_3$  precursor, which might result from the different microstructures from different iron precursors. We dip coated the sample once, twice and three times to see the effect of thickness on photoelectrochemical performance. The result shows that samples dip-coated twice exhibit the highest photocurrent.

**Interfacial Effect:** A thin layer between FTO and active photocatalyst may help to improve the charge transfer between them, resulting in a higher charge separation efficiency [4]. Therefore, we compare the PEC results from bare FTO, a thin layer of  $\text{TiO}_2$  or  $\text{SnO}_2$  coated FTO. It can be seen from Figure 3 that  $\text{SnO}_2$  shows better PEC performance than the other interfaces used.

**Temperature and Method Effects:** The undoped sample calcined at  $550^\circ\text{C}$  does not show any photocatalytic performance as shown in Figure 4. However, when the sample was calcined at  $700^\circ\text{C}$ , it shows appreciated photocurrent, which could be due to the higher crystallinity obtained at high temperature calcinations, resulting in a better charge transfer. One can also see that the undoped sample prepared by sol-gel method shows slightly better PEC performance than that of sample prepared by the electrodeposition method.

## Conclusion:

In conclusion, nanostructured iron oxide thin films were prepared by different methods. Doping effect, precursor effect, interfacial effect, temperature effect and method effect were investigated. Adding 5% Ti to the sample improves the PEC performance. Among the three iron precursors used, iron chloride shows the best result. Using tin oxide as an interface for electron transfer shows better results than titanium oxide and bare FTO. Calcination at a higher temperatures improves photoelectrochemical performance. Samples synthesized by sol-gel method show increased photoelectrochemical performance than samples synthesized by electrodeposition.

## Acknowledgments:

I would like to acknowledge my PI Prof E. W. McFarland, my mentor, Dr Yong-Sheng Hu, NNIN REU and NSF for their help and support.

## References:

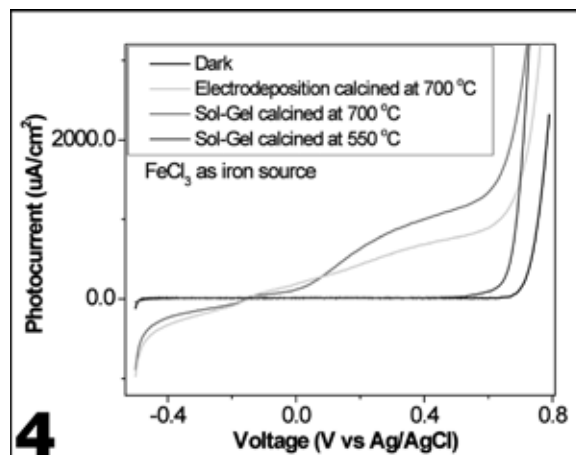
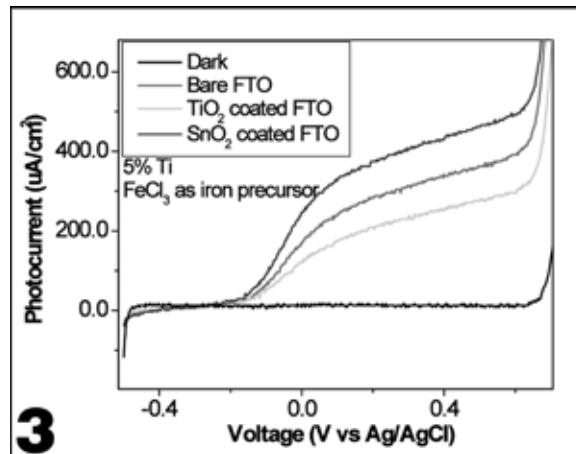
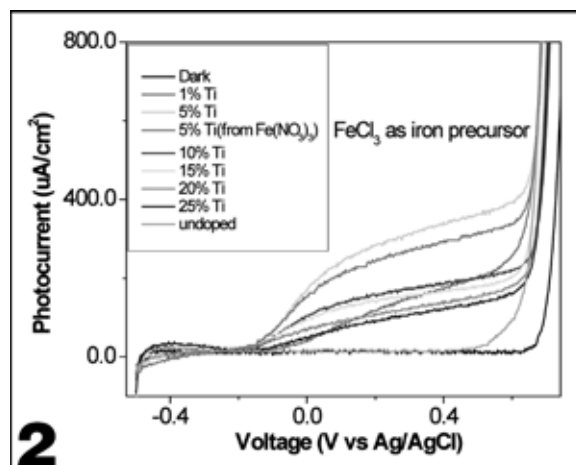
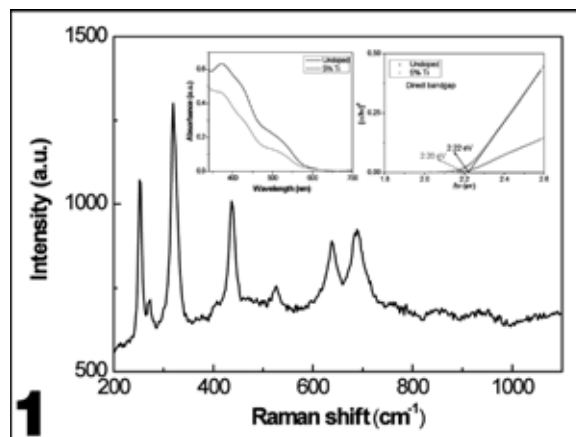
- [1] Fujishima, A.; Honda, K. *Nature* 1972, 238, 37.
- [2] Khaselev, O.; Turner, J. A. *Science* 1998, 280, 425.
- [3] Gratzel, M. *Nature* 2001, 414, 338.
- [4] Kay, A.; Cesar, I.; Gratzel, M. *J. Am. Chem. Soc.* 2006, 128, 15714.
- [5] Hu, Y. -S., et al; *Chem. Mater.* 2008, 20, 3803.

Figure 1: Typical Raman spectrum of iron oxide thin films. (Inset showing the UV-Vis absorption spectra (left) and  $T_{auc}$  plots (right) of iron oxide thin films.)

Figure 2: IV curves showing dark current, undoped sample, X % Ti doped samples from  $\text{FeCl}_3$  iron precursors and 5% Ti sample from  $\text{Fe}(\text{NO}_3)_3$  iron precursor.

Figure 3: A very thin layer of  $\text{TiO}_2$  or  $\text{SnO}_2$  was between FTO and iron oxide.

Figure 4: IV curves comparing preparation by electrodeposition and sol gel methods.



# Synthesis of Copper (II) Oxide Particle and Detection of Photoelectrochemically Generated Hydrogen

Yu Li

Chemical Engineering, University of California, Davis

**NNIN REU Site: Nanotech @ UCSB, University of California, Santa Barbara, CA**

NNIN REU Principal Investigator(s): Professor Martin Moskovits, Chemistry, University of California, Santa Barbara

NNIN REU Mentor(s): Nick Hight-Huf, Department of Chemistry, University of California, Santa Barbara

Contact: yugli@ucdavis.edu, mmoskovits@lsc.ucsb.edu, nhighthuf@chem.ucsb.edu

## Abstract:

Nano-sized copper (II) oxide (CuO) particles (size ranging from 100-400 nm) were synthesized by ultrasonic spray pyrolysis (USP) starting from aqueous copper (II) nitrate with varying reaction conditions (reactor temperature 450K-1180K, residence time 2s-5s). The products were confirmed by Fourier transform infrared spectroscopy (FTIR) (1384  $\text{cm}^{-1}$  assigned as  $\text{Cu}^{2+}\text{-O}^{2-}$  stretching mode). Decreasing the reactor temperature resulted in an attenuation of x-ray diffraction (XRD) peak intensity (corresponding to apparent decreased crystallinity) coupled with an increase in mean particle size and deviation. The direct band gap was estimated to be  $\sim 1.6\text{-}1.9$  eV from UV-Vis spectra.

## Introduction:

Hydrogen has great potential as an environmentally friendly fuel since the byproduct of its combustion is water, yet the current method of hydrogen production is very inefficient and costly [1]. Solar energy is a large source of energy available for consumption, yet it is not utilized very efficiently [2]. The photoelectrochemical splitting of water as a method of hydrogen production using solar energy as a driving force to produce hydrogen is of great interest due to its ability to take advantage of abundant and renewable natural resources and convert them into highly deployable energy medium.

The focus of this research is on synthesizing nano-sized CuO nanoparticle that can absorb visible light to produce hydrogen from water. Objectives of this research project are to synthesize CuO nanoparticle and study their characterizations, also to test their hydrogen production performance.

## Experimental Procedures:

**Ultrasonic Spray Pyrolysis (USP).** 0.1 M of  $\text{Cu}(\text{NO}_3)_2$  solution was prepared by mixing 2.326 g of  $\text{Cu}(\text{NO}_3)_2 \cdot 2.5\text{H}_2\text{O}$  solid and 100 ml of DI water in a volumetric flask. The solution was stirred for 30 minutes. 50 ml of the  $\text{Cu}(\text{NO}_3)_2$  solution was then nebulized (Sunpentown SU-2000) and carried into furnace (Linberg BlueM TF55035A) by air for heat treatment ranging from 450K-1180K. CuO nanoparticles were collected through a bubble trap of DI water after the furnace. CuO nanoparticles were cleaned in a sonicator. Reactor temperatures and air flow rates were varied to obtain different characterizations of CuO. Characters of CuO were studied by FTIR, XRD, TEM, SEM, and UV-Vis. Data explained in the "Result" section.

**Improvement to Ultrasonic Spray Pyrolysis:** Modifications to USP were attempted to decrease the particle size of CuO nanoparticle. Surfactants including soap and hexanol were

added to reduce the surface tension and reduce the size of the micronized droplets entering the tube furnace portion of the reactor. The  $\text{Cu}(\text{NO}_3)_2$  solution was preheated before nebulization as an alternative method of reducing surface tension which according to literature [3] will reduce particle size of final products.

**Photoelectrochemical Reaction:** Only initial data was obtained from the hydrogen production analyser. Please refer to "Future Work" section for planned procedures for hydrogen production performance.

## Results:

By the ultrasonic spray pyrolysis method, CuO was successfully synthesized at different reaction conditions (resident time between 2s-5s). CuO nanoparticles were confirmed by FTIR (NICOLET 4700 FT-IR) exhibiting a

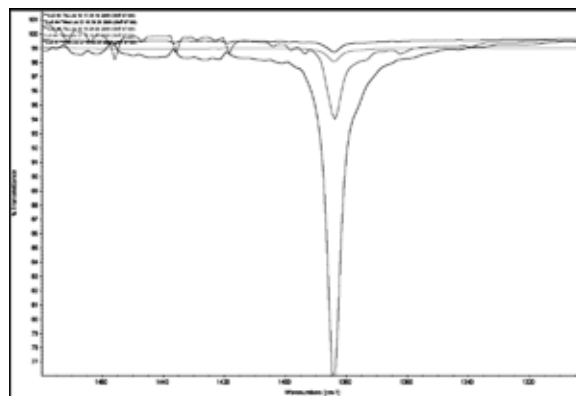


Figure 1: FT-IR,  $\text{Cu}^{2+}\text{-O}^{2-}$  stretching mode peak at 1384  $\text{cm}^{-1}$ . Confirmed the CuO nanoparticle actually was presented in final products.

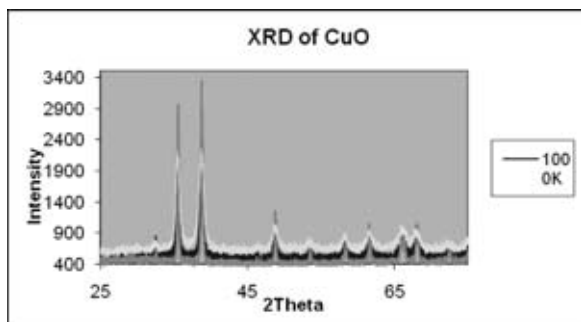


Figure 2: X-ray diffraction graph. Strong peaks showed the CuO hold crystalline structure. An increase in reactor temperature show an increase in peak intensity which suggest increase in crystallinity.

$\text{Cu}^{2+}\text{-O}^{2-}$  stretch mode peak at around  $1384\text{ cm}^{-1}$  (Figure 1). X-ray diffraction graph (Figure 2) indicated all the CuO nanoparticle samples had strong crystalline structure. Intensity of the XRD peak at 1180K was higher than 1000K and 726K. It was suggestive that at higher reactor temperature, stronger crystalline structures were obtained. The particle sizes of CuO were investigated by scanning electron microscope (SEM) and transmission electron microscopy (TEM) in Figure 3. It is shown that sizes of CuO ranged from about 100-400 nm. The images also showed that there was a decreasing trend in particle size as reactor temperature increased. This trend makes sense as higher reactor temperatures resulted in lower residence times, lower resident times resulted in lower collision frequency, therefore reduced particle sizes.

Ultraviolet-visible spectra showed a display of absorbance corresponding to wavelength. According to the equation [4],  $ah\nu = A(h\nu - E_g)^{n/2}$ —where  $a$  is absorbance,  $h$  is Planck's constant,  $\nu$  is frequency,  $A$  is proportional constant,  $n$  is assumed to be 1, and  $E_g$  is the band gap—the band gap can be calculated after rearrangements and necessary calculations were done (Figure 4). It was found that the direct band gap of CuO samples deviate between 1.6eV to 1.9eV with no noticeable pattern.

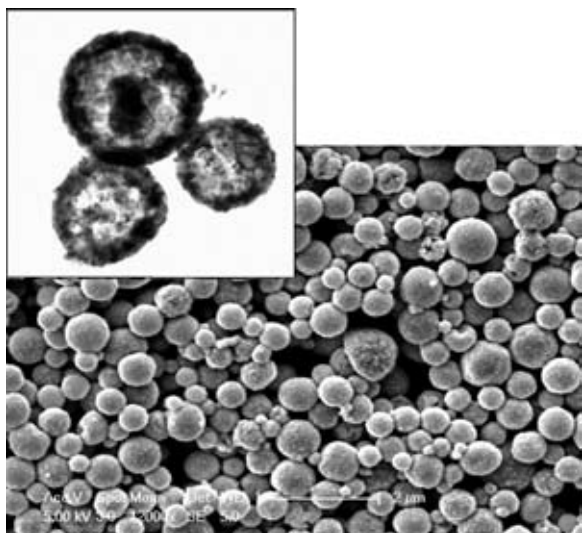


Figure 3: SEM and TEM image. CuO particle sizes were showed to be around 100 nm to 400 nm.

The efficiency rate of the hydrogen product is yet to be determined.

## Conclusion:

Copper (II) oxide nanoparticle was fabricated by the ultrasonic spray pyrolysis method. CuO products were confirmed to be presented in the final products. CuO nanoparticles all showed strong crystalline structure. CuO particle sizes ranged from 100 nm to 400 nm according to TEM and SEM. Direct band gap of the CuO samples was measured to be about 1.6eV to 1.9eV by UV-Vis spectra.

## Future Work:

**Photoelectrochemical Reaction Testing.** More investigation needs to be done on hydrogen evolution rate. Procedures for the investigation are planned as following: Mix 20 ml of DI water with 0.05g CuO sample in a test tube. Shine UV light on the test tube with a mercury lamp in a closed chamber. Collect any gas produced and analyzed the gas with a gas chromatography machine.

## Acknowledgements:

I would like to thank the follow people who made this internship possible for me: my mentor Nick Hight-Huf, my coordinator Angela Berenstein, my principal investigators Professors Eric McFarland and Martin Maskovits, and the National Nanotechnology Infrastructure Network Research Experience for Undergraduates (NNIN REU) Program.

## References:

- [1] Bellona, <http://www.interstatetraveler.us/Reference-Bibliography/Bellona-HydrogenReport.html>.
- [2] Eric McFarland, and Martin Maskovits, "High Efficiency Colloidal Photo Electro catalysts by Plasma Synthesized  $\text{Fe}_2\text{O}_3$  Nanoparticles."
- [3] Department of Energy, <http://www.newton.dep.anl.gov/askasci/phy00/phy00627.htm>.
- [4] Diwakar Chauhan, V R Satsangi, Sahab Dass, and Rohit Shrivastav. "Preparation and Characterization of Nanostructured CuO Thin Films for Photoelectrochemical Splitting of Water." Bulletin of Materials Science. Vol. 29, No. 7. December 2006.

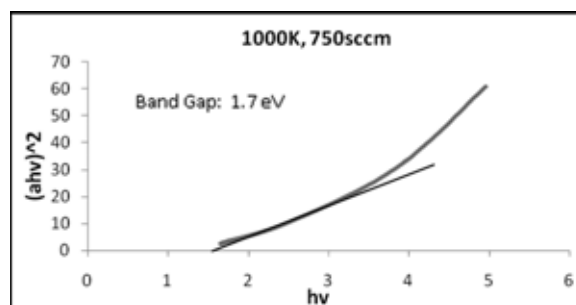


Figure 4: UV-Vis spectra after modification by  $ah\nu = A(h\nu - E_g)^{n/2}$  (explained in result section).  $E_g$ , the direct band gap was obtained by the x intercept of the linear fit of the first part of spectra before it changes slope. Band gap for this sample was estimated to be 1.7eV. for all CuO samples, band gaps were between 1.6eV to 1.9eV.

# Fabrication of Synthetic Trees for the Investigation of Water at Negative Pressures

Logan Osgood-Jacobs

Engineering, Swarthmore College

**NNIN REU Site: Cornell NanoScale Science and Technology Facility, Cornell University, Ithaca, NY**

NNIN REU Principal Investigator(s): Abraham Stroock, Chemical and BioMolecular Engineering, Cornell University

NNIN REU Mentor(s): Juho Song, Chemical and BioMolecular Engineering, Cornell University

Contact: losgood1@swarthmore.edu, ads10@cornell.edu, js954@cornell.edu

## Abstract:

Water is one of the most well-researched materials on earth, however, its properties at large negative pressures have been relatively unexplored. The current methods for studying water at negative pressures do not allow the manipulation needed to explore the thermodynamic, dynamic, and structural properties of water. Trees have an elegant mechanism to transport water from root to leaf through transpiration using water at negative pressures of up to -100 atms [1]. The Stroock group successfully imitated this mechanism using a hydrogel membrane to create negative pressures in water. Recreating this mechanism with a solid-state platform rather than a gel would allow direct pressure sensing, avoid deformation and collapse due to stress, and, potentially, further possibly increase achievable tensions by exposure to highly hydrophilic surfaces. This study describes a new strategy for forming a “Synthetic Tree” in which the key element is a silicon-supported, nanoporous membrane: through-etched holes in a silicon wafer provide the mechanical support for the nanoporous glass; anodic bonding of this membrane to a Borofloat glass wafer containing wells will allow macroscopic volumes water to be put under tension.

## Introduction:

In nature, water is manipulated and used at negative pressures through transpiration, as shown in Figure 1. With transpiration, the roots extract, from sub-saturated soil, liquid water that then travels up the xylem and evaporates from the leaf. The evaporation creates negative pressure in the water in the xylem. The plant thereby maintains a stabilized flow of liquid water at large negative pressures. With a root membrane connected by a channel to a leaf membrane, the synthetic tree replicates this system in the simplest way. The water evaporates through capillaries in the leaves, and to imitate this system effectively requires many capillaries in the leaf membrane. The equation for the pressure of a liquid in a capillary is

$$P_l = P_v - \frac{2\gamma}{r} \cos \theta$$

( $P_l$  = liquid pressure,  $P_v$  = vapor pressure,  $\gamma$  = surface tension,  $r$  = capillary radius,  $\theta$  = angle of meniscus from side wall), which implies that to increase the magnitude of the achievable negative pressures, one must make the radius of the pores as small as possible [2]. This constraint necessitates a nanoporous material.

The previous model of the synthetic tree used hydrogel, a nanoporous organic material, to create the leaf and root membranes. In the new model, spin-on-glass (SOG) serves

as the nanoporous membrane. Typically used in electronics and not as a membrane, it was uncertain how SOG would work for this purpose. Two types of SOG were tested, silicate-based and organosilicate. Silicate-based has the advantage of being more hydrophilic, however it is more prone to cracking during curing due to large amounts of stress. Although more hydrophobic, organosilicate SOG has less stress and was therefore better to work with.

SOG acted as the membrane in both the root and leaf structures of the synthetic tree, and a silicon structure, as pictured in Figure 2, provided support necessary for mechanically stability. In addition, the silicon structure allowed for the future integration of pressure sensors.



Figure 1: California redwood using negative pressures up to -10 atm for transpiration.

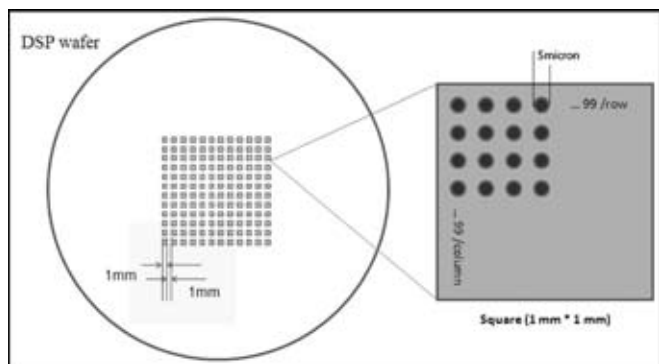


Figure 2: Silicon support structure.

### Fabrication:

The first step in creating the leaf/root membrane was fabricating the silicon support structure, which provided the foundation for the SOG. Starting with a double-sided polished 400  $\mu\text{m}$  thick silicon wafer, an array of 1 mm squares were etched 350  $\mu\text{m}$  deep using standard photolithography followed by the Bosch process in a deep reactive ion etcher. Silicon dioxide ( $\text{SiO}_2$ ) was then deposited as an etch block, enabling a later through-wafer etch. Next, a layer of aluminum was evaporated onto the unetched side, protecting the silicon surface for later anodic bonding. An array of 5  $\mu\text{m}$  diameter holes were then etched through in each of the previously opened squares, using standard photolithography, then an aluminum etch, followed by a descuming oxygen plasma, leading to the through-etch using the Bosch process.

Without any previous research on using SOG for this purpose, we had to find a way to fill the through-etched holes. Our first method was applying the SOG to the flat underside of the wafer using a synthetic paintbrush and using capillary action to wick the SOG into the holes. Our second method was to first partially dry the SOG, making it more viscous, then spread it over the wafer with the flat side up, using a PDMS squeegee to push the SOG into the holes and wipe off the excess. After filling and drying, the SOG was cured at 400°C for an hour. SEM images in Figures 2 and 3 show the tops of the 5  $\mu\text{m}$  diameter holes in a sample with painted SOG and squeegeed SOG. The visible menisci indicates that most if not all holes are well filled and few cracked, making both of these methods viable.

We proposed to bond the SOG-filled membrane to a glass wafer with small wells by anodic bonding. These wells would later be used to hold the water under tension. To prepare the membranes for bonding, first, the excess spin on glass had to be removed. We found chemical mechanical polishing (using SS12 slurry) to be the best method to remove the SOG, leaving a clean silicon surface ready for bonding. Time constraints permitted only one trial of anodic bonding. This test was unsuccessful, however, numerous scratches from aligning by hand, the possibility of the polarity being reversed and numerous other factors, indicate that anodic bonding may still be possible.

### Future Work:

Although the device has not yet been finished and tested, we

know of some changes to the process that would be beneficial. First, removing excess SOG by chemical mechanical polishing rather than etching eliminates the need for the aluminum layer. Second, adding a protective layer to the front side would help prevent scratches while opening up the backside windows.

The next step would be more precise anodic bonding tests to obtain a successful seal. After that, the device can be tested using Raman Spectroscopy to investigate properties of water at negative pressures. If successful at putting water at high negative pressures, this device can then be incorporated with a pressure sensor and eventually connected to create the synthetic tree.

### Acknowledgements:

National Nanotechnology Infrastructure Network Research Experience for Undergraduates (NNIN REU) Program; National Science Foundation; Cornell NanoScale Facility; CNF staff; Abraham Stroock; Juho Song.

### References:

- [1] Wheeler, T.D and Stroock, A.D., "The transpiration of water at negative pressure in a synthetic tree", *Nature*, (August, 2008).
- [2] Stroock, A.D., "Fundamental Studies to Advance the Science and Engr of Water at Negative Pressures", CAREER grant proposal, 2007.

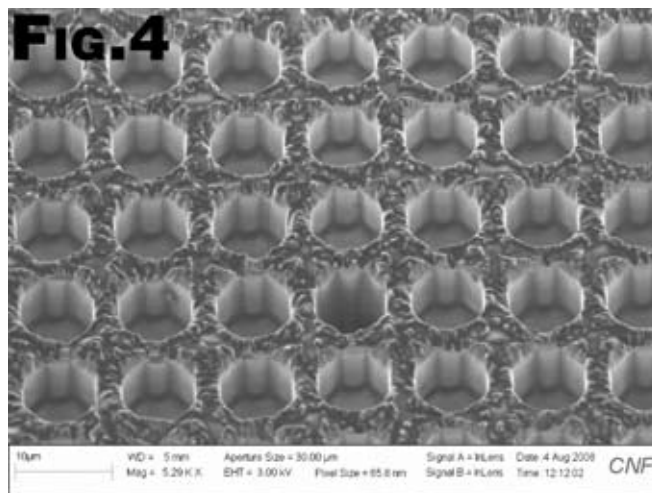
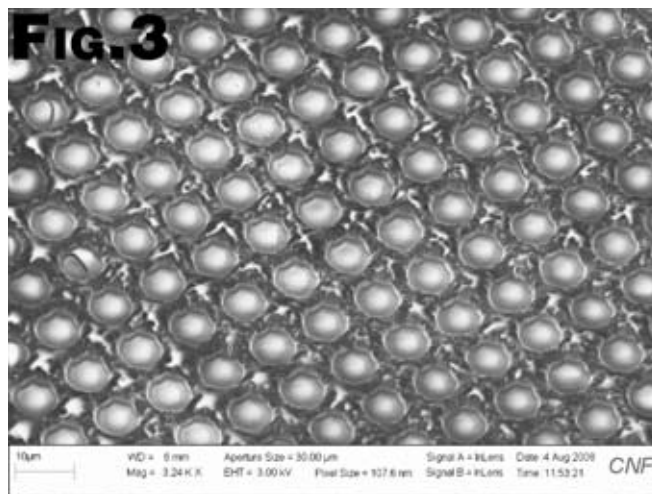


Figure 3: SEM image of 5  $\mu\text{m}$  holes with painted on SOG.  
Figure 4: SEM image of 5  $\mu\text{m}$  holes with squeegeed on SOG.

# Carbon-Based Supercapacitor Test Cell Assembly Optimization

Jennifer Caraway

Chemistry, The University of the Incarnate Word

**NNIN REU Site: Microelectronics Research Center, University of Texas, Austin, TX**

*NNIN REU Principal Investigator(s): Dr. Rodney S. Ruoff, Mechanical Engineering, The University of Texas at Austin*

*NNIN REU Mentor(s): Meryl Stoller, Mechanical Engineering, The University of Texas at Austin*

*Contact: jenn.caraway@gmail.com, r.ruoff@mail.utexas.edu, mstoller@mail.utexas.edu*

## Introduction:

Electrochemical double-layer capacitors (EDLCs), also called “supercapacitors,” are an important component for energy storage technology due to their high power densities, yet their energy densities are less than those of most batteries [1]. As stated by the Office of Basic Energy Sciences, advances in electrical energy storage technology are critical to meeting future energy demands [2].

Our project focused on optimizing the assembly process of a test cell for developing EDLCs. Using a two-electrode cell design with activated carbon[3] and an organic electrolyte, it was found that in initial measurements the assembled cells met the specific capacitance and power density goals, however this capacitance degraded rapidly after a few hundred cycles. We outlined alterations for drier assembly, which showed some improvement under electrochemical testing, but still demonstrated a decline in capacitance. Ongoing research seeks to determine the mechanism of degradation and attempts to improve reliability of the cell.

## Experimental Procedure:

The test cell design outlined in Figure 1 incorporated several commercial materials, including mylar sheets as shims, aluminum metal current collectors, and separator film. For optimizing the assembly process, we began by using activated carbon as our electrode material. The activated carbon was mixed with 3% by weight polytetrafluoroethylene as a non-conductive binder. As attempts to mix solid polymer with the carbon were unsuccessful, the binder in both versions of the method was added in an aqueous solution (20% by weight H<sub>2</sub>O) and mixed evenly. The material was flattened to a nominal thickness of 80 μm, cut to shape, and weighed. These electrodes were then placed under low vacuum and dried at 100°C.

The electrolyte was 8M tetraethylammonium tetrafluoroborate in acetonitrile. In the proposed dry method, the salt sample was heated under vacuum at 100°C prior to mixing the solution. After immersing the electrodes in electrolyte for 12 or more hours, the test cell was assembled (see Figure 1). Un-optimized assembly allowed the test cell to be assembled in open air, whereas our dry method involved dry box assembly under nitrogen flow, where humidity was maintained near zero. Electrochemical tests were performed using the Autolab cyclic voltammeter and frequency response analyzer. Capacitance was determined using the formula in Figure 2.

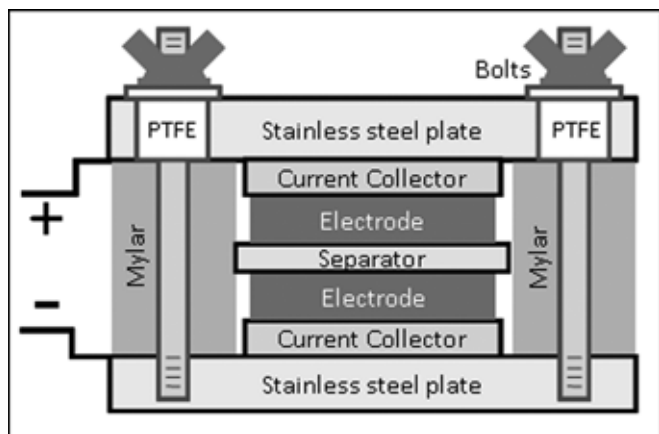


Figure 1: Diagram of two-electrode cell [4].

$$C = 4 * I \div [(V/s) * m]$$

Figure 2: Equation for capacitance. *I* represents current, (*V/s*) is the scan rate (volts per second), and *m* represents the mass of the electrode materials.

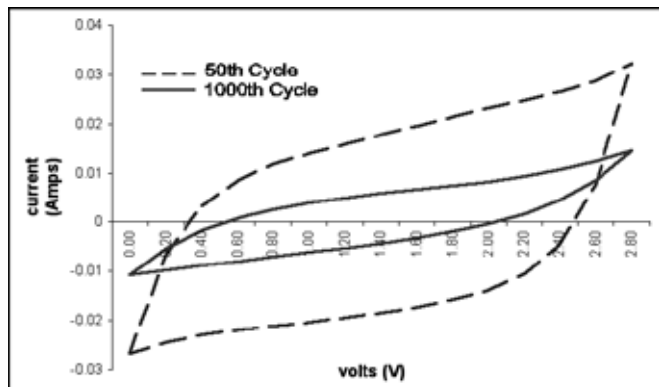


Figure 3: Cyclic voltammogram comparison of 50<sup>th</sup> and 1000<sup>th</sup> cycles in an unoptimized test cell.

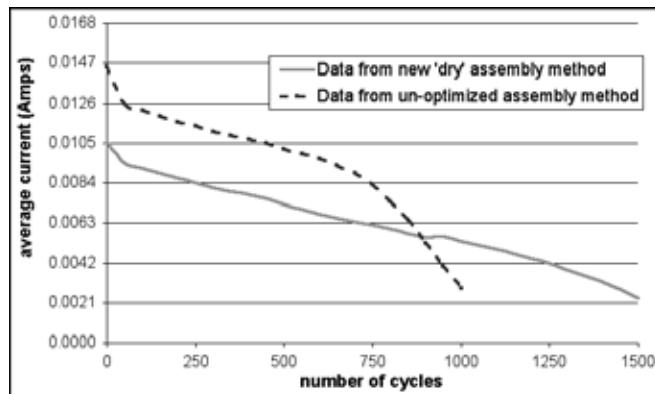


Figure 4: Plot comparison of degrading average current in assembly methods.

## Results and Conclusions:

Figure 3 depicts a cyclic voltammogram of an un-optimized test cell. While initial cycles recorded high values for current, for which a capacitance of 100 F/g was calculated, after 1000 cycles this value was greatly reduced. We proposed that this observation was due to water contamination in the electrolyte, which led to our development of the dry assembly method. The decline in average capacitance from the un-optimized method under long-term testing was compared with that of the drier method and is presented in Figure 4.

It should be noted in Figure 4 that the initial average current is higher in the un-optimized test cell, however this may be due to slight differences in the masses of activated carbon in the electrodes or variations in the concentration of the electrolyte. Of particular importance is that, while both plots show a general decline in average current throughout the course of testing, the dry-method test cell had a longer cycle life. Comparison of the data also showed the sharp drop-off observed near 700 cycles during prior testing was not present in the drier assembly test, generating linear decline.

## Future Work:

As the results indicated an improvement, especially in regard to the linear character and rate of capacitance loss, we will continue to use drier assembly methods for the test cell and seek further improvements upon the method. We will also continue to seek out a non-aqueous binder for the electrodes. We will also address other potential sources of degradation, such as material failure and shorts in the circuit. Should the issue of capacitance loss be minimized, the test cell will be more effective for testing the cycle life of new materials in the electrodes.

## Acknowledgments:

I would like to thank Dr. Rodney Ruoff, Meryl Stoller, and the entirety of our research group at UT Austin for their guidance and support, as well as Dr. John Stankus and the site coordinators at the Microelectronics Research Center at The University of Texas. A special thanks to the National Nanotechnology Infrastructure Network REU Program, the NSF, and the McNair Scholars Program for financial support.

## References:

- [1] Conway, B.E. Electrochemical supercapacitors: Scientific fundamentals and technological applications. Kluwer Academic / Plenum Publishers: New York, 1999; pp 12-37.
- [2] Basic research needs for electrical energy storage: Report of the basic energy sciences workshop on electrical energy storage. April 2-4, 2007. Office of Basic Energy Sciences, Department of Energy, July 2007.
- [3] Pandolfo A.G., Hollenkamp A.F. "Carbon properties and their role in supercapacitors"; Journal of Power Sources, 157(1), pp 11-27 (2006 April 4).
- [4] M. D. Stoller, S. Park, Y. Zhu, J. An, and R. S. Ruoff. 'Graphene-Based Ultracapacitors', Nano Letters, (2008 Sept 13).

# Post 22 Nanometer, III-V MOSFET Fabrication

Megan Connors

Electrical Engineering, University of Maryland, College Park

**NNIN REU Site: Nanotech @ UCSB, University of California, Santa Barbara, CA**

NNIN REU Principal Investigator(s): Professor Mark Rodwell, Electrical and Computer Engineering, UCSB

NNIN REU Mentor(s): Gregory Burek, Electrical and Computer Engineering, University of California, Santa Barbara

Contact: mconnors@umd.edu, rodwell@ece.ucsb.edu, burek@ece.ucsb.edu

## Abstract:

In order to increase the number of transistors on an integrated circuit (IC) in accordance with Moore's Law, we must find new ways to decrease transistor size. As we reach the limits of silicon transistors, new materials such as III-V's, i.e. indium gallium arsenide (InGaAs), may be used for complementary metal oxide semiconductors (CMOS) in sub-22 nm transistors. Key steps in this new process include epitaxial re-growth using molecular beam epitaxy (MBE), planarization, very thin sidewalls, and deposition of gold for self-aligned source/drain contacts. Gold deposition using electroplating will be one of the final steps in creating a functional transistor.

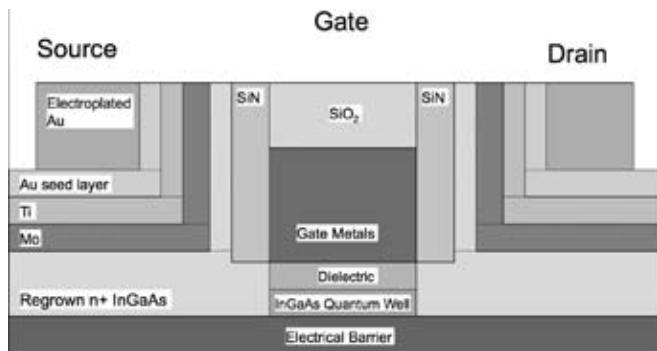


Figure 1: Model of complete InGaAs transistor.

## Introduction:

Moore's Law predicts that the numbers of transistors on an integrated circuit will double every two years. In order to continue this trend, the size of transistors must be minimized. In the past, most transistors were made using silicon dioxide as the oxide insulator between the gate electrode and the path. However as transistors become smaller than 45 nm, the silicon dioxide insulator becomes too thin to prevent leakage of electrons to the gate electrode. Silicon is expected to be able to scale to 22 nm, but after that other material alternatives, such as III-V's, may be used in CMOS fabrication (Figure 1).

The group objectives are to demonstrate a working concept transistor using III-V technology, confirm the record breaking current density of  $6 \text{ mA}/\mu\text{m}$  that theory predicts, and then scale the device to sub-22 nm gate lengths.

## Experimental Procedure:

The major focus of this summer research was to achieve self-aligned source/drain contacts using an electroplating system.



Figure 2: SEMCON 1000 electroplating system.

Self-aligned contacts are important because they decrease access resistance and increase the overall speed of the device. Using an electroplating system makes this process easier because we are able to control where our contacts will grow.

The electroplating system that we used was called the SEMCON 1000 (Figure 2). It consisted of a bath full of gold salts, water, and various chemicals, and a drag out cell that rinsed our wafers with de-ionized water. There were also controls for time, temperature, and current. The tool was

a new addition to the clean room, so part of our job was to characterize it for future users. Our main focus was to determine the rate of deposition for gold, based on variations of time and current.

The wafers that we used to run our tests were 2 inch diameter silicon wafers covered with a seed layer of titanium and a seed layer of gold. We then patterned the wafers with LOL 2000 and photo resist AZnLOF5510, and broke them into quarters. We attached our wafers to a plastic wafer carrier, and attached probes to them. The wafer carrier was then immersed in the bath, and a current was applied. The current caused the gold ions in the bath to deposit uniformly on the wafer (Figure 3). We experimented with a variety of currents and times in order to achieve our ideal growth of 100-200 nm.

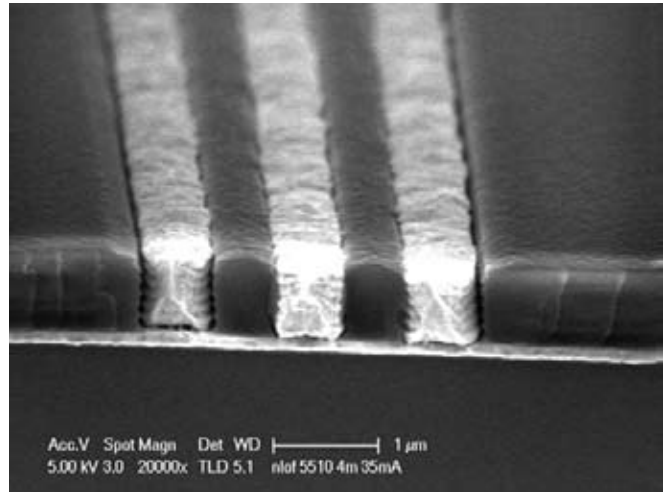


Figure 3: Electroplated gold grown between towers of photo resist.

### Results and Conclusions:

We found that the gold deposition seemed to increase fairly linearly with respect to both time and current (Figure 4). We ran experiments varying the current between 20 mA and 45 mA, and varying the time between 1 minute and 4 minutes. Our ideal growths occurred at 25 mA or 30 mA for about 2 minutes. There were some inconsistencies in our results which we suspect are due to the chemistry of the bath.

Although there are still more experiments to be run, we were very encouraged by our results.

### Future Work:

The future work for the project will be to build a working proof of concept transistor. There are still issues with making extremely thin sidewalls and using molecular beam epitaxy (MBE) to re-grow InGaAs. Once these issues have been

resolved, self-aligned, electroplated, source/drain contacts will be the final step before testing the properties of these new metal oxide semiconductor field effect transistors (MOSFETs).

### Acknowledgements:

I would like to thank my mentor Gregory Burek, my principal investigator Dr. Mark Rodwell, the members of Rodwell group, and the UCSB clean room staff for all their support this summer. I would also like to thank the National Nanotechnology Infrastructure Network Research Experience for Undergraduates (NNIN REU) Program, the NSF, and the SRC for their generous funding.

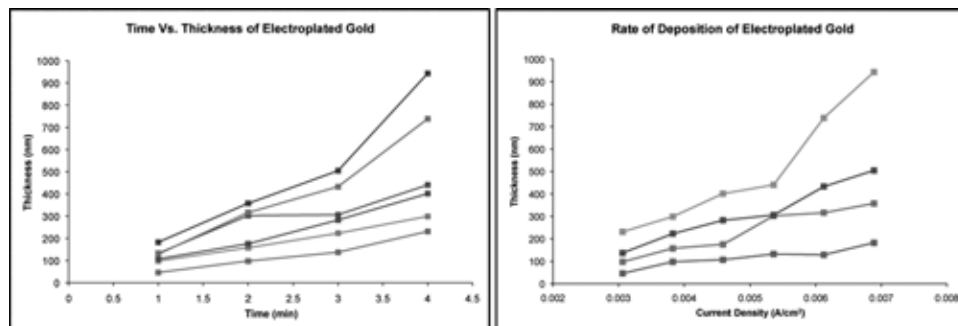


Figure 4: Results of gold electroplating experiments.

# The Integration of Nanowire Electronics with Top-Down CMOS through Direct Growth

Jaime Lee

Materials Science and Engineering, Georgia Institute of Technology

**NNIN REU Site: Lurie Nanofabrication Facility, University of Michigan, Ann Arbor, MI**

NNIN REU Principal Investigator(s): Dr. Wei Lu, Electrical Engr. and Computer Science, University of Michigan Ann Arbor

NNIN REU Mentor(s): Wayne Fung, Electrical Engineering and Computer Science, University of Michigan Ann Arbor

Contact: jaime\_a\_lee@gatech.edu, wluee@umich.edu, fungw@umich.edu

## Abstract:

Nanowires have shown significant potential for future electronic, optical and bio/environmental sensing applications. Here we discuss our efforts to integrate semiconductor nanowires with on-chip micro-scale components by combining the bottom-up nanowire synthesis with top-down fabricated growth sites. Pairs of electrodes were first defined by conventional lithography methods and were used as nanowire growth sites. Gold (Au) nanoparticles with diameters of 20 nm were then deposited on the sample to serve as catalysts during the nanowire growth. We developed a process to successfully isolate the Au nanoparticles on the sidewalls of the electrodes. Tin oxide ( $\text{SnO}_2$ ) and silicon (Si) nanowires were then grown on the samples using the vapor-liquid-solid (VLS) method. After growth, the samples were examined with scanning electron micrograph (SEM) for evidence of controlled nanowire placement.

## Introduction:

Nanowires (NWs) are single-crystals with diameters as small as a few nanometers and lengths up to tens of micrometers. The small sizes and excellent material properties of NWs have led to the demonstration of an array of NW-based electronic, optical and bio/environmental sensing devices. Most NWs are grown by the vapor-liquid-solid (VLS) method [1] using nanoparticles as catalysts. In a typical process, the as-grown, haystack-like NWs are processed after growth [2,3], e.g., via solution sonication and random dispersion onto target wafers, where electrical contacting and/or characterization are subsequently performed. However, the locations of the nanowires are not controlled in this approach and working devices have to be designed manually. Instead of following the “bottom-up synthesis first, top-down fabrication next” approach, it may be desirable to grow nanowires precisely and rationally in predetermined device architectures [4]. Direct integration of NW growth into device fabrication will markedly simplify the process flow and allow the access of individual NWs in a parallel fashion. In this research, we attempted to tackle the integration of nanowire electronics by the direct growth of semiconducting nanowires from desired locations on micro-scale components. This approach can potentially eliminate the post-growth processing steps and solve the “position registry” problem for nanowire-based electronics.

## Device Fabrication:

A negative photoresist layer, with a monolayer of HDMS serving as adhesive, was applied to a 600 nm oxide substrate,

followed by the patterning of experimental designs using photolithography, and pattern transfer to the oxide layer by wet etching, to produce electrode pairs with exposed sidewalls. A thin coat of nickel was then evaporated, followed by the deposition of gold nanoparticles with diameters of 20 nm to serve as catalysts during the nanowire growth. The nickel layer as well as the photoresist layers were removed which isolated the gold nanoparticles on the sidewalls of the oxide.  $\text{SnO}_2$  nanowires were then grown from the gold nanoparticles using the well-known VLS method. An array of gold dots was also fabricated using electron beam lithography to demonstrate that silicon nanowires can be grown from controlled locations.

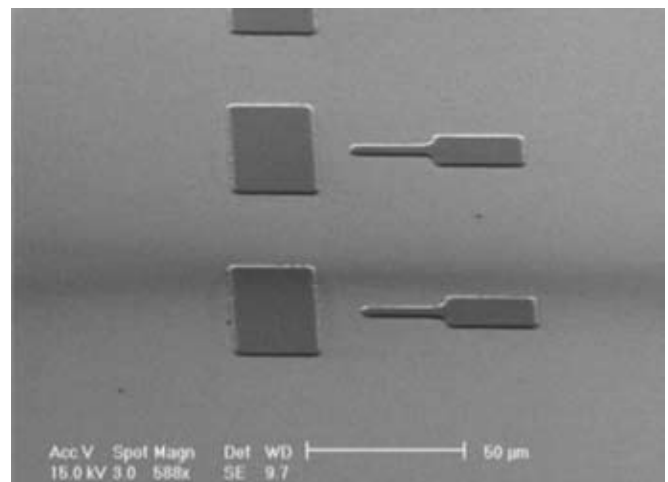


Figure 1: SEM image of two pairs of electrodes before the nanowire growth process.

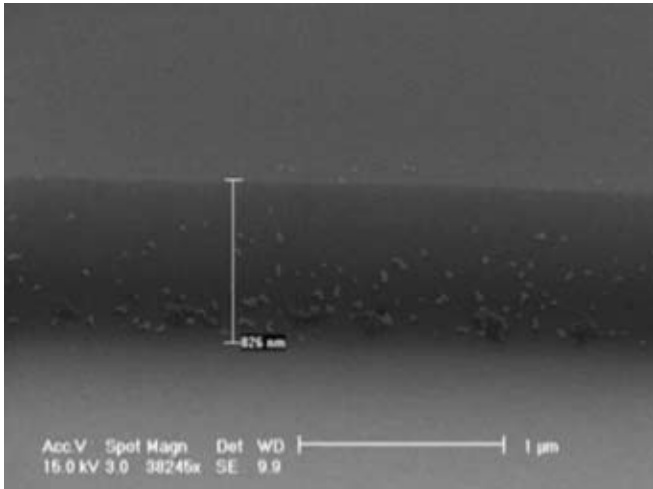


Figure 2: SEM image of Au nanoparticles isolated on the sidewall of an oxide structure.

### Results and Conclusion:

Figure 1 shows pairs of micro-scale electrodes from which nanowire growth would be initiated. In Figure 2, 20 nm gold nanoparticles were successfully isolated along the sidewalls of the oxide structures. Since gold serves as a catalyst for  $\text{SnO}_2$  nanowire growth, the isolation of gold nanoparticles suggested that localized growth was possible. Indeed, localized growth of  $\text{SnO}_2$  nanowires from the micro-scaled electrodes was achieved as shown in Figure 3; however, it was very difficult to visibly conclude if nanowires actually connected any components because of the large number of nanowires that were present.

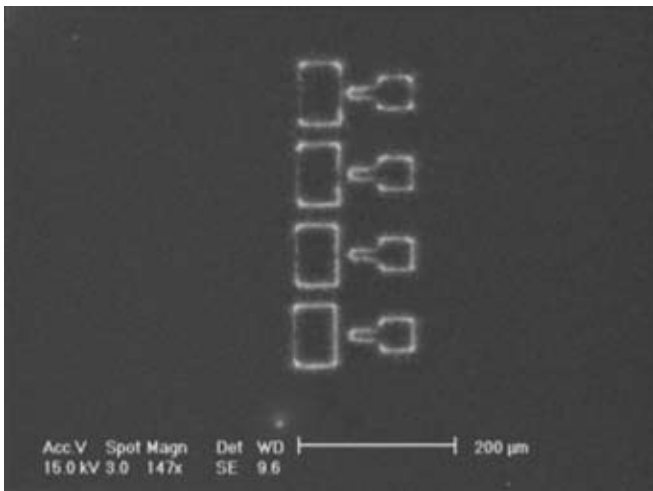


Figure 3: SEM image of localized growth of  $\text{SnO}_2$  nanowires from the oxide structures.

To unambiguously verify the controlled growth of nanowires, we performed another experiment in which Si nanowires were grown from gold dots placed in desired locations by e-beam lithography. The results are shown in Figure 4 and clearly demonstrated the one-to-one correspondence between the nanowires and the gold dots, and the controlled growth of Si nanowires from pre-defined catalyst sites.

In conclusion, the findings of catalysts isolation, localized nanowire growth, and controlled growth of Si nanowires from pre-defined locations provided strong evidence that integrating semiconducting nanowires with on-chip micro-scale devices can be done with the appropriate conditions.

### Future Work:

The growth process for  $\text{SnO}_2$  and Si nanowires needs to be further optimized for experimental conditions. Ideally, one nanowire will be grown from and bridge a pair of electrodes. This requires further adjusting the catalyst density and electrode design. Epitaxial growth from the sidewalls of the electrodes is also desired and it requires preferential etching of the material to expose the desired surface orientation. These improvements would greatly increase the probability of integrating bottom-up nanowire growth with top-down fabricated micro-scaled devices.

### Acknowledgements:

This work was supported by the National Science Foundation and the National Nanotechnology Infrastructure Network Research Experience for Undergraduates Program and was completed in Lurie Nanofabrication Facility. I would like to thank God, my family and friends, Dr. Wei Lu, Wayne Fung, and the rest of the Lu group for their guidance and support.

### References:

- [1] Wagner, et. al; Appl. Phys. Lett. 1964, 4, 89.
- [2] Lieber, et. al; "Directed Assembly of 1D Nanostructures into Functional Networks"; Science, New Series, V291, 630-633 (2001).
- [3] Lieber et. al; "Large-area blown bubble films of aligned nanowires and carbon nanotubes"; Nature Nanotechnology 2, 372 - 377 (2007).
- [4] Fan R, et al; "Si nanowire bridges in microtrenches: Integration of growth into device fabrication"; AdvMats, Vol.17, 2098 (2005).

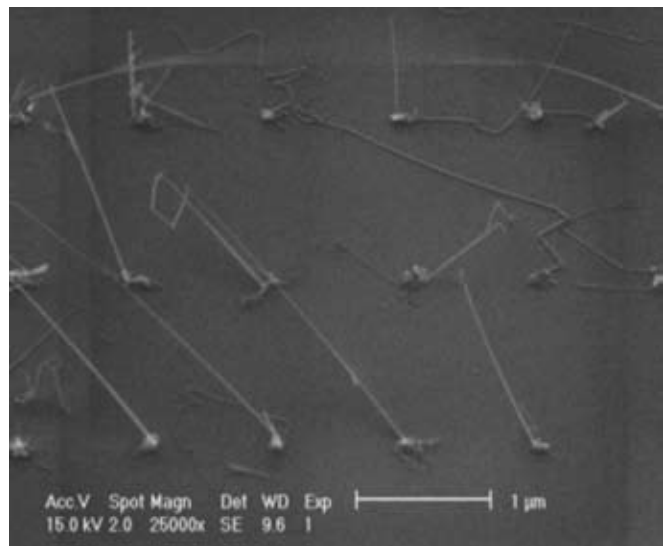


Figure 4: SEM image of controlled growth of Si nanowires from pre-defined Au nanodot sites.

# Heat Removal of Microelectronics through Plasma Technology

Jessica Lehman

Physics, University of Mary Washington

**NNIN REU Site: Center for Nanotechnology, University of Washington, Seattle, WA**

NNIN REU Principal Investigator(s): Dr. Alexander Mamishev, Electrical Engineering, University of Washington

NNIN REU Mentor(s): Chih-Peng Hsu, Electrical Engineering, University of Washington

Contact: jes.lehman@gmail.com, mamishev@ee.washington.edu, cphsu@u.washington.edu

## Abstract:

Rotary fan technology is an inadequate cooling method of microelectronics and does not meet existing technology needs. Electrostatic fluid accelerators (EFAs) have been proven as a promising alternative cooling technology, but break down due to electrode degradation. To increase EFA lifetime, longevity tests were conducted in order to identify electrode erosion. Conductive inert chemicals were investigated as coating materials to increase electrode longevity.

## Introduction:

Existing thermal management methods for electronics do not meet technology needs and remain a major bottleneck in the evolution of computing, sensing, and information technology. The decreasing size of microelectronics components and the increasing thermal output density require a dramatic increase of thermal exchange surface.

In standard cooling technology, heat sinks are used for thermal management of microelectronics. As a result of increasing component density, heat sinks become denser and the channels become narrower. This causes gases to be viscous which decreases cooling efficiency. Traditional rotary fan technology has reached its limit in size reduction. It requires large surface and high speed moving parts causing noise and vibrations.

Electrostatic fluid accelerators offer numerous benefits over the heat sink-rotary fan technology. Advantages include no moving parts, nearly silent operation and no vibration effects. EFAs create laminar airflow with controllable velocities, which increases heat transfer performance. EFA technology is also not limited by geometry, shape or size.

Figure 1 shows a schematic diagram of ion stream generating from a DC electrohydrodynamic ionic wind pump [1]. This mechanism uses a pin-rod geometry with a high tip-curvature corona electrode and a low tip-curvature collecting electrode. Application of a high electric potential difference between the electrodes results in a high intensity electric field in the vicinity of the corona electrode tip, ionizing the surrounding air molecules. These ionized air molecules, which are propelled by the electric field, transfer part of their kinetic energy to neutral air molecules via collisions and create airflow called corona wind.

Electrode degradation results in the break down of an electrostatic fluid accelerator. Electron collisions with the major constituents of gas ( $O_2$ ,  $N_2$ ,  $H_2O$ ) produce relatively high densities of reactive species such as O, N, and OH. In addition, columbic forces acting on these molecules lead to their sedimentation on the electrodes [2]. The material of the corona electrode influences ozone generated by corona discharge because the material affects the current-voltage characteristic in air [3]. Electrodes can become contaminated by deposition of products from chemical reactions in the corona plasma, deposition of air-borne particles and surface oxidation.

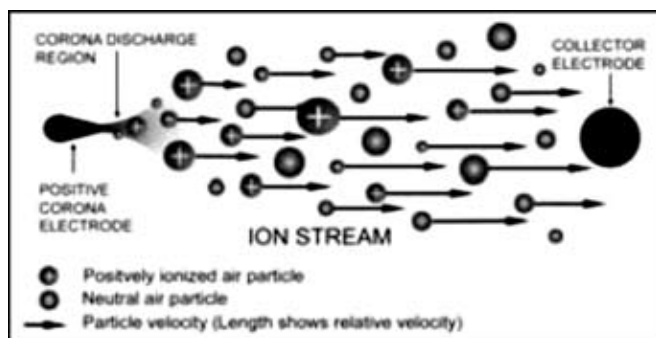


Figure 1: Corona wind from EFA operation.

## Experimental Procedure:

Microfabricated atomic force microscopy (AFM)-cantilever corona electrodes were fabricated from silicon wafers using a three-step photolithography procedure: cantilever structure patterning, corona tip patterning and corona tip shaft patterning. An isotropic reactive ion etching process was used for corona tip sharpening and an anisotropic deep reactive ion etching process was used for high aspect ratio tip shaft formation. Figure 2 shows the schematic diagram of the EFA configuration for EFA-enhanced forced convection cooling. For current-time testing, the microfabricated AFM-

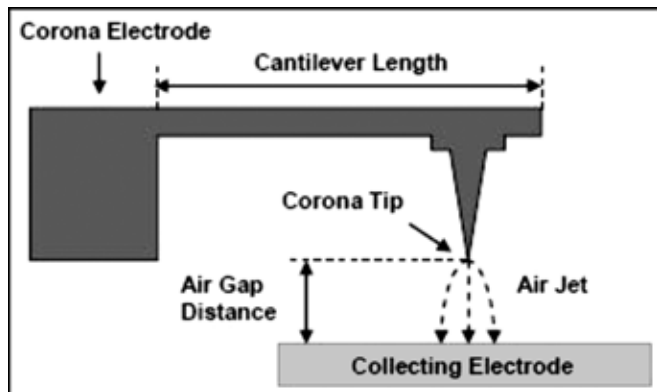


Figure 2: Concept diagram of configuration for EFA-enhanced forced convection cooling

cantilever corona electrodes were suspended 5 mm over a flat collecting electrode in ambient air conditions of 22°C. During operation, 5 kV of positive DC voltage was applied to the corona electrodes.

Uncoated, titanium-tungsten coated and platinum-coated microfabricated AFM-cantilever corona electrodes were tested for the investigation. Unsharpened electrodes were used for the testing because of ease of experimental analysis. Scanning electron microscope (SEM) and energy-dispersive x-ray spectroscopy (EDX) were used to image the degradation and analyze the electrode erosion.

## Results:

Corona current trends for uncoated silicon corona electrodes showed a stable current for hour 1. Current peaks resulted from streamers in hours 2 and 3. The overall trend decreased over time. Pt-coated and TiW-coated electrodes produced a constant current for all three hours with no streamers. Uncoated corona current trends indicated that the electrode surface changed. This effected the electric field distribution, which caused streamers resulting in high current peaks. Dust attachment, material deposition or oxidation can cause surface change.

Experimental results verified that the electrode erosion was caused by oxidation. Materials coating corona electrodes demonstrated chemical inertness. Chemical analysis and imaging before and after tests showed significant reduction in oxidation and electrode corrosion. Titanium-tungsten and platinum materials proved to increase corona electrode longevity.

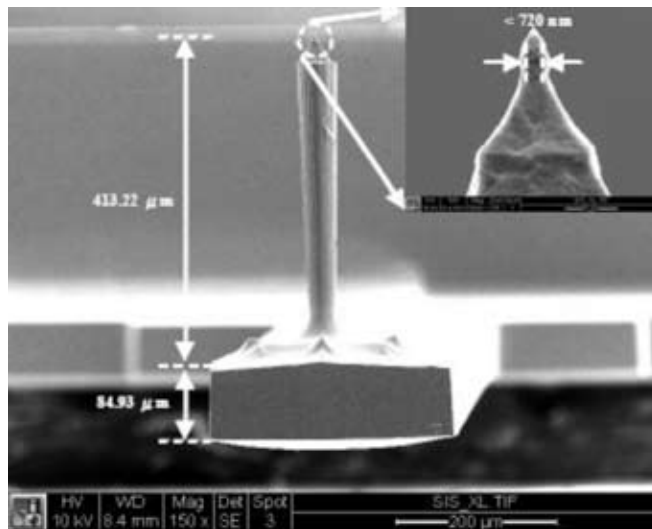


Figure 3: SEM image of microfabricated AFM-cantilever corona electrode.

Future work includes further miniaturization of electrostatic fluid accelerators for integration into chip structures. Also, additional longevity testing will show the EFA break down point for Pt-coated and TiW-coated electrodes.

## Acknowledgements:

The mentorship of Professor Alexander Mamishev and Chih-Peng Hsu was greatly appreciated, as was the donation of time and resources from the NanoTech User Facility at the University of Washington, National Nanotechnology Infrastructure Network Research Experience for Undergraduates Program and the National Science Foundation.

## References:

- [1] C.P. Hsu, N.E. Jewell-Larsen, C. Sticht, A. Mamishev, "Heat Transfer Enhancement Measurement for Microfabricated Electrostatic Fluid Accelerators," Department of Electrical Engineering, University of Washington, 2008.
- [2] L M. Dong, S. Ian, J. X. Yang, X. C. Chi, "Plasma chemical reaction for nitric oxide and sulfur dioxide removal in corona discharge reactor," 2003 Annual Report, Conference on Electrical Insulation and Dielectric Phenomena, Harbin University of Science and Technology, China.
- [3] A. Yehia, A. Mizuno, "Silver discharge electrode for suppression of ozone generation in positive dc corona," Department of Physics, Faculty of Science, Assiut University, Egypt.

# Nanoscale Inhomogeneous Metal/Semiconductor Contacts

Yaw Owusu-Boamah

Electrical Engineering and Physics, Virginia Commonwealth University

**NNIN REU Site: Penn State Nanofabrication Facility, The Pennsylvania State University, State College, PA**

**NNIN REU Principal Investigator(s):** Dr. Suzanne Mohney, Materials Science and Engr., The Pennsylvania State University

**NNIN REU Mentor(s):** Karthik Sarpatwari, Materials Science and Mechanics, The Pennsylvania State University

**Contact:** owusuboaamahy@vcu.edu, sem2@psu.edu, kzs127@psu.edu

## Abstract:

Schottky contacts are commonly used in different high frequency, high temperature and high power electronic devices. Their electrical characteristics, and performance, critically depend on the nature of the metal/semiconductor interface. For a variety of reasons, diodes often contain small (typically 10 to 250 nm) patches of low-barrier height regions embedded in a background with a higher barrier height. Depending on the size and density of the patches, the diodes can exhibit significant non-ideality. In addition, determining the barrier height and density of the patches generally requires complementary materials characterization techniques coupled with modeling of the current-voltage characteristics. The goal of this project is to engineer inhomogeneous Schottky diodes by intentionally introducing low barrier regions to help us gain more insight into how to analyze the data from naturally-occurring inhomogeneous diodes. The size and density of these patches is controlled by the nanofabrication process, and we intend to correlate the observed electrical characteristics to the physical patch parameters.

## Introduction:

Despite decades of intensive research about the formation of Schottky barriers (SBs) at metal-semiconductor interfaces (MS), they are still not fully understood [1]. Outstanding issues in the formation of SBs include the role of interface defect formation, electrode interdiffusion, and chemical reaction induced inhomogeneity at the interface of the metal and semiconductor [2]. The inhomogeneity is usually made up of low-barrier height regions embedded in a background with a higher barrier height. Depending on the size and density of the patches, the diodes can exhibit significant non-ideality. Therefore the goal of this research is to introduce low barrier regions with sizes ranging from 50 nm to 200 nm and various densities. The electrical characteristics will be compared with the physical characteristics to gain a better understand of naturally occurring inhomogeneous diodes.

## Experimental Procedure:

Our substrate was p-type silicon. 60 nm of aluminum was evaporated on the back of the

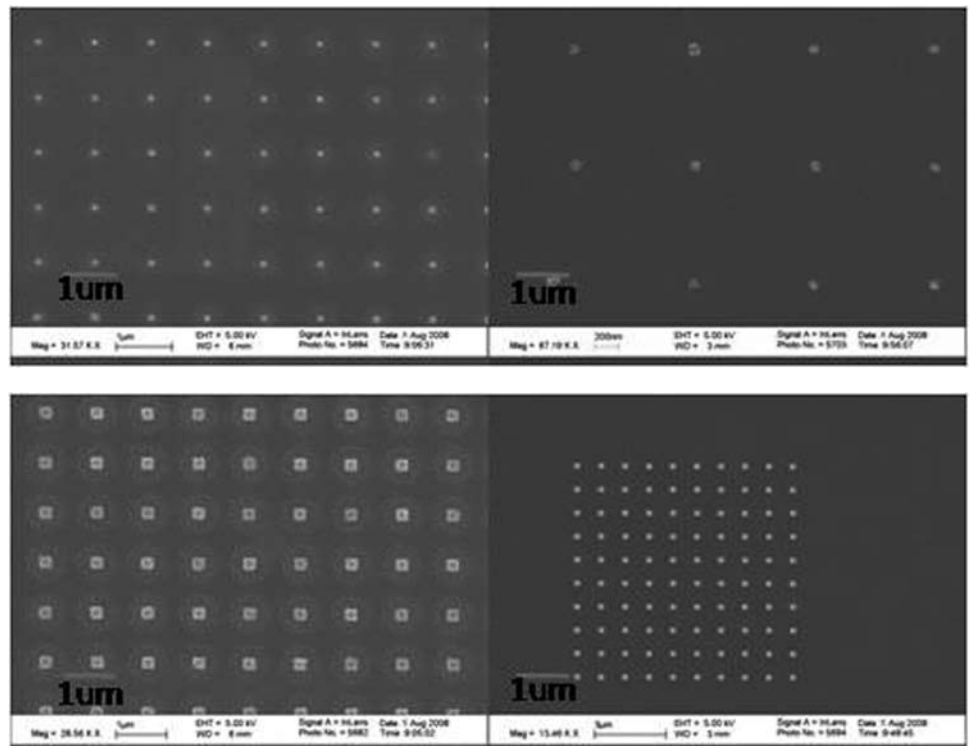


Figure 1, top: 50 nm dot before and after BOE etch.  
Figure 2, bottom: 200 nm dots before and after BOE etch.

our wafers. The samples were then annealed at 600°C for 30 seconds to form an ohmic back contact. ZEP520A resist was then spun on our samples at 4200 rpm for 45s to form a thickness of about 380 nm. Electron beam lithography was then performed to pattern the nanodots ranging from 50 nm to 200 nm, in three different areas. 95 nm of copper was evaporated at  $2 \times 10^{-7}$  torr in a vacuum for the low barrier metal. Liftoff was performed to define the low barrier regions. The samples were then etched in buffered oxide etch (BOE) which was made of 10:1 of ammonium fluoride and hydrofluoric acid for 10s to prepare the semiconductor surface for deposition of the higher barrier metal.

After the surface preparation, Shipley 1827 photoresist was spun on our samples at 4000 rpm for 45s. The samples went through the photolithography process. Alignment marks were utilized to pattern our 50  $\mu\text{m}$  size high barrier regions on top of the nano dots. 65 nm titanium was then evaporated at  $3 \times 10^{-7}$  torr in a vacuum to form the high barrier metal. Liftoff was also performed to finish the inhomogeneous diode. Figures 1 and 2 are the 50 nm dots and the 200 nm dots before and after being etch in BOE for about 10s.

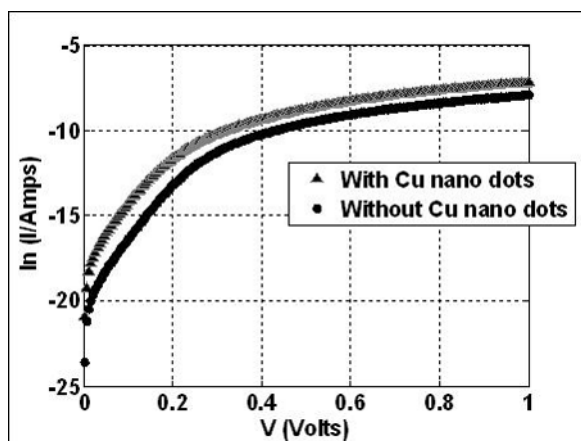


Figure 3: Plot of the homogenous and the inhomogeneous diodes.

### Conclusions and Future Work:

Figure 3 is the plot of the homogenous and the inhomogeneous diodes. There was an upward shift in the current-voltage curve of the inhomogeneous diodes, which yielded a lower barrier height. The 0.1 increase of the ideality factor in the inhomogeneous diode may be due to the inhomogeneous nature of our diodes. Table 1 is the summary of our results. In the future, low temperature measurements will be performed to observe the double diodes' behavior of the inhomogeneous diodes.

M/S diode	Ideality factor (n)	Barrier height (eV)
Homogeneous	1.09	0.61
Inhomogeneous	1.19	0.57

Table 1: Ideality factor and barrier height extractions.

### Acknowledgements:

I would like to thank Dr. Suzanne Mohny, PI, for giving me this opportunity, Karthik Sarpatwari, my mentor, and other members in their research group, Chad Eichfeld, Bangzhi Liu, and the Penn State Nanofabrication Facility staff of The Penn State Center for Nanotechnology Education and Utilization. I also thank the National Science Foundation, the National Nanotechnology Infrastructure Network Research Experience for Undergraduates (NNIN REU) Program, and The Pennsylvania State University for funding, and the School of Engineering at Virginia Commonwealth University. Above all I want to thank GOD.

### References:

- [1] R.T. Tung, Phys. Rev. 24, 23 (1992).
- [2] L.J. Brillson, Surf. Sci. Rep. 2, 123 (1982).

# Capacitance Studies on Organic-Inorganic Thin Film Transistors for Chemical Vapor Sensing Applications

Arun Swain

Electrical & Computer Engineering, Cornell University

**NNIN REU Site: Microelectronics Research Center, University of Texas, Austin, TX**

NNIN REU Principal Investigator(s): Prof. Ananth Dodabalapur, Electrical Engineering, University of Texas at Austin

NNIN REU Mentor(s): Dr. Soumya Dutta, Electrical Engineering, University of Texas at Austin

Contact: [aps97@cornell.edu](mailto:aps97@cornell.edu), [ananth@mer.utexas.edu](mailto:ananth@mer.utexas.edu), [soumya@mail.utexas.edu](mailto:soumya@mail.utexas.edu)

## Abstract:

A dual channel, four terminal (4T) organic-inorganic hybrid thin film transistor is presented in which each channel gates the other. These devices are relatively inexpensive as they function in room temperatures and were fabricated using a combination of solution based processes and thermal evaporation. This metal insulator semiconducting field effect transistor (MISFET) functions as a chemical vapor sensor. Sensing response to isopropyl alcohol (IPA) gas was characterized by capacitance voltage (C-V) measurements and time dependent current measurements.

## Introduction:

Inorganic transistors based on silicon and other inorganic semiconductors exhibit high charge carrier mobilities, high on-off current ratios, and environmental stability. Organic transistors, on the other hand, have attractive properties such as low temperature processing, mechanical flexibility, and compatibility with plastics [1]. Merging both inorganic and organic semiconductors in a dual channel thin film transistor combines the favorable characteristics of both types of semiconductors. We demonstrate such a device whose purpose is to function as a chemical vapor sensor. Organic semiconductors are especially known for their excellent chemical sensing properties and therefore a hybrid dual channel structure best serves our purposes.

The organic semiconductor functions as a gas sensor exposed to the ambient. Analyte delivery causes a decrease in the threshold of the organic layer which in turn induces a gating effect on the inorganic semiconductor, resulting in a net change in the current through the inorganic semiconductor, generating a stronger signal compared to the organic semiconductor.

## Experimental Method:

The 4T device (Figure 1) was fabricated on an n-doped silicon substrate on which a 150 nm layer of silicon oxide was grown in a furnace. The substrate was cleaned using acetone, IPA, and deionized water in an ultrasonic bath for five minutes each. Next, we spin-coated 0.6 mM zinc chloride and 0.6 mM tin chloride in 5 mL of acetonitrile solution at 6000 rpm for 60 seconds after which post annealing was conducted at 500-600°C for 1 hour with oxygen exposure to create the zinc tin oxide (ZTO) semiconductor. We grew 50 nm layer of aluminum using 2 cm × 100 μm inter-digitated shadowmasks for bottom electrodes in a thermal evaporator. Next, we spin-coated D121, a polymer dielectric, at 5000 rpm for 90 seconds and annealed it at 140°C for 15 minutes, exposing it to a UV-ozone clean for 2 minutes. We coated 35 nm of pentacene, the organic semiconductor, using a thermal evaporator. Finally, we deposited 50 nm of gold electrodes by thermal evaporation with the same shadowmasks as before.

We also fabricated an organic field effect transistor (OTFT) control device to study the effects of the organic semiconductor. We use an indium tin oxide (ITO) coated glass substrate on which we deposit D121 followed by pentacene and gold electrodes with the exact specifications as that in the 4T device.

Electrical testing was conducted in ambient conditions. For analyte measurements, we squirted IPA on a filter paper which was loaded on a peristaltic pump and positioned on top of a device.

## Results and Discussion:

Both the 4T device and the OTFT yield good transistor characteristics in current-voltage measurements, exhibiting good gate modulation. In the 4T device, the top layered (Au-

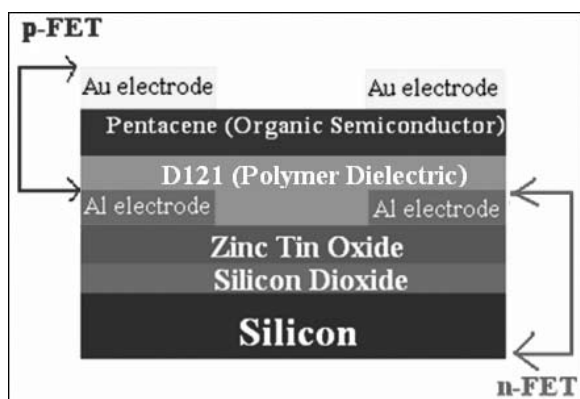


Figure 1: Schematic representation of 4T device.

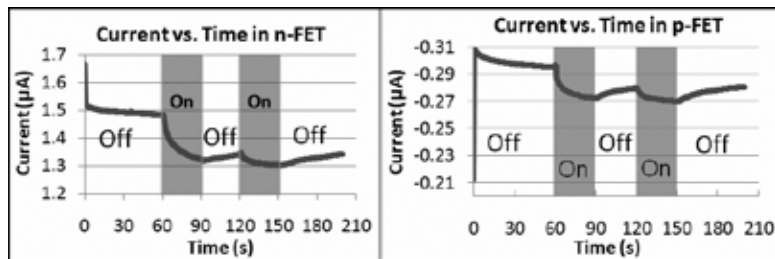


Figure 2: Transient current response in p-FET and n-FET in 4T device to analytes.

Pentacene-D121) p-type field effect transistor (p-FET) has a mobility of  $10^{-3} \text{ cm}^2/\text{V}\cdot\text{s}$  whereas the bottom layered (Si-SiO<sub>2</sub>-ZTO-Al) n-FET reports a mobility of  $0.1 \text{ cm}^2/\text{V}\cdot\text{s}$ .

In Figure 2, transient current curves show that the current decreases in both the p-FET and n-FET upon analyte delivery and increases when analytes are off. Upon analyte delivery, the IPA molecules align themselves such that their negative poles are trapped in the pentacene. Such trapped charges lower the charge carrier (hole) density of pentacene layer, thereby reducing the current. Decreasing carrier density in the pentacene is mirrored in the ZTO layer due to capacitive effects across the polymer dielectric. A decrease in ZTO carriers (electrons) causes current to decrease, as observed in Figure 2. It is important to note that the transient current in the n-FET is greater than the p-FET by a factor of 10, further proof of the n-FET's better amplifying characteristics. As shown in Figure 3, C-V measurements of the p-FET show a significant drop in capacitance upon analyte delivery which proves that there is a decrease in accumulated charges following simple  $Q = C \cdot V$  relation.

C-V measurements on the control device (Figure 4) show that the capacitance drop due to analyte delivery is much smaller than that in the 4T device. The absence of the bottom n-FET results in smaller signal. Therefore, the majority of the capacitance decrease in the 4T device is actually due to a reduction of the ZTO-silicon coupling capacitance across the SiO<sub>2</sub>. Hence it is evident that the role of the top layers in the 4T device is to modulate the accumulation of charges in the ZTO layer which transduces (with amplification) the response to the analytes of the top sensing layers.

### Future Work:

In our 4T device, uniform deposition of pentacene over the entire chip spanning 50 devices causes spreading effects. Pentacene will be patterned between the electrodes of a single device using shadowmasks. Analytes other than IPA such as ketones and aldehydes will be used and the response will be studied.

### Acknowledgements:

I would like to thank Prof. Ananth Dodabalapur for his guidance and my mentor Dr. Soumya Dutta for his constant help and support. Additionally, I would like to thank Jeannie Toll and Melanie-Claire Mallison for coordinating the summer research experience. Funding for this project was provided by the National Science Foundation and the National Nanotechnology Infrastructure Network Research Experience for Undergraduates Program.

### References:

- [1] Dodabalapur, A; "Organic and Polymeric Transistors for Electronics"; Materials Today, Volume 9, No. 4, 24-30 (2006).
- [2] Sharma, S. et al; "Organic and hybrid organic/inorganic transistors for chemical and bio sensing"; IEDM Technical Digest (2005).

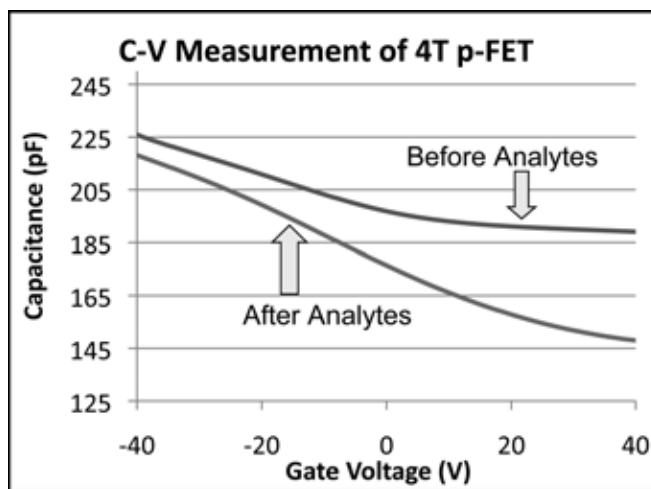


Figure 3: Effect of analytes on capacitance across p-FET in 4T device.

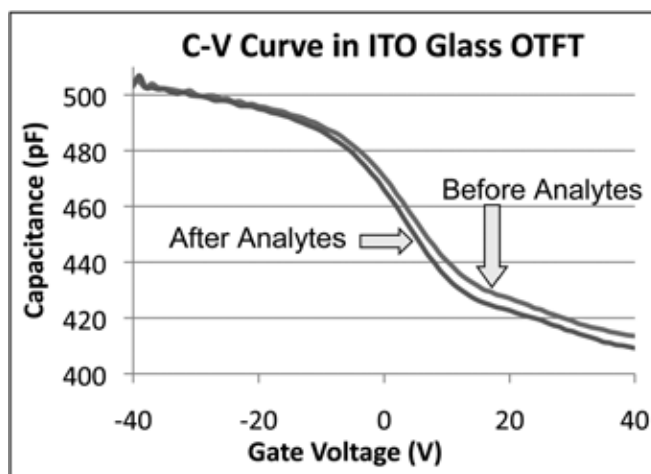


Figure 4: Effect of analytes on OTFT capacitance.



# Multiple Transfers of Single-Walled Carbon Nanotubes on Silicon Wafers

Alan S. Teran

Electrical Engineering, University of Florida

**NNIN REU Site: Stanford Nanofabrication Facility, Stanford University, Stanford, CA**

NNIN REU Principal Investigator(s): Prof. H.-S. Philip Wong, Electrical Engineering, Stanford University

NNIN REU Mentor(s): Albert Lin, Electrical Engineering; Nishant Patil, Computer Science, Stanford University

Contact: [ateran89@ufl.edu](mailto:ateran89@ufl.edu), [hspwong@stanford.edu](mailto:hspwong@stanford.edu), [mrlin@stanford.edu](mailto:mrlin@stanford.edu), [nppatil@stanford.edu](mailto:nppatil@stanford.edu)

## Abstract:

Single-walled carbon nanotubes (SWCNTs) have many applications, including high speed transistor devices (see Figure 1). SWCNTs are grown on single-crystal quartz wafers and then transferred onto silicon wafers by a process that involves gold evaporation and thermal release tape. When they are grown, there are usually between 4 to 10 SWCNTs per micrometer on the surface of the quartz wafer. Increasing the number of SWCNTs per micrometer increases the electrical performance of transistor devices linearly [1]. In this project, we attempt to perform multiple transfers of SWCNTs onto the same wafer in order to increase their density. One of the problems we face is that residue from the initial transfer is preventing any additional transfers from succeeding. We approach this quandary using two different techniques: applying different adhesives and using various chemical solutions to clean any tape residue that may affect the transfer process. We use scanning electron microscopy (SEM) to detect any improvement in surface cleanliness and observe the damage, if any, done to the SWCNTs by our process using probing equipment to measure I-V characteristics and performance. From our results we were able to show that multiple transfers did indeed improve performance even though the multiple transfers were not 100% successful.

## Introduction:

Carbon nanotubes are nanostructures that are members of the fullerene family. Their diameters vary from 0.5 nm to 5 nm and the SWCNTs we worked with were between 1 to 2 nm. SWCNTs can be either metallic or semi-conducting depending on its chirality. We grew the SWCNTs using chemical vapor deposition (CVD) where we placed iron catalyst in lithographically defined stripes approximately 50 μm apart on a single-crystal quartz wafer [2]. The SWCNTs grew from catalyst stripe to catalyst stripe and were well aligned. The density of the SWCNTs as grown was between 4 to 10 SWCNTs/μm. Our target density was between 200 and 250 SWCNTs/μm.

## Experimental Procedure:

Although we were able to grown well-aligned SWCNTs on quartz wafers, we needed to transfer them onto silicon wafers while maintaining their density and alignment. After we grew SWCNTs, we deposited 100 nm of gold, using electron beam evaporation, onto the quartz wafer. We applied a thermal release tape and peeled off the tape along with the gold and SWCNTs. Once we successfully removed the SWCNTs from the quartz wafer we applied the thermal release tape on a silicon wafer and heated up the wafer at 120°C at which point the thermal release tape fell off, leaving the layer of gold on top of the SWCNTs. We removed the gold layer using a dry

**TABLE 1**

Cleaning Techniques		
Chemical Name	Formula	Result
Ethyl Ether	CH <sub>3</sub> -CH <sub>2</sub> -O-CH <sub>2</sub> -CH <sub>3</sub>	Failed
Ethyl Acetate	CH <sub>3</sub> COOCH <sub>2</sub> CH <sub>3</sub>	Failed
Petroleum Ether	C <sub>7</sub> H <sub>16</sub> + C <sub>6</sub> H <sub>14</sub> + C <sub>6</sub> H <sub>12</sub>	Failed
Hexane	C <sub>6</sub> H <sub>14</sub>	Failed
Cyclohexane	C <sub>6</sub> H <sub>12</sub>	Failed
Toluene	C <sub>7</sub> H <sub>8</sub> (C <sub>6</sub> H <sub>5</sub> CH <sub>3</sub> )	Failed
Acetonitrile	CH <sub>3</sub> CN	Failed
Piranha	H <sub>2</sub> O <sub>2</sub> + H <sub>2</sub> SO <sub>4</sub>	Destroyed CNTs
Aqua Regia	HNO <sub>3</sub> + HCl	Inconclusive
Hydrazine	N <sub>2</sub> H <sub>4</sub>	Failed
Ozone	O <sub>3</sub>	Failed

**TABLE 2**

Adhesion Promoters		
Name	Original Purpose	Result
Omnicoat	Improves adhesion to gold	Failed
BCB	Advanced Electronic Resin	Failed
Polymide	High-Temperature Adhesive	Failed
AP410	Photoresist Adhesion Promotor	Failed

Table 1, top: Table of cleaning techniques we used in our attempt to clean off the tape residue.

Table 2, bottom: Table of adhesion promoters we used in our attempt to promote the adhesion of gold.

etch with oxygen plasma followed by a wet etch with gold etchant [2].

Since our target density was from 200 to 250 SWCNTs, we needed to perform multiple transfers to increase the density.

When we attempted to perform multiple transfers using our standard procedure, the gold and SWCNTs did not adhere to the surface of the wafer because the layer of gold would come off along with the tape when it was heated. We found out that there was a layer of residue, whose properties were unknown, on top of the original transfer and that was preventing any additional transfers taking place.

We attempted to remove the residue using all of the chemicals listed in Table 1 by soaking the wafer with residue in those chemicals for different periods of time ranging from 30 seconds to several hours. None of the chemicals were successful in cleaning the residue with the exception of Piranha, but Piranha also destroyed the SWCNTs. We tried using Aqua Regia as a substitute for our gold etchant, but our results were inconclusive. In addition to cleaning, we tried using different adhesion promoters as listed in Table 2 to promote gold adhesion. All of the adhesion promoters failed to create successful multiple transfers and, sometimes they performed worse because they did not allow the gold etchant to remove the layer of gold thoroughly.

From our results, we concluded that we needed to try a different procedure of transfer. We developed a process in which we used standard photolithography to cover with photoresist the specific areas of the wafer where the transistor channels would be. That area was now protected from dry etching where as the area with SWCNTs not covered in photoresist was not protected. We then used oxygen plasma as a dry etch to etch away all of the residue and SWCNTs where we didn't need SWCNTs and then performed a second transfer.

## Results and Conclusion:

Our results from this new procedure were successful. The removal of residue and SWCNTs in places where we did not intend on having transistor channels increased the overall clean area of the wafer and thus improved the overall adhesion of the second transfer even in those areas where we left the residue and SWCNTs. We tested the performance of our second transfer by measuring the current density of transistors that experienced a second transfer and of those who only experienced one transfer (see Figure 2). From our results, we were able to show that transistors with two transfers performed almost twice as well as those with only one transfer. This proves that we increased the density of our SWCNTs by a factor of two.

## Acknowledgments:

I would like to thank Prof. H.S. Philip Wong, Albert Lin, Nishant Patil, Cara Beasley and Gordon Wan for giving me the opportunity to work with them in this research project. I would

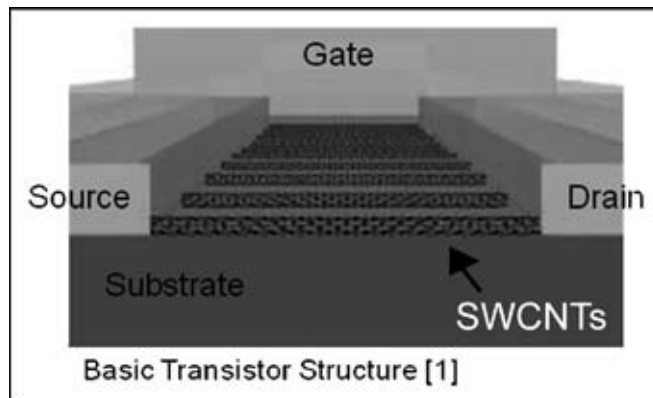


Figure 1: The SWCNTs serve as the channel between the source and the drain.

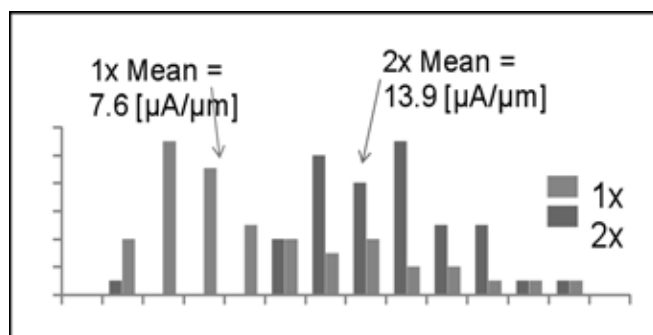


Figure 2: We can clearly see that the 2x distribution is shifted towards the right while the 1x distribution is shifted towards the left.

like to thank the National Nanotechnology Infrastructure Network Research Experience for Undergraduates Program, National Science Foundation, and Intel Foundation for funding.

## References:

- [1] Kang, S.J., et al.; "High-performance electronics using dense, perfectly aligned arrays of single-walled carbon nanotubes"; *Nature Nanotechnology*, Vol.2 No.4, 230-236 (2007).
- [2] Patil, N, et al.; "Integrated Wafer-Scale Growth and Transfer of Directional Carbon Nanotubes and Misaligned-Carbon-Nanotube-Immune Logic Structures", *Proceedings of the 2008 VLSI Technology Symposium*, June17-20 (2008).
- [3] Shimauchi, H, et al.; "Suppression of Hysteresis in Carbon Nanotube Field-Effect Transistors: Effect of Contamination Induced by Device Fabrication Process"; *Japanese Journal of Applied Physics*, Vol. 45 No. 6B, 5501-5503 (2006).

# High Efficiency Light Emitting Diodes with Nanostructured Surfaces

Steven Weber

Physics, Dartmouth College

**NNIN REU Site: Lurie Nanofabrication Facility, University of Michigan, Ann Arbor, MI**

NNIN REU Principal Investigator(s): Dr. Pei-Cheng Ku, Electrical Engr and Computer Science, University of Michigan

NNIN REU Mentor(s): Taeil Jung, Electrical Engineering and Computer Science, University of Michigan

Contact: [steven.j.weber@dartmouth.edu](mailto:steven.j.weber@dartmouth.edu), [peicheng@umich.edu](mailto:peicheng@umich.edu), [taeilj@umich.edu](mailto:taeilj@umich.edu)

## Abstract:

Low extraction efficiency is one of the major obstacles preventing a more widespread use of light emitting diodes (LEDs) for solid-state lighting. Previous efforts to increase LED extraction efficiency through surface texturing have proven effective, but they require additional *ex situ* processing steps after material growth. We have developed an inexpensive, simple, and effective method of nanoscale surface texturing for gallium nitride (GaN) LEDs, which can be performed *in situ*, directly after the material growth, using standard tools. We compare ordinary planar GaN LEDs to surface textured GaN LEDs, in order to demonstrate the effectiveness of this method. Our devices are characterized by photoluminescence and electroluminescence techniques, which include optical intensity vs. current, and current vs. voltage characteristics. We aim to improve LED extraction efficiency by at least a factor of two.

## Introduction:

Light emitting diodes (LEDs) are promising semiconductor devices for solid state lighting. Due to their high capacity to produce photons, they could potentially replace inefficient fluorescent and incandescent lighting. However, state-of-the-art LEDs are far from reaching the required level of efficiency. One major obstacle is the low extraction efficiency due to total internal reflection. Most of the photons generated in the active region are reflected off of the device's surface and cannot escape the device. A typical GaN light emitting diode has extraction efficiency as low as 4% [1].

Surface texturing has proven to be an effective method of increasing LED extraction efficiency. Prior approaches use either random photoelectrochemical etching [2] or a patterned photonic crystal grid [3]. Both methods require additional *ex situ* processing steps after material growth, costing extra time and money. We have developed a new *in situ* technique of surface texturing that can be integrated with the material growth and requires no additional *ex situ* processing. Therefore, it can be a much more practical option for implementation in the LED industry.

## Experimental Procedure:

Our goal was to compare planar LEDs to surface textured LEDs, in order to demonstrate the effectiveness of our new method of surface texturing. Our GaN devices were grown by metal-organic chemical vapor deposition (MOCVD). Immediately following the material growth, we exposed the sample surface with silane, while maintaining an ammonia over-pressure, which prevented the unintentional decomposition of GaN from the surface. This *in situ* silane treatment (ISST) roughened the LED surface, producing random nanoscale textured features (Figure 1). It took

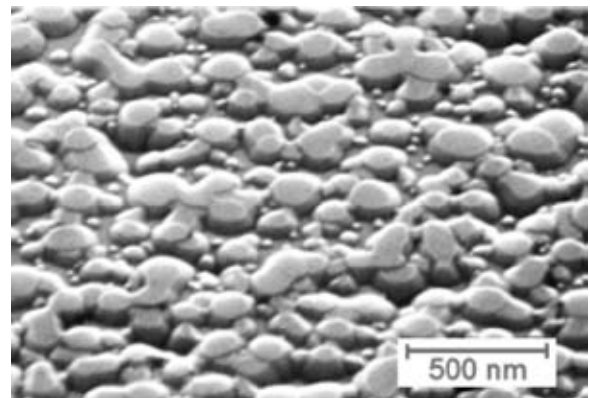


Figure 1: SEM image of the ISST surface (300 sec). Notice that most of the features are smaller than 100 nm.

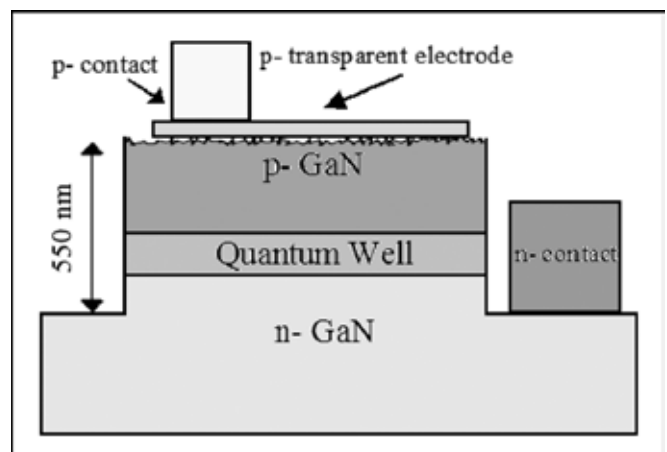


Figure 2: Cross-sectional view of our processed LED.

less than ten minutes to perform, required only standard tools and no *ex situ* processing. The photoluminescence characterization of our samples revealed that ISST increased the photoluminescence (PL) intensity by a factor of two. Such promising results provided sufficient motivation for us to begin processing the samples to produce electrical devices.

The processing of the electrical LEDs with ISST induced surface-textures is as follows. We first deposited the p-transparent electrode (Figure 2), made of Ni and Au, using photolithography and thin film evaporation. The p-transparent electrode was only 10 nm thick, thin enough to allow light to pass through. Then, we used rapid thermal annealing to enhance the contact between the p-transparent electrode and the LED surface. Next, we used reactive ion etching to etch 550 nm down to the n-type GaN, creating a mesa. This allowed us to place a Ti/Au n-contact on the n-type GaN. Finally, we deposited a gold p-contact on the p-transparent electrode. We tested our devices using a pulsed current source. The pulsed current was used to avoid the excessive heating of the device, allowing us to inject higher currents into the device without active cooling.

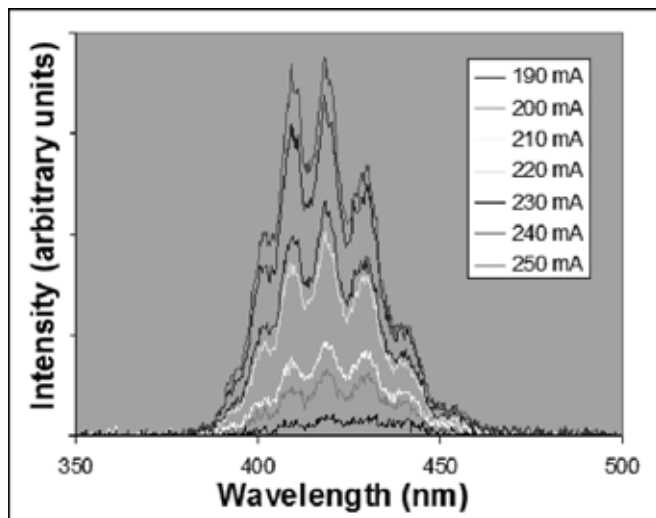


Figure 3: Electroluminescence emission spectrum for ISST.

## Results:

One of the issues that our project addressed is the difficulty of placing an electrical contact on a textured surface. The ISST surface was suitable for placement of the p-transparent electrode because the textured features are very small (< 100 nm wide and < 10 nm tall). We demonstrated electroluminescence in our ISST sample (Figure 3), which indicated that there was electrical contact between the p-electrode and the textured surface. However, the contact has not been optimized, so we were unable to make a direct comparison between the planar and ISST samples at this point.

The current vs. voltage and optical intensity vs. current characteristics of our devices (Figure 4) illustrated the problems with the p-electrode. The ISST sample had a higher turn-on voltage than the planar sample. Therefore, the ISST sample had a higher resistance, probably due to un-optimized

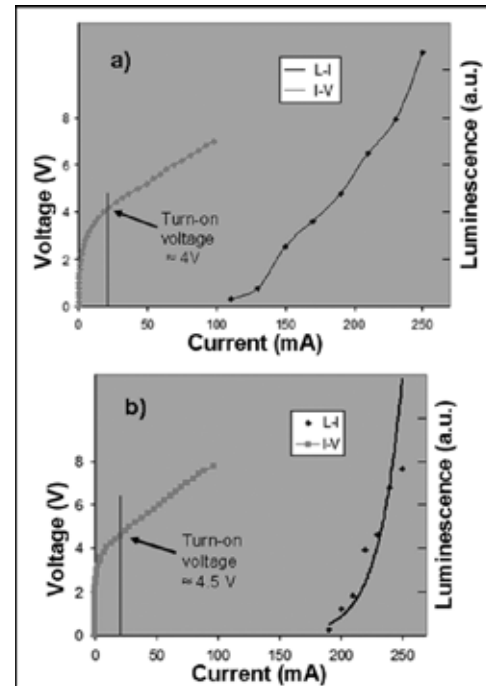


Figure 4: L-I and V-I for: a) planar LED; b) ISST LED.

contact between the p-electrode and the textured surface. The L-I curve for the ISST sample was much steeper than for the planar sample, which also indicated poor electrical contact.

## Conclusion:

We have developed GaN LEDs, using our ISST method to produce nanoscale surface textures. This method is simple and cost effective, and could easily be implemented in the LED industry. Photoluminescence characterization showed an improvement in extraction efficiency by a factor of two compared to planar devices. We fabricated electrical devices, and demonstrated electroluminescence in ISST samples. However, p-contact resistance still needs to be optimized before we can compare ISST devices to planar devices.

## Acknowledgments:

National Nanotechnology Infrastructure Network Research Experience for Undergraduates (NNIN REU) Program, National Science Foundation, The University of Michigan, Taeil Jung, P.C. Ku, Sandrine Martin, the other REU interns, the staff at EECS, and my professors at Dartmouth.

## References:

- [1] Schubert, E.; Light Emitting Diodes; Cambridge Univ. Press; 2006.
- [2] Wierer, J. et al.; "InGaN/GaN quantum-well heterostructure light-emitting diodes employing photonic crystal structures"; Applied Physics Letters, Volume 84 Number 19, 3885 (2004).
- [3] Fujii, T. et al.; "Increase in the extraction efficiency of GaN-based light-emitting diodes via surface roughening"; Applied Physics Letters, Volume 84 Number 6, 855 (2004).

# Effects of Annealing on the Electronic Properties of GaAsN

Christer Akouala

Physics, Appalachian State University



NNIN REU Site: Lurie Nanofabrication Facility, University of Michigan, Ann Arbor, MI

NNIN REU Principal Investigator(s): Dr. Rachel S. Goldman, Materials Science and Engineering;

Dr. Cagliyan Kurdak, Physics; University of Michigan, Ann Arbor

NNIN REU Mentor(s): Yu Jin, Physics, University of Michigan

Contact: ca79043@appstate.edu, rsgold@umich.edu, kurdak@umich.edu, jinyu@umich.edu

## Abstract:

In this work, we have investigated the influence of post-growth annealing on the electronic properties of gallium arsenide nitride (GaAsN) alloys films. Following annealing, substantial improvements in the electron mobility and free carrier concentration were observed. Temperature dependent Hall measurements reveal a thermally activated increase in free carrier concentration for temperatures higher than 150K, presumably due to N-related deep-level defects within the GaAsN bandgap. Post-growth annealing leads to a temperature-independent free carrier concentration, suggesting that annealing reduced the concentration of these N-related deep-level defects.

## Introduction:

Indium gallium arsenide nitride ((In)GaAsN) alloys with a few percent nitrogen have potential applications in infrared laser diodes, high efficiency solar cells, and other electronic devices [1-4]. However, as-grown films often exhibit photoluminescence (PL) efficiencies and electron mobilities substantially lower than those of (In)GaAs [5]. Although post-growth annealing has been extensively used to improve the PL efficiency of (In)GaAsN [4], the mechanisms for this improvement are not well understood, and the influence of annealing on the electronic properties remains unknown. In this work, we have investigated the influence of annealing on the electronic properties of bulk GaAsN films. We find that annealing substantially improves the transport properties of GaAsN, presumably by reducing the concentration of N-related deep-level defects.

## Methods/Materials:

GaAs<sub>1-x</sub>N<sub>x</sub> films, with N composition up to  $x = 0.019$ , were grown by plasma-assisted molecular beam epitaxy, using Ga, As<sub>2</sub> and an N<sub>2</sub> radio frequency (rf) plasma source. For all films, n-type doping was achieved using a GaTe source for Te. Post growth annealing was performed from 650 to 800°C for 60s in a N<sub>2</sub> ambient, with a GaAs proximity cap to prevent As out-diffusion. To determine the electron mobility and free carrier concentration, transport measurements were implemented in both Van der Pauw and Hallbar geometries. Variable temperature resistivity and Hall measurements were performed from 50K to room temperature (300K).

## Results and Discussion:

Figure 1 (a) and (b) show the free carrier density,  $[n]$ , and electron mobility,  $\mu$ , as a function of annealing temperature,

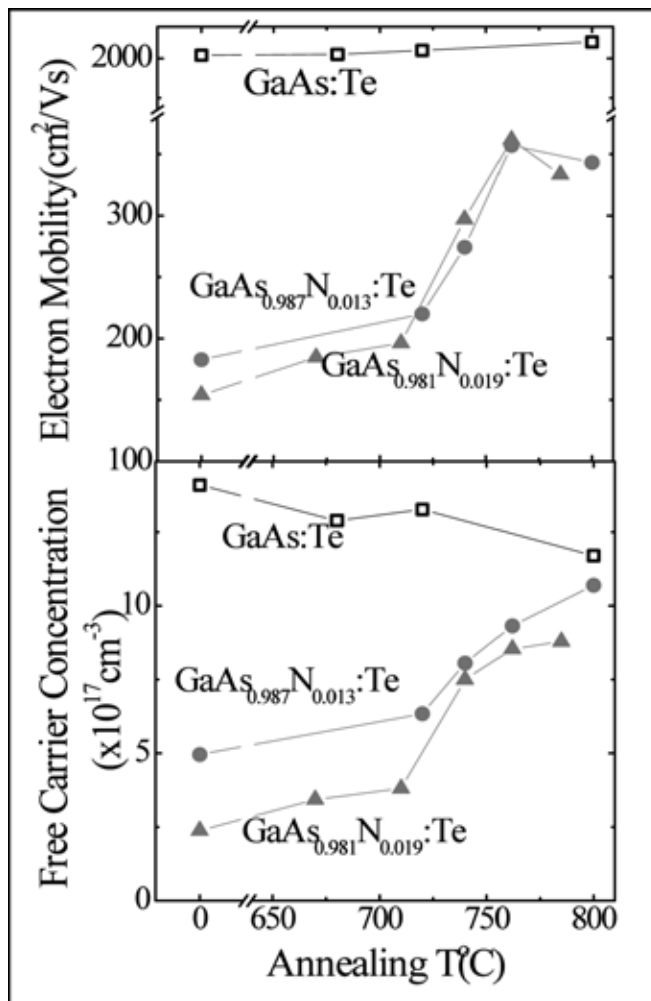


Figure 1: Electron mobility (a) and free carrier concentration; (b) for GaAs(N):Te films as a function of annealing temperature.

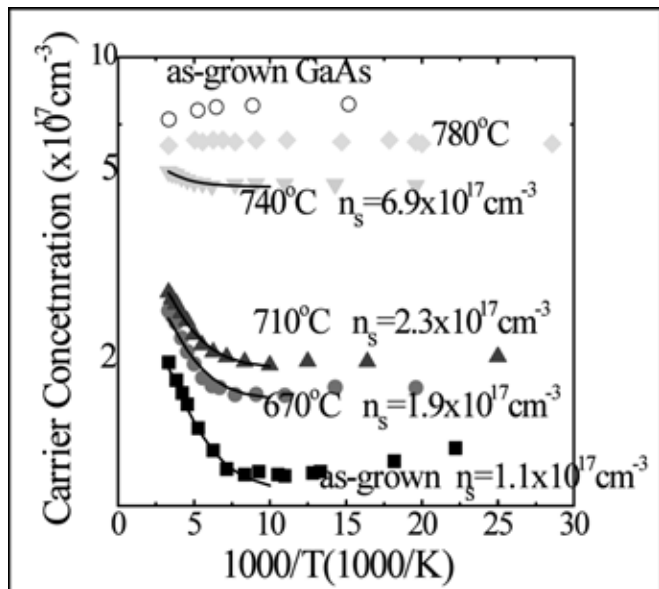


Figure 2: Free carrier concentration as a function of measurement temperature for as-grown GaAs:Te and GaAsN:Te films annealed at different temperatures.

for GaAsN films in comparison with GaAs control films, doped with the same target Te doping concentration. For GaAs:Te, insignificant variations in  $[n]$  or  $\mu$  with annealing temperature were observed. However, for GaAsN:Te films, we observed a remarkable increase in both  $[n]$  and  $\mu$  as the annealing temperature is increased.

Figure 2 shows the log of the carrier density vs. reciprocal temperature for an as-grown bulk GaAs:Te films, in comparison with GaAsN:Te films annealed at various temperatures. For GaAs:Te,  $[n]$  is temperature-independent in the explored temperature range, 50 to 300K, typical of degenerate III-V semiconductors [6]. However, for the as-grown GaAsN:Te films,  $[n]$  decreases exponentially as the temperature decreases down to 150K, indicating the presence of thermally activated deep donor levels within the GaAsN bandgap, presumably N-related deep-level defects. The saturation of  $[n]$  at low temperature ( $T < 150K$ ) is attributed to shallow donors such as Te donors. As the annealing temperature increases, the saturation value of  $[n]$  increases. Finally, for 780°C annealed GaAsN:Te films, the carrier concentration is temperature independent.

To extract the activation energy of the N-related deep donor level,  $E_N$ , we use an expression for semiconductors with two distinct donor levels [6],

$$\sqrt{n(n - n_s)} \propto \exp\left(-\frac{E_N}{2k_B T}\right)$$

where  $k_B$  is Boltzmann constant,  $n$  is the apparent carrier concentration, and  $n_s$  is the saturated shallow donor concentration. As shown in Figure 2,  $n_s$  increases with annealing temperature, suggesting that the deep-level defect concentration is reduced as the annealing temperature

increases. For all annealing temperatures, the activation energy of the deep-level trapping centers,  $E_N$ , is 57 meV, which is much greater than the activation energy of hydrogen-like shallow donor levels in GaAs, which are typically 5-6 meV. Thus, the deep donors act as carrier trapping/scattering centers, leading to the low  $[n]$  and  $\mu$  in the as-grown GaAsN:Te films. After annealing, as shown in Figure 1,  $[n]$  and  $\mu$  are substantially increased, suggesting that the annealing-induced improvement in electronic properties of GaAsN is due to the removal the N-related deep-level defects.

### Summary and Conclusions:

In summary, we have studied the effect of rapid thermal annealing on the electronic properties of GaAsN films. For the as-grown films, the free carrier concentration increases exponentially with increasing measurement temperature up to room temperature, suggesting the presence of N-related deep-level defects within the GaAsN bandgap. An analysis of temperature-dependent Hall and resistivity measurements reveals a 57 meV activation energy for the N-related deep-level defects. For the annealed films, the free carrier concentration and electron mobility are substantially improved with increasing annealing temperature, which is presumably related to the removal of the N-induced deep level trapping centers.

### Acknowledgements:

I would like to thank my PIs, Dr. Goldman and Dr. Kurdak for their guidance; Yu Jin for being a great mentor and an inspiration, Ryan Jock for his assistance and tutoring, and the Goldman group for their kindness and help; Dr. Sandrine Martin, Trasa Burkhardt, the LNF Staff, NNIN REU U. of M. students; my family and friends for their support and encouragement; also the National Nanotechnology Infrastructure Network for their organization of this program, the National Science Foundation and the Intel Foundation for their contributions to this project and to the advancement of education.

### References:

- [1] M. Fischer, D. Gollub, and A. Forchel, Jpn. J. Appl. Phys. Part 1 - Regul. Pap. Short Notes Rev. Pap. 41, 1162 (2002).
- [2] J. F. Geisz and D. J. Friedman, Semicond. Sci. Technol. 17, 769 (2002).
- [3] S. R. Kurtz, A. A. Allerman, E. D. Jones, J. M. Gee, J. J. Banas, and B. E. Hammons, Appl. Phys. Lett. 74, 729 (1999).
- [4] J. S. Harris, Semiconductor Science & Tech 17, 880 (2002).
- [5] M.Reason, Y.Jin, H.McKay, N.Mangan, D. Mao, R.Goldman, X. Bai, and C. Kurdak, J. Appl. Phys 102, 103710 (2007).
- [6] E. F. Schubert, Doping in III-V semiconductors (Cambridge University Press, UK, 1993).

# Nanoscale Chemical Patterning for Layer-by-Layer Assembly of Conductive Polymers

Amy Beasten

Chemical Engineering, Tulane University

**NNIN REU Site: Penn State Nanofabrication Facility, The Pennsylvania State University, State College, PA**

NNIN REU Principal Investigator(s): Dr. Michael A. Hickner, Materials Science and Engr, The Pennsylvania State University

NNIN REU Mentor(s): Stephanie Petrina, Materials Science and Engineering, The Pennsylvania State University

Contact: [abeasten@tulane.edu](mailto:abeasten@tulane.edu), [hickner@matse.psu.edu](mailto:hickner@matse.psu.edu), [sap262@psu.edu](mailto:sap262@psu.edu)

## Abstract:

Surface chemical templates were created by microcontact printing 3-aminopropyltrimethoxysilane (APTMS) using a composite poly(dimethylsiloxane) (PDMS) stamp. The composite PDMS stamp with a hard PDMS patterned layer and a softer backing layer was required to produce line feature widths of 208 nm or 139 nm. The amino functional groups on APTMS were quaternized with iodomethane to give patterned positive charges on the surface, which could then be used in layer-by-layer (LbL) assembly. LbL assembly was used to create nanometer-sized conducting polymeric wires by the sequential electrostatic deposition of poly(styrene sulfonic acid) (PSS) and poly(aniline) (PANI) onto the quaternized patterns. The geometry of the patterns and wires were characterized with atomic force microscopy. Conductivity measurements were made on the wires, parallel and perpendicular to their long axis, after each successive layer of LbL.

## Introduction:

Microcontact printing is a nanofabrication technique that uses a patterned polymer stamp upon which a chemical ink is deposited. Placing the inked stamp in contact with a flat substrate, such as a silicon wafer, creates a functional pattern that is determined by the initial polymer stamp dimensions. Layer-by-layer (LbL) assembly is the process of self-assembly to create multilayer films. LbL employs electrostatic interactions between polyelectrolytes of alternating charge to build up structures one layer at a time. Using this technique, characteristics such as total assembly thickness can be easily tailored. Additionally, polyelectrolytes with different properties, such as electrical conductivity, can be used to impart functionality to the layered assemblies.

## Experimental:

Silicon diffraction gratings with periods of 416 and 278 nm were used as master templates for creating the h-PDMS composite stamp. The h-PDMS was spun cast on the templates, and Sylgard 184 PDMS solution was placed on top. Once both PDMS layers were cured for one hour at 70°C, the stamps were peeled from the substrate, rinsed with ethanol, and dried to remove any debris. Silicon wafers were cleaned and exposed to oxygen plasma for ten minutes, with four minutes additional exposure of the cleaned stamps to increase their hydrophilicity. The stamps were inked for 30 seconds with 5% APTMS in a 95:5 ethanol-water solution and were then blown dry. The patterns were immediately printed onto the silicon wafers by placing the stamp on the wafer, waiting 30 seconds, then removing the stamp.

The APTMS functional wafer was quaternized in a 1 M solution of iodomethane, which converted the primary amines to quaternary ammonium groups. The quaternized print was immersed for 30 seconds in a 5 mM solution of poly(styrene sulfonate) (PSS) in water, which was acidified with two drops of H<sub>2</sub>SO<sub>4</sub>. The pattern was then rinsed in deionized water for 30 seconds to remove any debris, and dried. The print was then immersed in a 5 mM solution of poly(aniline) (PANI) in formic acid for 30 seconds, then immersed in formic acid for one second to remove any excess PANI. The print was rinsed in deionized water and dried. One layer of PSS and one layer of PANI constituted one layer pair.

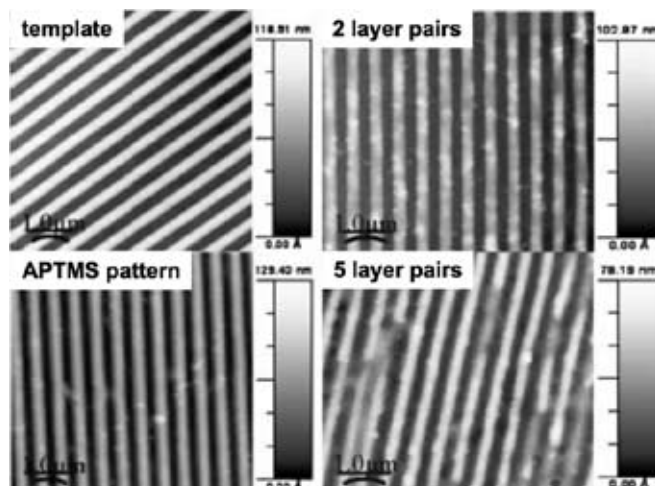


Figure 1: AFM of microcontact printing template, printed APTMS pattern, and one, two and five layer pair samples.

Conductivity was measured across the surface of the prints, both parallel to and perpendicular to the nanowires using a DC probe station. The tungsten probe tips were set directly on the surface of the pattern approximately 4 mm apart to measure DC current. A sweeping potential of -3 to 3 V was applied.

## Results and Discussion:

Figure 1 shows atomic force microscope (AFM) images of 416 nm period prints with deposition of different numbers of layer pairs. Increasing line thickness, as evidenced by the bright features, was observed with increasing layer pairs. The AFM images confirmed that polymer deposition was only occurring on the patterned APTMS, not on the bare silicon substrate. The increasing thickness of the lines indicates that deposition did occur on the quaternized patterns and not on the unpatterned substrate.

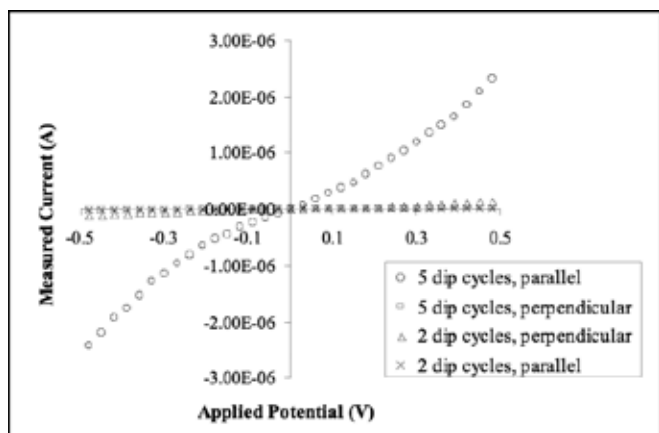


Figure 2: Current-Voltage curves parallel and perpendicular to two and five layer pair features

Figure 2 shows conductivity for 416 nm period prints with varying LbL layer pairs both parallel and perpendicular to the features. It was observed that the conductivity was greater when measured parallel to the nanowires as opposed to perpendicular, and that the conductivity increased with increasing layer pairs. The conductivity is greater across the five LbL layer pair sample than across the two LbL layer pair sample.

Ellipsometry was conducted in order to determine the thickness of the deposited polymer layers. Figure 3 illustrates the thickness of each adsorbed layer on an unpatterned sample. The exact refractive index was not known for the layers of polymer, so a value of 2.22 was selected to use as a

baseline measurement. A built-in algorithm in the ellipsometer software was used to determine the refractive index, which was calculated from a two-angle measurement. A similar trend was observed for both cases. We found that the thickness of the sample increased as more LbL layer pairs were applied, and that this increase ranged from 2-5 nm.

## Conclusions and Future Work:

Patterning of an amino functionalized silane was observed on small length scales, and LbL was successful for creating nanowires of conducting polymer. The conductivity increased with increasing LbL pairs, and the conductivity was greater parallel to the nanowires rather than perpendicular. These experiments demonstrated that asymmetric conducting structures can be formed in this manner. However, refinements to the printing process are needed to increase its robustness in varying relative humidity conditions and improve large-area patterning on the order of the size of an entire wafer. Future work will include using gold electrodes and measuring conductivity of the samples in 2-point and 4-point mode to gain a better understanding of the conductivity properties of the samples.

## Acknowledgements:

A.B. would like to thank the National Science Foundation and the National Nanotechnology Infrastructure Network for funding and support. A.B. would also like to thank Dr. Hickner and Stephanie Petrina, as well as Andrzej Mieczkowski, Guy Lavallee, Tad Daniel, and the rest of the staff at the Penn State Nanofabrication Facility.

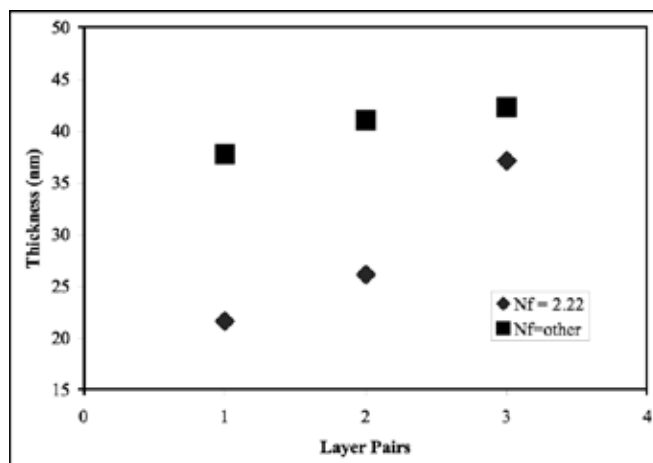


Figure 3: Thickness of layer pair deposition determined by ellipsometry.

# Synthesis of Shaped Nanoparticles for Two-Dimensional Assemblies

Molly Beernink

Chemistry, Gustavus Adolphus College

**NNIN REU Site: Minnesota Nanotechnology Cluster, University of Minnesota-Twin Cities, Minneapolis, MN**

NNIN REU Principal Investigator(s): Dr. Andreas Stein, Department of Chemistry, University of Minnesota

NNIN REU Mentor(s): Fan Li, Department of Chemistry, University of Minnesota

Contact: mbeernin@gustavus.edu, a-stein@umn.edu, lixxx326@umn.edu

## Abstract:

Hybrid molecular orbitals with specific bonding directions provide a useful model to correlate bonding of atomic building blocks with molecular structure. The concept of directional bonding can, in principle, be translated to larger, shaped nanoparticles when these are assembled into extended arrays. Directional interactions established by chemically controlled reactive sites may promote the association of particles similar to sigma bonding of atoms in molecules. We synthesized particles that model the trigonal planar shape of  $sp^2$  hybrid orbitals by a two-dimensional template methodology. A two-dimensional silica film was fabricated on a substrate coated with physically and chemically adhered polymer spheres. Removal of the spheres resulted in pores of uniform size and shape in the film. The optimized conditions for polymer sphere deposition to promote an ordered sphere array and creating a film on the substrate were determined. The porous silica film was removed from the substrate and separated into smaller structures through a series of etching and mechanical stress techniques.

## Introduction:

Atoms are viewed as the building blocks of a molecular structure. The molecular packing geometry is dictated by the particular bonding directionality of hybrid orbitals of the atoms involved. A larger-scale model of nature's concept of directional bonding can be accomplished by shaping nanoscale particles to the same geometries as hybrid molecular orbitals and organizing these particles into ordered assemblies. The shaped nanoparticles have the unique ability to act as anisotropic building blocks for complex structures [1]. For example, directional interactions established by chemically controlled reactive sites on each particle would promote an association of particles similar to sigma bonding of atoms in molecules.

A two-dimensional template methodology was proposed for the synthesis of uniform particles shaped to model the trigonal planar shape of  $sp^2$  hybrid orbitals. The proposed process involved: creating a polymer sphere template on a silicon wafer substrate, forming a thin film of biologically-compatible silica on the templated substrate, removing the spheres and substrate from the film, separating the film into individual nanoparticles, and functionalizing particle surfaces. This proposed triangular nanoparticle synthesis procedure was optimized.

## Experimental Optimization and Results:

Prior to being used, the surface of the silicon wafer was functionalized with hydroxyl groups for favorable sphere dispersion. Spin-coating of a polystyrene (PS) sphere dispersion in a 1:1 mixture of ethanol and ethylene glycol onto a silicon wafer followed by  $O_2$  reactive-ion etching (RIE)

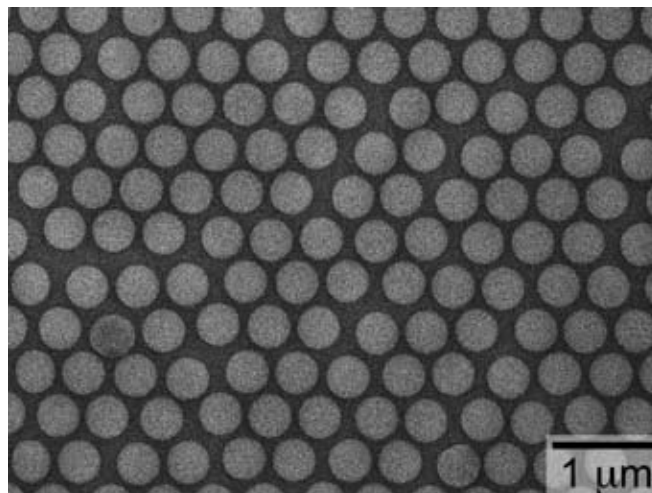


Figure 1: A top-view SEM image of ordered spheres on a substrate.

created a regular, non-close packed sphere array (Figure 1). To avoid aggregation and irregularity of the sphere packing, the spheres had to be well dispersed in solution prior to deposition. The  $O_2$  etching decreased the size of each sphere, increasing the area between the spheres in the array.

Immediately after etching, the spheres had to be further adhered on the substrate in order to keep them in place in the array. Annealing the substrate at  $115^\circ\text{C}$  converted the spheres to a dome-like shape with improved adhesion. Untreated spheres were only weakly bonded to the substrate, allowing the spheres to float to the surface of the silica film resulting in a cratered-surfaced film rather than fully penetrated pores.

The strength of the sphere array before and after annealing was evaluated and diffuse UV-Vis spectral data showed significant improvement of adhesion after annealing.

The substrate surface was coated with dichloromethylvinylsilane through a chemical vapor deposition (CVD) method. Then, a silica precursor of tetraethyl orthosilicate, hydrochloric acid, and water was spin-coated onto the sphere template in a vented vessel. The surface modification was imperative for uniform film thickness and correct pore shape. Without CVD, the resulting film had curved pore walls and the film thickness was greater around the pores, but with the modification, the pores had vertical walls of consistent thickness. Adjusting the solvent evaporation rate allowed for fabrication of films with different uniform thicknesses.

Complete removal of the PS template from the film and substrate was achieved by dissolution of PS in dichloromethane and an O<sub>2</sub> RIE process. The nanopore film on the substrate was viewed via high-resolution scanning electron microscopy (SEM) (Figure 2). To detach the intact silica film from the silicon substrate, a combined dry etching (SF<sub>6</sub>) and wet etching (tetramethyl ammonium hydroxide) process was developed. Figure 3 shows an SEM image of film retrieved after being removed from the substrate. The freestanding film was collected in toluene and broken up by sonication into triangular nanoparticles (Figure 4).

### Conclusions and Future Possibilities:

The process for synthesizing a two-dimensionally ordered nanoporous thin film was optimized. A freestanding membrane was formed using a fast, inexpensive, and parameter-controlled approach. This structure could have future possible applications as a mask for patterned surfaces, soft-lithography, photonics, photovoltaics, separations, and bioprocess simulation.

Small-tripodal particles were produced by this optimized technique. The surfaces of these sp<sup>2</sup>-shaped nanoparticles can be functionalized for many purposes. Most predominately, these functionalized particles could be used as building blocks for nanostructure self-assembly and other multifunctional assemblies. Other possible applications of these nanoparticles include: surface patterning, liquid crystals, and bio-targeted drug delivery. These synthetic approaches could be translated to other materials, increasing the potential uses of these anisotropic nanoparticles.

### Acknowledgments:

I would like to thank Dr. Andreas Stein, Fan Li, and everyone in the Stein research group for their invaluable guidance. I also thank the University of Minnesota especially the ECE and Chemistry departments, the Nanofabrication Center, and the NNIN coordinators. My work was funded by the National Science Foundation through the National Nanotechnology Infrastructure Network Research Experience for Undergraduates Program.

### References:

- [1] Glotzer, S. C., Solomon, Michael J.; "Anisotropy of building blocks and their assembly into complex structures;" Nat. Mater, 6, 557 (2007).

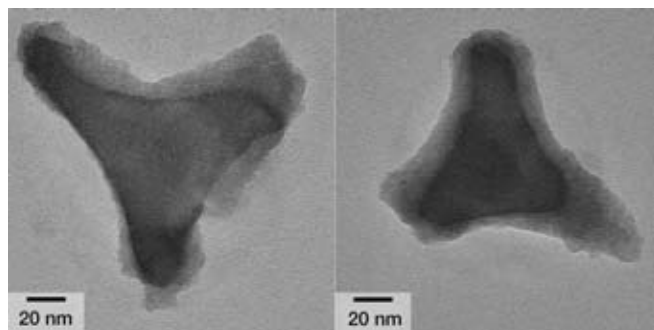
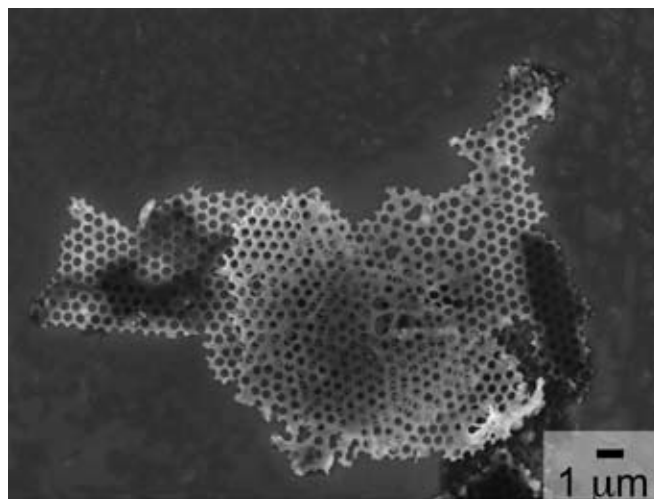
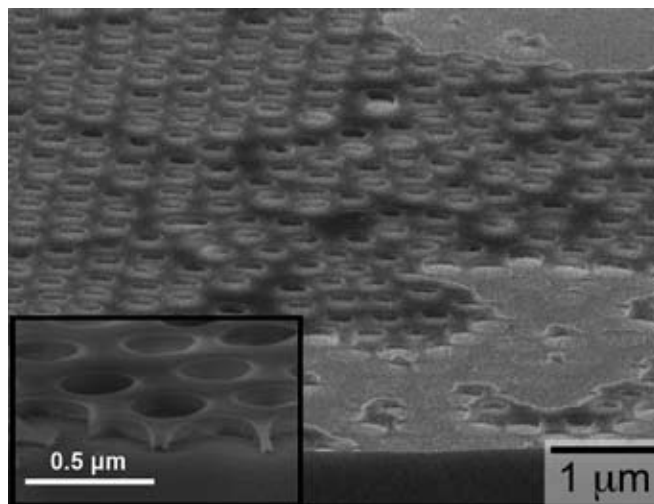


Figure 2: SEM images of porous silica films on a substrate.

Figure 3: SEM image of freestanding film collected from solution.

Figure 4: TEM images of final triangular nanoparticles.

# Growth of 3C-Silicon Carbide Nanowires using Chemical Vapor Deposition

Wendi Chang

Physics, Optics, University of Rochester

**NNIN REU Site: Howard Nanoscale Science and Engineering Facility, Howard University, Washington, DC**

*NNIN REU Principal Investigator(s): Dr. Gary Harris, Electrical Engineering, Howard University*

*NNIN REU Mentor(s): Crawford Taylor, Electrical Engineering, Howard University*

*Contact: wendi.chang@rochester.edu, gharris@msrce.howard.edu, crawford@msrce.howard.edu*

## Abstract:

The focus of this project was the characterization and growth of 3C-silicon carbide ( $\beta$ -SiC) nanowires using the vapor-liquid-solid method. Chemical vapor deposition (CVD) occurred at temperatures ranging from 1050°C to 1100°C using silane and propane as precursor gases. Experimentation with various surface preparations, including metal catalysts such as nickel (Ni) and aluminum (Al) deposited by electron beam evaporation on silicon and silicon dioxide ( $\text{SiO}_2$ ) coated silicon substrates, were found to be the most effective in aiding SiC nanowires growth. Nanowires with lengths up to 50  $\mu\text{m}$  and with diameters of 50-100 nm were achieved. The SiC nanowire growth parameters are compared to that of Si. The nanowires grown were further characterized using scanning electron microscope (SEM) and electron dispersion spectroscopy (EDS).

## Introduction:

Silicon carbide has many advantages over other semiconducting materials. Some of these advantages include its wide bandgap energy, high thermal conductivity, high electric field breakdown strength, and its high mechanical strength [1]. These properties make SiC highly desirable over many other materials for semiconducting nanowires for the next generation of electronics. SiC nanowires also have the ability to withstand high temperature and harsh environments.

## Experimental Procedure:

To optimize the growth, different parameters were tested using data from previous literature and the theory on the vapor-liquid-solid process for nanowire growth as a guideline [1,2]. Low resistivity Si(100) substrates, cut in 1 cm  $\times$  1 cm sizes, were cleaned using detergent, trichloroethylene, acetone, and methanol. Different metal catalysts and surface treatments were performed on the samples. Gold (Au) particles of 50 nm in diameter were deposited on one set of samples using poly-L-lysine as an adhesive. A second and third set had Al and Ni deposited respectively, with varying thicknesses by electron beam evaporation. An undulated surface was created on a final set of samples by removing the manufacturer's polish with an abrasive pad. With each set of growths, an untreated Si sample was used as a control. The horizontal CVD growth system employed for this work was a cold wall reactor with a maximum growth temperature over 1500°C. Both time and temperature were variables in the reaction, with all reactions being performed at a pressure of 200 torr.

Silane ( $\text{SiH}_4$ ) and propane ( $\text{C}_3\text{H}_8$ ) were the precursor gases in the reaction and hydrogen ( $\text{H}_2$ ) was the carrier gas. Hydrogen also served to create a reducing growth environment and a laminar flow within the reaction chamber. For comparison, Si

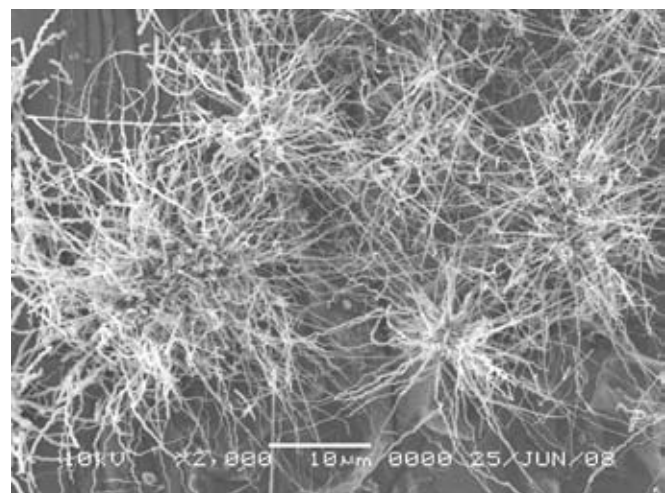
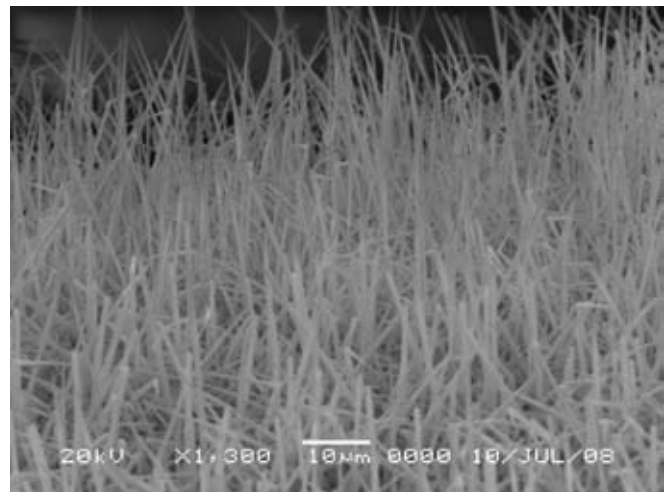


Figure 1, top: SEM image of SiC nanowires with 100\_Ni catalyst.

Figure 2, bottom: SEM of SiC nanowires with 100\_Al catalyst.

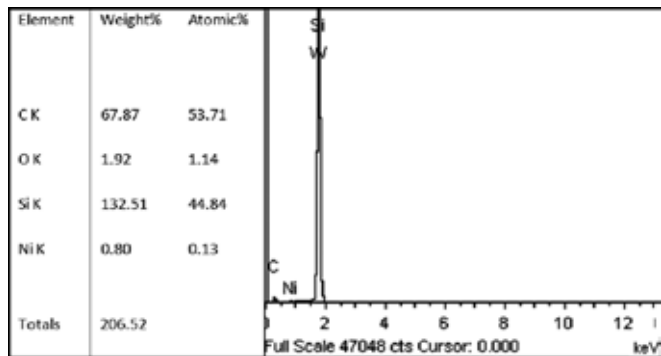


Figure 3: EDS plot of SiC nanowires on Si with Ni catalyst.

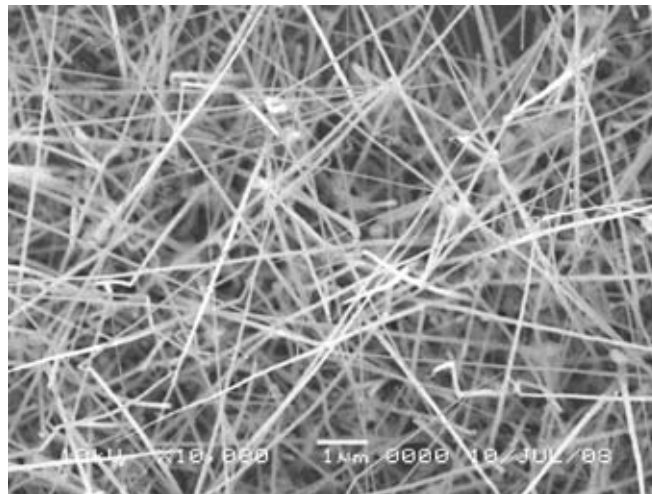


Figure 4: SEM image of Si nanowires on undulated Si.

nanowires were grown using similar wafers and catalysts, with silane as the single precursor gas. In addition to the Si(100) substrates, different substrates such as Si(111), Si(110), Si with 2  $\mu\text{m}$  SiO<sub>2</sub> were also tested for growth.

## Results and Conclusion:

The growth of  $\beta$ -SiC nanowires was successfully achieved using the CVD system. Although different parameters produced varying results, the optimum growth condition was found at temperatures between 1100-1150°C. This temperature was substantially higher than the 750-800°C for Si nanowires. This was due to the higher energy needed for the formation of SiC crystal structures in comparison with Si structures. For both sets of growths, the optimal growth time was around 60 minutes. In support of earlier literature, the length of the nanowires seemed to be dependent on the time of growth up to a certain threshold point, and temperature was the main factor in determining this point. The most effective catalysts for SiC growth were the evaporated layers of 100Å of Ni and 100Å of Al. These two catalysts produced differing results in terms of structural appearance of the nanowires as seen through scanning electron microscopy (SEM) images in Figure 1 and Figure 2.

The nanowires were confirmed using electron dispersion spectroscopy (EDS) to be a compound of Si and carbon (C), see Figure 3. As predicted by the vapor-liquid-solid theory of nanowire growth, a small trace of the catalyst remained on the tip of the nanowires throughout the reaction. These metal traces were also confirmed by EDS.

On average, the SiC nanowires grown were about 50-200 nm in diameter and about 40-80  $\mu\text{m}$  in length. In comparison, the Si nanowires had diameters of around 30-50 nm and lengths between 100-150  $\mu\text{m}$ . It is interesting to note that Si nanowires grew best on the undulated surface for Si(100) samples, Figure 4, and moderately well on samples with 50 nm particles of Au, which seems to suggest that a catalyst is not necessary for Si nanowire growth.

Overall, the research has supported the vapor-liquid-solid process of growth for SiC nanowire and optimized the growth of both SiC and Si nanowires. In theory, the nanowires grown should be  $\beta$ -SiC, having 3-C crystalline structure due to the growth conditions.

## Future Work:

Further work with tunneling electron microscopy (TEM) of the nanowires will be necessary to characterize the crystal structure, stacking faults, and other properties of the nanowires. Further characterization of the growth parameters may also be beneficial. Instead of the heterogeneous growth of SiC on various substrates, SiC nanowire growth on SiC substrates or SiC epilayers may produce better results.

## Acknowledgements:

I would like to thank Dr. Gary L. Harris, Crawford Taylor, James Griffin, and all other faculties at the Howard Nanoscale Facility. I also thank both the National Nanotechnology Infrastructure Network Research Experience for Undergraduates Program and National Science Foundation for the funding of this project.

## References:

- [1] Kang, B. C. et al; "Growth of  $\beta$ -SiC nanowires on Si(100) substrates by MOCVD using nickel as a catalyst"; Thin Solid Films, 464-465, 215-219 (2004).
- [2] Lu, W. et al; "Semiconductor nanowires"; J. Phys. D : Appl. Phys., 39, 387-406 (2006).

# Fabrication of an Array of Thin Film Solid Oxide Fuel Cells

José Fonseca

Department of Chemistry and Mathematics, University of Puerto Rico, Rio Piedras

**NNIN REU Site: Cornell NanoScale Science and Technology Facility, Cornell University, Ithaca, NY**

*NNIN REU Principal Investigator(s): R. Bruce van Dover, Material Science and Engineering, Cornell University*

*NNIN REU Mentor(s): John Gregoire, Physics; Sara Barron, Material Science and Engineering; Cornell University*

*Contact: jose.j.fonseca@uprrp.edu, vandover@ccmr.cornell.edu, jmg232@cornell.edu, scb43@cornell.edu*

## Abstract:

Thin film solid oxide fuel cells (SOFC) offer unique advantages for diverse applications because of their high efficiency and small size. Thin film SOFCs can operate at much lower temperatures than common large-scale SOFCs. Planar thin film SOFCs ranging from  $10^2$  to  $1.2 \times 10^5 \mu\text{m}^2$  in area were fabricated using conventional microelectromechanical systems (MEMS)-based photolithographic, etching and deposition techniques. Radio frequency (RF) sputtering was utilized to deposit 150-300 nm of yttria-stabilized zirconia (YSZ) to form the electrolyte membrane. The YSZ was then annealed to improve crystallinity. Layers of 6 nm porous platinum (Pt) were deposited as catalyst on both sides of the YSZ membranes to form the anode and cathode electrodes. The array of these small devices will ultimately allow for the investigation of new electrolyte materials using a combinatorial approach.

## Introduction:

In recent years, fuel cells have been investigated for clean, portable energy production. Of the different types of fuel cells, the solid oxide fuel cells (SOFC) is among the most common. Normal large-scale SOFC require high temperatures, above  $700^\circ\text{C}$ , to be functional. This is caused by the high ionic transfer resistivity in the oxide membrane which necessitates large amounts of kinetic energy in order for trans-membrane oxide movement to occur. Recent research has focused on lowering the operating temperature of SOFC; thus far researchers have been able to fabricate working low-temperature SOFC ( $300^\circ\text{C}$ - $500^\circ\text{C}$ ). To overcome the ionic transfer resistivity in low-temperature SOFC, the thickness of the oxide membrane has been reduced down to the nanoscale; this reduction in the oxide path from cathode to anode reduces the overall resistivity of the cell. This device with a nanoscale membrane is called a low-temperature Thin Film SOFC.

## Procedure:

The fabrication process requires a double side polished silicon wafer. 500 nm of low stress silicon nitride ( $\text{Si}_3\text{N}_4$ ) was deposited on each side of the wafer by low pressure chemical vapor deposition. Photoresist was spun, exposed and developed on one side of the wafer. The exposed silicon nitride on this side of the wafer was reactively ion etched (RIE) to form a robust mask for the potassium hydroxide (KOH) wet etch later in the fabrication process. After the RIE, the remaining photoresist was removed. On the unpatterned side of the wafer 150-300 nm of YSZ ( $\text{Y}_{0.1}\text{Zr}_{0.9}\text{O}_{2.8}$ ) was RF-sputtered and annealed at  $600^\circ\text{C}$  to form the oxide electrolyte membrane.

On the YSZ side of the wafer, the previously delineated photolithographic techniques were employed with identical

photoresist. 6 nm of porous Pt was then evaporated onto the YSZ side to function as the cathode catalyst. A platinum metal lift-off was subsequently performed to expose the Pt pads over the YSZ. A KOH wet etch test showed that the KOH slowly etches the YSZ; therefore, a protective layer of ProTEK B1-18 was coated on the YSZ. A  $105^\circ\text{C}$  50% KOH solution was used to wet etch the exposed Si, on the patterned  $\text{Si}_3\text{N}_4$  side of the wafer, all the way through the wafer. Upon termination of the KOH wet etch a transparent membrane ProTEK™-Pt-YSZ-silicon nitride is observed, after which the ProTEK™ was removed. Removing the  $\text{Si}_3\text{N}_4$  makes the membrane very delicate, so the wafer was first cleaved into single die. RIE was used to remove  $\text{Si}_3\text{N}_4$  on the membranes, leaving the desired Pt-YSZ membranes. In the last step of the fabrication process, 6 nm of evaporated porous Pt was deposited as the anode catalyst, on the KOH side of the die.

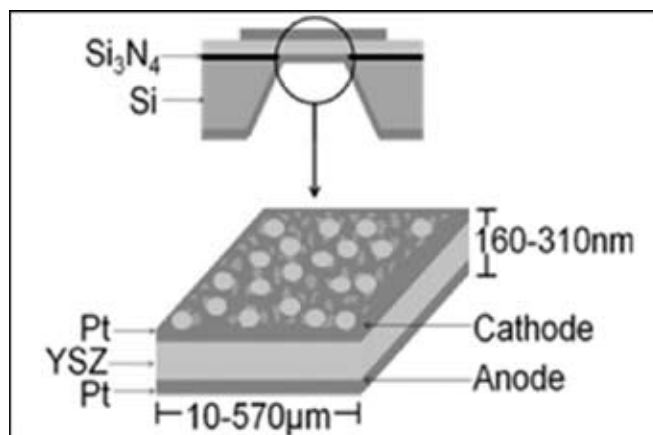


Figure 1: SOFC's YSZ membrane and porous Pt scheme.

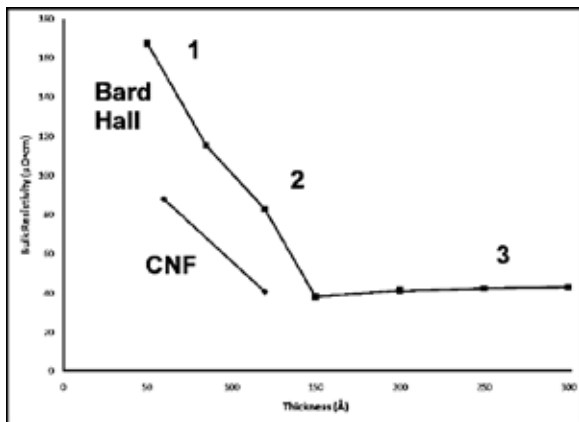


Figure 2: Bulk resistivity vs thickness. Four point resistivity measurements, on different Pt thickness. Interpretation: Region 1; isolated Pt, Region 2; porous Pt, and Region 3; continuous Pt. Pt samples evaporated in two systems located in the CNF and Bard Hall, at Cornell University.



Figure 3: SEM of  $1 \times 10^4 \mu\text{m}^2$  YSZ membrane and Pt pad.

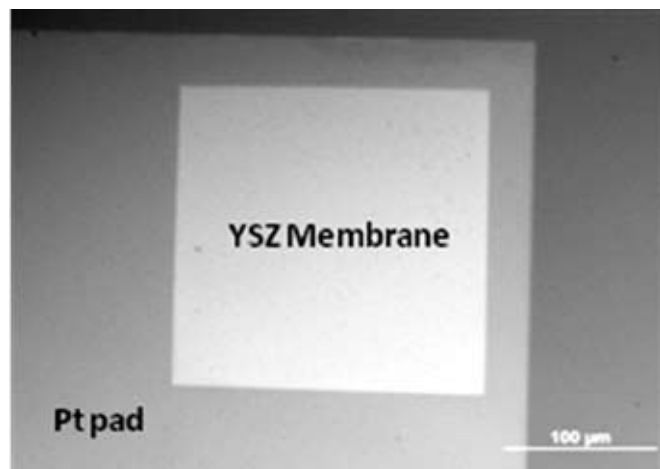


Figure 4: Optical micrograph of  $4 \times 10^4 \mu\text{m}^2$  YSZ membrane and Pt pad.

### Accomplishments:

The evaporated Pt films on anode and cathode must be porous to form a “triple boundary” interface between the YSZ, the Pt and the gases. This interface allows the reactants, intermediates, and products to permeate the YSZ surface to complete the reaction. The Pt film porosity as result of the Pt thickness film was determined by bulk and sheet resistivity measurements. These measurements allowed us to infer that a Pt film nominally 6 nm thick is porous, therefore this thickness was chosen for all the Pt layers in our thin film SOFCs.

We developed a reliable recipe for fabrication procedure for  $10^2$  to  $3.2 \times 10^5 \mu\text{m}^2$  membranes of the novel material YSZ. Membranes up to  $1.2 \times 10^5 \mu\text{m}^2$  survived all the fabrication processes. At this point only the smaller membranes (up to  $1 \times 10^4 \mu\text{m}^2$ ) successfully survived temperatures up to  $500^\circ\text{C}$ .

### Future Plans:

The next step of the project will be electrical characterization of the thin film SOFCs. I-V curves and power curves will be constructed to determine the maximum power output of the cell. Once the fabrication process has been standardized, and functional thin film SOFC can be fabricated routinely, the focus of the research will change to find new catalysts and oxide electrolytes to enhance performance.

### Acknowledgements:

I would like to acknowledge Dr. van Dover and the van Dover research group for support in conducting this project, as well as the National Nanotechnology Infrastructure Network (NNIN) REU program and the Cornell NanoScale Science & Technology Facility (CNF) for the summer research experience. Finally, the National Science Foundation (NSF) for the research funding.

### References:

- [1] Huang, H.; Nakamura, M.; Su P.; Fasching, R.; Saito, Y.; Prinz, F.B., J.Electrochem. Soc., 154 (1), B20-B24 (2007).
- [2] La O, G. J.; Hertz, J.; Tuller, H.; Shao-Horn, Y., J. Electroceramics, 13, 691-695 (2004).
- [3] Politova, T. I.; Irvine, J. T. S., Solide State Ionics, 168, 153-165 (2004).
- [4] Hui, S.; Roller, J.; Yick, S.; Zhang, X.; Decès-Petit, C.; Xie, Y.; Maric, R.; Ghosh, D., J. Power Sources, 172, 493-502 (2007).



# Characterization of the Diffusivity of Alkanes Using Lateral Diffusion in Nanoporous Thin Film Glass

LeMoyne Habimana-Griffin

Biomedical Engineering, Rose-Hulman Institute of Technology

**NNIN REU Site: Stanford Nanofabrication Facility, Stanford University, Stanford, CA**

NNIN REU Principal Investigator(s): Dr. Reinhold Dauskardt, Materials Science Engineering, Stanford University

NNIN REU Mentor(s): Taek Soo Kim, Mechanical Engineering, Stanford University

Contact: habimalm@rose-hulman.edu, dauskardt@stanford.edu, tskim1@stanford.edu

## Abstract:

The mobility of molecules when highly confined in nanometer-sized regions is a topic of significant interest in emerging areas of nanoscience. These include creating heterojunction solar cells by filling nanoporous media with organic molecules, to the operation of molecular sieves, the diffusion of process environments into nanoporous films in device technologies, and the separation and sensing of biomolecules. The diffusivity of nano-confined molecules has been characterized dominantly using nuclear magnetic resonance (NMR) and small-angle neutron scattering (SANS) techniques. However, the usage of these techniques has been limited by their complex implementation and data analysis. We present a novel technique to characterize the diffusivity with straightforward optical measurements of the motion of the liquid diffusion front in a nanoporous thin film glass. Using this technique, the diffusion of alkanes under nanoconfinement was tested at varied temperatures and the scaling in terms of molecular weight is similar. Increasing molecular weight resulted in decreasing diffusivity. Also increasing temperature resulted in increased diffusivity.

## Introduction:

The mobility of molecules in the highly confined interconnected nanoporous regions presents interesting fundamental and technological questions. Nanoporous films are being actively developed for use as size-selective molecular nanofilters, biosensors, biological scaffolds, optical waveguides, and ultra-low dielectric constant layers in electronic devices [1-4]. The pores in nanoporous materials containing more than ~ 20 vol.% porosity are nearly always interconnected and the films are frequently exposed to molecular species in process or service environments. The fixed pathways in the interconnected nanoporous films provide ideal nanoscale environments to explore mobility of confined molecules and the results have implications for a number of technologies where nanoporous materials are in contact with molecules. We show that alkane behavior in nanoporous glass is very different than in bulk alkane fluid.

## Experimental Details:

A 200 nm transparent layer of silicon nitride was deposited on top of methyl silsesquioxane (MSSQ) glass film (average pore size: 2.1 nm) using plasma enhanced vapor deposition (PECVD). Samples of with approximate dimensions 10 × 10 mm were cleaved and affixed on aluminum sample mounts using adhesive dots. Next, approximately 18 ml of alkane was poured into a Petri® dish and the dish was placed onto a hot plate and warmed for approximately 30 minutes and then the temperature was measured using a glass thermometer. Now ready to begin the experiment, simultaneously a sample was immersed in the alkane and a timer was started. In the capped

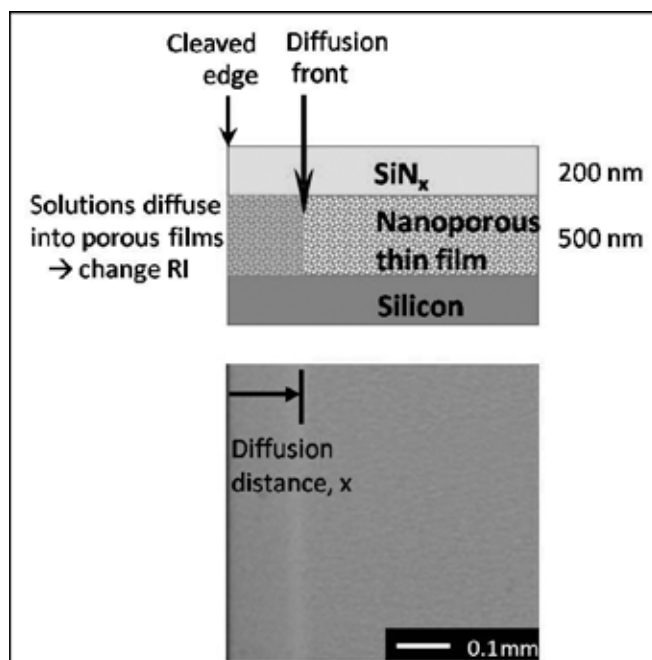


Figure 1: Diffusion front in silicon nitride capped MSSQ film.

MSSQ film, a one-dimensional diffusion front could be measured. As the fluid penetrated into the film, the refractive index of the film changed and left a visible trail as can be seen in Figure 1. The hot plate was moved underneath an optical microscope with a CCD camera and onto a height adjustable platform. The height was adjusted to bring the image into

focus and pictures were taken at roughly even intervals throughout the duration of the test.

## Results and Conclusions:

Previous work suggested that the diffusivity through the glass film would follow a square root time dependence. As you can see below the plots were quite linear when graphed in this manner and therefore were consistent with Fick's First Law:  $x = \sqrt{Dt}$ , where  $D$  is the diffusivity and  $x$  is the diffusion distance. In the diffusivity vs. square root time plots as in Figure 2, the diffusivity is the valued slope of the best fit line through the plot squared. In comparing the diffusivities of the same alkanes at different temperatures, we found that the diffusivity increased as temperature increased. We also observed a scaled dependency of the alkanes as a function of molecular weight where  $D \sim M^{-\alpha}$ .

In our results, this dependency increased as function of temperature as can be seen in Figure 3. Consequently, we found that the diffusivity dependence on molecular weight changed differently with temperature in bulk fluid than in nanoconfinement. In the bulk it has been observed that the molecular weight dependence decreases as a function of temperature. Also diffusion coefficients are lower in nanoconfinement than in bulk fluid as can be seen in Figure 3 and Figure 4.

Overall our technique allowed for the diffusion coefficient to be easily calculated using optical microscope measurements so that diffusion trends could be investigated. In addition, Fickian diffusion was observed in the MSSQ film. Moreover, diffusivity scales similarly with molecular weight in both bulk fluid and nanoconfinement. However, the diffusivity under the nanoconfinement decreased by factor of 5 compared to that in the bulk. Lastly, as temperature increases, diffusivity depends more on molecular weight in nanoconfinement, and less on molecular weight in bulk fluid.

## Acknowledgements:

I would like to thank my mentor, Taek-Soo Kim, my principal investigator, Dr. Reinhold Dauskardt, as well as the rest of the Dauskardt group. Additionally, I would like to thank Dr. Michael Deal, Maureen Baran, and the rest of the staff of Stanford Nanofabrication Facility. Moreover, I thank Ms. Melanie-Claire Mallison, the National Nanotechnology Infrastructure Network Research Experience for Undergraduates Program, the National Science Foundation, and the Intel Foundation.

## References:

- [1] Martini, Ignacio B, et al. "Controlling optical gain in semiconducting polymers with nanoscale chain positioning and alignment." *Nature*. 2, 647-652 (2007).
- [2] Kresge, C. T. et al. "Ordered mesoporous molecular sieves synthesized by a liquid-crystal template mechanism." *Nature* 359, 710-712 (1992).
- [3] Hedrick, J. L. et al. "Templating Nanoporosity in Thin-Film Dielectric Insulators." *Adv. Mater.* 10, 1049-1053 (1998).
- [4] Guarini, K., Black, C., Milkove, K. R. & Sandstrom, R. L, J. "Nanoscale Patterning Using Self-Assembled Polymers for Semiconductor Applications." *Vac. Sci. Technol. B* 19 (6), 2784-2788 (2001).
- [5] Reused with permission from E. von Meerwall, S. Beckman, J. Jang, and W. L. Mattice, *Journal of Chemical Physics*, 108, 4299 (1998). Copyright 1998, American Institute of Physics.

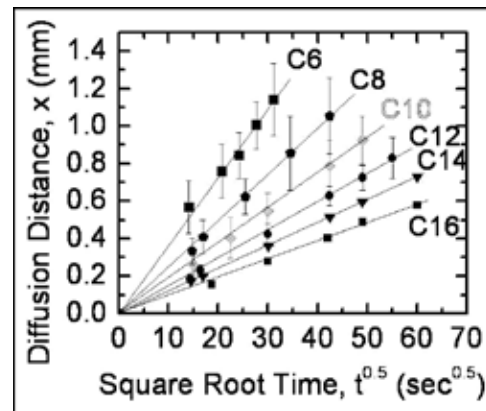


Figure 2: Fickian plot of the diffusivity of alkanes at room temperature ( $22.0 \pm 1^\circ\text{C}$ ).

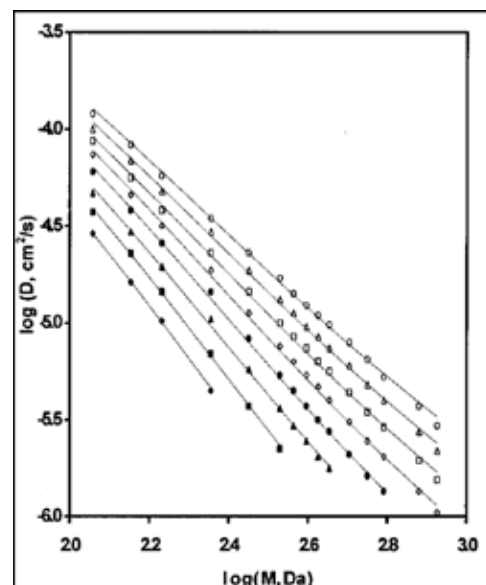


Figure 3: Power law plot of the diffusion coefficient as a function of molecular weight in MSSQ at varied temperatures.

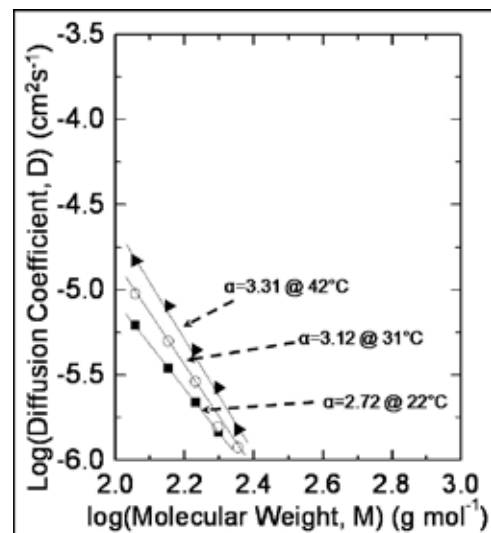


Figure 4: Power law plot of the diffusion coefficient as a function of molecular weight in bulk fluid at varied temperatures [5]. The bottommost line has  $\alpha = 2.72$  at  $30^\circ\text{C}$ , and the topmost line has  $\alpha = 1.85$  at  $170^\circ\text{C}$ .

# Characterization and Modeling of Silicon Migration by Hydrogen Annealing

Tom Hartsfield

Physics, Applied Mathematics, New College of Florida

**NNIN REU Site: Stanford Nanofabrication Facility, Stanford University, Stanford, CA**

NNIN REU Principal Investigator(s): Prof. Roger Howe, Electrical Engineering, Stanford University;

Prof. Olav Solgaard, Electrical Engineering, Stanford University

NNIN REU Mentor(s): Rishi Kant, Dr. J. Provine, Electrical Engineering;

Shrestha Mallick, Applied Physics; Stanford University

Contact: thomas.hartsfield@ncf.edu, rthowe@stanford.edu, solgaard@stanford.edu,

rik9@stanford.edu, jprovine@stanford.edu, sbasumal@stanford.edu

## Abstract:

In this work, we studied silicon migration rates as a function of ambient temperature and pressure. We etched periodic trenches in crystalline silicon with a width of 400 nm and a separation of 500 nm, and then examined the effect of annealing them in various hydrogen ambient conditions. Anneals were performed at pressures between 20 and 80 Torr and temperature values of 1050°C and 1100°C. We then measured the change in the surface topology by imaging cross sections under an scanning electron microscope (SEM). The resulting change was then compared to a dimensionless transient simulation of the phenomenon to characterize the magnitude coefficient. Experimental values for the magnitude coefficient can be calculated with the model and the dependence of this coefficient upon pressure and temperature can then be determined. This work will bring the micro and nanotechnology community closer to building an accurate quantitative model for silicon migration induced shape transformations as well as a better understanding of the effectiveness of direct applications of the process.

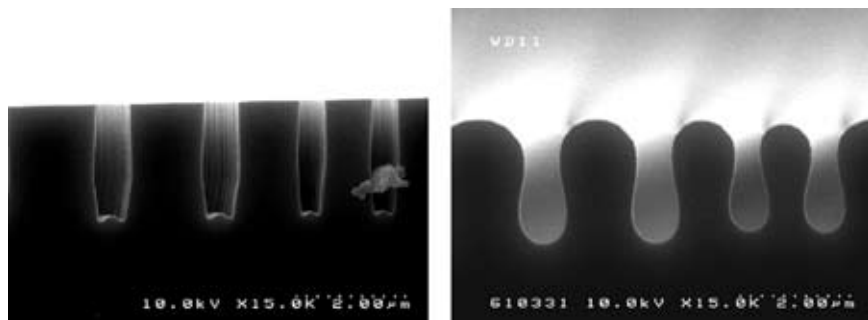


Figure 1: Four plasma etched trenches before (left) and after (right) silicon migration.

## Introduction:

A key challenge in creating devices with structure in the nanometer regime is creation of smooth, symmetric, defect-free surfaces with high reproducibility. Silicon migration is a diffusive process that increases symmetry and smoothness of silicon surfaces as atoms flow into lower energy configurations. This process is distinctly different from the usual methods of shaping silicon, as it is a fluidic transformation as opposed to a sharp cut or etch (Figure 1).

Applications for this process are currently being developed, such as enhancement of photonic crystal optical properties via symmetry improvement. A more complete characterization of the process as a function of temperature and pressure would greatly improve the ease and potential effectiveness of process applications.

## Experimental Procedure:

Wafers were put through a standard process of oxide hard mask growth, patterning via optical lithography, and oxide removal. The completed wafers were then annealed in hydrogen ambient in a hot wall epitaxial chemical vapor deposition system. The main anneal steps in the recipe were a basic run up period to allow the machine to reach main anneal temperature and pressure, a 300 second anneal period at those values and then a cool down period. A wafer was run through the warm up and cool down steps of the recipe without the

main anneal step and analyzed to verify these steps were not observably effecting results. The pressure quickly attained the desired value in both steps, the temperature lagged a bit but ultimately reached the desired level linearly in the span of approximately one minute. Upon removal from the reactor, wafers were then immediately spin coated with a 7  $\mu\text{m}$  layer of photoresist to prevent particle contamination during the cleaving process. The wafers were then cleaved across the surface trench features by hand with a diamond scribe. The photoresist was then removed and the samples were mounted in cross-section under SEM and imaged. Several rounds of procedure modifications were undertaken to reach this final process.

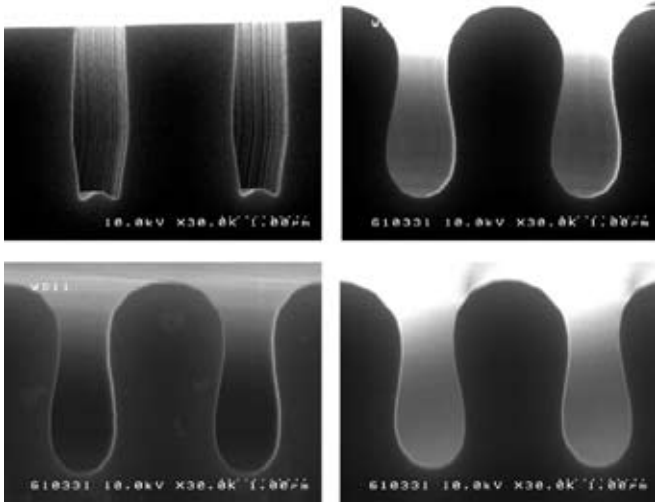


Figure 2: Close-ups of trenches (clockwise from top left) without anneal; with anneal for 300 seconds at 1050°C, 20 torr; 1050°C, 80 torr; 1100°C, 80 torr.

### Results:

Of the thirty wafers that were initially prepared, twenty three reached the annealing stage (several were lost to etcher malfunction). Of these, seven reached the analysis stage and produced quality images (Figure 2).

To define the process quantitatively, a mathematical model of the Mullins equation (Figure 3) for surface diffusion [1] was implemented using level set modeling techniques. We then implemented the Canny edge detection algorithm [2] for finding the surface edges in an image. Images of the initial surface geometry of a sample, which had gone through the entire process without the anneal, were then scanned into the model using this method and the model was run to time-evolve the surface (Figure 4).

### Future Work:

Obtaining a more precise image of the initial surface geometry of the samples can lead to a more accurate final prediction

### Mullins Equation:

$$r_n = \frac{D_s \Omega^2 v}{kT} \frac{\partial^2 K}{\partial s^2} = B \frac{\partial^2 K}{\partial s^2}$$

- $r_n$  → normal velocity
- $D_s$  → diffusion const.
- $\gamma$  → surface tension const.
- $v$  → # atoms per unit area
- $\Omega$  → molecular volume
- $K$  → surface curvature

Figure 3: Mullins equation.

from the modeling software. We hope to eventually use the model to evaluate the final images and then work backwards to bring it into exact agreement with the data. Magnitude coefficient values can be extracted and then plotted versus temperature and pressure of the anneal to generate an equation for it as a function of these variables. With a small amount of improvement it will be ready to be packaged and used as a system capable of inputting any surface geometry and outputting an image of the final surface for a given time and pressure, allowing far greater application in various areas of MEMS and nano-scale engineering.

### Acknowledgements:

I would like to thank especially my mentor and day to day boss on this project, Rishi Kant for all of his help, tutelage and enthusiasm. I would also like to thank Professor Howe, J Provine and Shrestha Mallick for knowledge and wisdom imparted. Finally, thanks to the National Nanotechnology Infrastructure Network Research Experience for Undergraduates (NNIN REU) Program and SNF for giving me this amazing opportunity.

### References:

- [1] Mullins, W.W., J. of Applied Physics, 1957. 28(3): p. 333-339.
- [2] Canny, J.F., IEEE Trans. Pattern Analysis and Machine Intelligence, 1986. p. 679-698.

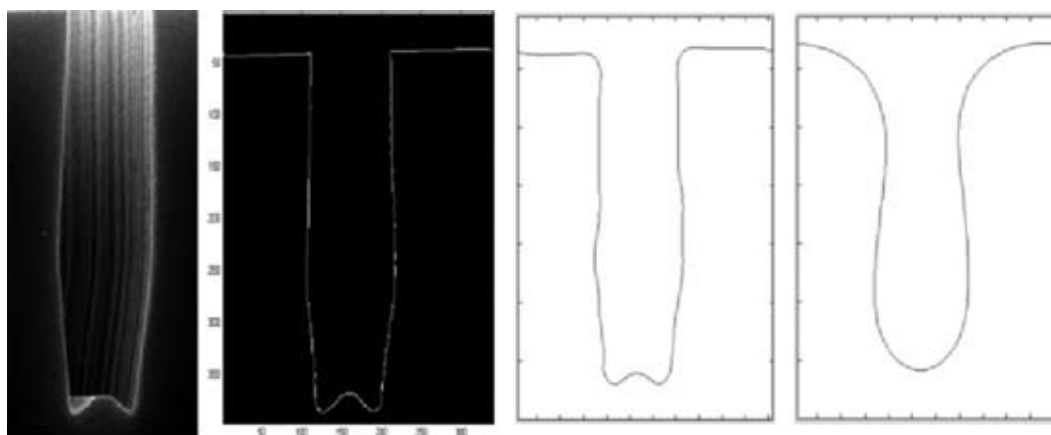


Figure 4: Four steps in the model (from left); Initial surface image, surface edge detection, fitting of an initial condition, image of evolved surface after migration.

# Spray Pyrolysis of $\text{CuInSe}_2$ for Thin Film Photovoltaic Solar Cells

Oluwatosin Jolaoso

Chemical Engineering, Cooper Union

**NNIN REU Site: Howard Nanoscale Science and Engineering Facility (HNF), Howard University, Washington, DC**

NNIN REU Principal Investigator(s): Dr. Gary L. Harris, HNF, Howard University

NNIN REU Mentor(s): Mr. James Griffin, HNF, Howard University

Contact: jolaos@cooper.edu, gharris@msrce.howard.edu, griffin@msrce.howard.edu

## Abstract/ Introduction:

With the increasing costs of traditional sources of energy, and depleting resources, photovoltaic energy is becoming a feasible energy alternative. Copper indium diselenide ( $\text{CuInSe}_2$ ) cells may provide a cost effective way to produce electricity as their efficiencies are increased. The focus of this project was to grow  $\text{CuInSe}_2$  cells by spray pyrolysis using a solution of copper chloride, indium chloride, and dimethylselenide, onto soda-lime glass coated with molybdenum (Mo). After deposition of  $\text{CuInSe}_2$ , cadmium sulfide (CdS) was deposited by chemical bath deposition. This arrangement of cells is called "tandem," or stacked, which also decreases costs and space. Molybdenum acts a back contact and it was deposited by evaporation or sputtering. The deposition rate was determined to be  $50 \text{ \AA}/\text{min}$  for sputtering, and the rate for evaporation depended on filament current. The  $\text{CuInSe}_2$  serves as the light absorbing layer, and was grown at  $250\text{-}350^\circ\text{C}$  in a chamber where the pressure was kept at atmosphere or slightly above atmospheric pressure. Electron dispersive spectroscopy (EDS) confirmed the presence of copper, indium, and selenium. The CdS acted as a window layer, and was deposited in a chemical bath of thiourea, cadmium chloride, and ammonium hydroxide at  $70^\circ\text{C}$ . Spectrophotometer measurements of the CdS layer determined the band gap to be  $2.1\text{eV}$ , which is slightly lower than the  $2.30\text{-}2.60\text{eV}$  range reported in the literature. Discrepancies could be attributed to the non-uniform surface.

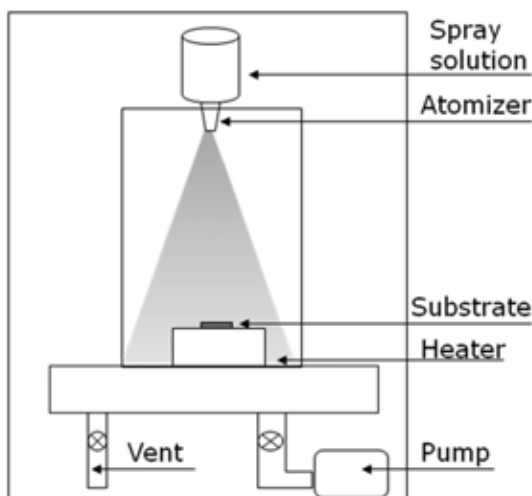


Figure 1: Schematic drawing of spray pyrolysis system.

## Experimental Procedure:

The molybdenum (Mo) layer was deposited on a clean soda-lime glass slide by electron beam evaporation or by sputtering using a Mo target. Mo sputter rates were determined by surface profilometry measurements [1]. The  $\text{CuInSe}_2$  layer was deposited onto a Mo-coated substrate by spray pyrolysis (see Figure 1). Initial stock solutions of copper chloride ( $\text{CuCl}_2$ ) and indium chloride ( $\text{InCl}_3$ ) had to be made. A vial of 5 grams of  $\text{CuCl}_2$  was dissolved in 1.48 L

of de-ionized water for a  $2.5 \times 10^{-2} \text{ M}$  solution. A vial of 5 grams of  $\text{InCl}_3$  was dissolved in 362 mL of  $0.1 \text{ M HCl}$  to form a  $6.25 \times 10^{-2} \text{ M}$  solution. The dimethylselenide (DMS) was mixed fresh before each run and was mixed in  $0.1 \text{ M}$  to  $0.165 \text{ M}$  solutions, then left to dissolve for 2 hours, shielded from light. Two drops of hydrochloric acid were added to the selenium solution after dissolving. In the final solution, 4.5 mL of  $\text{CuCl}_2$ , 2.0 mL of  $\text{InCl}_3$ , 2.5 mL of DMS, 48.2 mL of ethanol, and 198.2 mL of deionized water were used.

Growth temperatures were kept between  $250\text{-}350^\circ\text{C}$ , and growth lasted between 1-2 hours. Modifications to this procedure included doubling concentrations of  $\text{CuCl}_2$ ,  $\text{InCl}_3$ , and selenium, pH adjustments using acid/base to a value of  $\text{pH} = 3$ , and slower spray rates. The conditions for  $\text{CuInSe}_2$  growth are tabulated in Table 1 [2].

The cadmium sulfide layer was deposited by chemical bath deposition. Initial stock solutions of thiourea, cadmium chloride, and ammonium hydroxide were made. Given a 10 gram vial of thiourea, 96 mL of de-ionized water was used to make a 50 mM solution. Given a 5-gram vial of cadmium chloride, 92 mL of de-ionized water was used to make a 10 mM solution. Ammonium hydroxide was added in a 14.8 M solution, and 278.2 mL of de-ionized water was added to dilute it to 1 M. The deposition process started with 92 mL of cadmium chloride added to 33.78 mL of ammonium hydroxide. The solution was heated to  $70^\circ\text{C}$  in a water bath. Next, 96 mL of thiourea was added. The acid/base levels were adjusted to maintain a pH of 11. A clean glass substrate was

	Substrate	Concentrations (20% ethanol in DI water)	Temp./Atomizer and Chamber Pressure	Results
1	Molybdenum on glass slide	CuCl <sub>2</sub> 4.5x10 <sup>-4</sup> M InCl <sub>3</sub> 5.0x10 <sup>-4</sup> M DMSeU 1.65x10 <sup>-3</sup> M	340°C 60 psi/ 0.5 psi	No traces of copper, indium, or selenium
2	Molybdenum on half of a soda-lime glass		290°C 60 psi/ 0.4 psi	Traces of indium
3	Molybdenum on soda-lime glass		340°C 35 psi/ 0.5 psi	No traces of copper, indium, or selenium
4	Molybdenum on soda-lime glass	CuCl <sub>2</sub> 9x10 <sup>-4</sup> M InCl <sub>3</sub> 10x10 <sup>-4</sup> M DMSeU 3.33x10 <sup>-3</sup> M PH adjustment with NaOH and HCl.	330°C 35 psi/ 0.3 psi	Traces of copper, indium, and selenium
5	Molybdenum on soda-lime glass		210°C 35 psi/ 0 psi	Traces of copper, indium, and selenium
6	Molybdenum on half of a soda-lime glass		240°C 35 psi/ 0 psi	No growth
7	Molybdenum on soda-lime glass.		392°C 35 psi/ 0 psi	Traces of copper, indium, and selenium
8	Molybdenum on soda-lime glass. (evaporated)		Temp. not measured 35 psi/ 0 psi	More uniform traces of copper, indium, and selenium

Table 1: Spray pyrolysis growth conditions for CuInSe<sub>2</sub>.

lowered into the solution and left for 45 minutes. Modifications to this procedure included reducing the solution concentration by 40%, and using a magnetic stirrer [3].

### Results and Conclusions:

The sputter rate for Mo was found to be approximately 50 Å/min after measurements with a profilometer. Electron dispersion spectroscopy performed on the initial samples showed no traces of copper, indium, or selenium, but after the modifications were made, all the elements were present as seen in Figure 2 in a good ratio. To confirm that cadmium sulfide was deposited, spectrophotometer measurements were taken to obtain an absorbance vs. wavelength graph, as seen in Figure 3. The wavelength axis was converted into energy to reveal a bandgap of 2.1eV, which is very similar to literature values of 2.3-2.6eV. Ellipsometry readings of the surface revealed a CdS layer thickness of approximately 100 nm.

### Future Work:

In the future, layer uniformity would have to be improved so that all the layers can be stacked. With the stacked cell, tests for efficiency could be made. Gallium could also be added to form copper indium gallium diselenide, which should also improve efficiencies.

### Acknowledgements:

I would like to acknowledge the National Science Foundation, the National Nanotechnology Infrastructure Network Research Experience for Undergraduates (NNIN REU) Program, and Howard University Nanoscale Facility for the opportunity to work on this research project. I would also like to acknowledge my principal investigator, Dr. Gary L. Harris, my mentor James Griffin, and the other staff and students at HNF including Tony Gomez, Crawford Taylor, Bokani Mtengi, and Mpho Musengua, for their help, guidance, and support with this research project.

### References:

- [1] Albin, D.; Ballard, B.; Duda, A; Predecki, P; Scofield, J; "Sputtered Molybdenum Bilayer Back Contact for Copper Indium Diselenide-Based Polycrystalline Thin-Film Solar Cells"; 1-5 (1994).
- [2] Varner, E; "Factors Influencing the Performance of Copper Indium Diselenide/ Cadmium Sulfide Solar Cells Made by Chemical Spray Pyrolysis"; 45-54 (1996).
- [3] Hodes, G; "Chemical Solution Deposition of Semiconductor Films"; 50-55 (2003).

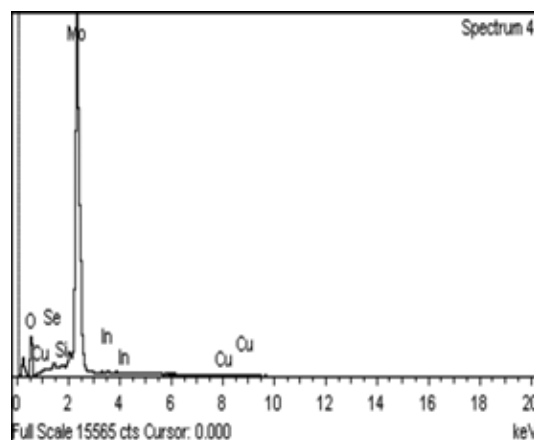


Figure 2: EDS results from the CuInSe<sub>2</sub> layer.

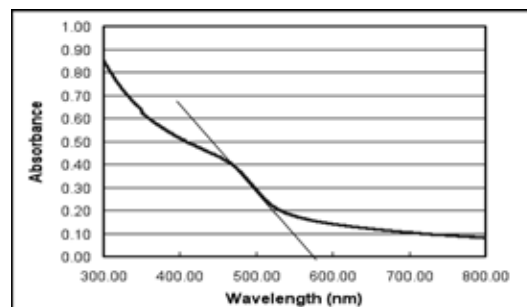


Figure 3: Spectrophotometer results of cadmium sulfide layer.

# Polymer-Mediated Nanoparticle Assembly for Catalyst and Energy Applications

Jill Lowman

Chemistry, Old Dominion University

**NNIN REU Site: Penn State Nanofabrication Facility, The Pennsylvania State University, State College, PA**

NNIN REU Principal Investigator(s): Prof. Melik Demirel, Engineering Science and Mechanics, PSU

NNIN REU Mentor(s): Dr. Hui Wang, Engineering Science and Mechanics, The Pennsylvania State University

Contact: jlowm002@odu.edu, Mdemirel@engr.psu.edu, wanghuichem@yahoo.com

## Abstract:

Polymer-mediated nanoparticle assembly offers applications ranging from catalyst to energy. We have recently demonstrated that nanostructured polymers of poly-(*p*-xylylene) (PPX) can be fabricated by an oblique-angle polymerization method. The nanostructured polymers offer the possibility of fabricating surfaces exhibiting tunable physical properties by systematically varying and controlling the surface chemistry and morphology at the same time. The nanostructured polymers were deposited on a micropatterned substrate from a directional vapor source in an evacuated chamber. The micropatterned substrate consisted of posts 10  $\mu\text{m}$  in diameter with 10  $\mu\text{m}$  spacing between each post. The substrate was oriented obliquely relative to the vapor flux, typically at an angle of 10°, which created a porous and low-density film of columns. The columnar components of our nanostructured PPX films constitute a carpet of densely-packed fibers. The nanostructured PPX film deposited on the top of the micropatterned posts created gaps in the film. We propose to create structured PPX-nanocomposite sandwich films and control the dispersity of the nanoparticles by controlling the porosity of the structured polymer film. In our approach, PPX films were immersed in ligand solutions, where ligands adsorb to the columns. The ligand adsorbate performed the function of binding both to the PPXs and nanoparticles. The adsorbate ligates nano-colloids in sufficient quantities. The ligand adsorbate was chosen from the group consisting of an alkylamine and a nitrogen-containing heterocycle capable of covalently binding the metal species. The micropatterned PPX-nanocomposite acted as a catalyst for electroless metallization.

## Introduction:

We attempted to develop a catalyst using a nanostructured polymer surface deposited on a micropatterned silicon wafer substrate. The nanostructured polymer allows for more surface area of our metal catalyst which was deposited on the polymer. If using this catalyst for hydrogen release, the surface area of the catalyst is proportional to the hydrogen release rate [1]. In order for the metal catalyst to form on the nanostructured polymer, a metal nanoparticle seed must be present. The seed attached to the ligand, pyridine or a thiol containing arene, which adsorbed to the nanostructured polymer surface by aromatic interactions [2]. Palladium or copper were the seeds used in this experiment.

## Experimental Procedures:

A micropattern was created on the surface of a silicon wafer by using photolithography. Silicon wafers were treated with 50/50 hydrochloric acid/methanol solution, then concentrated sulfuric acid, and finally washed with acetone before being placed in the allyltrimethoxysilane solution. Allyltrimethoxysilane self assembled into a monolayer on the surface of the silicon wafer. The wafers were then deposited with a nanostructured poly-(chloro-*p*-xylylene) (PPX-Cl)

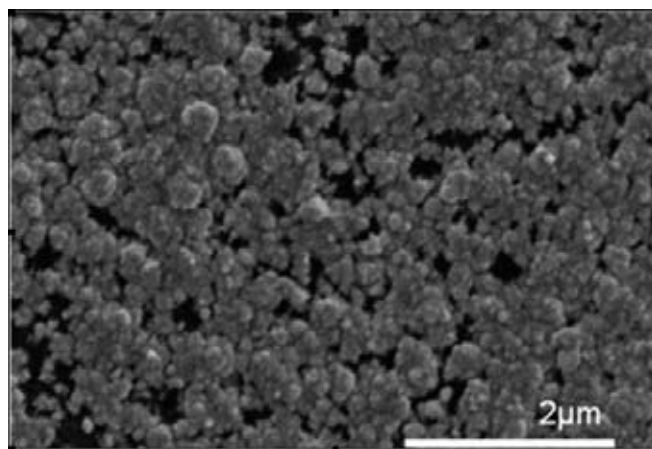


Figure 1: SEM of copper plated on PPX-Cl using palladium nanoparticles as catalysts for copper growth.

polymer by vapor deposition [3]. Planar deposition of the polymer on silicon wafers was also carried out to act as a control. The polymer was treated with a 1 M pyridine solution which served as the ligand for palladium nanoparticle adsorption. Palladium nanoparticles were synthesized using

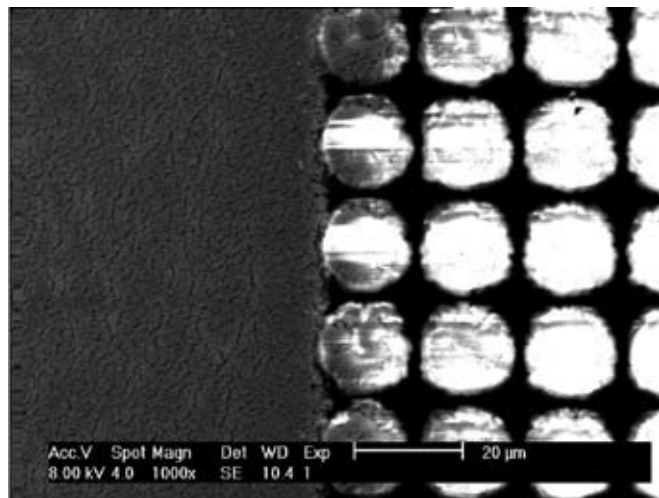


Figure 2: SEM of micropatterned nickel plated on PPX-Cl using palladium nanoparticles as catalysts for nickel growth.

the procedure described by Brandow, S.L. et al. [4]. Copper electroless metallization was performed according to Ma, Z.H. et al. [5]. The wafers were observed under scanning electron microscopy (SEM) as shown in Figure 1. Nickel electroless metallization was performed according to Demirel, M.C. et al. [2]. The SEM image can be seen in Figure 2. Various ligands were tested with copper nanoparticles to determine the optimal ligand for copper nanoparticle attachment.

### Results and Conclusions:

Copper metallized on the nanostructured polymer surface better than on the planar polymer surface. This was due to the fact that the ligand has more adsorption on the nanostructured polymer due to its increased surface area compared to the planar polymer. Therefore, there was more binding between the palladium nanoparticles and the ligand on the nanostructure polymer which led to more seeds for metallization.

Nickel metallized on the micropatterned substrate which contained a helical nanostructured polymer. The polymer was deposited at an angle of 25° so that none would be deposited between the columns. Figure 2 shows that there was no nickel plating between the columns which confirms that there was no polymer between columns.

For this experiment the optimal ligand was pyridine because the nanoparticle seed used was palladium. Palladium binds

to the nitrogen in pyridine. When using copper nanoparticles as seeds, 1,2-benzenedithiol is the best ligand compared to benzenethiol and hydroxyl functionalized benzenes. Thiol is a more liable ligand than hydroxyl because sulfur is softer than oxygen. Images were taken with a triple-laser confocal microscope with a 40× objective to assess the ligand's ability to bind with the nanoparticles. It was observed that thiols are better than hydroxides and multiple ligand sites are better than one site. It was also observed that a ligand must be present for nanoparticle attachment to occur.

### Future Work:

The copper and micropatterned nickel catalysts need to be tested for their ability to release hydrogen from an aqueous sodium borohydride solution kept in alkaline conditions.

### Acknowledgements:

I would like to thank Dr. Melik Demirel and his group, National Nanotechnology Infrastructure Network Research Experience for Undergraduates (NNIN REU) Program, NSF, and PSU MRI staff.

### References:

- [1] Malvadkar, N., Park, S., Urquidi-MacDonald, M., Wang, H., Demirel, M.C. "Catalytic activity of cobalt deposited on nanostructured poly(*p*-xylylene) films", *J. Power Sources*, Vol. 182, pg. 323-328, (2008).
- [2] Demirel, M.C., Cetinkaya, M., Singh, A., Dressick, W.J. "Noncovalent deposition of nanoporous Ni membranes on spatially organized poly(*p*-xylylene) film templates", *Adv. Mater.*, Vol. 19, pg. 4495-4499, (2007).
- [3] Demirel, M.C. "Emergent properties of spatially organized poly(*p*-xylylene) films fabricated by vapor deposition", *Colloid. Surface. A*, Vol. 321, pg. 121-124, (2008).
- [4] Brandow, S.L., Chen, M., Wanq, T., Dulcey, C.S., Calvert, J.M., Bohland, J.F., Calabrese, G.S., Dressick, W.J. "Size-controlled colloidal Pd(II) catalysts for electroless Ni deposition in nanolithography applications", *J. Electrochem. Soc.*, Vol. 144, pg. 3425-3434, (1997).
- [5] Ma, Z.H., Tan, K.L., Kang, E.T. "Electroless plating of palladium and copper on polyaniline films", *Synthetic Metals*, Vol. 114, pg. 17-25, (2000).

# Effects of Phase Separation on Charge Mobility in Polymer Solar Cells

Andrey Malyutin

Chemistry, Kalamazoo College

**NNIN REU Site: Center for Nanotechnology, University of Washington, Seattle, WA**

*NNIN REU Principal Investigator(s): Prof. David S. Ginger, Department of Chemistry, University of Washington*

*NNIN REU Mentor(s): Obadiah G. Reid, Department of Chemistry, University of Washington*

*Contact: malyutinag@gmail.com, ginger@chem.washington.edu, obadiah@gmail.com*

## Abstract:

One of the limiting factors in polymer solar cell performance is charge carrier mobility through the cell. Recently, it has been reported that the hole mobility in certain blends can be enhanced by adding additional electron transport material. Our hypothesis is that the phase segregation process induces local ordering which increases hole mobility. We study how the hole mobility changes as a function of blend composition and domain size in solar cells with active layers consisting of various mixtures of [6,6]-phenyl C61-butyric acid methyl ester (PCBM) (electron acceptor) and poly[2-methoxy-5-(3,7-dimethyloctyloxy)-*p*-phenylene vinylene] (MDMO-PPV) (electron donor). We show that charge carrier mobility increases as the ratio of PCBM to PPV in the active layer increases. We present AFM images of each blend, and show that phase separation between the two molecules and increase in feature size of PCBM are correlated with the increase in hole mobility.

## Introduction:

Solar energy will play a significant role in future energy production. However, the present generation of silicon solar cells cannot compete on \$/kWh basis with energy generated from fossil fuels. Polymer solar cells made from a donor/acceptor blend are one potential inexpensive alternative to silicon based devices because they can be processed from solution under standard conditions. However, their performance is not yet adequate for widespread applications [1].

The most efficient polymer solar cells fabricated to date have an active layer consisting of a mixture of two organic compounds, one acting as an electron donor and other as electron acceptor (in our case PPV and PCBM respectively). It has been observed that as concentration of PCBM increases hole mobility also increases [2]. We measured hole mobility in blends with varying PCBM concentration and observed topographical features using atomic force microscopy (AFM). From this data we propose that as concentration of PCBM increases, there is an increase in ordering of the PPV structures, which allows for more efficient charge transport through the cell.

## Experimental Procedure:

Devices were fabricated on indium tin oxide (ITO) coated glass substrates, with active areas defined by the overlap of patterned ITO and evaporated electrodes. Substrates were cleaned by sequential sonication in acetone and isopropyl alcohol (20 min), followed by an air plasma treatment (5 min). Immediately after plasma cleaning a 40 nm thick layer of poly(3,4-ethylenedioxythiophene) poly(styrenesulfonate)

(PEDOT:PSS) was spin coated onto the substrate, and the devices were annealed in nitrogen atmosphere for 30 min at 130°C. The active layers were spin coated onto the substrates from warmed solutions (45°C) at speeds between 2000 and 4000 RPM. The devices were completed with 40 nm thick thermally evaporated gold top contacts.

The active layer solutions were prepared in chlorobenzene with an MDMO-PPV concentration of 8mg/mL, and MDMO-PPV:PCBM ratios of 1:0, 2:1, 1:1, 1:2, and 1:4. The solutions were heated (40-50°C) and stirred for 6+ hours before spin coating. Device measurements were made in a nitrogen atmosphere, using a custom-built sample chamber and a source-measure unit (Keithley 2100). We made current density-voltage (J-V) measurements, applying varying potential to individual pixels until a curve exhibiting space-charge limited current properties was obtained. The topography and thickness of each device was measured by tapping mode atomic force microscopy (Asylum Research MFP-3D).

$$J = \frac{9}{8} \epsilon \epsilon_0 \mu e^{0.89\gamma} \left(\frac{V}{L}\right)^{1/2} \frac{V^2}{L^3}$$

Equation 1: Modified Mott-Gurney Law.

## Results and Conclusions:

We calculated the hole mobility for our devices from the J-V data using the modified Mott-Gurney law (Equation 1). Figure 1 shows a representative J-V curve and the fit using Equation 1. Figure 2 shows the calculated hole mobility at PCBM

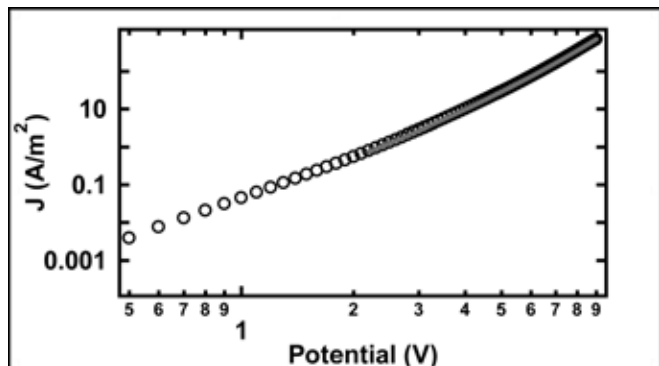


Figure 1: J-V graph with modified Mott-Gurney Law fit.

concentrations of 0%, 33%, 50%, 67%, and 80% for five sets of devices. Each set shows a different trend, but on average the hole mobility increases with increasing PCBM concentration. Figure 3 shows AFM topography measurements of the 67% and 80% PCBM blends. For mixtures with 0%, 33%, and 50% concentration of PCBM topography images are nearly identical to the 67% mixture, with no distinguishable features. Active layers with 80% PCBM show very well defined PCBM formations (high regions).

The mobility data in Figure 2 shows an average trend of increasing hole mobility with PCBM content, and this correlates with an increasing degree of phase separation between PPV and PCBM measured by AFM. This observation supports our hypothesis, that increasing amount of PCBM in the active layer increases the ordering of PPV structures, allowing for more efficient charge transport. However, there is significant variation in calculated hole mobility from set to set, which makes it difficult to draw firm conclusions.

### Future Work:

We would like to further characterize our samples and explore affects of phase separation on charge carrier mobility by using conductive atomic force microscopy (c-AFM). Using this technique will both enable us to resolve smaller structural features, and provide a direct mapping of hole transport through the film. In addition, using other solvents, such as

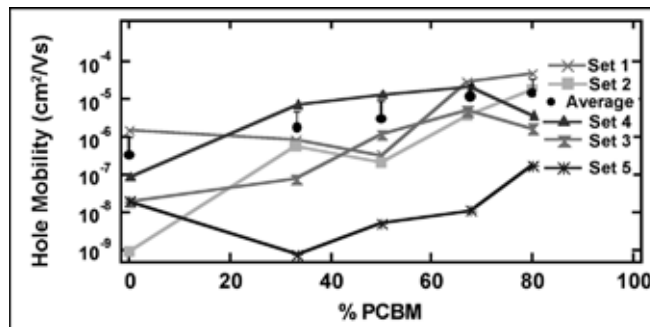


Figure 2: Five sets of PPV:PCBM in CLB devices.

dichlorobenzene and xylenes, or organic materials, such as P3HT instead of MDMO-PPV, will produce different phase separation and allow us to study how it affects the mobility. Preparing samples in a glove box might also prove useful, as exposure to ambient atmosphere may affect the performance and reproducibility of our devices [3].

### Acknowledgments:

I would like to thank Prof. David S. Ginger, Obadiah Reid, and the rest of the Ginger Lab, National Nanotechnology Infrastructure Network Research Experience for Undergraduates Program, National Science Foundation, Ethan Allen, and the University of Washington.

### References:

- [1] Shaheen, S.; Ginley D.; Jabbour, G. "Organics-Based Photovoltaics: Toward Low-Cost Power Generation", MRS Bulletin, Vol.30, pg. 10-19, 2005.
- [2] Tuladhar, S. M.; Poplavskyy, D.; Choulis, S. A.; Durrant, J. R.; Bradley, D. D. C.; Nelson, J. Advanced Functional Materials 2005, 15, (7), 1171-1182.
- [3] Alexeev, A., Loos, J., "Conductive atomic force microscopy (C-AFM) analysis of photoactive layers in inert atmosphere", Organic Electronics, Vol. 9, pg. 149-154, 2008.

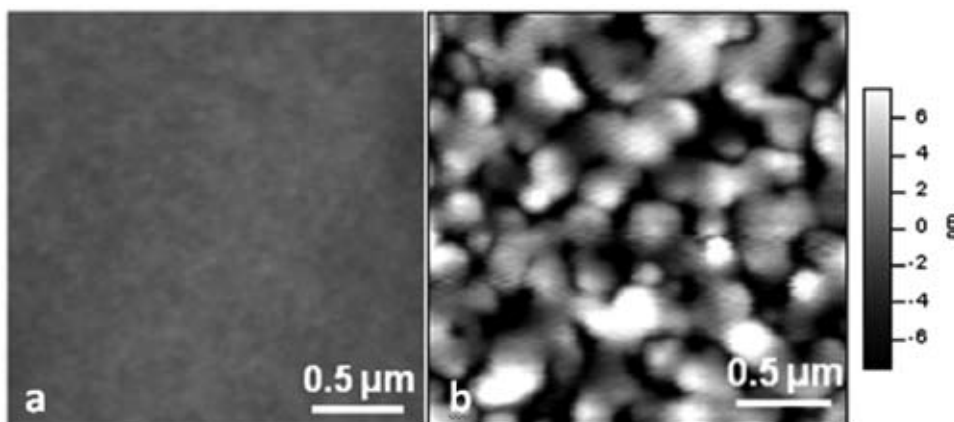


Figure 3: AFM images of devices with PCBM concentration of (a) 67% and (b) 80%.

# Design and Fabrication of Microfluidic Devices for the Study of Flow through Carbon Nanotubes

Michael Moebius

Materials Science and Engineering, and Applied Physics, Rensselaer Polytechnic Institute

**NNIN REU Site: Lurie Nanofabrication Facility, University of Michigan, Ann Arbor, MI**

NNIN REU Principal Investigator(s): Professor A. John Hart, Mechanical Engineering, University of Michigan

NNIN REU Mentor(s): Sameh Tawfick, Mechanical Engineering, University of Michigan

Contact: moebim@rpi.edu, ajohnh@umich.edu, stawfick@umich.edu

## Abstract:

Carbon nanotubes (CNTs) have been investigated for manifold applications due to their amazing properties, including stiffness and strength exceeding steel, thermal conductivity exceeding diamond, and ballistic electron transport over micron scales. Additionally, fluid flow experiments through CNTs have shown extraordinarily high slip, reflecting unique flow dynamics. Voltages induced by flow over the length of nanotubes have also been observed. Relevant applications include the use of CNTs in flow sensors, filtration, energy conversion, and the study of chemical reactions where nanotubes may be used as “miniature test tubes.” Previous studies of flow through CNTs have primarily investigated flow through membranes containing low densities of short nanotubes. This study is focused on developing methods for fabricating flow cells and permeable membranes with pores of CNTs using millimeter long, dense bundles of CNTs grown by chemical vapor deposition (CVD).

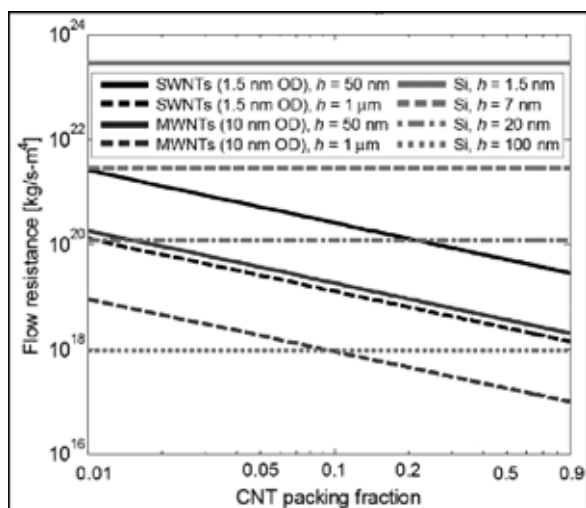


Figure 1: Chart comparing flow resistances of CNT pipes and Si channels.

## Introduction:

Fluidic devices for the purposes of studying nano-scale confined flow have been fabricated [1]. At these scales flow rates are usually limited due to the no slip condition at the channel walls. Experimental results have shown high slip for fluid flow through CNTs and a lack of interaction between molecules inside the CNT, leading to greatly enhanced flow rates over hydrodynamic flow [2]. Figure 1 compares flow resistance through a “CNT pipe” consisting of a packed bundle of aligned nanotubes to that of shallow channels in silicon. In this model,  $h$  is channel depth and CNT packing is the fraction of cross sectional area of the bundle taken up by CNTs.

## Procedure:

Two initial designs were pursued. The first allows for fluid flow through a polydimethylsiloxane (PDMS) membrane with nanotube pores produced by spin-coating PDMS (an elastomer commonly used for microfluidics) onto vertically aligned CNT columns. This design will be used for early investigations of flow dynamics and shows potential for applications requiring large scale filtration. Advantages include relatively quick processing with limited clean room fabrication but provide limited control over CNT characteristics such as packing.

Columns of aligned nanotubes ranging from  $75 \times 75$  to  $200 \times 200 \mu\text{m}$  were grown on a silicon substrate with patterned iron

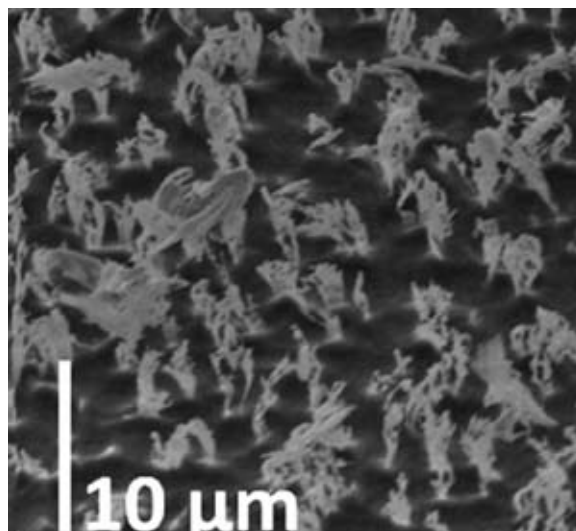


Figure 2: Surface of an etched CNT membrane.

catalyst [3], then spin coated with PDMS. Vacuum degassing ensured the removal of all air from the CNT bundles to produce a sealed membrane. A PDMS etch with  $\text{CF}_4$  and  $\text{O}_2$  followed by a CNT etch with  $\text{O}_2$  and Ar, was performed to expose and open the CNTs to enable flow [4]. Figure 2 shows an SEM image of a membrane with CNT bundles exposed by etching.

The second design utilizes microfluidic channels patterned by UV lithography into SU-8 photoresist. Highly densified, horizontally aligned CNTs are embedded in a membrane across these channels, forming a “CNT pipe” to facilitate flow. Advantages of this design include potential for integration with microfluidic systems and precise control of CNT characteristics such as length and packing. This comes at the cost of extensive clean room fabrication.

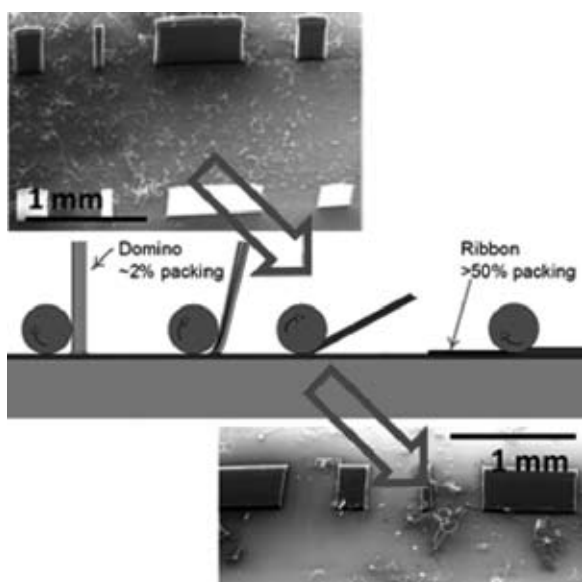


Figure 3: Schematic of CNT growth rolling.

Growth of vertically aligned “dominos” of CNTs is followed by a rolling process developed by the Mechanosynthesis group at UMich to horizontally align and densify the CNTs, as shown in Figure 3 [5]. This produces the dense bundles of CNTs that will form the “CNT pipes.” Spin coating the rolled bundles with SU-8 and performing UV lithography produces the channels of the microfluidic device. A wall of SU-8 across the channels with the “CNT pipes” embedded within it restricts flow through the CNTs. A CNT etch is used to open up the pipes to allow flow. Figure 4 shows an overview of a “CNT pipe” device before etching and an etched “CNT pipe.” The device is packaged by bonding a PDMS cover to the SU-8. Inlets for pressure sensors and fluid flow into and out of the device are punched into the PDMS cover.

This process requires further improvement to produce useable devices. SU-8 bonding to the substrate and PDMS cover must be improved to provide a seal capable of withstanding pressures necessary to push fluids through the “CNT pipe.” The infiltration of CNT bundles with SU-8 will be further

examined by sectioning SU-8 infiltrated bundles with a focused ion beam and imaging to ensure no gaps are visible between the CNTs.

### Future Work:

Future work will strive to solve the challenges faced in fabrication of functional microfluidic devices. Initial flow tests will be run to verify that flow travels exclusively through the CNTs by filtering a solution of nanoparticles with diameters greater than the interior diameter of the CNTs using the flow cells. A resulting nanoparticle free solution will help verify successful infiltration of the nanotubes bundles. Data from flow tests will enable development of flow dynamics and comparison to theoretical models.

### Acknowledgements:

This work was made possible by the National Nanotechnology Infrastructure Network Research Experience for Undergraduates Program, the National Science Foundation, and the Lurie Nanofabrication Facility at the University of Michigan. I would like to thank Professor John Hart, Sameh Tawfick, the Mechanosynthesis Group, Dr. Sandrine Martin, and the LNF staff for their guidance and support.

### References:

- [1] Abgrall, P. and N. T. Nguyen; “Nanofluidic Devices and Their Applications”; *Analytical Chemistry*, 80, 2326-2341 (2008).
- [2] Majumder, M. et al.; “Nanoscale Hydrodynamics: Enhanced Flow in Carbon Nanotubes”; *Nature*, 438, 44 (2005).
- [3] Hart, A. and A. Slocum; “Rapid Growth and Flow-Mediated Nucleation of Millimeter-Scale Aligned Carbon Nanotube Structures from a Thin-Film Catalyst”; *Journal of Physical Chemistry B*, 110, 8250 (2006).
- [4] Hayamizu, Y. et al.; “Integrated Three-Dimensional Microelectromechanical Devices from Processable Carbon Nanotube Wafers”; *Nature Nanotechnology*, 3, 289-294 (2008).
- [5] S. Tawfick, K. O’Brien, M. Moebius, A. J. Hart; “Dense horizontally-aligned carbon nanotube ribbons for next-generation microelectronic interconnects and active microstructures”, 2008 MRS Fall Meeting.

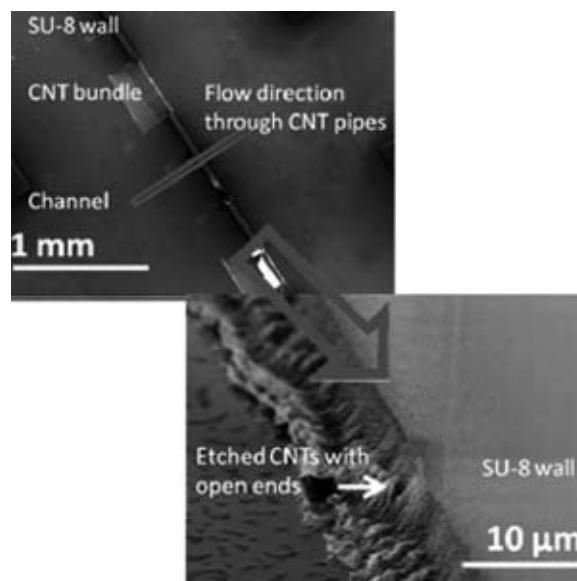


Figure 4: CNT pipe device before and after etching.

# Effect of Deposition Parameters in RF-Sputtering of Titanium Dioxide Thin Films for Non-Volatile Memory

Jiaomin Ouyang

Materials Science and Engineering, University of Florida

**NNIN REU Site: Stanford Nanofabrication Facility, Stanford University, Stanford, CA**

*NNIN REU Principal Investigator(s): Yoshio Nishi, Peter Griffin, Electrical Engineering, Stanford University*

*NNIN REU Mentor(s): Mihir Tendulkar, Applied Physics, Stanford University*

*Contact: nimoaj@ufl.edu, nishiy@stanford.edu, griffin@stanford.edu, mihirt@stanford.edu*

## Abstract:

Resistive switching of titanium dioxide ( $\text{TiO}_2$ ) has attracted attention due to its potential application in non-volatile memory devices. However, the exact mechanism of switching is unknown. In this work,  $\text{TiO}_2$  thin films are deposited onto platinum substrates using reactive radio-frequency (RF) magnetron sputtering. We vary the substrate deposition temperature and substrate bias in order to modify the chemical composition, microstructure, and electrical properties of the  $\text{TiO}_2$  film. After photolithography, platinum electrodes are sputtered. The final device structure is Pt/ $\text{TiO}_2$ /Pt. IV curves are measured to characterize the switching behavior of the  $\text{TiO}_2$  films. The results of this work will help us understand how deposition conditions affect the electrical properties of the film and give us insight into the optimization of  $\text{TiO}_2$  films for non-volatile memory applications.

## Introduction and Motivation:

$\text{TiO}_2$  exhibits bistable resistance switching behavior as a resistance change memory material [1]. It can reversibly switch between high and low resistance states when appropriate voltages are applied, either unipolar or bipolar [2]. The technical difficulties that hinder the application of  $\text{TiO}_2$  are reproducibility, large set/reset current and voltage, and the required electrical forming process. In addition, how switching happens on an atomic level is unknown even though it has been determined that the formation and disruption of conducting filament is the mechanism [3]. The goal for this project was to study how varying sputtering parameters would affect the electrical properties of the film and hopefully gain some insight into how switching works.

## Experimental Procedures:

Forty nanometers of  $\text{TiO}_2$  thin film was deposited on Pt/Ti/ $\text{SiO}_2$ /Si and Si substrates by reactive RF magnetron sputtering using a titanium target. 27 sccm of argon and 3 sccm of oxygen gases were used to form a film consisting of  $\text{TiO}_2$ ,  $\text{Ti}_2\text{O}_3$ , TiO, and Ti. We varied the substrate deposition temperature (room temperature, 100°C, and 200°C) and the substrate bias (0V, 60V, and 100V) to study their effects on the electrical properties of the film. After deposition, photolithography was used to pattern the film and 50 nm top platinum electrodes were sputtered. Excess photoresist and platinum were removed to get the final device that had the structure Pt/ $\text{TiO}_2$ /Pt. IV characteristics were tested using a probe station with an Agilent 4156C semiconductor analyzer.

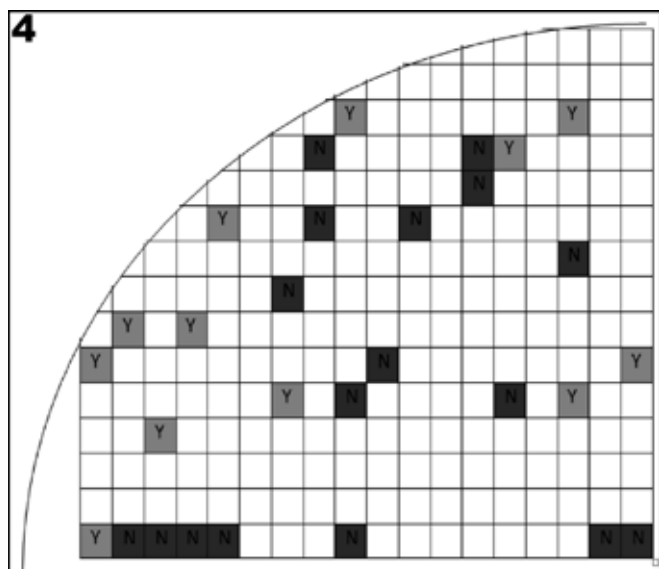
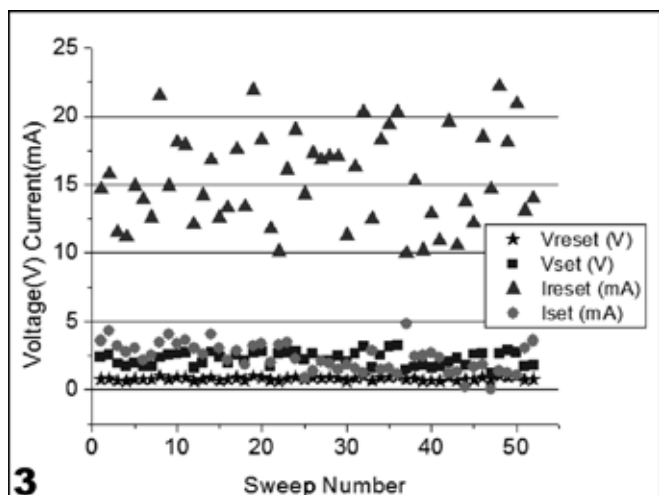
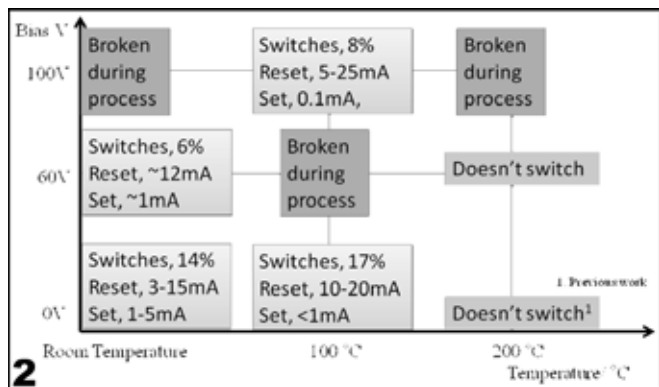
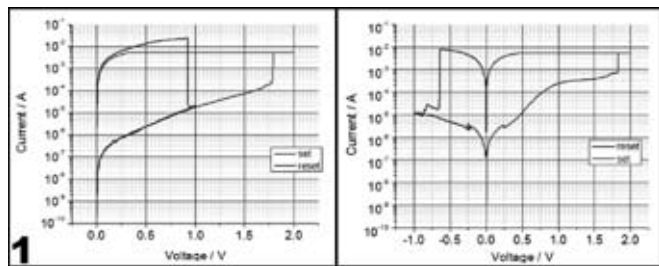
## Results and Discussion:

All the devices were found to require an electrical forming process regardless of the deposition conditions, which suggested that changing sputtering parameters would not eliminate the forming process. The forming voltage was ~4-5 V and forming current was ~5-10 mA. The device was then in a low resistance state and could not return to its fresh state after forming.

$\text{TiO}_2$  film exhibited both unipolar and bipolar switching behavior [2], as shown in Figure 1. The switching window of unipolar switching was ~1000 and is larger than for bipolar switching, which was ~100, as shown in Figure 1. This difference might be explained by the conducting filament mechanism.

Film performance for different deposition conditions were plotted (Figure 2). The set and reset voltage were roughly in the same range for different conditions, with set voltage ~1-2V and reset voltage ~0.6-0.8V. The reset current seemed to get larger, from 5 mA for 0V, room temperature, to 25 mA for 100V, 100°C, while the set current was getting smaller, from more than 1 mA to less than 0.1 mA, as we increased substrate temperature and applied bias. All the films deposited at 200°C were conductive, possibly because the film was reduced from the heat and had more oxygen vacancies.

Multiple bipolar sweeps were conducted on one device to test endurance. Figure 3 shows the distribution of set/ reset current and voltage. The set voltage was higher than the reset voltage. The set current was lower than the reset current. Over time, they were scattered and there was no obvious trend. However, there were large variations between each sweep. This suggests



that the film was unstable and film performance might have depended on the previous sweep.

The 10% to 20% yield was low. The location of working and non-working devices on a quarter silicon substrate was plotted (Figure 4). Each block had 100 devices and 5 to 10 devices were tested from each block. “Y” represents area with working devices and “N” represents non-working ones. The devices on the perimeter worked better than the ones in the center of the film. This kind of distribution was probably related to the photoresist process. The distribution pattern was consistent with the circular photoresist pattern after spinning.

It is possible that the thicker photoresist at the edges protected the devices from outgasing. The distribution might also relate to the sputtering process because of different film thickness and stress of the film.

**Summary:**

We explored how different deposition parameters affect the switching behavior of a TiO<sub>2</sub> film and studied device variation and tested film endurance. We found out that for different deposition conditions, the reset current seems to get larger and the set current seems to get smaller, as we increase substrate temperature and apply bias. Large device variation exists for the same film possibly due to film stress from deposition or trace contamination from the photolithography process.

**Future Plans:**

We will characterize the TiO<sub>2</sub> film deposited on Si substrates to study how sputtering parameters affect the physical properties of the film and how they correlate with electrical properties. We will also test endurance with transistor in series so we can precisely control the current through the device.

**Acknowledgements:**

The author wishes to thank the National Nanotechnology Infrastructure Network Research Experience for Undergraduates Program, National Science Foundation, Stanford Nanofabrication Facility, Mihir Tendulkar, Professor Nishi, Dr. Peter Griffin, Dr. Michael Deal, and Maureen Baran.

**References:**

- [1] ARGALL, F.: ‘Switching phenomena in titanium oxide thin films’.. Solid-State Electron., 1968, 11, pp. 535-541.
- [2] Doo Seok Jeong, Herbert Schroeder, and Rainer Waser, Electrochem. and Solid-State Letters, 10 (8) G51-G53 (2007).
- [3] G. Dearnaley, A. M. Stoneham, and D. V. Morgan, Rep. Prog. Phys. 33,1129 (1970).

Figure 1: Left: IV characteristics of device showing unipolar switching; right: characteristics showing bipolar switching.

Figure 2: Device performance for different deposition conditions.

Figure 3: Bipolar switching endurance test.

Figure 4: Schematic of a quarter silicon wafer showing tested devices, with working devices labeled with Y and non-working labeled with N.

# A Study of Silicon Nanoparticles with Applications to Medical Resonance Imaging

Daniel Reeves

Physics, Colby College

**NNIN REU Site: Center for Nanoscale Systems, Harvard University, Cambridge, MA**

NNIN REU Principal Investigator(s): Prof. Charles Marcus, Physics, Harvard University

NNIN REU Mentor(s): Maja Cassidy, Physics, Harvard University

Contact: dbreeves@colby.edu, marcus@harvard.edu, cassidy@fas.harvard.edu

## Introduction:

Nuclear magnetic resonance imaging (MRI) is a non-invasive medical imaging technique that uses a magnetic field to align protons in the body. By combining field gradients and radiofrequency excitation, three-dimensional images of proton density and nuclear spin lattice relaxation times (T1s) can be created [1]. The use of silicon (Si) nanoparticles as an imaging agent provides an alternative to conventional proton imaging that allows sensitive targeted imaging. They are hyperpolarizable [2], non-toxic and using silicon minimizes background noise problems because it is found in insignificant amounts in the body. T1 determines the time it takes for the nuclear polarization to return to its original orientation aligned with the field, and so determines the length of time that pre-hyperpolarized particles will be able to be imaged once injected into the body.

Various-sized crystalline nanoparticles were fabricated by ball-milling high resistivity ( $> 30 \text{ k}\Omega\text{cm}$ ) Si wafers. These particles were separated by centrifugation into different size distributions—confirmed by scanning electron microscopy (SEM). Hydrogen has been shown to passivate surface states at the Si/SiO<sub>2</sub> interface in nanocrystals [3]. We saw hydrogen passivation as a possible method to reduce imperfections and consequently increase T1. The nanoparticles were annealed (Jiplec Rapid Thermal Processor) under a forming gas mixture of 3% hydrogen and 97% nitrogen for 1 and 10 minutes at 350°C. Commercially available crystalline and amorphous nanoparticles were studied in the same manner for comparison.

## Experiment:

Silicon Quest boron-doped wafers were ground using mortar and pestle. The shards were massed to 9.6 grams using a digital balance and spun in a Retsch ball mill with ten, 1 cm diameter zirconium oxide balls for 10 minutes dry and then together with 20 mL of anhydrous ethanol for 4 more hours. The 1 cm balls were replaced with 40 grams of 2 mm diameter zirconium oxide balls and milled again for between 8 and 26 hours depending on the desired final nanoparticle size. The solution was sonified at 25% for 10 minutes in a Bronson Digital Sonifier and aliquotted into four 50 mL test tubes.

$$V_s = \frac{2(\rho_p - \rho_f)}{9\mu} g R^2$$

Equation 1: Stoke's Law.

The behavior of small spherical objects in solution can be described using Stoke's Law (Equation 1). Using this, we created a model to predict the expected size of particles remaining in solution after being spun in the centrifuge [4]. Stoke's Law has:  $V_s$  = the particles' settling velocity (m/s),  $g$  = the acceleration ( $\text{m/s}^2$ ),  $\rho_p$  and  $\rho_f$  = the mass densities of the particles and the fluid ( $\text{kg/m}^3$ ),  $\mu$  = the fluid's dynamic viscosity (in Pa s) and  $R$  = the particle diameter. The input parameters for our algorithm include the height of solution in tube compared to the radius of the centrifuge, revolutions per minute in the centrifuge, and time in seconds.

Centrifuge tubes were filled to 37.5 mL and spun for a time and speed determined by our model. Particles sized greater than our desired upper cutoff would be spun to the bottom of the tube (the pellet). The remaining liquid (supernatant) was poured out into a round bottom flask. The tube with pellet was filled with ethanol, sonified at 25% for 3 minutes and

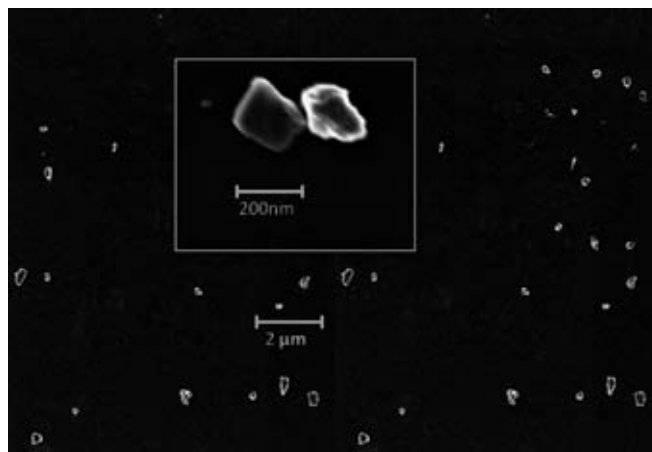


Figure 1: Sample SEM image of silicon nanoparticles average size 150 nm.

spun at the same parameters before pouring the supernatant out into the same flask. This whole procedure was repeated a third time. Then the supernatant was condensed using a rotary evaporator (Buchi) and divided into two test tubes, again at 37.5 mL. These tubes were spun such that sizes less than our lower cutoff would remain in the supernatant. This left a pellet of particles with sizes within the two estimated cutoffs. The supernatant was removed and replaced with ethanol. The tubes were spun for the lower limit six more times. The nanoparticle distributions were verified by scanning electron microscopy (see Figure 1). These procedures were also successfully applied to commercial nanoparticles.

We then annealed dried nanoparticles and characterized them using NMR spectroscopy. Approximately 0.5 g of dried particles were placed on a silicon wafer and tests were done in forming gas (3% hydrogen, 97% nitrogen) and also in pure nitrogen as a control. Time was varied from 1 to 10 minutes for heat (350°C) and gas exposure.

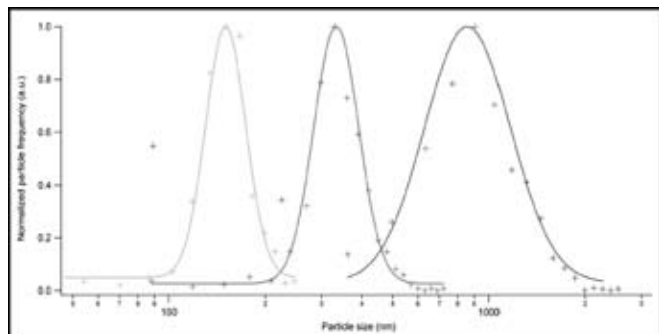


Figure 2: Normalized distributions of particles with average sizes of 150 nm, 350 nm, and 1000 nm.

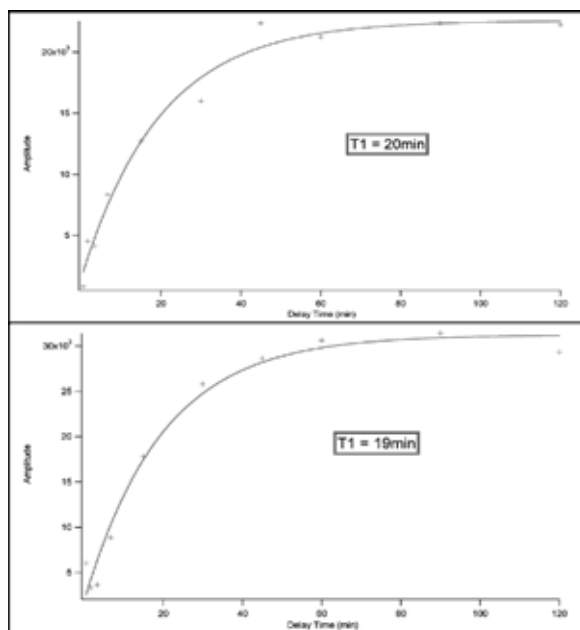


Figure 3: T1 measurements of forming gas annealed (a) and control (b) nanoparticles sourced commercially (American Elements).

## Results/Discussion:

Using the model we developed, we were able to obtain non-overlapping size distributions of particles using centrifugal separation, as shown in Figure 2. T1 measurements by NMR showed no increase after any of the tested annealing procedures, for either controlled-size or commercially available products (see Figure 3).

## Conclusions:

We have developed a repeatable procedure for centrifugal size separation that works on both on commercially synthesized and top-down fabricated silicon nanoparticles. Although some errors may have resulted from the use of two different NMR magnets and exposure to air, we believe that these factors would not have overshadowed any real improvement in T1 by annealing in forming gas. The ability to control size distributions of silicon nanoparticles is an important step in understanding the NMR properties of these particles, and also their impact on biological systems.

## Acknowledgements:

The author gratefully acknowledges Prof. Charles Marcus, mentor Maja Cassidy, Dr. Fettah Kosar, Chinh Vo and the Marcus Group for their valued assistance. The National Nanotechnology Infrastructure Network Research Experience for Undergraduates Program and the National Science Foundation generously provided the support and funding for these studies.

## References:

- [1] Weishaupt, D., K.chli, V., & Marincek, B. How does MRI work?; Springer: New York, 2003.
- [2] Demytyev, A., Cory, D., & Ramanathan, C. Dynamic Nuclear Polarization in Silicon Microparticles. *Phys. Rev. Lett.* 100, 127601 (2008).
- [3] Edwards, A. Interaction of H and H<sub>2</sub> with the Silicon Dangling Orbital at the {111} Si/SiO<sub>2</sub> Interface. *Phys. Rev. B.* 44, 1832-1838 (1991).
- [4] Batchelor, G. An Introduction to Fluid Dynamics. Cambridge University Press: New York, 1967.

# Metal Oxide Thin Films for LED Applications

Stephen Rudisill

Chemistry, Beloit College, WI

**NNIN REU Site: Minnesota Nanotechnology Cluster, University of Minnesota-Twin Cities, Minneapolis, MN**

NNIN REU Principal Investigator(s): Stephen A. Campbell, Electrical Engineering, University of Minnesota

NNIN REU Mentor(s): Gagan Aggarwal, Electrical Engineering, University of Minnesota;

Margaret Broz, Chemical Engineering/Materials Science, University of Minnesota

Contact: s.g.rudisill@gmail.com, campb001@umn.edu, aggar014@umn.edu, broz@cems.umn.edu

## Abstract:

Electroluminescence (EL) of silicon nanoparticles (Si NPs) holds promise for a new generation of light-emitting diodes (LEDs). While recently reported values for EL efficiency max out at around 1.6% [1], these numbers could be increased via improvement of charge delivery to the particles—optimization of the electron and hole transport layers (ETL, HTL). For the HTL, thin films of ZnO and Al-doped ZnO (AZO) were deposited on glass and silicon substrates via atomic layer deposition (ALD). Films' physical and electrical properties were determined by means of Auger electron spectroscopy (AES), atomic force microscopy (AFM), UV-VIS spectroscopy, profilometry, ellipsometry, and four-point probe measurements; resistivities in the range of  $1.75 \times 10^{-3} \Omega\text{cm}$  were achieved while maintaining an 85% transparency across the visible spectrum. For the ETL, thin films of NiO and  $\text{WO}_3$  were deposited in an RF plasma sputtering system. Deposition rates for each oxide were determined and tuned to be within range of each other for future co-deposition experiments. Oxygen concentration in process gases was found to have a significant impact on NiO film quality and deposition rates. Further investigation of the films and their properties is necessary to begin device construction.

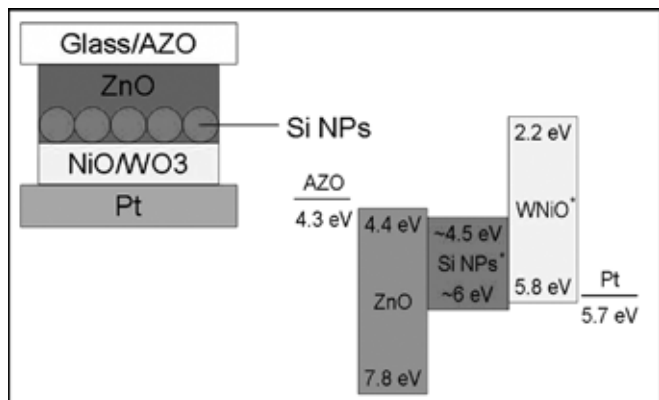


Figure 1: Theoretical device construction, including band gap data (some projected values).

## Device Structure:

Electroluminescence requires hole-electron recombination within a semiconducting material. Thus, producing an efficient LED necessitates a series of layers to generate holes and electrons and transport them to the luminescent material for recombination. Figure 1 demonstrates a theoretical construction of this device. It should be noted that the band gaps for WNiO and Si NPs are projected values that will hopefully be obtained through further experimentation.

## Experimental Procedures:

**Atomic Layer Deposition.** Thin films of Al-doped ZnO (AZO) were deposited on glass and silicon substrates via atomic layer deposition (ALD) in a Cambridge Nanotech Savannah ALD system. All laboratory work took place in a class 10 clean room. Substrates were sonicated for 10 min in each of the following solvents: deionized water, acetone, methanol, and isopropanol, then cleaned in an ozone atmosphere for 5 minutes (to produce a hydrogen-terminated surface) before

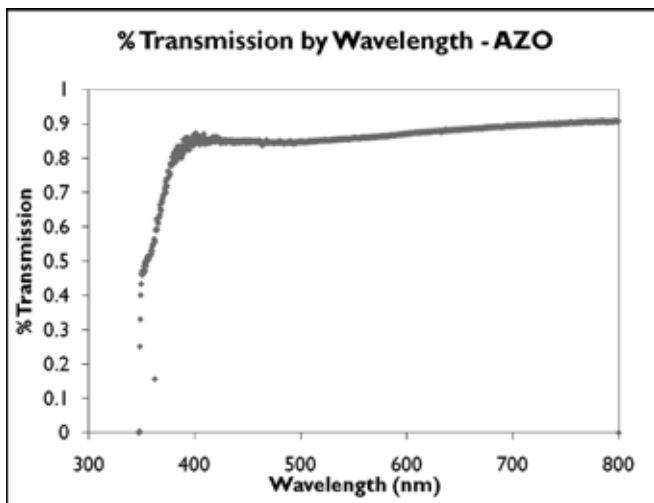


Figure 2: Optical transmittance of a ~50 nm AZO film (30:1) measured with a UV-VIS spectrometer.

being transferred to the ALD system. The precursor gases—trimethyl aluminum (TMA), diethyl zinc (DEZ), water vapor ( $\text{H}_2\text{O}$ )—were pulsed at 0.015 s, with a purge time of 5 s in 40 sccm of  $\text{N}_2$  at  $180^\circ\text{C}$ . Doping ratios were varied from 10:1 to 50:1 ( $\text{ZnO}:\text{Al}_2\text{O}_3$ ). Samples were characterized with single-wavelength ellipsometry, AFM, four-point probe, and AES.

**RF Sputtering.** Thin films of NiO and  $\text{WO}_3$  were deposited on quartz and silicon substrates via RF-regulated plasma sputtering in an AJA ATC 2000 sputter system. Substrates were cleaned via the method detailed above, with the exception of the ozone cleaning. Deposition rates were determined by measuring film thickness via single-wavelength ellipsometry.

## Results and Conclusions:

Figure 2 shows light transmission through the AZO thin film, which is 85% or greater throughout the visible spectrum. A 30:1 doping ratio maintained this transparency while having resistivities as low as  $1.75 \times 10^{-3} \Omega/\text{cm}$ . This is comparable to low resistivity values found in the literature for these films,  $9.7 \times 10^{-4} \Omega/\text{cm}$  [2]. Films produced by this method are very smooth, exhibiting RMS roughness values of  $\sim 1$  nm. Doping ratios and film purity were verified by AES, showing virtually no contamination in the deposition process. These results are very promising for both charge transport and device integration.

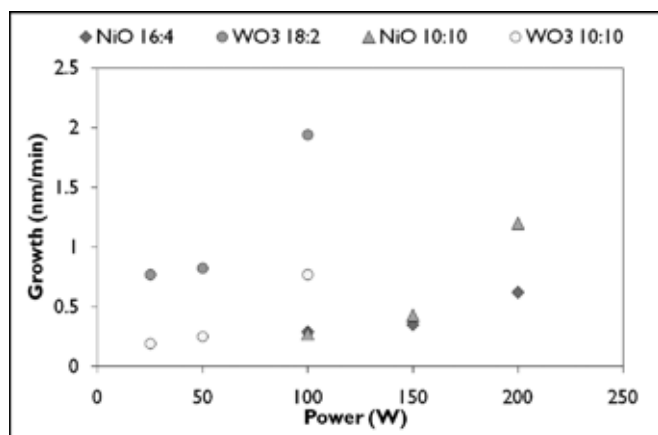


Figure 3: Deposition of metal-oxide films by an RF sputtering process. Atmosphere ratios ( $\text{Ar}:\text{O}_2$ ) given in sccm.

Figure 3 illustrates deposition rate trends for the NiO and  $\text{WO}_3$  films sputtered in different atmospheres of  $\text{Ar}:\text{O}_2$ . Ideally, NiO and  $\text{WO}_3$  deposition rates would be identical within a certain range of wattages. With higher Ar concentrations, we found high rates of  $\text{WO}_3$  deposition and low rates of NiO deposition. When the  $\text{O}_2$  concentration in the sputtering atmosphere was increased, the  $\text{WO}_3$  deposition rate decreased and the NiO deposition rate increased. This brought the two rates more in line with each other, below our system's upper limit of 200 W.

## Future Work:

The deposition rate tuning detailed above paves the way for deposition and characterization of various  $\text{WO}_3/\text{NiO}$  alloys. Tuning the alloy ratios should lead to variations in the HTL material's band gap, which can then be optimized for the device. Further work should lead to a functional inorganic device, which will, in the best scenario, exceed previously disappointing electroluminescence efficiencies for Si NPs.

## Acknowledgements:

The author would like to thank Dr. Stephen Campbell, Gagan Aggarwal, Margaret Broz, and Rick Liptak for their help, advice, and guidance. The author also gratefully acknowledges the National Nanotechnology Infrastructure Network Research Experience for Undergraduates Program and the National Science Foundation for their generous funding and support. Finally, most of this work was carried out in the Institute of Technology Characterization Facility and Nanoscale Fabrication Center, University of Minnesota, which also receive partial support from NSF through the NNIN program.

## References:

- [1] K. Cho, N. Park, T. Kim, K. Kim, and G. Sung, Appl. Phys. Lett. 86, 071909 (2005).
- [2] S. Kwon, H. Lee, Y. Seo, H. Jeong, J. Kor. Phys. Soc. 43; 5. p. 709-713 (2003).

# Capillarity-Based Reversible Super-Adhesion

Sarah Grice

Mechanical Engineering, University of Maryland, College Park

**NNIN REU Site: Cornell NanoScale Science and Technology Facility, Cornell University, Ithaca, NY**

*NNIN REU Principal Investigator(s): Prof. Paul Steen, Chemical Engineering, Cornell University*

*NNIN REU Mentor(s): David Anderson, XiuMei Xu, Chemical Engineering, Cornell University*

*Contact: sgrice@umd.edu, phs7@cornell.edu, anderson.da@gmail.com, xx44@cornell.edu*

## Abstract:

This project draws inspiration from the palm beetle's defense mechanism by creating an adhesion pad in which a large array of water droplets is controlled by an electro-osmotic pump to achieve reversible super-adhesion. In order to enhance the adhesion performance, three modifications were made to a previous design. First, the droplet diameters were reduced from the previously fabricated 150-500  $\mu\text{m}$  hole devices to 50-100  $\mu\text{m}$ , which allows more liquid bridges per unit area and thereby increases the adhesion force. Second, a raised frame around the array was fabricated to allow easy detachment and is a first step in optimizing the liquid bridge length during attachment. Third, the depth of the water reservoir was varied. The functionality of these devices was tested.

## Introduction / Background:

The palm beetle defends itself from predators by using small droplets of oil that it manipulates using the bristles of its tarsi. These droplets form liquid bridges with a substrate leaf, allowing the beetle to stick with a force equivalent to approximately 60-100 times its body weight. When the danger has passed, the beetle can then break these liquid bridges and continue on its way, leaving behind small amounts of oil residue.

This strategy is ideal for creating reversible adhesion, which has been accomplished by creating adhesion pads that use large arrays of droplets of water in place of the palm beetle's oil. Such devices are predicted to increase in the adhesive force per unit area they can exert as the droplet size is decreased. However, scaling features down in size is a significant fabrication challenge.

## Objectives:

The goal of this project was to create a new generation of adhesion pads that would reduce the droplet diameter from 100  $\mu\text{m}$  to 50 and 75  $\mu\text{m}$ . Two variations on the basic design of the adhesion pad were also fabricated: first, a raised lip or frame around the array of holes was created on half the plates created, and second, the depth of the water reservoir was varied.

## Device Design and Operation:

The adhesion pad consists of a sandwich of silicon plates with an array of holes fabricated in them using a reactive ion etcher (Labels 1 and 5 in Figure 1). These plates are coated on their inside-facing sides with a thin gold electrode (Labels 2

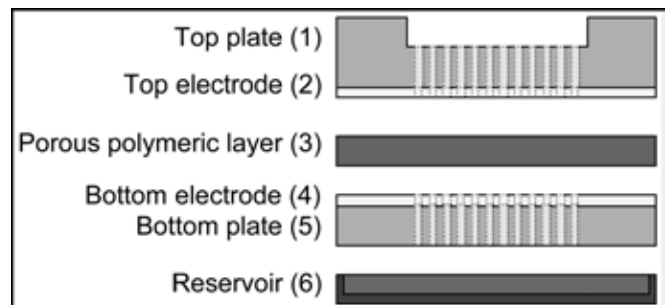


Figure 1: Adhesion pad design.

and 4). A porous polymeric layer—in the case of the devices fabricated, made of polyethersulfone, or PES—is placed between the plates (3), and a small reservoir of water (6) is attached to the bottom.

When a voltage is applied across the electrodes, electro-osmosis, enhanced by the small pores of the PES layer, pulls water up from the reservoir and forces it out of the holes in the top plate. This creates an ordered array of droplets, which may then contact a substrate and form liquid bridges.

## Fabrication and Testing:

Three adhesion devices were assembled: (1) a 75  $\mu\text{m}$  unframed device with a 6 mm deep reservoir, (2) a 50  $\mu\text{m}$  framed device, and (3) a 75  $\mu\text{m}$  unframed device with a 2 mm deep reservoir.

Two types of tests were performed on the devices: syringe-pumped tests and electro-osmosis-pumped tests. In the first

case, water was forced into the device's reservoir using a syringe and tube arrangement. In the second case, voltage was applied across the PES layer so that electro-osmosis could be used to move the water.

## Results:

**Syringe-Pumped Testing.** Difficulties in assembly and testing made overall array uniformity difficult to achieve with syringe testing. Pump condition and position proved especially important to overall performance, as porous layer misalignment resulted in the formation of abnormally large droplets.

In comparing their performance during syringe pumping, the shallow (2 mm) and deep (6 mm) reservoir devices were shown to have roughly comparable droplet distributions after variations in assembly are discounted, as can be seen in Figures 2 and 3. This performance is surprising because the reservoir depth at which significant variation in droplet height from the edge to the center of the array was predicted to be around 2 mm.

**Electro-Osmosis-Pumped Testing.** Of the three devices tested, two of the electro-osmotic (EO) pumps were functional. In the case of the 50  $\mu\text{m}$  framed device, EO pumping resulted in significantly better performance than syringe pumping, as holes or folds in the PES layer did not result in large droplets, as can be seen in Figure 4. EO pumping the 75  $\mu\text{m}$  shallow reservoir device did not provide as much of an improvement in performance, and in fact seemed to increase the incidence of large droplet formation.

## Conclusions and Future Work:

50  $\mu\text{m}$  and 75  $\mu\text{m}$  droplet diameter adhesion pads were fabricated, and initial tests of their functionality were carried out. These devices were found to have the best performance characteristics when operated using their integrated EO pump at relatively low voltages. The performance of shallow and deep reservoir devices during syringe pumping was found to be comparable after accounting for variations in assembly such as frit misalignment.

In the future, adhesion measurements of the assembled devices will be performed, determining how much adhesion force per unit area was gained relative to the reduction in droplet size.

## Acknowledgements:

I would like to thank my wonderful PI, Prof. Paul Steen, and awesome mentors, David Anderson and Xiumei Xu, for all their support and encouragement during my time at Cornell. I would also like to acknowledge the National Nanotechnology Infrastructure Network Research Experience for Undergraduates Program and the National Science Foundation for helping to make this experience possible for me.

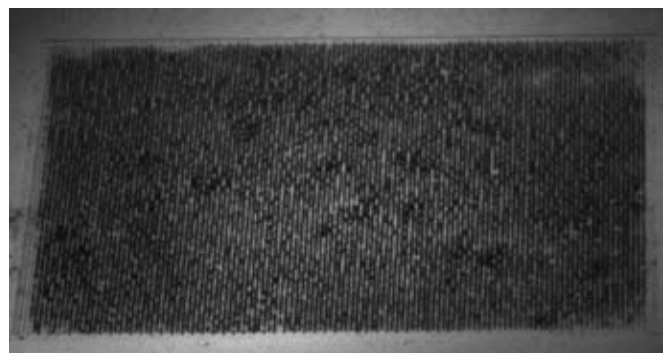
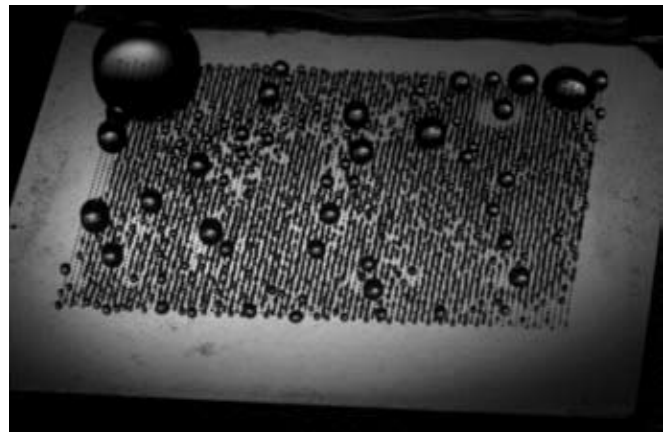
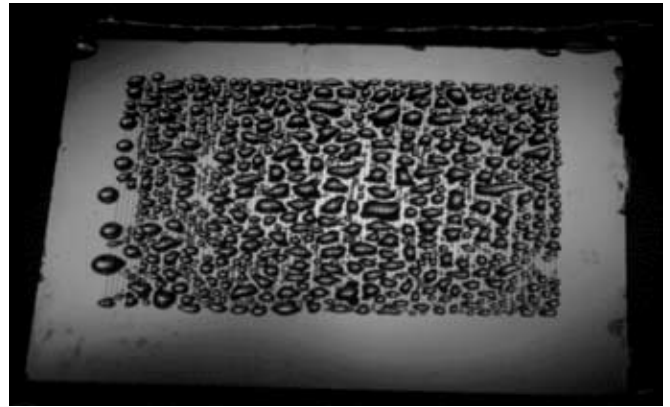


*Figure 2, top: 75  $\mu\text{m}$  shallow reservoir device, syringe pumped (photographed using a macro lens).*

*Figure 3, middle: 75  $\mu\text{m}$  deep reservoir device, syringe pumped (photographed using a macro lens).*

*Figure 4, bottom: 50  $\mu\text{m}$  deep reservoir device, EO pumped (photographed using a macro lens).*

# Fabrication of a Microelectromechanical Device for On-Chip Mechanical Testing of Nanoscale Thin Films in a Transmission Electron Microscope

Sarah Koehler

Mechanical Engineering, Cornell University

**NNIN REU Site: Penn State Nanofabrication Facility, The Pennsylvania State University, State College, PA**

NNIN REU Principal Investigator(s): Dr. Aman Haque, Mechanical and Nuclear Engr, The Pennsylvania State University

NNIN REU Mentor(s): Mohan Manoharan, Mechanical and Nuclear Engr, The Pennsylvania State University

Contact: smk269@cornell.edu, mah37@engr.psu.edu, mxm1002@psu.edu

## Abstract:

Typically, deformation and failure mechanisms in materials and interfaces are studied either quantitatively (measuring stress-strain behavior) or qualitatively (post-mortem or off-line imaging with a microscope). The transmission electron microscope (TEM) is unique in the sense that it visualizes specimen microstructures (dislocations, grain boundaries, precipitates, cracks) with very high resolution. Therefore, if experiments could be conducted *in situ* inside a TEM, we could avoid ‘modeling’ as the tool for bridging the mutual exclusiveness of the quantitative and qualitative streams of materials behavior research. Unfortunately, the TEM chamber is very small; it allows a volume of 3 mm diameter and 0.5 mm thickness in which the specimen and the force and displacement sensors must be accommodated.

The objective of this research is to shrink an entire tensile testing machine (on the order of meters) to 3 mm diameter size using nanofabrication techniques. Such drastic miniaturization involves photolithography, thin film deposition and bulk micromachining techniques on both sides of a silicon-on-insulator (SOI) wafer.

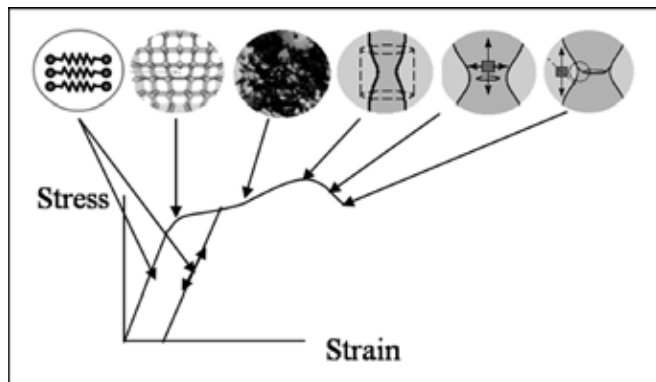


Figure 1: How materials fail—qualitatively and quantitatively.

## Introduction:

Figure 1 includes a typical graph of stress versus strain that shows quantitative material deformation. The linear portion of the curve is the elastic region, where material deformation is reversible and the material acts much like an elastic spring. The non-linear portion of the curve is the plastic region, where deformations are irreversible, and dislocations have occurred in the material. The pictures above the graph demonstrate qualitative analysis of material deformation. We would like to be able to match up this qualitative and quantitative data better than we have previously been able to using post-mortem techniques.

The devices that we design for this purpose have to be capable of straining a nanoscale thin film while in the TEM. The design utilizes a thermal actuator to place a tensile load on the specimen. The thermal actuator consists of pairs of micro-beams, as seen in the right hand side of Figure 2. To actuate, a voltage is applied across the ends of the inclined beams actuator. This causes the beams to heat and expand. The beams are inclined so that the net force on the specimen (once the beams expand) is to the right in Figure 2.

Another important feature of the device is that it has a hole etched through the backside. This is needed because the TEM passes electrons through a specimen in order to acquire an

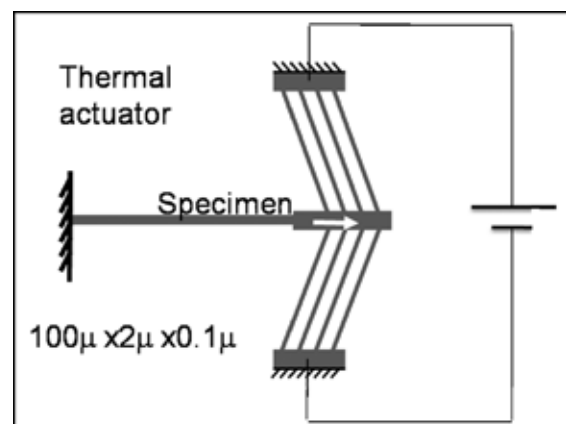


Figure 2: Diagram of thermal actuator.

image. The thick silicon layer is “opaque” to electrons, so it is important to have a nanoscale thin film that is free-standing above the backside hole.

### Experimental Procedure:

The procedure for fabricating the devices consists of multiple lithography and etching steps. The devices were made on a silicon-on-insulator (SOI) wafer. The wafer consists of a 35  $\mu\text{m}$  silicon device layer, a 1-2  $\mu\text{m}$  silicon dioxide layer, and a 350  $\mu\text{m}$  silicon handle layer. Before lithography processes begin, a metal layer on the order of nanometers was deposited on top of the device layer.

First, a 100 nm metal layer was evaporated onto the front side of the wafer. Next, the front side of the device was patterned using the Karl Suss MA 6/BA 6 lithography tool. The metal was then etched, and the silicon device layer was etched using deep reactive ion etching (DRIE). After these steps, the device was essentially complete except for the backside hole that is required for imaging in the TEM.

To etch the backside hole, a circular-shaped hole was patterned on to a thick photoresist (SPR 220-7) using the backside alignment technique in the Karl Suss MA 6/BA 6. DRIE was used again for anisotropic backside etching. The oxide was then etched anisotropically using the Plasma Therm. DRIE was again used to etch the device layer just underneath the specimen so that it would be freestanding. Finally, HF vapor was used to release the beams for mobility.

### Results and Conclusions:

We were able to etch the frontside of several devices, but had more difficulty fabricating the backside hole. We were able to produce SEM compatible devices to nearly one hundred percent yield, but the backside hole required for TEM compatibility was more difficult to fabricate. The backside etching was a problem because the wafer broke easily during backside DRIE. The residual stress of the SOI wafer was a big factor contributing towards the breakage.

We were able to etch through the handle layer using a xenon difluoride ( $\text{XeF}_2$ ) isotropic etch of silicon, and we completed the first backside etching of the device. Figure 4 shows the backside of a device that was successfully etched and we can see through the optically transparent silicon dioxide layer to the beams on the front side that attach the device to the SOI wafer.

### Future Work:

We plan to continue developing a better method to etch the backside hole of the device. We will continue to etch isotropically with xenon difluoride, and may try a different mask with a smaller backside hole so that an isotropic etch is anticipated. Once the devices are successfully made, we will then do simultaneous quantitative and qualitative testing in the TEM.

### Acknowledgements:

I would like to thank my principal investigator Aman Haque, my mentor Mohan Manoharan, and other members of our research group. Also, thanks to members of the Pennsylvania State University Nanofabrication Staff. I would also like to thank the National Nanotechnology Infrastructure Network Research Experience for Undergraduates Program and the National Science Foundation for funding.

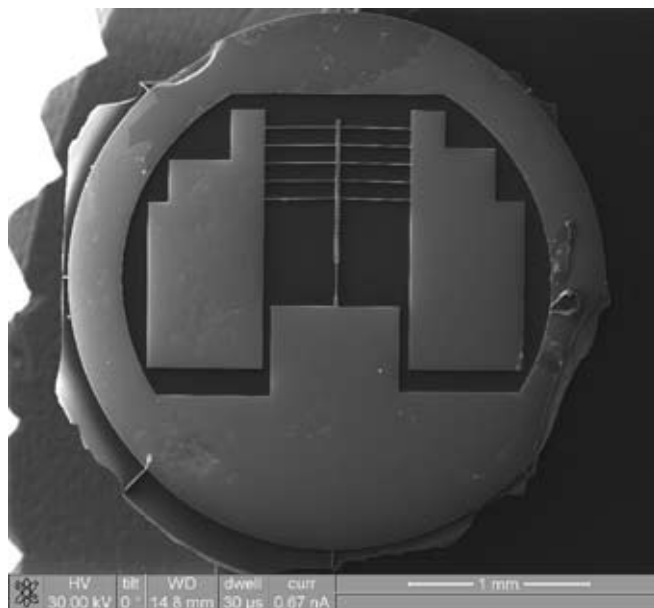


Figure 3: SEM image of a device.



Figure 4: Backside image of a device with isotropically etched handle layer.

# Optimization of MEMS Fabrication for Electrical Detection

Joshua Ott

Electrical Engineering, Southern Methodist University



**NNIN REU Site: Cornell NanoScale Science and Technology Facility,  
Cornell University, Ithaca, NY**

NNIN REU Principal Investigator(s): Harold Craighead, Applied and Engineering Physics, Cornell University

NNIN REU Mentor(s): Darren Southworth, Josh Cross, Applied and Engineering Physics, Cornell University

Contact: hgc1@cornell.edu, drs59@cornell.edu, jdc47@cornell.edu

## Abstract:

The much-celebrated potential of resonate microelectromechanical systems (MEMS) in sensing and electrical filter technologies has been limited by convenient methods of device readout. Our purpose is to optimize MEMS devices for electrical detection, enabling integration into real-world devices. We fabricated device arrays in which the parameters of etch orifice size, sacrificial oxide thickness, and device geometry were varied in order to maximize electrical coupling.

## Introduction:

MEMS resonant technology is used for biological sensing and electric filtering technologies. These resonators have a certain resonance frequency. Shifts in resonant frequency from accretion of mass onto the device, for example, could indicate the presence of an analyte. We are developing an electrical method of resonance frequency detection. Historically, these resonators lack convenient methods of device readout. Some methods require large apparatus' such as superconducting magnets or aligned optics. With the advent of electrical detection we have a means for real-world integration of these devices since the simple circuitry required lends itself to packaging. All that is required is a capacitor and inductor.

In the past, electrical readout was limited by small signal detection. We fabricated device arrays with varied resonator geometries in attempt to increase the signal. The goal of these geometries was to reduce the motional resistance, which is the figure of merit in our experiment.

$$R_m = \frac{d^2 m \omega_0}{V_g^2 C_g^2 Q}$$

Figure 1: Motional resistance equation.

The motional resistance equation can be seen in Figure 1. Variable  $d$  is the sacrificial oxide thickness,  $m$  is the resonator mass,  $\omega_0$  is the angular frequency,  $V_g$  is the voltage applied to the resonators,  $C_g$  is the resonator capacitance, and  $Q$  is the quality factor.

We attempted to reduce motional resistance by changing the resonator geometries and etch hole orifices, which altered the variables  $m$ ,  $\omega_0$ , and  $C_g$ . We also grew varying oxide thicknesses, which reduced the distance ( $d$ ) and increased the capacitance ( $C_g$ ). The resulting correlations gave the oxide

thickness a fourfold effect on the motional resistance, making it one of the most important aspects of our devices. However, if we created a thickness too thin, the devices would not resonate properly and stick to the silicon wafer.

## Experimental Procedure:

An array of devices, including different geometries and different etch hole sizes, were fabricated on each die. The etch holes were created using a reactive ion etch. A buffered oxide etch was then used to release the resonators from the oxide.

The most important devices from fabrication were our "drums," a flat membrane with a single etch hole. This device can be seen in Figure 2. The light areas correspond to where the device is released from the wafer. The drums were created with etch hole diameter's varying from 2-10  $\mu\text{m}$ , in 2  $\mu\text{m}$  increments. Actual membrane diameters measured

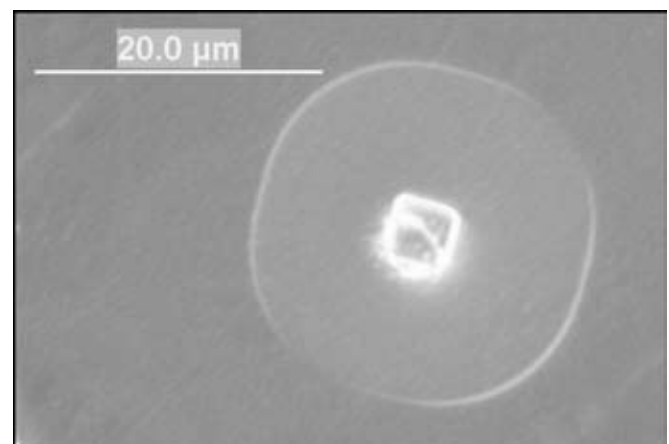


Figure 2: 4  $\mu\text{m}$  etch hole drum resonator.

approximately  $20\ \mu\text{m}$ . The drums were comprised of polysilicon grown on silicon dioxide. The polysilicon was  $\text{N}^+$  doped, made tensile (in order to create a flat membrane) and grown to approximately 330 nm. Oxide thicknesses of 645, 223, and 95 nm were the targets, with 223 nm being the only viable resonator.

An LC impedance matching circuit was used to detect the electrical signal. The resonators were placed under vacuum. By interchanging capacitors and inductors, the circuit was matched to the resonance frequency of each resonator. Using LabView, the quality factor and resonance frequency was then calculated. With these variables we did back calculations to get the motional resistance.

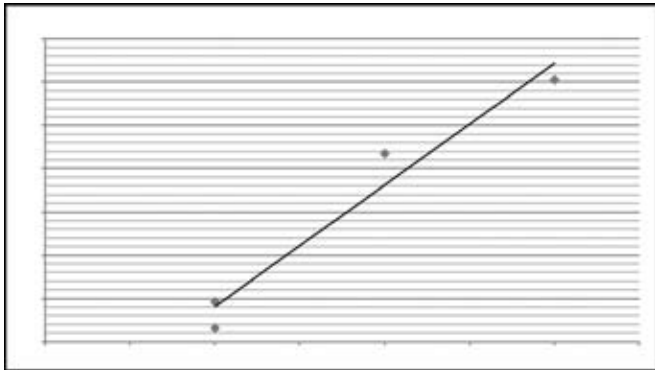


Figure 3: Motional resistance vs. etch hole diameter.

### Results and Conclusion:

There was a definite trend when comparing etch hole diameter and signal strength. As etch hole size was decreased so did motional resistance (Figure 3), which indicates that a smaller etch hole produces a larger signal. We also discovered that the quality factor of our devices was independent of etch hole size. The actual drum diameter was independent of etch hole size as well.

### Future Work:

Since the largest factor for motional resistance is oxide thickness, it is our greatest chance for increasing the signal. Therefore, going for an even smaller oxide thickness would increase the signal. Work could also be done to create an even smaller etch hole to see the results: a larger increase in signal power, no increase in signal power, or simply diminishing return in signal power. Lastly, multi-hole membranes should be studied to see how their geometries affect the electrical signal.

### Acknowledgments:

I would like to thank the National Science Foundation and, in particular, the National Nanotechnology Infrastructure Network, for allowing me to be involved in this REU program, and the Intel Foundation for sponsoring my research. I would like to thank Harold Craighead for his support, and Darren Southworth and Josh Cross for their assistance. Acknowledgment is also given to the Cornell NanoScale Facility Staff, especially Melanie-Claire Mallison.

# Enhanced Light Emission Using Plasmonic Gold Nanoparticles

Damian Ancukiewicz

Applied Physics, Columbia University

**NNIN REU Site: Nanoscience @ UNM, University of New Mexico, Albuquerque, NM**

NNIN REU Principal Investigator(s): Prof. Ravi Jain, Center for High Technology Materials (CHTM), UNM

NNIN REU Mentor(s): Jiayu Chen, CHTM, University of New Mexico; Li Wang, CHTM, University of New Mexico

Contact: da2260@columbia.edu, jain@chtm.unm.edu, jychen@ece.unm.edu, liwang@unm.edu

## Abstract/Introduction:

Gold nanoparticles with diameters of approximately 5-100 nm can exhibit localized surface plasmons, which are quantizations of oscillations in the electric field and charge distribution of the particles. We attempted to use such “plasmonic” nanoparticles to enhance the emission intensity of two phenomena: quantum dot fluorescence and light emission from metal-insulator-metal (MIM) tunnel junctions (TJs), as elaborated below.

(1) One goal of this project was to enhance the fluorescence of quantum dots, which hold promise for medical imaging, by taking advantage of the strong local electric field around metallic nanoparticles. In this project, enhancement was attempted using 50 nm gold nanoparticles, ~ 5 nm CdSe/ZnS quantum dots and a 10 nm SiO<sub>2</sub> spacer layer between the two to minimize fluorescence quenching. The intensity and rate of fluorescence was observed to increase by approximately two-fold.

(2) In a tunnel junction, electrons tunnel through a thin oxide layer placed between two metals with a potential difference. Lambe and McCarthy [1] observed light emission from Al/Al<sub>2</sub>O<sub>3</sub>/Au junctions roughened with the use of a MgF<sub>2</sub> layer, due to coupling of surface plasmons generated by tunneling electrons to light.

In this project, gold nanoparticles (Au-NPs) were investigated as a means of increasing the surface roughness of TJs to enhance light emission. Several Au-NP deposition methods were attempted, but in all cases the emission intensity was insufficient to obtain spectra before or after deposition. Nevertheless, unusual light emission characteristics were observed from TJs roughened with MgF<sub>2</sub>.

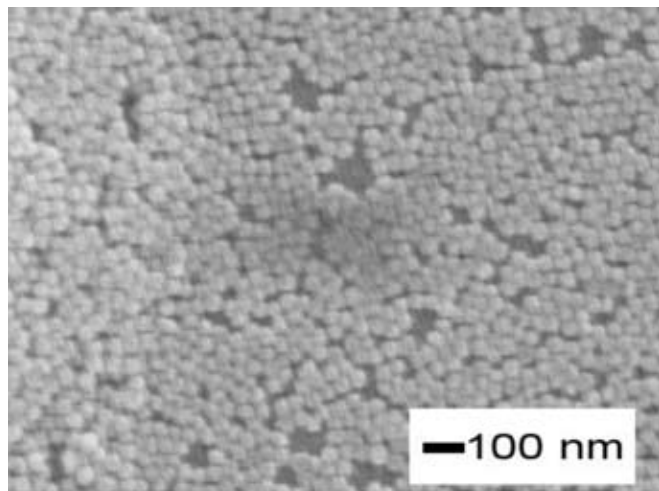


Figure 1: SEM of a 50 nm Au nanoparticle layer deposited by a droplet evaporation method.

## Experimental Procedure:

To enhance quantum dot fluorescence, arrays of quantum dots and nanoparticles were built. First, cadmium selenide (CdSe)/zinc sulfide (ZnS) quantum dots with an absorption peak of 522 nm were spin-coated onto a glass slide. Next, a 10 nm

spacer layer of silicon dioxide (SiO<sub>2</sub>) was deposited on top of the previous layer using evaporative deposition. Finally, a layer of 50 nm gold nanoparticles (Au-NPs) was deposited using several different methods. The simplest successful method consisted of putting a droplet of Au-NPs in ethanol solution on the desired surface and evaporating the solvent quickly using a microwave oven. Figure 1 shows a scanning electron microscope (SEM) image of such a deposited layer (using 50 nm Au-NPs).

Fluorescence spectra were measured using a monochromator, photomultiplier tube (PMT) and a lock-in amplifier. The fluorescence rates were also measured in order to verify enhancement. To accomplish this, phase fluorometry was used: a blue (465 nm) light-emitting diode (LED) was modulated at frequencies of 1-5 MHz, and the phase shift between the modulated excitation light and the resulting fluorescence was used to calculate the fluorescence rate.

To test tunnel junction light enhancement, Al/Al<sub>2</sub>O<sub>3</sub>/Au TJs were constructed using the same procedure as Lambe and McCarthy [1]. 10 nm nanoparticles were deposited onto several TJs using two methods. In the first method, a droplet of nanoparticles in ethanol solution was simply placed onto the junction. The second method involved using a method developed by Pang et. Al [2] in which nanoparticles in poly-(dimethylsiloxane) (PDMS) form a monolayer on a water

interface. Other TJs were “roughened” by first evaporating a rough  $\text{MgF}_2$  layer (with an rms period of  $\sim 100$  nm) onto the substrate and constructing the TJ on top of this “roughened” substrate.

The junctions were connected to a voltage source, with a positive bias applied to the gold side, and light emission was observed. Light emission spectra were measured at different excitation voltage.

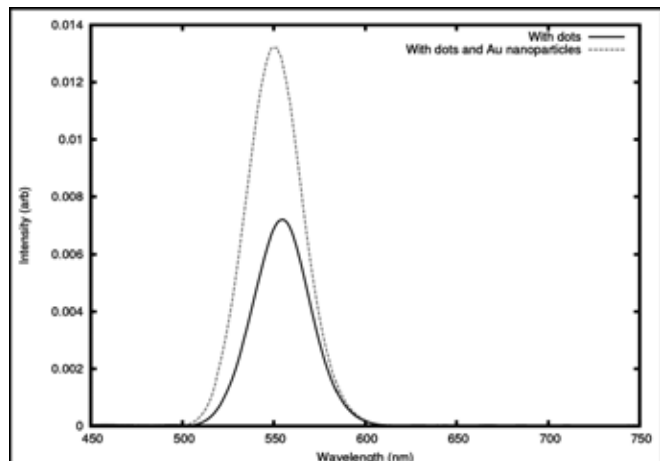


Figure 2: Fluorescence spectra of 522 nm CdSe/ZnS quantum dots (QDs) with and without 50 nm Au nanoparticles (Au-NPs) and a 15 nm spacer layer between the QDs and the Au-NPs.

### Results and Conclusions:

Figure 2 shows fluorescence spectra of the quantum dots with and without the Au-NP layer. An approximately two-fold increase in fluorescence intensity is evident. Additionally, preliminary phase fluorometry results indicate that the fluorescence rate of the quantum dots increased from approximately  $8 \times 10^7 \text{ s}^{-1}$  to approximately  $13 \times 10^7 \text{ s}^{-1}$ , presumably due to increased coupling to the Au-NPs.

Measurement of tunnel junction emission enhancement was less successful; the intensity of the light outputs from “nominally” smooth junctions with Au-NPs was too low to measure reliably. However, as stated above, the brighter light emission obtained from junctions roughened with  $\text{MgF}_2$  was easier to quantify with spectral measurements. Some of these junctions exhibited an interesting phenomenon; their light output intensity and spectra changed drastically as the excitation voltage increased to 4.1 V, as seen in Figure 3. However, the shape of the spectra characteristics did not revert back to the originally observed spectra when the voltages were subsequently lowered, suggesting a permanent change, possibly caused by heat or high current density.

### Future Work:

Further enhancement of quantum dot fluorescence should be achievable by optimizing the  $\text{SiO}_2$  spacer thickness or the type and sizes of quantum dots and Au-NPs used. Moreover improved theoretical models need to be developed.

Further methods of nanoparticle deposition on tunnel junctions should be evaluated in order to attempt to obtain spectra. In addition, the spectral shift observed on some junctions should be investigated in order to determine the structural changes involved.

### Acknowledgments:

I would like to thank my mentors, Jiayu Chen and Li Wang, as well as my PI, Prof. Ravi Jain, for guiding me with this project. Additionally, I would like to thank the National Nanotechnology Infrastructure Network Research Experience for Undergraduates (NNIN REU) Program and the University of New Mexico for giving me the opportunity to conduct this exciting research.

### References:

- [1] Lambe, J. and McCarthy, S.L; “Light Emission from Inelastic Electron Tunneling”; Phys. Rev. Lett. 37, 923 (1976).
- [2] Pang J. et. al; “Free-Standing, Patternable Nanoparticle/ Polymer Monolayer Arrays Formed by Evaporation Induced Self-Assembly at a Fluid Interface”; J. Am. Chem. Soc. 130, 3284 (2008).

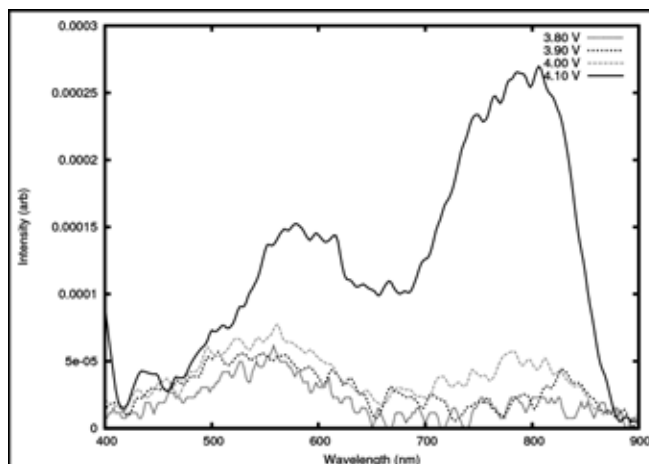


Figure 3: Emission spectra of a  $\text{MgF}_2$  roughened  $\text{Al-Al}_2\text{O}_3$ -Au tunnel junction as a function of the voltage applied across the junction.

# Do Silicon Nanoparticles Exhibit Optical Gain?

Justin Foley

Applied Physics and Civil Engineering, Michigan Technological University

**NNIN REU Site: Minnesota Nanotechnology Cluster, University of Minnesota-Twin Cities, Minneapolis, MN**

*NNIN REU Principal Investigator(s): Dr. Anand Gopinath, Electrical Engineering, University of Minnesota*

*NNIN REU Mentor(s): Jaesong Oh, Richard Liptak, Electrical Engineering, University of Minnesota;*

*Jonathon Hinke, Chemistry, University of Minnesota*

*Contact: foley209@umn.edu, gopinath@umn.edu, ohxx0058@umn.edu, lipt0010@umn.edu, hink0075@umn.edu*

## Abstract:

Room temperature photo-luminescent (PL) silicon nanoparticles (Si-nps) have been shown to emit across the visible light spectrum (400-800 nm) and have been used in light emitting diodes (LEDs). These same particles may be used as the active medium in a laser if they exhibit optical gain. This research focuses on determining if these particles produce net stimulated emission by utilizing a frequency doubled titanium-sapphire laser in a pump-probe configuration. With a pump wavelength of 400 nm and a probe of white light incident on a solution of hydrosilylated Si-nps in toluene, absorption across spectrum dominates any stimulated emission present.

## Introduction/Background:

The focus of this research is whether photo-luminescent (PL) silicon nanoparticles (Si-nps) exhibit enough optical gain to produce a lasing medium. The Si-nps tested are created through silane ( $\text{SiH}_4$ ) plasma by Dr. Stephen Campbell's and Dr. Uwe Kortshagen's groups, both of the University of Minnesota. Unlike bulk silicon that does not emit light because of its indirect band gap, these particles emit across the visible spectrum when optically excited [1]. The emission spectrum is dependent on the particle's size: the smallest particles at 3 nm emit blue light while larger particles, 5-6 nm, emit red light [1]. The size of the particle is determined by the residence time within the initial plasma and whether or not there is an etching plasma. The residence time is altered by changing the flow rates of the  $\text{SiH}_4$  and Argon (Ar) in the initial plasma and etching requires a sulfur hexafluoride ( $\text{SF}_6$ ) plasma [1]. As the wavelength decreases so does the quantum yield (QY): deep red ( $> 800$  nm) QYs of 70% have been realized and blue QYs rarely reach 5% [1,2]. These particles have been used in light emitting diodes (LEDs) but because of the poor electro-luminescence of the Si-nps efficiencies are  $< 2\%$  [3,4]. Because these Si-nps have high quantum efficiencies they are proposed to exhibit enough optical gain to allow an optically pumped laser to be produced.

## Experimental Methods:

To test for the optical gain of these Si-nps, a solution of the particles was opted for testing procedures. Suspending the Si-nps in toluene required the particles to be hydrosilylated which is accomplished with the use of the ligand dodecene [2]; this process replaces the hydrogen terminated surface of the Si-nps with carbon disallowing the particles to aggregate. The dried, oxygen-free hydrosilylated particles were then

suspended in toluene with a necessary optical density of approximately 0.2dB in a 1 mm static cell at 400 nm.

Several samples of particles were utilized to determine the concentration of Si-nps that was necessary to achieve a 0.2 dB optical density which would provide adequate signal. Two milliliters of solution were initially produced by using a 1 mL syringe; this solution had a concentration between 8 and 10 mg/mL. One mL was removed from this oxygen free vial and placed in a second non-evacuated vial. The original vial's concentration was then halved by injecting 1 mL of toluene in the vial and then sonicating the solution for two minutes. Another milliliter was removed and placed in a third vial for testing; this process was performed until a concentration of approximately 1 mg/mL was achieved. These different concentrations were then tested for their absorption characteristics in an Olis Cary 14 spectrophotometer. Figure 1 illustrates the absorption characteristics of different concentrations of Si-nps. From this information a concentration of approximately 2 mg/mL was chosen for testing. (See Figure 1.)

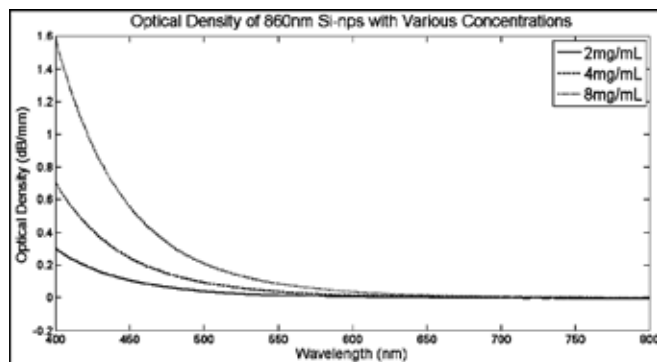


Figure 1: Optical density data for Si-nps.

The correct concentration colloid was then tested using a frequency doubled titanium-sapphire laser. The pulsed laser was incident on a static cell with a thickness of 1 mm which housed the colloid; 400 nm light was utilized for the pump and white light was used for the probe. Time delays of 500 fs, 1 ps, 10 ps, 50 ps and 500 ps were tested at five minute collecting times and a control delay of -5 ps was used.

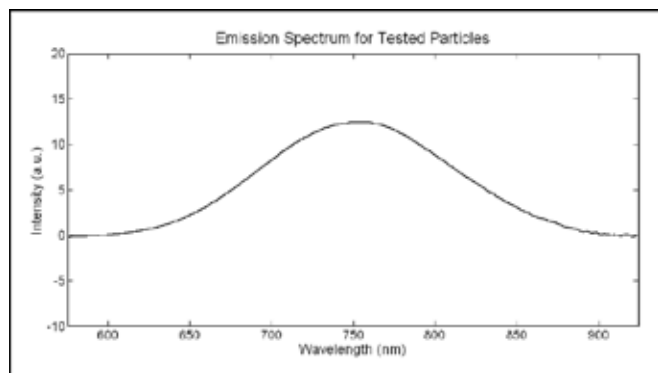


Figure 2: Spontaneous emission spectrum.

### Results and Analysis:

Figure 2 summarizes the spontaneous emission of the tested particles showing a peak wavelength of 750 nm and a QY of 8%; this data was obtained with the use of an integrating sphere. Figure 3 illustrates the results of a representative test performed and depicts changes in the optical density—positive numbers exhibiting net absorption and negative values depict emission. Absorption dominates any emission present which is apparent because all the values are positive. Stimulated emission is expected at the wavelength of spontaneous emission which can be observed in the reduction of the absorption around 750 nm. Although stimulated emission is present in these Si-nps the emission cross section is dominated by absorption.

### Conclusions and Future Work:

From the experiments performed thus far on the Si-nps, it appears optical gain is not observable with the current particles—implying laser applications are not feasible. If the quantum yield can be increased or stronger population inversion can be obtained there may still be a possibility of getting net emission which allows for future work.

### Acknowledgements:

I would like to thank the National Nanotechnology Infrastructure Network Research Experience for Undergraduates (NNIN REU) Program and the NSF for funding my research at the University of Minnesota. I would also like to thank Anand Gopinath for his advising, Stephen Campbell and Uwe Kortshagen and their graduate students, Richard Liptak and Rebecca Anthony for the nanoparticles, and David Blank and his graduate student Jonathon Hinke for testing my samples.

### References:

- [1] Pi, X., et al, “Air-stable full-visible-spectrum emission from silicon nanocrystals synthesized by an all-gas-phase plasma approach,” *Nanotechnology*, 19, 245603, (2008).
- [2] Mangolini, L., et al, “High efficiency photoluminescence from silicon nanocrystals prepared by plasma synthesis and organic surface passivation,” *Phys. Stat. Sol. (c)* 3, 11, 3975-3978, (2006).
- [3] Cho, K., et al, “High efficiency visible electroluminescence from silicon nanocrystals embedded in silicon nitride using a transparent doping layer,” *Appl. Phys. Lett.*, 86, 071909, (2005).
- [4] Ligman, R., et al, “Electroluminescence of surface oxidized silicon nanoparticles dispersed within a polymer matrix,” *Appl. Phys. Lett.*, 90, 061116, (2007).

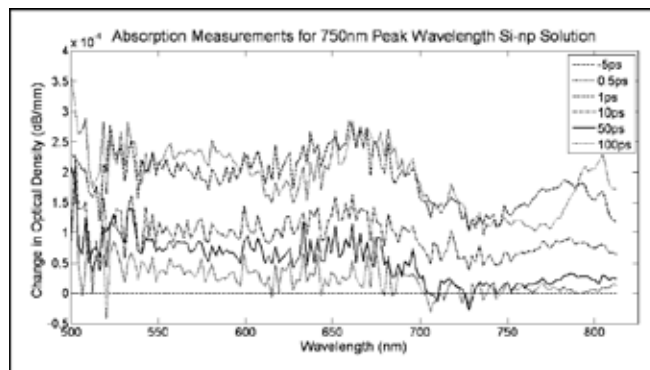


Figure 3: Pump-probe analysis of Si-nps.

# Optical Fiber Packaging for Integrated Photonic Structures

Brielle Graham

Physics, Richard Stockton College of New Jersey



**NNIN REU Site: Cornell NanoScale Science and Technology Facility,  
Cornell University, Ithaca, NY**

*NNIN REU Principal Investigator(s): Professor Michal Lipson, Electrical and Computer Engineering, Cornell University*

*NNIN REU Mentor(s): Dr. Carl Poitras, Electrical and Computer Engineering, Cornell University*

*Contact: bri.graham.nj@gmail.com, lipson@ece.cornell.edu, cpb8@cornell.edu*

## Introduction:

The focus of this summer project was the light coupling of chips. The Lipson group uses tapered fibers to bring laser light close to the edges of the chips they work with. The light is then coupled into waveguides patterned onto the surface of the chip. Each of these chips is fabricated as one of many on a wafer and, after fabrication, wafers have to be diced into the separate chips. This dicing procedure leaves very rough edges, which are not conducive to efficient light coupling. Therefore, after dicing, the edges of each individual wafer needs to be polished smooth. The polishing process takes about two hours per chip. The purpose of this research was to replace the dicing and polishing with a process that would leave smooth edges for better light coupling and, hopefully, reduce the amount of time needed. To this end, we decided to use an etching method.

The wafer we used was a silicon wafer with  $3\ \mu\text{m}$  of silicon dioxide grown on the surface. The waveguides would be patterned into this layer of silicon dioxide. The theory was that we could pattern the waveguides to be slightly longer than needed, then etch trenches through the layer of silicon dioxide into which it was patterned. The trenches would intersect the ends of the waveguides, exposing the edges. Then we would etch down into the silicon substrate, far enough that we could cleave the wafer without damaging the waveguides. This process is depicted in Figures 1 and 2. If the sidewalls of the trenches are smooth, then the exposed section of the waveguide should be able to couple light effectively.

## Experimental Procedure:

The first part of this process was resist characterization. We used SPR220-3.0 to get a  $3\ \mu\text{m}$  layer resist. The exposure dose was first characterized on the EV 620, and the resist development was also characterized. An exposure time of 3.0 seconds with a 90 second development (in MIF 300) were found to be optimal.

The next step was to characterize the etch rate of a whole wafer. For this process we used two machines: the Oxford 100 for silicon dioxide etching, and the Unaxis 770 for deep silicon etching. We evaluated the etch time to be 24 minutes for the Oxford, and the Unaxis etch required 150 to 170 etch cycles to go through approximately  $120\ \mu\text{m}$  of silicon.

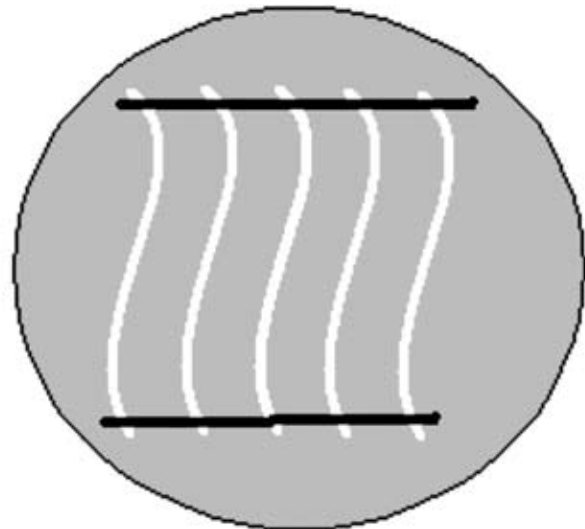


Figure 1: Diagram showing waveguides (white) and etched trenches (black).

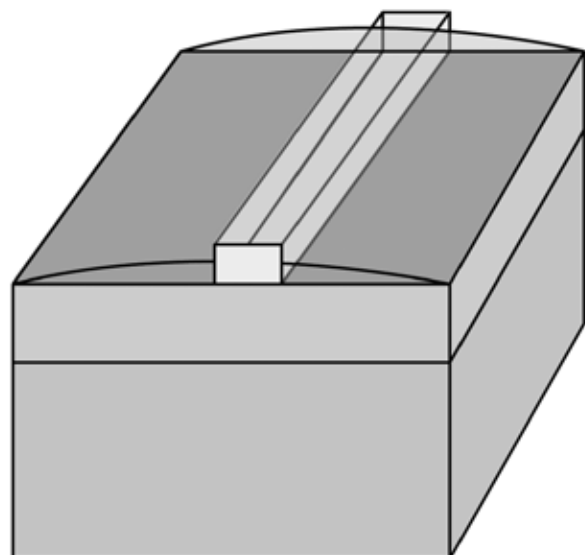


Figure 2: Cross-section of chip with exposed waveguide.

This etch process also had to be characterized on a piece of wafer. The etch time remained the same for the Oxford, however it decreased dramatically for the Unaxis as expected due to etch loading. We initially had been using virgin silicon wafers as carriers for the sample and, as a larger Si area is exposed during the etch, this increased the etch time. The etch loading was resolved by using a Si wafer which had a  $\sim 3 \mu\text{m}$  thick thermal oxide layer grown on it.

Since the HTG exposure tool is better suited to handle pieces, we had to perform a dose test on it as well. Before doing so, since we realized that a thicker resist was required so that the samples could undergo the etch steps (since the initial oxide etch had to remove  $\sim 5 \mu\text{m}$ ), a thicker resist layer was necessary. To this end, since the oxide etch time needed to be 48 minutes, we decided to use SPR220-4.5 to get a  $6.7 \mu\text{m}$  resist layer. After solving adhesion problems by lengthening the soft-bake time and adding a rehydration period, we characterized the exposure and development.

Our next major problem was reticulation. Our initial etch tests were performed with relatively thin photoresist layers, but the  $6.7 \mu\text{m}$  resist was near the range of thicknesses which required a change in process. After the development, we left the chip in a  $90^\circ\text{C}$  oven for approximately 4 hours to allow for any solvent remaining from the developer to evaporate. We also needed to etch in 6 minute intervals, leaving time for the sample to cool down between the etches. It was at this point that the Unaxis 770 went down, and remained unusable for the remainder of the summer.

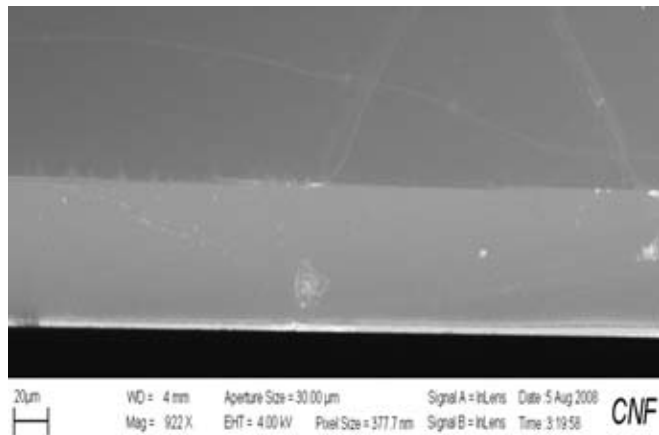


Figure 3: SEM image of trench sidewall.

We were unable to complete the project and verify that the side-wall was indeed smoother. We were, however, able to get some SEM images of the sidewalls that looked promising, one of which is shown as Figure 3. The entire process took approximately 8 hours for a wafer, which may or may not be comparable with the original dice and polish process that took 2 hours per chip.

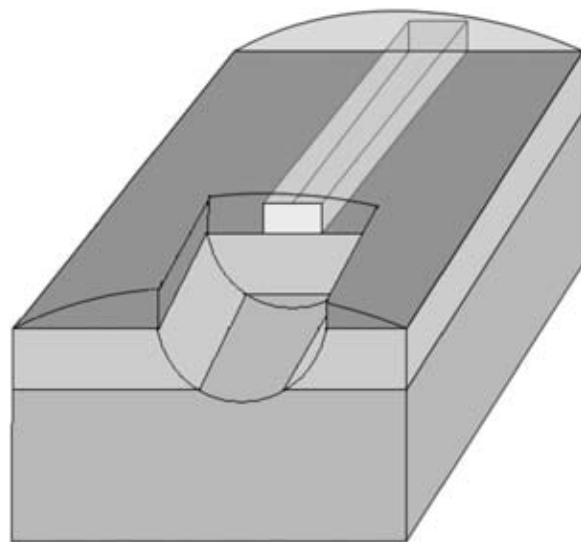


Figure 4: Diagram of chip with etched fiber-holder and exposed waveguide.

#### Future Work:

The next step in our process would be to etch  $125 \mu\text{m}$  diameter trenches into the chip intercepting and running parallel to the ends of the waveguides. This would act as a fiber holder, allowing the tapered fibers to sit close to the etched-through and exposed ends of the waveguides. Also, this set-up would make for more efficient packaging of the chip after the entire process was completed.

#### Acknowledgements:

I would like to thank my Principal Investigator, my mentor Carl, and all the members of the Nanophotonics Group, for always being there to answer questions and guide me in the right direction. I'd also like to thank the site coordinators and staff at the Cornell NanoScale Facility for doing everything possible to make this experience as bug-free as possible. I would also like to thank the Intel Foundation for funding this project, and the National Nanotechnology Infrastructure Network Research Experience for Undergraduates Program (NNIN REU) and National Science Foundation (NSF) for hosting. It wouldn't have been possible without any of you!

# Nanopatterned Electrodes for Organic Solar Cells

Jason Jewell

Materials Science and Engineering, University of Illinois

**NNIN REU Site: Lurie Nanofabrication Facility, University of Michigan, Ann Arbor, MI**

*NNIN REU Principal Investigator(s): Professor Max Shtein, Materials Science and Engineering, University of Michigan*

*NNIN REU Mentor(s): Denis Nothorn, Materials Science and Engineering, University of Michigan*

*Contact: jjewell2@illinois.edu, mshtein@umich.edu, dnothorn@umich.edu*

## Abstract:

Transparent conductors such as indium tin oxide (ITO) are used extensively in a wide range of optoelectronic devices. ITO is used in virtually all organic photovoltaic cells, which are of interest based on their potential for low-cost manufacturing on flexible substrates. Unfortunately, the high cost and brittle nature of ITO limit its application in organic solar cells, motivating the search for transparent, conductive thin-film alternatives. To address this challenge, we investigated nanostructured thin metal films that take advantage of surface plasmon resonances that can increase transparency relative to a flat metal film of the same thickness, while retaining nearly identical electrical conductivity. Structures of interest include metal films with semi-ordered arrays of holes producing a tight mesh. The nanostructuring is performed using mask-less lithographic techniques using a block copolymer that creates nanoscale features on the substrate. Selective etching of the self-patterned polymer followed by deposition of metal on top of the structure was used to produce a surface texture that will hopefully increase the transparency of the electrode.

## Introduction:

Organic semiconductors have shown to be promising for many novel solar cell designs due to their inherent flexibility and potential to be processed at room temperature and pressure [1]. One of the most difficult aspects of constructing efficient organic solar cells is finding contact materials with good conductivity and transparency as well as an acceptable work function for good carrier injection [2]. For the cathode, a very low-work-function material is typically required, and this is usually a thick layer of lithium fluoride or metal. The anode can be made of a large variety of high-work-function materials, leading to the use of doped semiconductors like ITO and highly conductive metals such as silver.

Recent research has focused on creating nanopatterned metal films which are transparent, conductive, and flexible [2]. Our experiment attempts to use polystyrene-*b*-polyisoprene (PS-PI), a self-assembling block copolymer, and reactive ion etching to transfer a periodic pattern onto a metal thin film. The periodicity of this structure is as small as 40 nm and has the possibility of enhanced solar cell efficiency through surface plasmon resonance (Figure 1) [3,4].

## Experimental:

Glass substrates were cleaned with a sequence of rinsing in deionized water, acetone, and isopropanol. Polystyrene-*b*-polyisoprene purchased from Polymer Source Inc. was dissolved in toluene to create a 0.5% solution by mass. This solution was spun onto 3" x 2" glass substrates at 3000 rpm for 30 sec and annealed in vacuum for 12 hours at 125°C. After

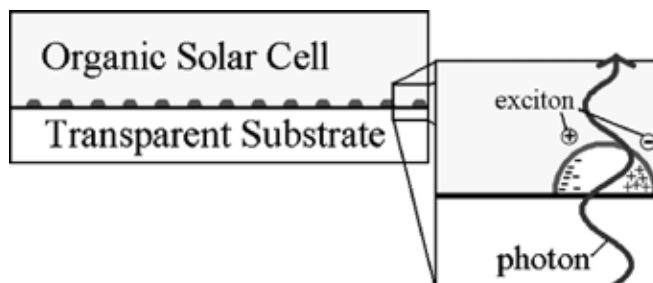


Figure 1: The surface plasmon generated in the structured metal film increases exciton generation near the electrode.

reactive ion etching with fluorine plasma for 10 sec, atomic force microscopy (AFM) was used to observe the surface pattern (shown in Figure 2). Electron beam evaporation was then used to deposit 2 nm of nickel and 15 nm of silver over the pattern. The nickel acts to increase adhesion of the silver to the sample. The pattern was then observed using AFM once again (shown in Figure 3). A 3-dimensional representation of the final structure is shown in Figure 4.

## Results and Conclusions:

After spinning the PS-PI solution onto glass substrates and annealing the films, the film thickness was measured to be 50-60 nm. Etch rates of the PS-PI film under the fluorine plasma etch were measured, and results revealed a 2 nm/sec etch rate. A 10 sec etch was used to completely etch the polystyrene

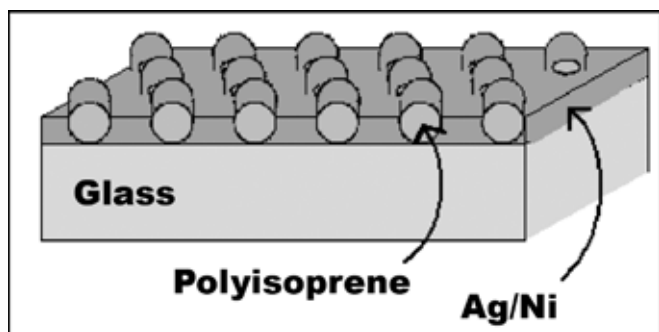
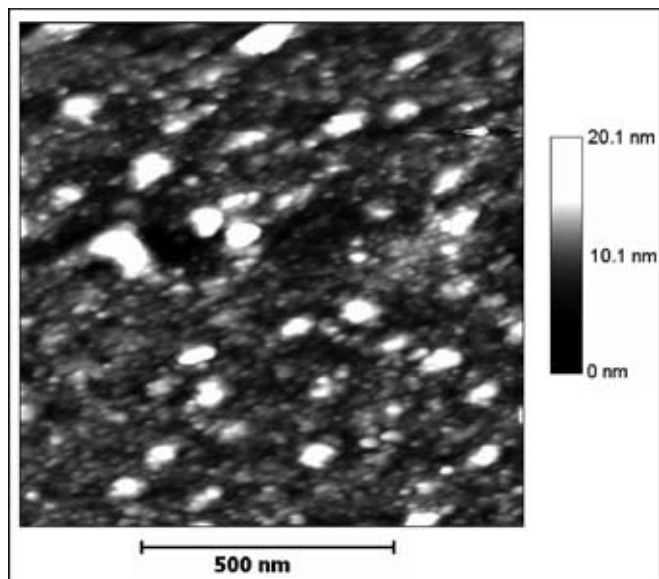
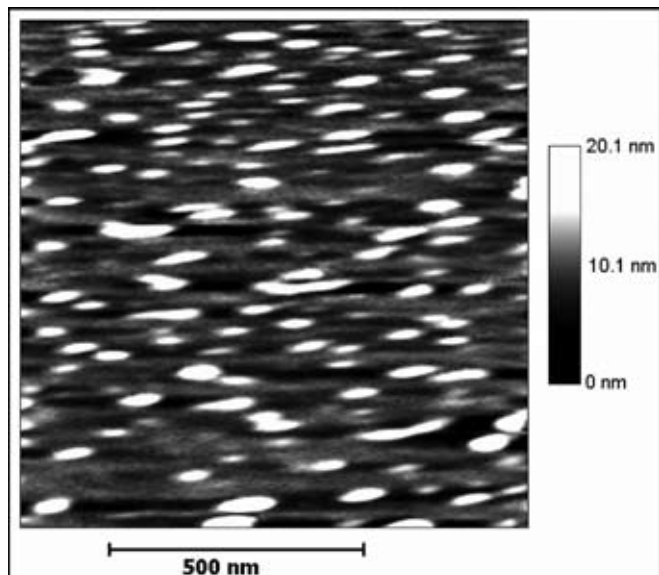


Figure 2, top: AFM image of self-assembled polyisoprene spheres after fluorine plasma etching.

Figure 3, middle: AFM image of metal film deposited on top of the polyisoprene spheres shown in Figure 1.

Figure 4, bottom: Desired final product; a thin metal film deposited on the self-assembled structure.

matrix, while leaving behind a  $\sim 30$  nm thick layer of the more robust polyisoprene spheres. Results of the fluorine etch are shown in Figure 2. The image is slightly distorted due to sample drift, but spherical structures are clearly visible on the surface. Figure 3 was taken after e-beam evaporation of nickel and silver. The image shows that the pattern was not lost.

Sheet resistances for the structured metal film were compared to those of an identical metal film deposited on clean glass. The structured metal film had an average  $R_s = 2.82 \Omega/\square$  whereas the planar metal film had an average  $R_s = 2.89 \Omega/\square$ . These results demonstrate that the surface texture does not reduce the film's conductivity.

### Future Work:

Devices should be built using the thin films created in this experiment as electrodes in order to measure their effectiveness in enhancing solar cell efficiency. A key to this is to increase the transparency of the metal film. Since the films created in this experiment are continuous, their transparency could be increased by etching the raised polyisoprene spheres to lift off the silver from those points.

Modifications on the attained metal film structure for future work could include an increased concentration of PS-PI in the initial solution to increase the concentration of polyisoprene spheres on the surface. This would increase plasmonic effects as well as increase transparency. An inverted PS-PI structure, where the spheres are etched more rapidly than the matrix would also prove useful for new fabrication methods. This could be accomplished by using a polar solvent to invert the PS-PI or by selectively etching the other PS-PI constituent, polyisoprene.

### Acknowledgements:

I would like to thank Sandrine Martin, Professor Shtein and his research group, and my mentor, Denis Nothert for their assistance and support. I also gratefully acknowledge the support of the Lurie Nanofabrication Facility and the financial support of the National Nanotechnology Infrastructure Network Research Experience for Undergraduates Program and the National Science Foundation.

### References:

- [1] Hadipour, A.; Adv. Funct. Mater.; 16, 1897 (2006).
- [2] Kang, M. G.; Adv. Mat.; 13, 1 (2007).
- [3] Park, M.; Science; 276, 1401 (1997).
- [4] Morfa, A. J.; Appl. Phys. Lett.; 92, 013504 (2008).

# Endomicroscopic Two-Photon Luminescence Imaging of Cancer Cells Using Molecularly Targeted Gold Nanocages

Alice F. Meng

Biomedical Engineering, Washington University in St. Louis

**NNIN REU Site: Center for Nanotechnology, University of Washington, Seattle, WA**

NNIN REU Principal Investigator(s): Xingde Li, Department of Bioengineering, University of Washington

NNIN REU Mentor(s): Yicong Wu, Department of Bioengineering, University of Washington

Contact: afm3@cec.wustl.edu, xingde@u.washington.edu, yicong@u.washington.edu

## Abstract:

Gold nanoparticles have been attractive as a new class of contrast agents for optical imaging of biological tissue. In this study, we demonstrate the use of gold nanocages with ~ 60 nm diameter as bright contrast agents for the two-photon luminescence (TPL) imaging of cancer cells. A breast cancer cell line, SK-BR-3, which overexpresses epidermal growth factor receptor HER2, was used to test the molecular specific binding of bioconjugated gold nanocages. Real-time TPL imaging of the monolayered SK-BR-3 cells was performed with a miniature nonlinear optical endomicroscope system. Overall, molecularly targeted gold nanocages are promising as contrast agents for *in vivo* optical cancer diagnostics combined with nonlinear optical endomicroscopy.

## Introduction:

Gold nanoparticles have become a new class of contrast agents in biological imaging because they are biocompatible and their surface plasmon resonance peak can be precisely controlled over a broad spectrum by changing their sizes and shapes [1]. Gold (Au) nanocages, in particular, are being studied because their optical resonance wavelengths can extend more easily to the near-infrared spectral region. Our studies have shown that the nanocages can be used as contrast agents in spectroscopic OCT imaging [1]. Recent results have also demonstrated that the gold nanocages are effective photo-thermal transducers and can be used for cancer diagnosis and therapy [2].

In this study, we observed that gold nanocages exhibited strong two-photon luminescence signals. Similar to gold nanorods, the metal nanoparticles can absorb two photons simultaneously and generate electron-hole pairs; then the electron-hole pairs can be recombined, emitting new photons [3]. Furthermore, we demonstrated the application of gold nanocages in cancer cells system with a homemade nonlinear endomicroscope system.

## Experimental Procedures:

First, gold nanocages were synthesized using a galvanic replacement reaction between silver nanocubes and chloroauric acid ( $\text{HAuCl}_4$ ). The size and wall thick-ness of the nanocages was controlled by varying the amount of  $\text{HAuCl}_4$  added. Figure 1(a) shows a typical scanning electron microscope (SEM) image of gold nanocages with 60 nm diameter.

Next, these nanocages were functionalized to succinimidyl propionyl poly (ethylene glycol) disulfide (NHS-activated PEG, M.W. = 1,109) by creating an Au-S linkage and then bonded to primary amine of the anti-HER2 antibody [4]. These molecularly targeted gold nanocages were then conjugated to SK-BR-3 breast cancer cells that overexpress the HER2 growth receptor. Figure 1(b) shows a typical SEM image of a SK-BR-3 breast cancer cell bioconjugated with nanocages.

## Microscope System:

Images were obtained using a homemade nonlinear optical endomicroscope system. Figure 2 shows the schematic of this system. Light centered at 810 nm was emitted from a femtosecond laser and directed through a double-clad fiber to the endomicroscope probe with an outer diameter of 2.4 mm. The probe consisted of a double-clad fiber (for both delivery

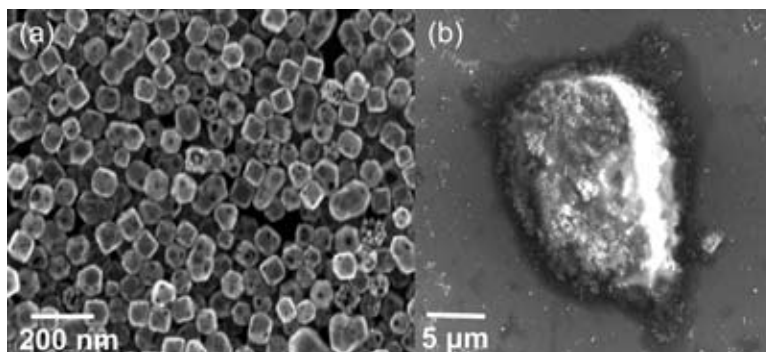


Figure 1: SEM images of (a) gold nanocages and (b) SK-BR-3 cell targeted with bio-conjugated gold nanocages.

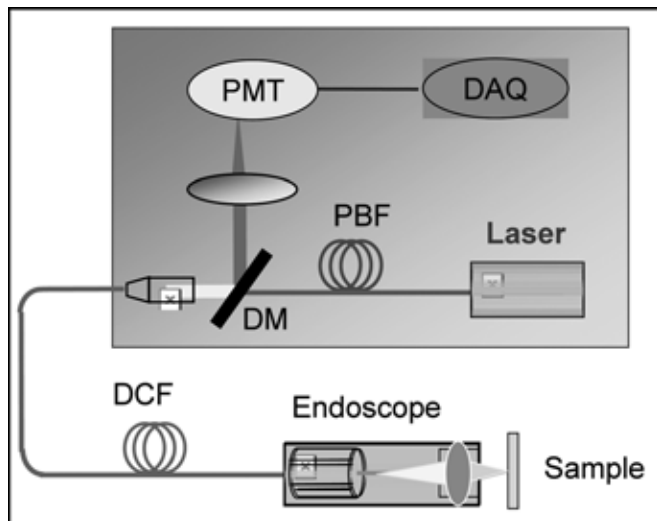


Figure 2: Schematic of the fiber-optic scanning endomicroscope system. DCF: Double-clad fiber; DM: dichroic mirror; PBF: photonic bandgap fiber; PMT: photo multiplier tube; DAQ: Data acquisition system.

of excitation light and collection of two-photon luminescence signals), a piezoelectric actuator (PZT) tube (for 2-D sweeping of the light on the sample), and a focusing lens (for focusing the light to the sample). In this endoscope, the frame rate was 3.3 Hz and about 160  $\mu\text{m}$  scanning range on sample was achieved.

## Results:

Figure 3(a) shows a typical two-photon luminescence image of the gold nanocages in a water solution. It is obvious that single gold nanocages are randomly distributed. Since they are not molecularly targeted to any objects, they do not form any patterns in the solution. Figure 3(b) shows the endomicroscopic TPL images of the SK-BR-3 cells conjugated with nanocages tagged with anti-HER2 antibodies. As can be seen, most cell membranes can be clearly identified, indicating the successful conjugation. Overall, the gold nanocages show strong two-

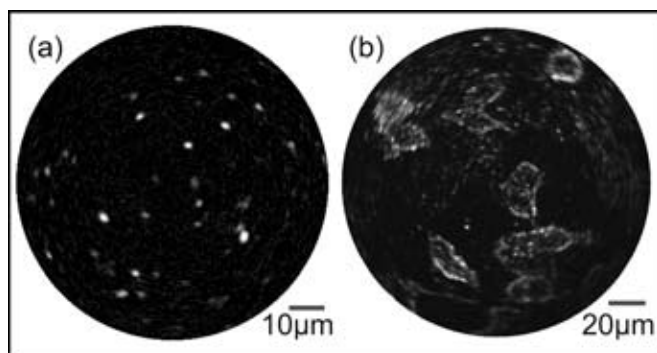


Figure 3: Two-photon luminescence (TPL) images of (a) gold nanocages of a 50 nm edge-length in water and (b) SK-BR-3 breast cancer cells targeted with bio-conjugated gold nanocages.

photon luminescence, but do not suffer photobleaching as organic dyes. Since they are more bio-compatible compared to quantum dots, the gold nanocages with the endomicroscopic TPL imaging are promising for *in vivo* application for early stage cancer diagnosis and treatment.

## Conclusion:

Gold nanocages are shown to be promising contrast agents for TPL imaging of cancer cells. Ongoing research is being done with three-dimensional imaging of phantom tissue made from collagen gel embedded with cells and bioconjugated nanocages. Future research will be focused on *in vivo* application of bioconjugated nanocages in tissue diagnosis by using the technology of nonlinear optical endomicroscopy.

## Acknowledgements:

I would like to thank the biophotonics lab at the Department of Bioengineering in University of Washington, especially PI Prof. Xingde Li, Mentor Dr. Yicong Wu and other group members Desheng Zheng, Yongping Chen. I would like to thank our collaborator Prof. Yongnan Xia in Department of Biomedical Engineering in Washington University at St Louis. Finally, I would also like to thank the National Nanotechnology Infrastructure Network Research Experience for Undergraduates Program and National Science Foundation for funding, and University of Washington site coordinator Ethan Allen for his guidance and support.

## References:

- [1] J. Chen, et al. "Gold Nanocages: Bioconjugation and Their Potential Use as Optical Imaging Contrast Agents." *Nano Letters*. 5, 473-477 (2005).
- [2] J. Chen, et al. "Immuno Gold Nanocages with Tailored Optical Properties for Targeted Photothermal Destruction of Cancer Cells." *Nano Letters*. 7, 1318-1322 (2007).
- [3] N. J. Durr, et al. "Two-Photon Luminescence Imaging of Cancer Cells Using Molecularly Targeted Gold Nanorods." *Nano Letters*. 7, 941-945 (2007).
- [4] H. Wang, et al. "*In vitro* and *in vivo* two-photon luminescence imaging of single gold nanorods." *PNAS*. 102, 15752-15756 (2005).

# Optimization of Ohmic Contacts and Current Spreading Layers for GaN Based Solar Cells

Micah S. Points

Electrical Engineering, University of Texas at Austin

**NNIN REU Site: Nanotech @ UCSB, University of California, Santa Barbara, CA**

NNIN REU Principal Investigator(s): Steven P. DenBaars, Department of Electrical and Computer Engineering and Materials Department, University of California, Santa Barbara

NNIN REU Mentor(s): Samantha Cruz, Materials Department, and Carl Neufeld, Department of Electrical and Computer Engineering, University of California, Santa Barbara

Contact: [mpoints@mail.utexas.edu](mailto:mpoints@mail.utexas.edu), [denbaars@engineering.ucsb.edu](mailto:denbaars@engineering.ucsb.edu), [scruz@umail.ucsb.edu](mailto:scruz@umail.ucsb.edu)

## Abstract:

Single-junction solar cells are approaching thermodynamic limits with peaked energy conversion efficiencies of  $\sim 25\%$ . These solar cells are limited to a theoretical efficiency of  $\sim 30\%$  because single-junction solar cells, like silicon (Si) and gallium arsenide (GaAs), can only efficiently absorb photons with energy near the bandgap energy ( $E_g$ ) of the material. Multi-junction solar cells avoid this limit by stacking several materials with different bandgaps, each absorbing a small portion of the solar spectrum at a higher efficiency. The theoretical efficiency of multi-junction solar cells is as high as 86% for an infinite stack. Bandgaps of indium gallium nitride (InGaN) alloys can span the solar spectrum enabling the design of nearly ideal multi-junction solar cells. The focus of this project is to optimize the p-ohmic contacts to InGaN/GaN solar cells to enhance device performance. Thin conductive films were used as current spreading layers in order to decrease contact resistance and enhance carrier collection. Devices with fill factors over 80% and with open circuit voltages near 2V were achieved. Performance was found to be more affected by the absorbance properties of the contact layers than their contact resistances.

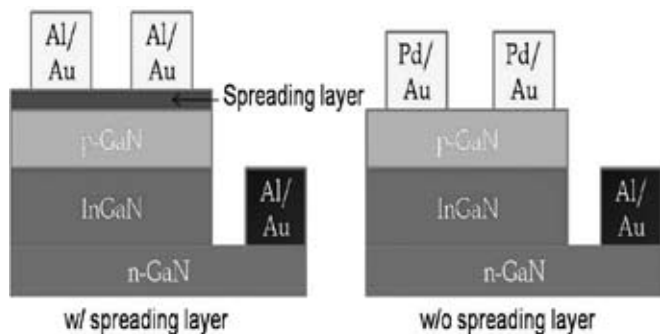


Figure 1: Device structure.

## Introduction:

There are only a few reports of InGaN solar cells [1] and there is much to be studied before high efficiency multi-junction solar cells can be achieved. For high efficiency cells, there is a balance between creating electron hole pairs and extracting usable photocurrent. P-type GaN is a difficult material to contact because of its large bandgap and lower hole mobility. A possible solution is to use a contact spreading layer for increased carrier collection. The device structure is shown in Figure 1. The problem with depositing anything on the cell is that it will decrease the amount of incident light transmitted into the cell. For solar cells we must balance transparency and conductivity.

## Experimental Procedures:

In this project, we studied three contact schemes: one with no contact spreading layer and a Pd/Au (300Å/3000Å) grid contact, and two spreading layers, Ni/Au, and Ni/Ni/ITO (100Å/2500Å). For Ni/Au, the Ni was held constant at 50Å, but the Au thicknesses were 10Å, 50Å, and 100Å. Contacts were made by electron beam evaporation on nominally 10% InGaN that was grown using metal oxide chemical vapor deposition (MOCVD) by Michael Iza of the Materials Department at UCSB. The Al/Au (300Å/3000Å) n-contacts were also electron beam deposited.

Those with contact spreading layers used Al/Au (300Å/3000Å) for grid contacts. The devices defined by mesa etching had an area of 250,000  $\mu\text{m}^2$  and grid spacings of 25  $\mu\text{m}$ , 50  $\mu\text{m}$ , 100  $\mu\text{m}$ , and 166  $\mu\text{m}$ . We used linear transfer length method (TLM) measurements to determine p-GaN specific contact resistance. Concurrently, sapphire substrates had the Ni/Au and Ni/ITO deposited on them. These were used to test the light transmission of each spreading layer. Current-voltage measurements were made using an Oriel solar simulator with a Xe lamp coupled to a fiber optic cable. All light measurements were conducted using an AM0 filter and were considered concentrated. Figures of merit from the current-voltage measurements were: short circuit current density,  $J_{sc}$ , open circuit voltage,  $V_{oc}$ , and fill factor, FF. The FF relates the maximum working power density achievable by the solar cell and the power defined by the  $J_{sc}$  and  $V_{oc}$ .

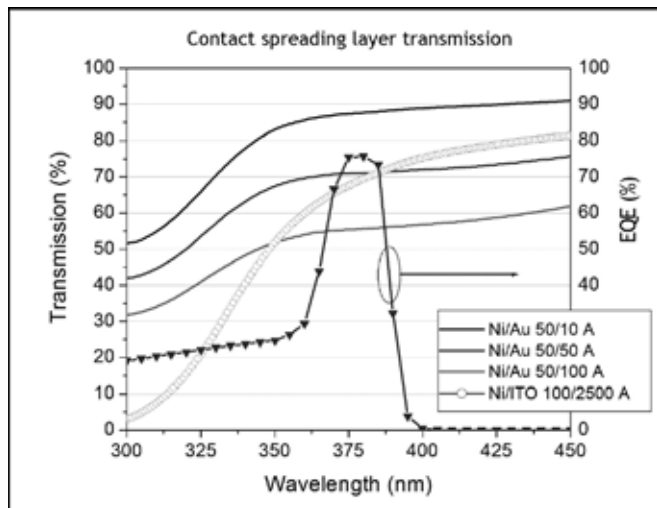


Figure 2. Optical transmission of contact layers.

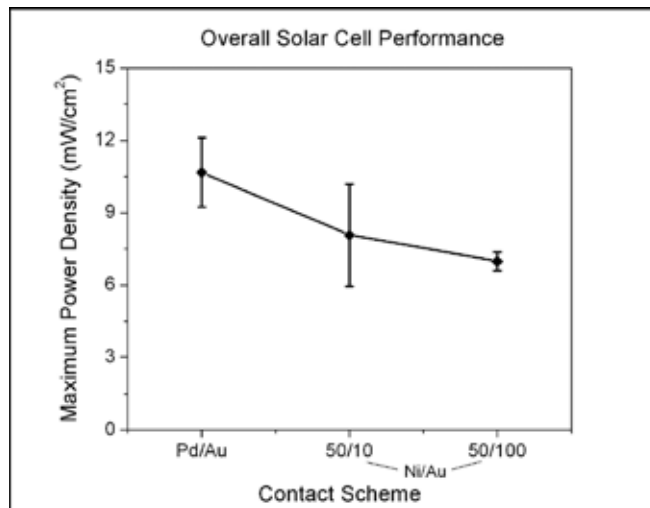


Figure 4: Maximum working power density.

## Results and Conclusions:

The transmission test (Figure 2) shows that the Ni/Au 50Å/10Å sample had the highest transmission percentage. The Pd/Au sample was not tested because we assumed that the transmission was ~ 100% since no spreading layer was used. The Ni/ITO transmission was worse than both the Ni/Au 50Å/10Å and the Ni/Au 50Å/50Å samples in the region where the solar cell has peak External Quantum Efficiency (EQE).

The product of FF,  $J_{sc}$  and  $V_{oc}$ , or maximum power density, gives us the cell power efficiency when divided by the power of the incident light. Pd/Au has the higher measurements for  $J_{sc}$ , 0.8 mA/cm<sup>2</sup>, and  $V_{oc}$ , 2.4V averages, even though FF was lowest. The Pd/Au sample has the higher power density maximum (Figure 4) at approximately 10.5 mW/cm<sup>2</sup>.

The results show that the metal contact spreading layer decreases series resistance and increases FF. It also decreases the amount of light that reaches the solar cell shown by the decrease in transmission. This decrease in usable light reduces the photogenerated current density which lowers the  $J_{sc}$  and  $V_{oc}$ . This decrease eliminates the benefits of the lower series resistance and decreases the efficiency of the solar cell. Therefore, the Pd/Au contact scheme performed better in these circumstances with higher efficiency.

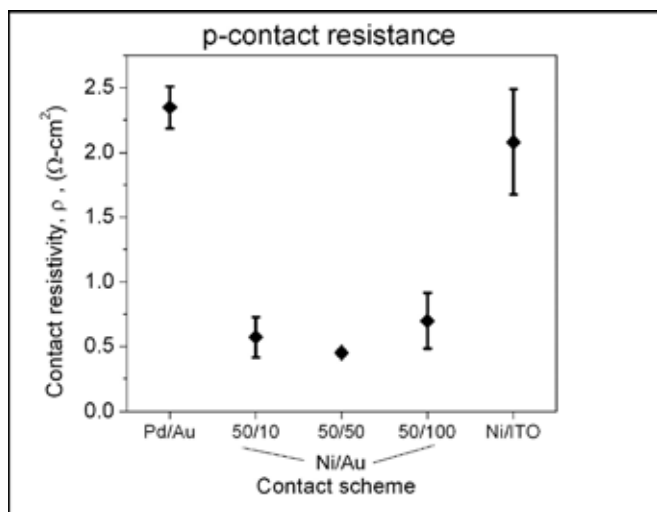


Figure 3. Specific contact resistivity of contact layers to p-GaN.

Figure 3 shows the average p-contact resistance of the samples. The Ni/Au contact schemes had lower specific resistivity (~0.5 Ω/cm<sup>2</sup>) than Pd/Au or Ni/ITO. Since FF is affected by series resistance and leakage current, the low series resistance compared with Pd/Au and Ni/ITO allowed the Ni/Au samples to have FF near 80% while the Pd/Au was closer to 56%. The contact layer seems to have a beneficial effect on the series resistance.

## Future Work:

The use of different metals for ohmic contacts to p-GaN for solar cells should be studied. Determining whether different surface treatments prior to deposition of the metal can help lower resistance can also be investigated. In this project we used a 1:3 mixture of HCl and deionized water, other treatments such as boiling aqua regia may improve the contact between the metal and p-GaN.

## Acknowledgments:

I would like to thank my PI Dr. DenBaars, my mentors Samantha Cruz and Carl Neufeld, and our site coordinator Angela Berenstein, for their assistance during my project. I would also like to thank the Solid State Lighting and Energy Center, the National Nanotechnology Infrastructure Network Research Experience for Undergraduates (NNIN REU) Program and the National Science Foundation for the opportunity to take part in this program.

## References:

- [1] Jani, Omkar et al., "Design and Characterization of GaN/InGaN Solar Cells", Applied Physics Letters, 91, 132117 (2007).

# Optical Waveguide Couplers Fabricated by Nano-Imprint Lithography

Adam Scofield

Electrical Engineering and Physics, Rensselaer Polytechnic Institute

**NNIN REU Site: Microelectronics Research Center, Georgia Institute of Technology, Atlanta, GA**

NNIN REU Principal Investigator(s): David Gottfried, Microelectronics Research Center, Georgia Institute of Technology

NNIN REU Mentor(s): Janet Cobb-Sullivan, Georgia Tech Research Institute

Contact: scofield.adam@gmail.com, david.gottfried@mirc.gatech.edu, janet.cobb-sullivan@gtri.gatech.edu

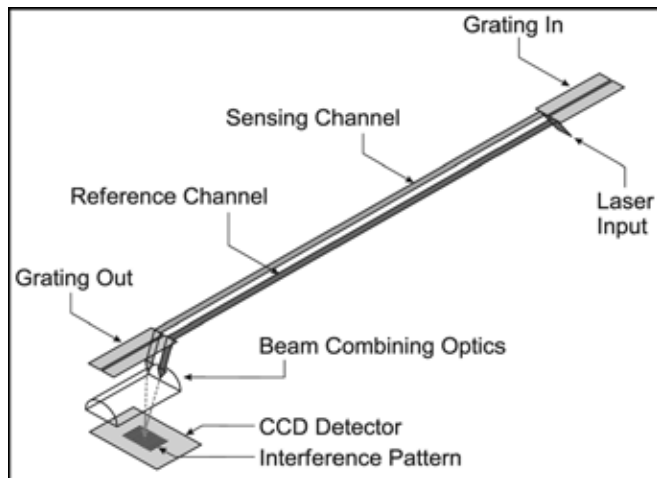


Figure 1: Schematic of the optical interferometric sensor.

## Introduction:

A chemical sensor can be created based on optical planar waveguide interferometry. Since waveguides have evanescent fields sensitive to index of refraction changes, optically combining a guided sensing beam with a reference beam generates an interference pattern that depends on the relative phases of the two beams. Applying a chemically selective film over the sensing arm of the interferometer provides the basis for a sensor (Figure 1). While achievements have been made using grating-coupled silicon nitride waveguides [1], further research is needed in development of inexpensive and more versatile fabrication methods. In particular, fabrication of the grating couplers poses the greatest challenge, as the line width of the gratings is only 360 nm. Nano-imprint lithography offers a solution to this problem, with the ability to replicate three dimensional patterns inexpensively at nanometer resolution. Using standard and grayscale electron-beam lithography, imprint templates for both the standard square grating and blazed gratings were successfully fabricated.

## Experimental Procedure:

The process development consisted of two basic stages. The first was creating the imprint template by electron-beam lithography (EBL). The second was transferring the pattern into quartz via nano-imprint lithography (NIL). EBL required the determination of exposure, developing, and plasma

etching parameters, while NIL required the determination of imprint, exposure, and plasma etching parameters.

Silicon was chosen as the template material because of its low cost and compatibility with EBL. Hydrogen silsesquioxane (HSQ) was chosen as the resist due to its high etch selectivity over silicon (~ 8.5:1). While contrast data for HSQ for various developer concentrations and immersion times has previously been collected, this data does not account for over-exposure due to back-scattered electrons from the substrate (proximity effect). Because of this, writing multiple grating patterns with a wide range of doses and developing parameters was necessary to determine a reliable process.

The proximity effect can be accurately modeled by a Gaussian distribution with a half-maximum radius of  $31.2 \mu\text{m}$ . With the smallest dimension of the sensor couplers being  $200 \mu\text{m}$ , the majority of the couplers' area will have the maximum over-exposure from the proximity effect. Appropriate sized test patterns were determined to have dimensions of  $200 \mu\text{m}$  by  $200 \mu\text{m}$  and verified by numerical computation of the proximity effect in MATLAB, showing that an approximately  $100 \mu\text{m}$  by  $100 \mu\text{m}$  area in the center of these patterns would show the maximum proximity effect (Figure 2). The patterns were written with doses ranging from  $290 \mu\text{C}/\text{cm}^2$  to  $1680 \mu\text{C}/\text{cm}^2$  on multiple wafers with resist thicknesses

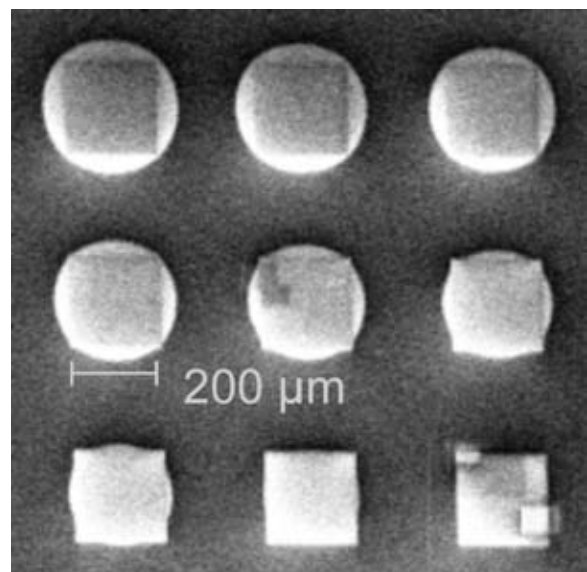


Figure 2: SEM of square grating test patterns (HSQ on Si).

ranging from 45 nm to 105 nm. These were then developed in tetramethylammonium hydroxide (TMAH) in concentrations ranging from 2.3% to 25% with times from 7 seconds to 70 seconds.

Several successful formulas were found after these patterns were etched in a  $\text{Cl}_2/\text{Ar}$  based inductively coupled plasma and remaining resist was stripped. The optimal formula was found to be exposure with  $290 \mu\text{C}/\text{cm}^2$ , 45 nm resist thickness, and development in 2.3% TMAH for 70 s. The criteria for selecting this formula was based on minimizing cost of production: the shortest fabrication time with minimal material costs.

Process development of the pattern transfer into quartz was the more difficult of the two stages. No previous work had been done towards this goal, so several imprint resists and etching gases were tested for selectivity. The first resist tested was polymethyl methacrylate (PMMA). This is a common thermally curable resist used for imprinting and is relatively inexpensive. The second was a proprietary UV curable resist (mr-UVCur06) from Micro Resist Technology. Both of these resists were tested as quartz etch masks in two different types of inductively coupled plasmas. PMMA was ineffective as an etch mask for both etch recipes. The mr-UVCur06 resist proved to be much more effective. The  $\text{Cl}_2$  based plasma yielded low selectivity of  $\sim 4:1$  over quartz, while the  $\text{CF}_4/\text{C}_4\text{F}_6$  based plasma yielded a much higher selectivity of 1:1.33.

The imprinting process was tested with arbitrary trench depths, but the sensor couplers require a trench depth of 70 nm for the maximum coupling efficiency of light to the waveguide. In order to accomplish this, accurate data was taken for the etch rates of both the resist and quartz substrate. Measurement of the resist etch rate was necessary because a residual layer of the resist remains after imprinting and must be etched down to the quartz surface. The required etch time was then calculated to be 65 s, and several substrates for actual sensors were fabricated.

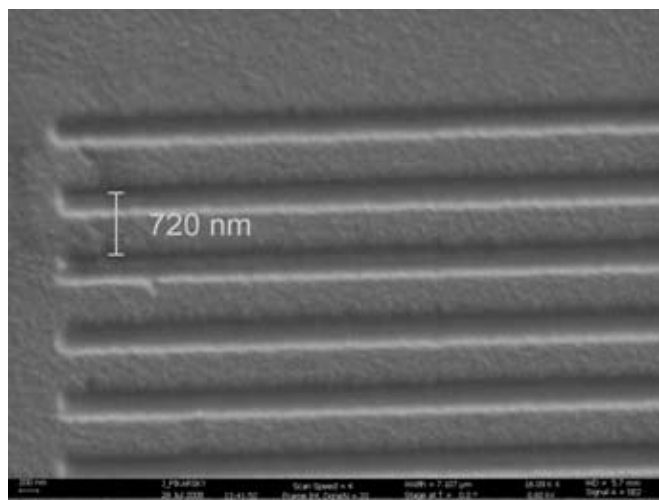


Figure 3: SEM of square grating pattern etched into quartz.

## Results and Future Work:

The square and blazed grating patterns for the waveguide couplers were demonstrated successfully with nano-imprint lithography. SEM images taken of the quartz after etching (Figure 3) show that the line widths are reproduced accurately to  $\pm 2$  nm. AFM images of the blazed grating template and etched quartz (Figure 4) show some degradation in pattern transfer. While the square and blazed grating shapes have been successfully transferred in quartz, there have yet to be any quantitative measurements of the coupling efficiency. The silicon nitride waveguide material will be deposited by plasma enhanced chemical vapor deposition (PECVD). A HeNe laser will then be used as the light source, and the relative intensity of light output from the waveguides will be measured by a CCD camera.

## Acknowledgments:

Thanks to Dr. David Gottfried and Janet Cobb-Sullivan for a challenging and interesting project, Devin Brown for training and assistance with EBL, as well as Jesal Zaveri, Rebhadevi Jeevagan, Joel Pikarsky, and Dr. James Meindl. Funding provided by the National Nanotechnology Infrastructure Network Research Experience for Undergraduates Program and the National Science Foundation.

## References:

- [1] J. Xu, D. Suarez, D.S. Gottfried. Analytical and Bioanalytical Chemistry. 2007 Oct; 389(4): 1193-9.

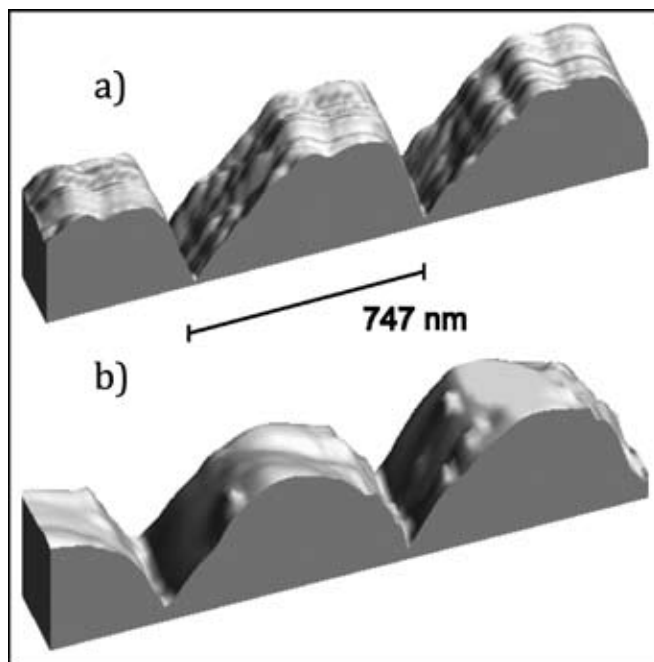


Figure 4: AFM scans of a) HSQ template of blazed gratings, and b) blazed gratings etched into quartz.

# Investigation of Propagation Loss of Passive Silicon Waveguides Using Two Different Etching Techniques

Alisha Shutler

Electrical Engineering, Oklahoma State University

**NNIN REU Site: Nanotech @ UCSB, University of California, Santa Barbara, CA**

NNIN REU Principal Investigator(s): Dr. John Bowers, Electrical and Computer Engineering, UCSB

NNIN REU Mentor(s): Hui-Wen Chen, Electrical and Computer Engineering, University of California, Santa Barbara

Contact: [alisha.j.shutler@okstate.edu](mailto:alisha.j.shutler@okstate.edu), [bowers@ece.ucsb.edu](mailto:bowers@ece.ucsb.edu), [hwchen@ece.ucsb.edu](mailto:hwchen@ece.ucsb.edu)

## Abstract:

This work characterizes the propagation losses of passive silicon waveguides of  $1.0\ \mu\text{m}$  and  $1.5\ \mu\text{m}$  width fabricated using two different processing techniques, known as Etch #1 and Etch #2. The Fabry-Perot method of loss measurement was used to determine the losses and the reflectivities of each waveguide, and using that information, the effective indexes were also then found. The final results compare the losses and the indexes vs. the wavelength of light being transmitted through each waveguide. It was found that for  $1.0\ \mu\text{m}$  widths, Etch #1 was less lossy, while for the  $1.5\ \mu\text{m}$  widths Etch #2 proved better.

## Introduction:

For decades now, silicon (Si) has been the material of choice for the fabrication of semiconductor devices. While electronic devices are widely fabricated on the Si platform, Si photonics devices are still under exploration because of the lack of efficient light source, which is mainly limited by the intrinsic indirect bandgap in Si. Researchers at Intel and at the University of California, Santa Barbara, have already demonstrated a hybrid Si evanescent platform where III-V epitaxial structures are bonded to silicon-on-insulator (SOI) wafers so that the optical mode inside the III-V region can be manipulated by changing the Si waveguide dimensions. The confinement factor inside the III-V layers can thus be changed for different photonic devices such as lasers, amplifiers, modulators, and photodetectors. As the waveguide dimension shrinks, based on the requirement for larger confinement factor in III-V, the propagation loss in Si waveguides are more affected by the fabrication process errors such as waveguide shape and sidewall roughness. In order for transmission to be most effective, the losses throughout the waveguide need to be minimized. In this work, two etching techniques with different amount of chlorine ( $\text{Cl}_2$ ) and boron trichloride ( $\text{BCl}_3$ ) flow have been used to fabricate the Si waveguides. The focus of this project is to determine what the propagation loss is for these two methods, thereby determining which etching technique produces the lower loss.

## Experimental Procedure:

Loss measurements were performed using the Fabry-

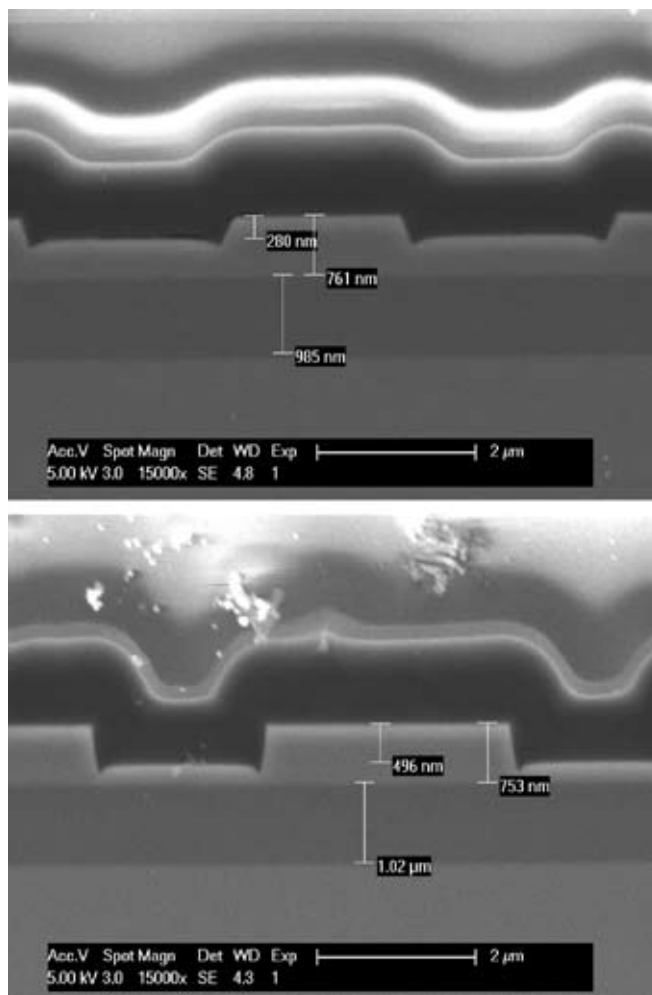


Figure 1: Etch #1 (top) and Etch #2 (bottom) waveguide dimensions.

**Table for Figure 1**

Technique	Gas (sccm)		Pressure (Pa)		Power (W)	
	$\text{Cl}_2$	$\text{BCl}_3$			FWD	SCR
#1	8	4	0.4		120	500
#2	0.8	0.6	0.24		40	400

Differences in gas, pressure, and power used for ICP etching.

Perot interferometer technique, which involved making the assumption that the highly polished waveguide end facets acted like partially transmissive mirrors, effectively creating

a Fabry-Perot cavity between them. By coupling a tunable laser onto an end facet of the waveguide and performing a frequency sweep, the periodicity of the light exiting the waveguide can be viewed and used for data analysis. The light source was swept over a range of 100 nm, starting at 1525 nm and ending at 1625 nm, and the data was sampled every 25 nm over a range of 1 nm. The light exiting the waveguide was collimated with a 100x objective lens and sent through a dielectric beamsplitter, which separated the light into its transverse electric and transverse magnetic components, which were then each collected by a photodetector and sent on to an oscilloscope for viewing and data collection.

The waveguides were fabricated using different techniques, the biggest differences being a) the gasses present in the inductively coupled plasma (ICP) chamber, used for etching, and b) their relative pressures, a lower pressure resulting in smoother waveguide walls [1]. Two chips were fabricated using the two etching techniques. Each chip contained waveguides of differing widths, of which the 1.0  $\mu\text{m}$  and 1.5  $\mu\text{m}$  widths were examined in this experiment. In Figure 1, #1 lists the differences in the ICP processing, and #2 lists the differences in the resulting dimensions.

### Results:

Upon obtaining the Fabry-Perot graphs of the light exiting the waveguides, the noise present in the figures was filtered out, and then calculations were made to determine the intensity ratio (min/max intensity). This ratio was then used with Equation 1, relating the loss coefficient and the reflectivity to the intensity ratio. By plotting the intensity function versus the length of each waveguide, the loss and reflectivity can then be determined from the slope and y-intercept of the fitted line on the resulting graph.

This process was repeated for every data measurement made for all the 1.0  $\mu\text{m}$  and 1.5  $\mu\text{m}$  waveguides on the 1.5 mm, 2.5 mm, and 4 mm chips for both Etches 1 and 2. Table 1 clearly lists the results of this analysis.

The equation that relates the measured values to the loss and reflectivity is given as:

$$\alpha L - \ln(R) = \ln\left(\frac{1+\sqrt{\xi}}{1-\sqrt{\xi}}\right)$$

Equation 1: This equation relates the min/max intensity ratio to the reflectivity and the loss.

The waveguide losses followed a general trend of being the least lossy around 1550 nm, becoming more lossy the greater or smaller the wavelength becomes. Since 1550 nm is one of the two most common optical communication wavelengths, this result means that devices operating with either of these waveguides in place will have the greatest signal strength at that nominal wavelength.

### Conclusions and Future Directions:

For now, it seems as though both fabrication techniques proved to yield rather similar results, although it would appear that waveguides fabricated using Etch #1 perform better than Etch #2 at a width of 1  $\mu\text{m}$ , while the opposite seems to hold true for a width of 1.5  $\mu\text{m}$ . However, it is unclear as to how much attenuation losses due to the roughness of the waveguides factored into the loss differences. To eliminate this, the fabricated waveguides should be examined after a baking process has performed during their fabrication, allowing for the photoresist to reflow (thereby smoothing out the sidewalls) before the fabrication process is fully complete.

### Acknowledgements:

Special thanks to my professor, Dr. John Bowers, and my mentor, Hui-Wen Chen, for giving me this opportunity. I would also like to thank Alexander Fang and Anand Ramaswamy for their continued support, and Geza Kurczveil and John Aveson for keeping me company in the lab. Lastly, thanks to the NNIN REU Program and the NSF for making this all possible.

### References:

- [1] Matsutani, Akihiro, "Vertical and Smooth Etching of InP by  $\text{Cl}_2/\text{Xe}$  Inductively Coupled Plasma," Jpn. J.Appl.Phys, vol. 38, pp. 4260-4261, 1999.

1.0 $\mu\text{m}$	Etch #1			Etch #2		
	Loss (db/cm)	Reflectivity	Index	Loss (db/cm)	Reflectivity	Index
1525nm	-8.975	0.340	3.793	-13.603	0.194	2.572
1550nm	-4.174	0.299	3.417	-6.843	0.305	3.464
1575nm	-9.533	0.338	3.778	-8.642	0.285	3.290
1.5 $\mu\text{m}$	Etch #1			Etch #2		
	Loss (db/cm)	Reflectivity	Index	Loss (db/cm)	Reflectivity	Index
1525nm	-4.658	0.327	3.668	-11.708	0.301	3.435
1550nm	-6.514	0.306	3.476	-5.294	0.303	3.446
1575nm	-9.121	0.333	3.732	-6.884	0.296	3.389

Table 1: Differences in loss, reflectivity, and effective index for Etches 1 and 2 at different wavelengths and waveguide widths.



# First Principle Interatomic Force Constants for Thermal Conductivity Applications

Garron Deshazer

Physics and Computer Science, Emory University

**NNIN REU Site: Cornell NanoScale Science and Technology Facility, Cornell University, Ithaca, NY**

NNIN REU Principal Investigator and Mentor: Dr. Derek Stewart, Cornell NanoScale Facility, Cornell University

Contact: gdes haz2@yahoo.com, stewart@cnf.cornell.edu

## Abstract:

An accurate knowledge of heat transfer across semiconducting interfaces is critical to the performance of electronic devices. A phonon transport model capable of determining the thermal resistance at interfaces would provide better understanding of heat transfer issues in microelectronics materials, and also serve as a framework for designing new material interfaces. In this work, we examine phonon transport across a silicon-germanium interface using force constants based on first principles calculations. A density functional approach with a localized orbital basis set is used to determine the self-consistent charge and potential for bulk silicon, germanium, and a silicon-germanium interface. Once the equilibrium structure is determined, the interatomic force constants between atoms are extracted from a series of supercell calculations. With these interatomic force constants, the phonon dispersions for silicon (Si) and germanium (Ge) can be calculated and compared to experiment. The strength of the force constant as a function of distance between interacting atoms is also considered for the three systems. For bulk Si and Ge, we find that a large supercell (250 atoms) is required to generate phonon dispersions in good agreement with experiment. When plotted as a function of distance, the force constants generated between the displaced atom and its nearest neighbors (NN's) along the interface were relatively higher than the force constants between the systems containing only silicon or germanium. We will also discuss how these first principle interatomic force constants can be incorporated into a non-equilibrium Green's function approach to determine the interface thermal resistance.

## Introduction:

Electronic devices that are made for consumer needs are expeditiously being created on the nanoscale [1]. As devices such as computer processors continue to be made smaller, the power density at semiconducting interfaces has increased dramatically as well. Interfaces are critical for removing heat from layers with a high power densities and thermal hot spots. Accurate modeling of the phonon movement across these semiconducting interfaces provides insight into the thermal resistance at these barriers. Building a phonon transport model capable of accurately calculating the thermal resistance at interfaces would provide greater understanding of heat transfer issues for electronic materials and help to design new materials that will optimize heat transfer. For this study we used the density functional theory program *Spanish Initiative for Electronic Simulations for Thousands of Atoms* (SIESTA) to determine the self-consistent charge and potential for bulk silicon and germanium, and a silicon-germanium interface [2]. The interatomic force constants calculated between atoms within the each lattice system were extracted and used to generate a phonon spectrum and incorporated in a Green's function to calculate the thermal conductance [1].

## Procedure:

In order to accurately model the phonon transport across the silicon-germanium interface, the model needed to be tested for bulk silicon and bulk germanium lattices. First, the lattice constant for the bulk silicon system were determined by relaxing the atomic spacing and plotting the energy of the system as a function of volume. The volume versus total energy curve was used to determine the equilibrium lattice constant and associated bulk modulus. This was done for bulk germanium as well. The obtained lattice constants and bulk modulus compared well with experimental data. Once accurate lattice constants for bulk silicon and bulk germanium were found, the unit cell for the each system was created. The unit cell for silicon

contained parameters such as the lattice constant, the type of atoms, and the number of atoms within the unit cell. Once the unit cell was created a program called *fcbuild* was used to create the super cell lattice. The program duplicated an individual unit cell in the  $x,y,z$  directions to create a larger lattice composed of many identical cells [3]. The density functional theory program SIESTA was then run on the supercells for bulk silicon and bulk germanium. SIESTA used a localized orbital set to describe wave function of the crystal structure being tested. The program calculated the self-consistent potential and self-consistent charge of the lattice being tested, made an initial guess on the wave function that describes the atomic movement within the lattice, and calculated the total energy of the system.

Next, SIESTA moved the central atoms within the lattice in six directions (positive and negative  $x,y,z$ ) and calculated the band structures, total energy, and force constants between atoms with each atomic movement. Next, a program called *vibra* was used to determine the phonon spectrum based on the force constants generated from the SIESTA calculations [3]. This process was done for bulk silicon and bulk germanium lattices containing 54 atoms and 250 atoms. The phonon spectrum generated for these calculations were compared to experimental data. Once the model produced accurate phonon spectrums for the bulk silicon and bulk germanium systems, the silicon-germanium interface was then created [4]. The unit cell for the interface contained twelve layers; the first five were germanium, the middle two were silicon, and the next five were germanium.

Using SIESTA, the atomic positions near the interface were relaxed to their minimum force configuration. The program *fcbuild* was then run to create the large super cell containing 108 atoms. The same process as the bulk systems was done for the interface to calculate force constants and generate the phonon spectrum [5].

## Results:

Shown in Figures 1 and 2 are the phonon spectrum for the bulk silicon and bulk germanium lattices. Figure 1 shows the theoretical phonon spectrum and experimental data for a 54 atom and 250 atom silicon lattices. Figure 2 shows the theoretical phonon spectrum and experimental data for a 54 atom and 250 atom germanium lattices. Figure 3 shows the calculated force constant plotted as a function of distance for bulk silicon and bulk germanium, while Figure 4 shows the force constant versus distance graph for the silicon-germanium interface.

## Discussion/Conclusions:

It is shown from Figure 1 and Figure 2 that in order to provide accurate modeling of phonon movement for bulk silicon and bulk germanium using SIESTA, a supercell containing at least 250 atoms is necessary. This increase in accuracy is seen when the 54 bulk cases and 250 bulk cases are compared along the (-K symmetry line in the Brillouin zone. Along this line, the 250 atom silicon and germanium curves are in better agreement with the experimental data than the 54 atom curves [1,6]. The increase in accuracy makes sense considering when the density functional approach was implemented there was a larger sample size to approximate the phonon frequencies with their associative vectors for the 250 atomic supercell. Figure 3 shows force constants that were calculated from the density functional theory for a central atomic shift. The accuracy of the model is reaffirmed when looking at the force constants for the nearest neighbors (NN's) of the shifted atom for the bulk silicon and germanium systems. The force constant values for the nearest neighbors for silicon are higher than germanium which is in agreement with their bulk modulus values. Figure 4 shows the force constant versus distance graphs for an in-plane atomic shift and out-of-plane atomic shift for a silicon atom in the middle layer of the silicon-germanium interface. It is seen that for the NN's from the bottom graph of Figure 4 that the interface force constant values for the in-plane shift are very close to the force constant values for silicon. This makes sense considering that if an atom was shifted within the plane interactions with other silicon atoms would dominate. Consequently, there would be more variance in the force constants along the interface for an out of plane shift because there are more atomic interactions incorporated [6,7].

In conclusion, the model is now accurate enough to be tested on a larger silicon-germanium. In the near future the phonon dispersions and force constants for the current interface will be used in a Green's Function approach to calculate the thermal conductance. This will lead the model becoming more accurate in testing the thermal conductance across more complex interfaces [6,7].

## References:

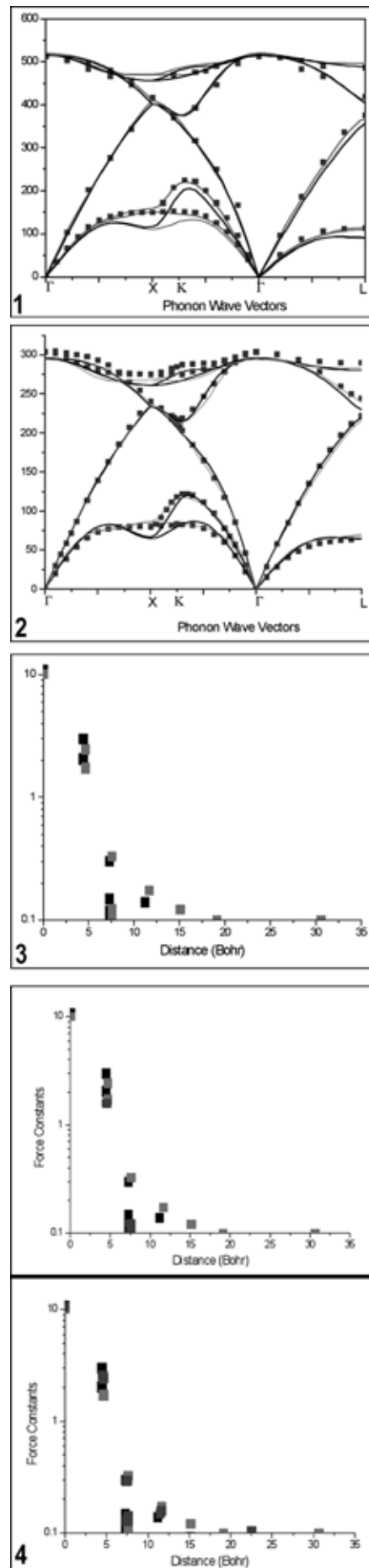
- [1] W. Zhang, T.S. Fisher, N. Mingo, J. of Heat Transfer, 129, 483 (2007).
- [2] J.Soler, E.Artacho, J.Gale, A.Garcia, J.Junquera, P.Orderjon, D. Sanchez-Portal, J. of Phys.: Condens. Matter 14, 2745 (2002).
- [3] Pablo Ordejon 2006 "Vibra Package, version 0.2".
- [4] M.Panzer, K.Goodson, J. of Appl. Phys. 103, 094301 (2008).
- [5] M. Aouissi, I. Hamdi, N. Meskini, and A. Qteish, Phys. Rev. B, 74, 054302 (2006).
- [6] Ho-Ki Lyeo, D.Cahill, Phys. Rev. B 73 144301 (2006).
- [7] M. Omini A. Sparavigna 1996, Physica B, 233 230 (1997).

Figure 1: The phonon spectrum for bulk silicon. The black line represents the 54 atom system, while the red line represents the 250 atom system. The blue squares are the experimental data.

Figure 2: The phonon spectrum for bulk germanium. The black line represents the 54 atom system, while the red line represents the 250 atom system. The blue squares are the experimental data.

Figure 3: Force constant versus distance for 250 atom bulk silicon and bulk germanium. The black squares represent the silicon atoms and the red squares represent germanium atoms.

Figure 4: Force constant versus atomic distance for the 108 atom silicon-germanium interface. The black squares represent the silicon atoms, the red squares represent germanium atoms, and the blue squares represent the interface interactions. The top graph depicts an out-of-plane shift of silicon atom in the central layer while the bottom graph depicts an in-plane shift of an Si atom.



# Fabricating a Magnetic Scanning Probe Microscope Tip

Sergio Oberlín González

Mechanical Engineering, University of Texas-Pan American

**NNIN REU Site: Center for Nanoscale Systems, Harvard University, Cambridge, MA**

NNIN REU Principal Investigator(s): Robert M. Westervelt, Ph.D., Applied Physics and of Physics, Harvard University

NNIN REU Mentor(s): Erin Boyd, Halvar Trodahl, Nanoscale Science and Engineering Center, Harvard University

Contact: sergy\_gonzalez@hotmail.com, westervelt@seas.harvard.edu, eboyd@fas.harvard.edu, htrodahl@fas.harvard.edu

## Abstract:

Electron spin in a quantum dot is an attractive candidate for spintronics and quantum information processing (QIP). However, the ability to controllably manipulate spin in quantum dot systems remains a challenge. One option is to use low temperature scanning probe microscopy (SPM) with a magnetic tip to influence spins in such systems. We present a method to fabricate a magnetic tip on an atomic force microscope (AFM) cantilever for use in a low temperature SPM. The method produces a fine samarium-cobalt (SmCo) tip that can generate a perturbative magnetic field to be applied to the sample when the tip is brought into proximity with a quantum dot.

## Introduction:

In conventional electronics, information is stored by charge [1], however, limits of lithographic processes are being reached and heat dissipation within integrated circuits is a problem. One alternative avenue that is being explored for computing is spintronics [2]. Information contained in electron spin current could move faster than information in conventional current, since only the spin of the electron would move rather than the electrons themselves [3]. Advantages of manipulating spin and spintronics technology, in comparison to conventional electronics, would be to greatly reduce heat in devices, decrease electric power consumption, and increase data processing speed.

We developed a procedure for fabricating a magnetic atomic force microscope (AFM) tip that can be used in the low temperature SPM used in the Westervelt lab at Harvard University. This microscope runs at liquid He-4 and He-3 temperatures, and has a magnet that can apply an external magnetic field of 7 Tesla to the sample and tip, therefore it is key that the tip be resistant to demagnetization. To manipulate spin, the tip should be 2-3  $\mu\text{m}$  high and have a diameter of no more than 100 nm that will be used to apply a localized magnetic field to quantum dots with 50 nm diameter.

## Materials and Processes:

The external magnetic field that can be applied in the SPM is 7T, thus the tip must be very resistant to demagnetization making SmCo an ideal choice for the tip material [4]. The cantilevers used are 250-350  $\mu\text{m}$  long and 30  $\mu\text{m}$  wide. We find and place on the cantilever particles that are 2-5  $\mu\text{m}$  in width and at least 2  $\mu\text{m}$  high. To create particles of this size we file a SmCo magnet then crush the filings with a mortar and pestle making a magnetic powder. Examination of this powder showed that particle sizes were appropriate for

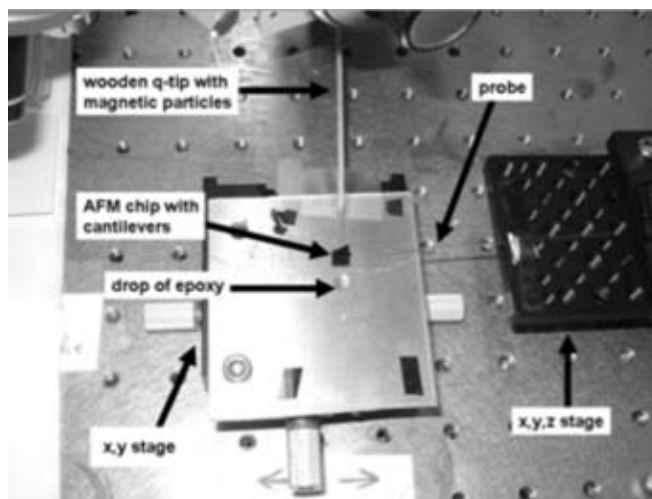


Figure 1: Stage setup used to transfer a magnetic particle onto a cantilever on an AFM chip.

placement on the cantilever. Transferring a magnetic particle onto a cantilever is accomplished by making a probe using a glass capillary that is 6 inches long and 1 mm in diameter; the capillary is placed in a micropipette puller that produces a probe with a 10  $\mu\text{m}$  diameter tip. Transferring a magnetic particle also requires an appropriate stage setup. This is carried out by using x,y and x,y,z stages. The probe is placed on the x,y,z stage that moves at a 5 $\mu\text{m}$  precision. All other materials go on an x,y stage (see Figure 1).

The epoxy used in this project is EPO-TEK 35ND which is appropriate for low temperature applications and will not shatter when exposed to the focused ion beam (FIB), discussed later in this report.

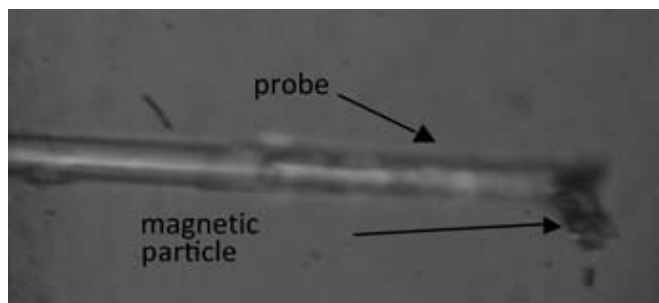


Figure 2, top: A glass probe transferring a magnetic particle onto a cantilever.

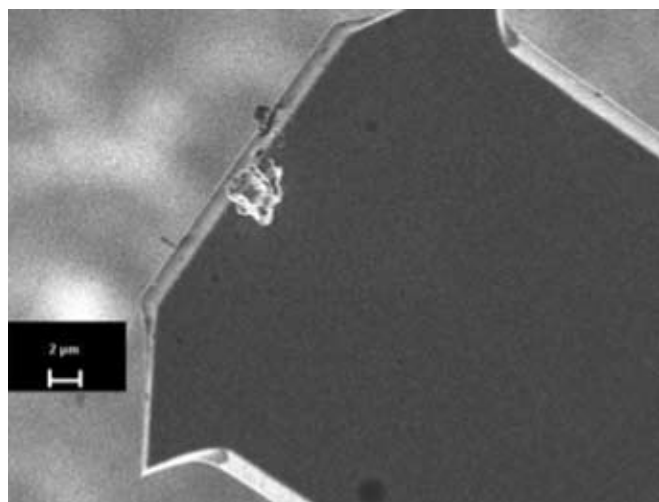


Figure 3, bottom: A magnetic particle about 3 μm across glued to the tip of a cantilever.

Working under a light microscope at 50x resolution, the probe is gently dipped into a drop of epoxy then repositioned to make contact with the cantilever leaving a small drop of epoxy. We attach a new probe to the x,y,z stage and focus on the wooden q-tip with the magnetic particles. The x,y stage is adjusted until a single magnetic particle is located on the q-tip. Taking advantage of Van der Waals forces, we remove a small magnetic particle from the q-tip by contacting the probe to a magnetic particle (see Figure 2) [5]; we select particles 2-5 μm in width and height (see Figure 3). Before the epoxy dries we place the attached particle 3/8 inch under a sintered ferrite ceramic magnet; this magnetic field repositions the particle on the cantilever so that poles are perpendicular to the cantilever. Twenty-four hours later samples are inspected with the light microscope to see if magnetic particles have repositioned and have a pole facing up. Samples are viewed in the scanning electron microscope (SEM) to verify there is only one magnetic particle on the cantilever. Appropriate samples are selected for the FIB; the FIB accelerates ions toward the sample and removes atoms in a process called milling.

For this project we milled SmCo which is a heavier material than the silicon cantilever where it sat, so we had to be careful

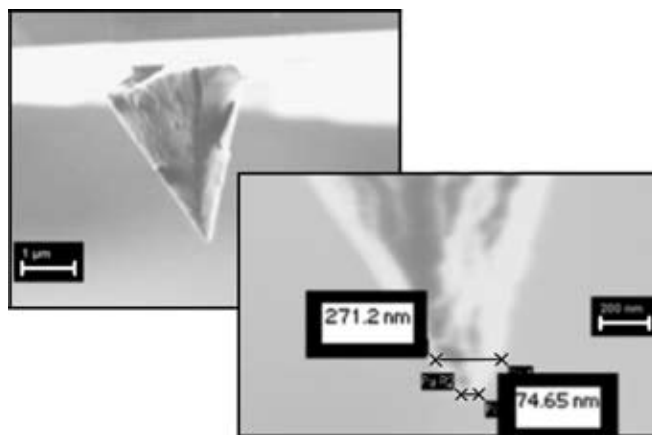


Figure 4: A SmCo magnetic particle milled into a tip.

not to inadvertently mill the cantilever. Also important, is that the FIB images with ions, which can potentially damage our sample, so we image at a low current of 10 pA and search for positions to begin milling. The ideal position for milling is when our view is perpendicular to the cantilever. With the object of interest in sight we adjust milling current to 150-180 pA and mill for approximately 60 seconds. These specifications worked well for fabricating a magnetic tip with tip diameter less than 100 nm (see Figure 4).

## Conclusions:

We have presented the techniques used to fabricate a magnetic SPM tip that could be used to manipulate spin in quantum dot systems. By following this procedure one can repeat this process and successfully fabricate a magnetic tip for future applications.

## Acknowledgements:

Thanks to Prof. R. Westervelt, Erin Boyd, Halvar Trodahl, Dr. K. Hollar, Prof. J. Free, Melanie-Claire Mallison, National Nanotechnology Infrastructure Network Research Experience for Undergraduates (NNIN REU) Program, NSF, and CNS at Harvard University.

## References:

- [1] Verity, J; "Electricity up to date for light, power, and traction"; 1896.
- [2] Allwood D.A. et al; Science 296, (2002).
- [3] Wolf, S. et al; Science 294, (2001).
- [4] Robinson, L; Science 223, (1984).
- [5] Parsegian, V.A; "Van der Waals Forces: A Handbook for Biologists, Chemists, Engineers, and Physicists"; 2006.

# Atomic Layer Deposition of Thin Film Hafnium Oxide as Top Gate Oxide in Graphene Field Effect Transistors

Derek Keefer

Chemistry, Beloit College

**NNIN REU Site: Penn State Nanofabrication Facility, The Pennsylvania State University, State College, PA**

NNIN REU Principal Investigator(s): Dr. Jun Zhu, Physics, The Pennsylvania State University

NNIN REU Mentor(s): Ke Zou, Physics, The Pennsylvania State University

Contact: Keeferd@stu.beloit.edu, jzhu@phys.psu.edu, kxz132@psu.edu

## Abstract:

Graphene is a single layer of  $sp^2$ -bonded carbon atoms arranged in a honeycomb lattice, which shows some unique electronic properties. Current field effect transistors based on graphene commonly use silicon dioxide/silicon ( $SiO_2/Si$ ) wafers as a global back gate. In order to locally control the carrier type and density, we plan to fabricate a hafnium oxide top gate. Using e-beam lithography and atomic layer deposition (ALD), we patterned and deposited a 45 nm thick layer of hafnium oxide across single and bi-layer graphene.

## Introduction:

As silicon electronics systems get smaller, they will eventually reach a limit as to how small their dimensions can become. There will be a need to find a new material with promising electronic properties on the nanoscale. Currently carbon-based materials display the most promise for these systems. Carbon nanotubes have many of the properties that are sought after in electronics, but controlling chirality and positioning the nanotubes for a circuit is difficult. A newly-discovered form of carbon-graphene, a two-dimensional material, shows great potential for applications in the electronic industry. Graphene, a single sheet of carbon atoms arranged in a honeycomb lattice, possesses a unique linear band structure and has higher carrier mobility than normal silicon devices. One way to make a p-n junction on graphene is to make a top gate oxide.

In previous experiments with a top gate oxide on graphene, a precursor molecule was needed so that  $Al_2O_3$  could be deposited on graphene [1]. The additional molecule layer between graphene and the oxide would change the properties of graphene; this is not ideal for a top gate material. Carriers are produced in graphene by applying an electric field. A positive electric field will cause graphene to be an N type carrier and a negative field will create a P type carrier. This property allows p-n junctions to be made on graphene. The process to make hafnium oxide ( $HfO_2$ ) top gates uses standard lithography techniques, so current semiconductor manufacturing equipment can be used.

## Experimental Procedures:

Thin sheets of graphene were produced by using mechanical exfoliation. A piece of scotch tape was placed on highly ordered pyrolytic graphite (HOPG) and a layer of HOPG was peeled away. The tape was then folded in half and separated several

times to spread out and cleave the graphite. The graphite was transferred to a silicon wafer coated with 300 nm of silicon dioxide. The surface of the tape was then rubbed gently with tweezers for 5-10 minutes, after which the tape was removed from the wafer. The wafer was then searched for thin layers of graphene using an optical microscope. Graphene could be optically identified on 300 nm thickness of silicon dioxide because graphene creates interference and contrast with the substrate.

After a suitable sheet of graphene was located, e-beam lithography was used to pattern the features for the top gate on graphene. After development of the e-beam resist, 45 nm of ( $HfO_2$ ) was deposited using ALD. ALD uses a two precursor gas system that alternates pulses of  $H_2O$  and  $Hf(NMe_2)_4$ . The two gases are pulsed over the graphene surface and when they react they form  $HfO_2$ . By changing the number of cycles, we are able to precisely control the thickness. The relatively low temperature of  $110^\circ C$  gave us a smooth film. Since ALD deposits a conformal layer, lift-off was more complicated. Lift-off was accomplished by soaking in warm ( $40^\circ C$ ) acetone for several hours.

## Results and Discussion:

It was found that of the two standard recipes for making hafnium oxide (one  $250^\circ C$  and the other  $110^\circ C$ ). They registered approximately 3 nm on the Roughness Measurement System (RMS) and 0.6 nm RMS respectively. The lower temperature recipe, therefore, yields a much smoother film. The roughness of the oxide film is important because it affects the evenness of the electric field and thus the carrier density. Even though graphite is hydrophobic, it was found that it is still possible to grow hafnium oxide on graphite without any coatings.

Figure 1 shows an AFM image of a square  $4\ \mu\text{m}$  by  $4\ \mu\text{m}$  of  $\text{HfO}_2$  that was deposited on a few layers of graphene. The hafnium oxide thin film has a consistent thickness of 45 nm and conforms to the profile of the surface. Figure 2 shows the roughness of hafnium oxide changes depending on whether it is on silicon dioxide or graphene. A second sample (Figure 3) was deposited under the same conditions, but lift-off consisted of only warm acetone. This yielded a cleaner  $\text{SiO}_2$  surface in addition to lifting off the  $\text{HfO}_2$ . The  $\text{HfO}_2$  is still rougher on graphene than on  $\text{SiO}_2$ . Figure 3 is an AFM image of the second trial. Figure 4 shows that the hafnium surface is still a little rougher on the graphene.

### Future Work:

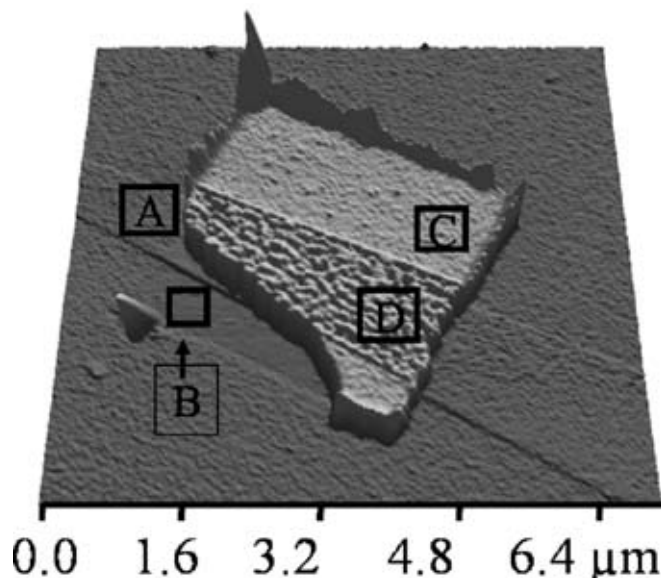
Primarily, we hope to improve lift off conditions. We hope to achieve this by decreasing the thickness and increasing the undercut. Moreover increasing the soaking temperature and possibly experimenting with sonication time could also help. Once lift off conditions are reliable the next step would be to test the effectiveness of the top gate oxide for carrier injection.

### Acknowledgements:

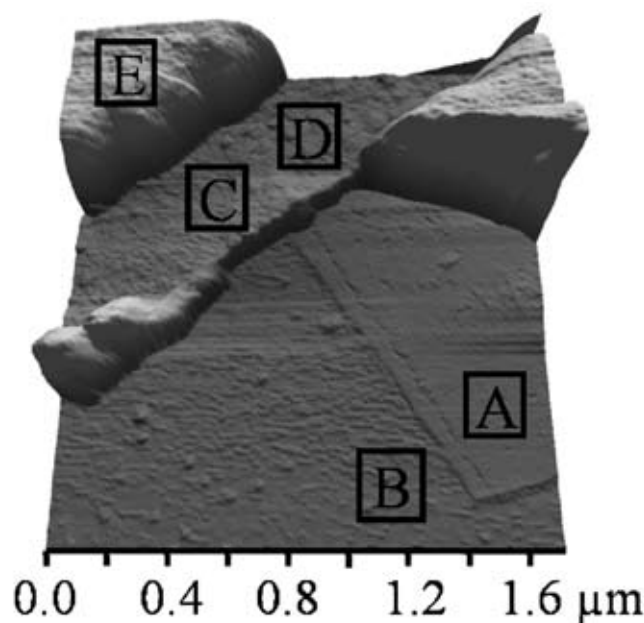
Ke Zou, Dr. Jun Zhu and Dr. Xia Hong and the Department of Physics. Funded by: National Science Foundation (NSF), National Nanotechnology Infrastructure Network Research Experience for Undergraduates (NNIN REU) Program, Penn State University (PSU).

### References:

- [1] Xinran Wang, Scott Tabakman and Hongjie Dai. Atomic layer deposition of metal oxide on pristine and functionalized graphene Department of chemistry and laboratory for advance materials, Stanford University, Stanford CA, 94305.
- [2] R.L. Puurunen. Surface chemistry of atomic layer deposition: A case study for the trimethylaluminum/water process. Journal of Applied Physics. Vol 90, No. 12, 15 June 2005.



Roughness RMS [nm]		Surface Type
A	0.4	Few layers of graphene on $\text{SiO}_2$
B	0.6	$\text{SiO}_2$ surface that was underneath $\text{HfO}_2$
C	1	45 nm of $\text{HfO}_2$ on top of $\text{SiO}_2$
D	3	45 nm of $\text{HfO}_2$ on top of few layers of graphene



Roughness RMS (nm)		Surface type
A	0.5	Few layers of graphene on $\text{SiO}_2$
B	0.8	$\text{SiO}_2$ surface that was underneath $\text{HfO}_2$
C	1	50 nm of $\text{HfO}_2$ on top of $\text{SiO}_2$
D	1.2	50 nm of $\text{HfO}_2$ on top of few layers of graphene
E	---	$\text{HfO}_2$ on resist

TOP

Figure 1: AFM image of  $\text{HfO}_2$  on graphene.

Figure 2: RMS values for Figure 1.

BOTTOM

Figure 3: AFM image of the second deposition of  $\text{HfO}_2$  on graphene.

Figure 4: RMS values for Figure 3.

# Grayscale Lithography and Its Application to Screw Dislocations in Colloidal Crystals

Jillian Kiser

Mechanical Engineering, Franklin W. Olin College of Engineering

**NNIN REU Site: Cornell NanoScale Science and Technology Facility, Cornell University, Ithaca, NY**

NNIN REU Principal Investigator(s): Itai Cohen, Physics, Cornell University

NNIN REU Mentor(s): Sharon Gerbode, Physics, Cornell University

Contact: jillian.kiser@students.olin.edu, ic64@cornell.edu, sjg53@cornell.edu

## Abstract:

In nature, screw dislocations cause atomic crystals to grow in upward spiral patterns [1], which is distinctly different from their typical island-like epitaxial growth patterns. However, the small size of these atomic crystals makes study of the growth of this dislocation-driven crystallization very difficult. Colloidal crystal growth, on the other hand, occurs on a scale that is visible using traditional microscopy techniques, and direct observations of such crystals allow an unprecedented glimpse of the particle-scale growth mechanisms.

The goal of this project was to study the spiral growth of colloidal crystals by providing the core of a screw dislocation and observing the growth of the crystals at the dislocation site. In order to accomplish this, grayscale lithography techniques were used to create a feature similar to a spiral staircase. Grayscale lithography is unique in that, unlike typical photolithography, some thickness of the photoresist remains after developing. For this application, we used a binary mask method, in which five different masks were created, each mask being assigned an exposure that is twice as long as the previous mask. Utilizing the additive properties of exposure doses, one wafer can be exposed using all five masks in order to create up to 32 different variations in height in the photoresist. Using this technique, we have achieved up to 24 steps in several variations of a spiral design and have begun to collect data regarding the colloidal crystal growth.

## Introduction:

The mechanisms of dislocation-driven growth in crystals are largely unknown, but have the potential to provide many insights into the natural world. By using grayscale lithography techniques to mimic the core of a screw dislocation, we hope to induce dislocation-driven growth in colloidal crystals to gain a better understanding of what causes this unique growth pattern.

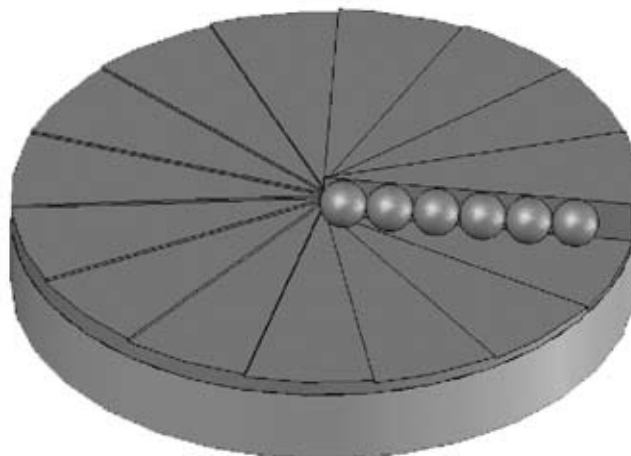


Figure 1: A cartoon of the 15 step spiral staircase design, with the crystal beginning to nucleate at the step edge.

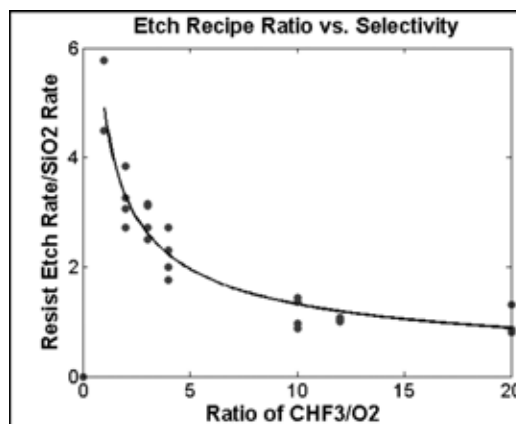


Figure 2: The relationship between the CHF<sub>3</sub>/O<sub>2</sub> ratio in the plasma etching recipe to the etch selectivity. The ratio of CHF<sub>3</sub>/O<sub>2</sub> used for this experiment was 30/25 ppm.

This research could lead to a more reliable process to grow thin films with less polycrystallinity. Currently, the manufacture of many circuitry devices relies on the epitaxial growth of atomic thin films, which can be difficult to produce without many grain boundaries and other dislocations. In dislocation-driven growth, however, the nucleation site at the dislocation is energetically favorable compared to nucleation sites at

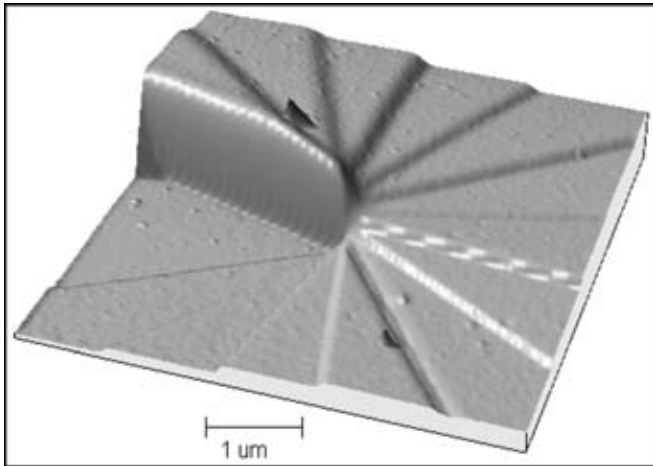


Figure 3: AFM of the 15 step spiral staircase design etched into oxide. The highest step is  $\sim 0.93 \mu\text{m}$  taller than the lowest step.

other points on the surface, which may help to minimize grain boundaries and other dislocations.

### Experimental Procedure:

A binary mask method was utilized to create a feature of varying heights. We used five masks, each of which was assigned a different dose ranging from 0.02 to 0.32 seconds, to create spiral staircase patterns of 15 different step heights in SPR 220-7 resist. Next, the resulting  $4 \mu\text{m}$  step height in the resist was transformed into a  $1 \mu\text{m}$  step height in a  $\text{SiO}_2$  layer on top of a glass coverslide. We did this by varying the selectivity through changing the ratio of  $\text{CHF}_3/\text{O}_2$  in the plasma. Because  $\text{O}_2$  etches photoresist quickly, but hardly etches oxide at all, increasing the amount of  $\text{O}_2$  in the plasma increases the rate at which the photoresist etches relative to the oxide. In this way we achieved a selectivity of 4:1, etching the photoresist 4 times more quickly as the oxide and changing the  $4 \mu\text{m}$  step in the photoresist to a  $1 \mu\text{m}$  step in the oxide.

With a  $12 \times 12$  array of this pattern etched into an oxide layer on the glass coverslide, we built a simple flow cell and deposited a colloidal suspension of  $1 \mu\text{m}$  silica particles dispersed in an index-matched solution of DMSO and water. In order to create an attractive force between these colloidal particles, we used polystyrene particles as a depletant. While allowing the particles to settle onto the coverslide over a period of 12 hours, we observed the crystallization using an inverted confocal microscope.

### Results and Conclusions:

As Figure 4 shows, the colloids are attracted to the step edge and heterogeneous nucleation has occurred at multiple locations along the step edge. In addition, these heterogeneously nucleated crystals seem to align with the step edge, which could lead to larger single-domain regions and less polycrystallinity.

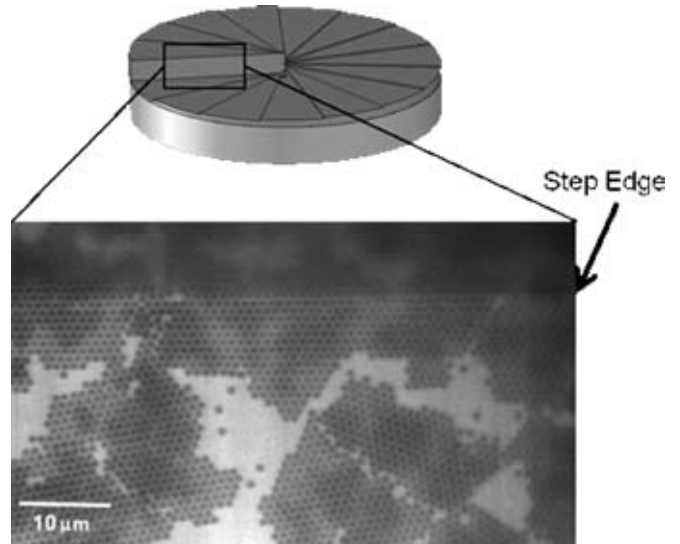


Figure 4: Colloidal crystals aligned with the step edge.

Homogeneous nucleation also occurred throughout the system. Until the depletion effect is properly tuned in order to eliminate the homogeneous nucleation, it is unlikely that the heterogeneous nucleation will be able to drive crystal growth in the type of spiral pattern that is seen in natural atomic systems.

### Future Work:

There are many exciting directions to explore related to the interactions between crystals and dislocations. First, we hope to examine the effects of using a different spiral pattern with two full revolutions and 24 steps, which we believe will more closely mimic the natural atomic system. We would also like to explore the interaction between two spirals in close proximity and the effects of applying shearing forces to the system. Examining the effect of these parameters on the polycrystallinity of the resulting crystal will help to elucidate whether dislocation-driven epitaxial growth can improve film quality, as would be desirable for such devices as microprocessors.

### Acknowledgements:

I'd like to thank the National Nanotechnology Infrastructure Network REU Program, the National Science Foundation, and Cornell NanoScale Facility for their financial support of this project. I'd also like to thank the Cohen Group, especially Itai Cohen and Sharon Gerbode, and Cornell NanoScale Facility staff for their great encouragement and support.

### References:

- [1] Kodambaka, S, S. V. Khare, W. Swiech, and K. Ohmori. "Dislocation-driven surface dynamics on solids." *Nature*. 429 (2004): 49-51.

# Probing the Microscopic Origins of Strain Stiffening in Biopolymer Gels

Victoria Reeves

Chemistry, Benedict College

**NNIN REU Site: Center for Nanoscale Systems, Harvard University, Cambridge, MA**

NNIN REU Principal Investigator(s): Professor David A. Weitz, School of Engineering and Applied Sciences/

Department of Physics, Harvard University

NNIN REU Mentor(s): Louise Jawerth, School of Engineering and Applied Sciences/

Department of Physics, Harvard University

Contact: vreeves16@yahoo.com, weitz@seas.harvard.edu, ljawerth@fas.harvard.edu

## Abstract:

Using microscopic imaging of sparsely cross-linked actin networks, we looked to better understand what is responsible for strain stiffening in biopolymer gels. Actin networks were labeled with fluorescent dye to see how the individual filaments reacted to shearing. By polymerizing these filaments, *in vitro*, within a larger sea of unlabelled actin, we were able to observe the deviations of thermal fluctuations in these filaments.

With further research, the non-linear rheology of gels formed by these viscoelastic biopolymers could allow for further mechanisms by which cells can be made to respond to, and model, the mechanical characteristics of these networks.

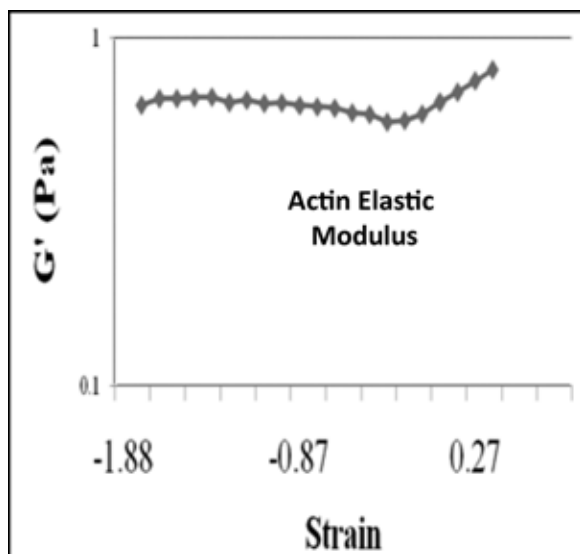


Figure 1: Nonlinear correlation between the strain applied to the network and stress until breakage.

## Introduction:

Cytoskeletal microfilaments, located just below the cell membrane, are responsible for resisting tension and maintaining cellular shape. Actin, a subunit of microfilaments, contributes in major aspects of cellular functions, including muscle contraction and motility. The mechanical elements and elasticity of these networks are, more specifically, critical in determining how forces act on and effect living cells.

*In vivo*, the mechanical characteristics of the cytoskeletal network are not only controlled by the concentration of actin, but by the cross-linkers that bind the actin filaments into

networks. Networks of biopolymers, like those of f-actin, have viscoelastic properties that are very different from those of other materials. When strain is applied to f-actin, the network is stressed more or less linearly, and then begins to stiffen, causing a nonlinear correlation between the strain applied to the network and stress until breakage, as shown in Figure 1. Models have been developed which explain this phenomenon from the dynamics of individual filaments. Rheological methods have been used to analyze this phenomenon, but no one, until now, has looked at individual actin filaments bound into a network by specific cross-linkers, in order to determine how the stress-strain relation actually effects the motility of the filament, network, and, in essence, the entire cell. *In vitro* methods were used to image the purely thermal fluctuations of actin, caused by Brownian motion.

## Materials/Methods:

We crosslinked the actin filaments with heavy meromyosin, the larger of two fragments, acquired from the full-length protein, myosin II, which comes from rabbit skeletal muscle. This *in vitro* actomyosin network was prepared from 93  $\mu\text{M}$  actin, obtained using purified monomeric actin from rabbit skeletal muscle, according to Spudich and Watt, and gel-filtered to remove capping proteins. All actin samples in this experiment were diluted with a combination of F-buffer and G-buffer. 93  $\mu\text{M}$  actin was prepared with Alexa 488 Phalloidin and buffer to yield 0.28  $\mu\text{M}$  F-actin, which was then added to a Rhodamine 532 fluorescent network prepared with buffer, heavy meromyosin (HMM/Actin ratio 1/100), and 93  $\mu\text{M}$  F-actin. Oxygen scavengers were prepared using 2.25 M glucose, 7.15 M 2-mercaptoethanol, 20 mg/ml glucose oxidase, and 3.5 mg/ml catalase. (Diluted x10) Upon

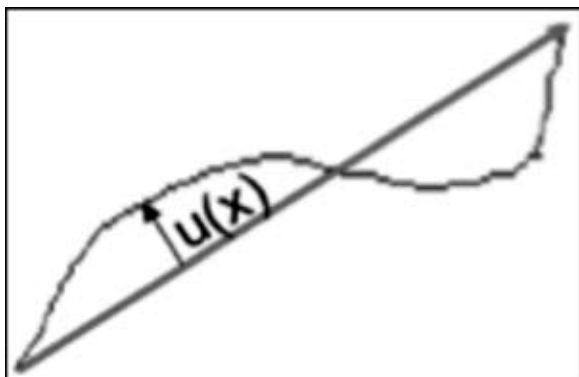


Figure 2: The straight line is the end-to-end distance of an individual filament while the function  $u(x)$  represents the deviation of this.

placing the network on the glass slide,  $1.0 \mu\text{l}$  of OS was added to help control bleaching of the filaments. Filament fluctuations were analyzed using the model shown in Fig. 2.

### Results/Discussion/Conclusions:

Using the parameters described, the total average deviation of a single actin filament from its original position was found to be approximately  $1 \mu\text{m}$ . This was calculated using the imaging program *imageJ*. The maximum projection of an image is done by taking the maximum intensity throughout an entire stack (Z axis) and making that the pixel value. If there is something moving, relative to time, within a given stack, its maximum projection indicates the magnitude of its motion, and roughly the size of its fluctuations. The deviation of these fluctuations, from specific end-to-end coordinates, more simply, represents their amplitude. More calculations must be conducted to better quantify the size of these fluctuations.

From this experiment we have concluded that the imaging of individual actin filament is very possible, though precise sample preparation is required, based on the concentration of the gels, and imaging equipment being utilized. Photo-bleaching inhibitors were of great necessity with the imaging of our particular actin gels. With the incorporation of catalase-based inhibitors, the available imaging time producing quantifiable images and videos improved from a mere 30 seconds to over five minutes for a single gels sample. We have also concluded rough measurements of filamentous

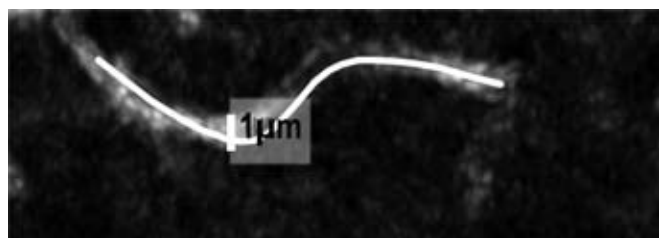


Figure 3: Max Projection Image Image of the greatest intensity values throughout the X, Y and Z positions of a single fluctuating filament in time.

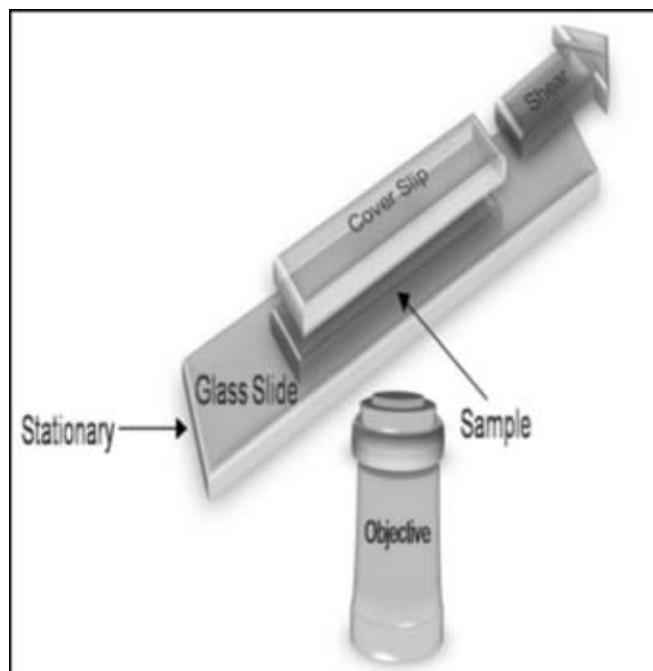


Figure 4: Our hypothesis is that the maximum projection of these filament fluctuations will decrease as a result of shearing.

fluctuation amplitudes can be conducted. Finally, we found that in a single Z-stack, the average fluctuation deviation from start to finish is  $1 \mu\text{m}$ .

### Future Work:

For future work, we would like to attach a shear cell, similar to the one in Figure 4, to a confocal microscope (Leica SP5, Germany) in order to apply stress to the network, and analyze the changes that occur in comparison to our un-sheared network. Confocal images would then be taken at different shear positions, until the network reaches critical strain and breaks. The shear cell would require a  $40 \mu\text{l}$  sample at the same concentrations described above.

### Acknowledgements:

Louise Jawerth, Chase Broedersz, Karen Kasza, Dr. David A. Weitz, Weitzlab at Harvard University, and the National Nanotechnology Infrastructure Network Research Experience for Undergraduates (NNIN REU) Program.

### References:

- [1] F.C. MacKintosh et al., Phys. Rev. Lett. 75, 4425 (1995).
- [2] J. Liu, K. E. Kasza, G. H. Koenderink, D. Vader, C. P. Broedersz, F. C. MacKintosh, and D. A. Weitz, preprint.
- [3] J. Spudich and S. Watt, J. Biol. Chem. 246, 4866 (1971).
- [4] Karen E Kasza, Amy C Rowat, Jiayu Liu, Thomas E Angelini, Clifford P Brangwynne, Gijsje H Koenderink and David A Weitz, Current Opinions in Cell Biology 19, 101-107 (2007).



# Using Near-Field Holography to Investigate Super Hydrophobic Surfaces

Noah Allen

Electrical Engineering, Georgia Institute of Technology

**NNIN REU Site: Cornell NanoScale Science and Technology Facility, Cornell University, Ithaca, NY**

NNIN REU Principal Investigator(s): Donald Tennant, CNF Director of Operations, Cornell University

NNIN REU Mentor(s): Garry Bordonaro, CNF Microlithographic Engineer, Cornell University

Contact: noah@gatech.edu, tennant@cnf.cornell.edu, bordonaro@cnf.cornell.edu

## Abstract:

Near-field holography is a photolithographic process that allows the transfer of nanoscale gratings from a phase mask into photoresist. In this project, the phase grating mask was transferred with a crossed double exposure on a substrate, forming an array of dots after development. Varying the ultraviolet exposure across the substrate created a gradient of printed dot sizes. Etching the dot array created a varying diameter pillar array which could then be tested for changes in hydrophobicity. The goal of the project was to utilize the near-field holography system so that surface wetting properties could be tested easily and cheaply. It was found that as the surface area on top of the pillars was increased the hydrophobicity of deionized water decreased exponentially from 180°. The resultant nanostructured surfaces produced a contact angle range from 130° to 155°.

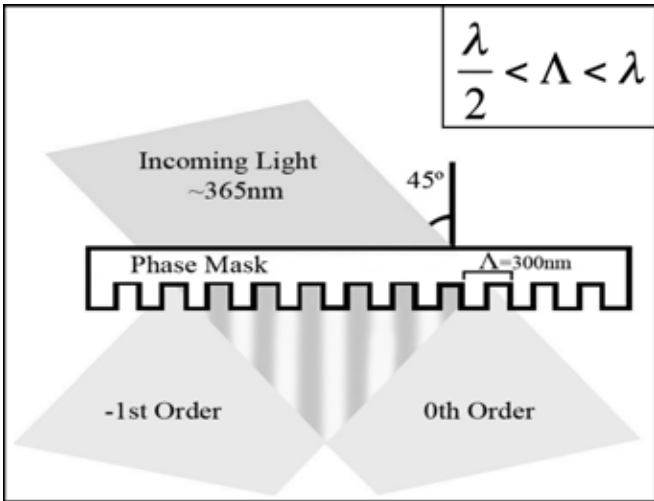


Figure 1: Schematic of NFH system.

mimics the period of the phase mask which is then transferred into the photoactive material.

We utilized this tool by using a double exposure in which the wafer was rotated 90° to create an array of dots printed onto the substrate. Etching the substrate using the patterned photoresist films as a mask, we were able to create nanopillars ranging from 30 nm to 300 nm in height. This was important so that we could investigate the properties of nanopillars in relation to surface wetting characteristics. Improving the hydrophobicity would have applications to research in fields such as thermal cooling solutions and microfluidic channel coatings [2].

## Materials and Methods:

The pattern was etched into 2 inch wafers because the smaller chuck size permitted vacuum contact on the NFH system. Before depositing any of the photoactive materials onto the wafer, a 40 nm thermally grown silicon dioxide layer was implemented to act as a hard mask layer. To reduce standing waves in the vertical direction, an XHRi-16 antireflective coating (ARC) was spun onto the substrate. The ARC was thinned because the first absorbance minima occurred when light traveled 60 nm through the film. In our setup, the UV light entered the film at an angle, increasing the distance traveled. It was found that the wave traveled at a 26° angle from the normal, allowing us to decrease the thickness from 60 nm to 54 nm. The ARC was diluted to 25% creating a 53 nm film spun at 1500 rpm and baked at 175°C.

Because the light source used was not a perfect point source, the interference patterns further below the mask became less well defined, presenting lower quality printing. This was solved by

## Introduction:

The near-field holography system [1] is a tool that utilizes i-line ultraviolet light just like most photolithographic tools except for two notable differences. Instead of guiding the light into the mask at a normal, the light generated by a point source typically enters at an angle near 45°. The spatial coherence of the source makes this system less suitable for printing arbitrary features; instead it utilizes a unique phase grating mask with a period ( $\Lambda$ ) that satisfies the condition shown in Figure 1. The incoming UV light diffracts only two orders, the -1<sup>st</sup> and 0<sup>th</sup> order, below the mask creating constructive and destructive interferences. The interference pattern, just below the mask,

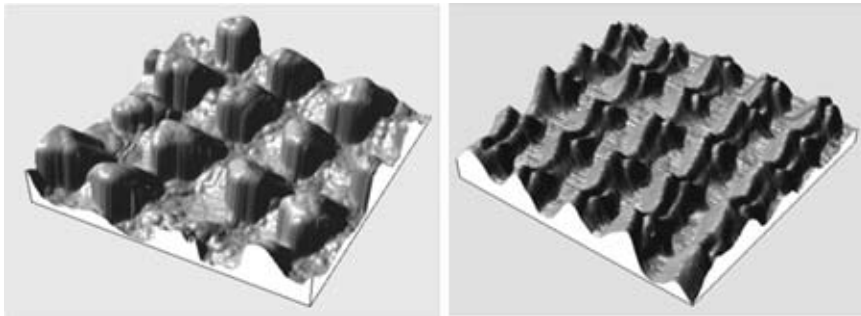


Figure 2: (L) Nanopillars created from Cl etch. (R) nanopillars created from SF<sub>6</sub> etch.

decreasing the thickness of the photoresist, Fujifilm OiR 620, so that the UV light interference pattern would not become incoherent before reaching the ARC layer. It was found that diluting the photoresist down to 25% could thin the film to 60 nm if spun at 6000 rpm. The optimum recipe included a softbake at 95°C for 10-15 seconds, then exposing the wafer with a total of 29.25 ml/cm<sup>2</sup>. After exposing the wafer, a hard bake, development in MF321 (0.21N tetramethyl ammonium hydroxide) and water rinse completed the process.

Etching was done in the Oxford 80 reactive ion etch system where, initially, an oxygen plasma was applied for 52 seconds as a clean up step. Next, a CHF<sub>3</sub>/O<sub>2</sub> etch was implemented to transfer the pattern down into the oxide layer. Finally the pattern was etched into the silicon wafer using either an isotropic SF<sub>6</sub> etch or anisotropic chlorine etch. Creating vertical pillars was done by executing a chlorine etch and creating a pyramid type structure was done by executing an SF<sub>6</sub> etch (see Figure 2). The deposition of a hydrophobic monolayer, FOTS (fluorooctatrchlorosilane), onto the wafer completed the fabrication process.

### Results and Conclusions:

The hydrophobicity was tested by placing a 2 μL drop of deionized water on the surface and using the VCA Optima tool to measure the contact angle with the surface. On a clean silicon control wafer, the hydrophobicity improved from a 38° contact angle to a 109° contact angle with the addition of FOTS. The observed results for the etched surfaces ranged between a 130° contact angle for the higher percentage surface area structures up to a 155° contact angle for the 20% surface area (see Figure 3). It was observed that as the

percentage of surface area in contact with the liquid drop increased linearly, the surface contact angle would decrease exponentially over the range of surface areas from 20% to 100%.

We therefore conclude that NFH is an effective method to achieve nanostructured surfaces capable of producing superhydrophobicity.

### Acknowledgements:

This work was funded by the Intel Foundation, hosted by the National Nanotechnology Infrastructure Network Research Experience for Undergraduates Program and the National Science Foundation, and used the Cornell NanoScale Facility (CNF).

### References:

- [1] J. M. Verdiell, T. L. Koch, D. M. Tennant, K. Feder, R. P. Gnall, M. G. Young, B. I. Miller, U. Koren, M. A. Newkirk, and B. Tell, "8-Wavelength DBR Laser Array Fabricated with a Single-Step Bragg Grating Printing Technique," IEEE Photonics Technology Letters, Vol. 5, NO. 6, June 1993.
- [2] Tom N. Krupenkin, J. Ashley Taylor, Tobias M. Schneider, and Shu Yang, "From Rolling Ball to Complete Wetting: The Dynamic Tuning of Liquids on Nanostructured Surfaces," Langmuir 2004, 20, 3824-3827.

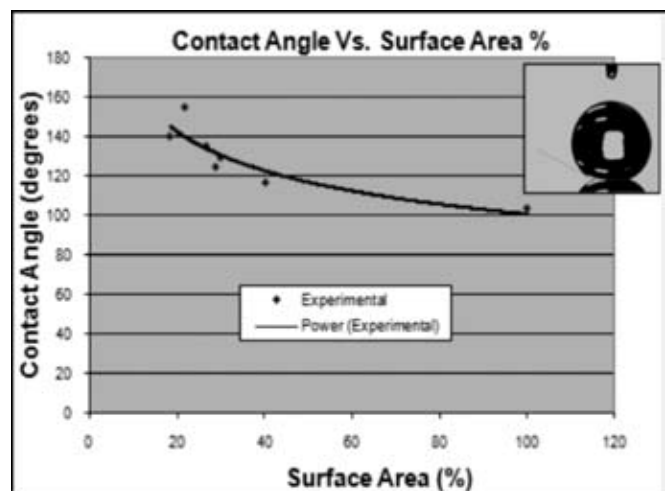


Figure: Dependence of contact angle on surface area of pillar structures for 2 μl water droplet. Inset shows droplet on 20% surface area pillars.

# Characterization of Graphene-Based Interconnects

Jason Brooks

Electrical Engineering, University of Memphis

**NNIN REU Site: Microelectronics Research Center, Georgia Institute of Technology, Atlanta, GA**

NNIN REU Principal Investigator(s): Dr. Raghunath Murali, Microelectronics Research Center, Georgia Tech

NNIN REU Mentor(s): Yinxiao Yang, Electrical Engineering, Georgia Institute of Technology

Contact: jmbrooks@memphis.edu, rm206@mail.gatech.edu

## Abstract:

Graphene shows a high potential in outperforming copper as the material of choice for next-generation complementary metal oxide semiconductor (CMOS) interconnects. In nanometer-wide channels of the same aspect ratio, graphene is expected to have a higher conductance compared to copper (Cu). Several important factors affect the performance of graphene and need to be explored to showcase its full potential. This project focuses on palladium-graphene contact interaction and the resistivity of graphene interconnects in comparison to Cu. Fabrication of 30 nm wide ribbons is performed via electron-beam lithography followed by a plasma etch to transfer the resist pattern onto graphene. The results show a low contact resistance and no measurable Schottky barrier at the contact. The interconnect resistivity is higher than that of Cu, though close to what is expected at a 30 nm line width.

## Introduction:

As the dimensions of integrated circuits steadily decrease, and integrated device speeds improve, copper-wire interconnects place increasingly significant limitations on circuit performance. In addition to reconstruction in systems architecture (e.g. multiple cores) to solve the global interconnect bottleneck, alternatives are being sought to replace copper with a more conductive material. One promising candidate is graphene, a single sheet of  $sp^2$ -bonded carbon atoms. Isolated only four years ago, graphene has already shown extremely high electron mobility at room temperature [1] along with ballistic transport.

On-chip interconnect delay is a bottle-neck for achieving increased chip performance; this problem is only exacerbated with transistor scaling. For 45 nm technology generations and below, size effects in Cu result in increased wire resistivity compared to its bulk value. Thus, there is a high motivation to identify materials and processes to overcome the limitation of Cu interconnects. Graphene nanoribbons (GNRs) are classified as metallic or semiconductor depending on their chirality. Recent conductance models indicate that when line widths are reduced below 8 nm, the resistivity of metallic GNRs levels off while that of Cu wires (with unity aspect ratio) exceedingly rises [2]. This project focuses on the characterization of graphene interconnects. The goals of the project are to (i) extract the contact resistance of palladium to graphene for 30 nm interconnects, and (ii) compare performance (by resistivity) of graphene to Cu interconnects.

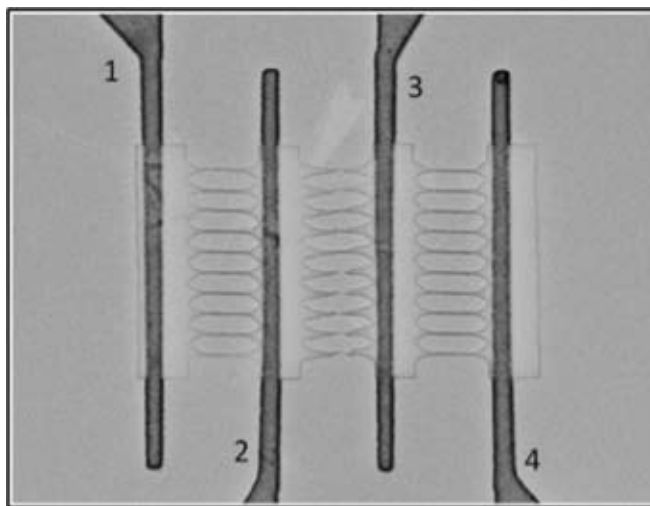


Figure 1: Top view of fabricated graphene channels with Pd/Au contacts.

## Experimental Procedure:

Mono and few-layer graphene was deposited onto a 300 nm thermally grown oxide layer (on doped p-type silicon) using a well-known mechanical exfoliation method [1]. The thickness of these graphene flakes was determined by visual contrast as well as atomic force microscopy (AFM).

A JEOL JBX-9300FS electron beam lithography (EBL) system was used to define contacts (1-4, Figure 1) as well as the ribbons in the graphene flake. A metal liftoff process was used to obtain contacts made of palladium (Pd) and gold (Au) and an oxygen plasma was used to etch nanoribbon patterns into graphene. The line widths of the ribbons were in the 30-nm range. Electrical properties were measured at room temperature using an HP4156 Semiconductor Parameter Analyzer.

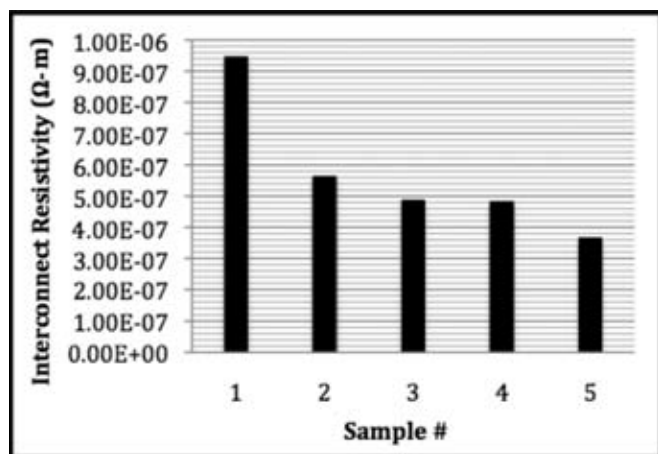


Figure 2: Graphene interconnect resistivity.

### Analysis:

The resistivity shown in Figure 2 is that of ten parallel ribbons; this value was determined after subtracting out the contact resistance. A majority of the interconnects exhibited a resistivity less than  $50 \mu\Omega\text{-cm}$ . The average interconnect resistivity was  $71 \mu\Omega\text{-cm}$ , with the lowest being  $37 \mu\Omega\text{-cm}$ . These values are an order of magnitude higher than the bulk resistivity of Cu ( $1.72 \mu\Omega\text{-cm}$ ) and resistivity of narrow Cu wires ( $5.0 \mu\Omega\text{-cm}$ ). Previously reported graphene resistivity in the literature ranges from 0.6 to  $200 \mu\Omega\text{-cm}$ . The measured resistances are an average of ten parallel ribbons, and variation in individual ribbon line widths and edge effects can contribute to a higher overall resistance. Recent results from the group have shown individual graphene ribbons to have comparable or even lower resistivity as compared to Cu interconnects.

The Pd-graphene specific contact resistance (Figure 3) for the same five samples had a mean value of  $6.9 \times 10^{-7} \Omega\text{-cm}^2$ , with the lowest being  $1.2 \times 10^{-7} \Omega\text{-cm}^2$ . Contacts were made to large areas ( $3 \mu\text{m} \times 0.2 \mu\text{m}$ ) to avoid a Schottky barrier. There was no measurable Schottky barrier even down to a few mV. The contact resistance may be further improved by cleaner fabrication and additional annealing.

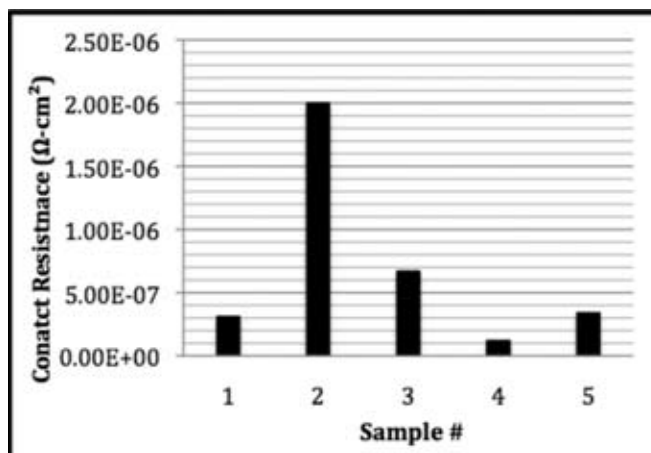


Figure 3: Pd-graphene specific contact resistance.

### Conclusions:

For a given sample, the Pd-graphene contact resistance was typically lower than the resistance measured across the corresponding parallel ribbons. On average, the contact resistance accounted for a tenth of the wire resistance. The resistivity of parallel ribbons measured in this experiment was much higher than theoretical projections – theory predicted a resistivity of  $0.1 \mu\Omega\text{-cm}$ ; but the measured values for 1D ribbons were within the range of previously published data for wide graphene ribbons and for 2D graphene.

This experiment concludes that graphene has realistic potential to outperform Cu for next-generation interconnects, though further research that expands upon graphene characterization will be necessary for a definitive conclusion.

### Acknowledgements:

We acknowledge the help of Jennifer Tatham Root, Dr. James Meindl, Thomas J. Beck, and the staff of the Georgia Tech Microelectronics Research Center. Funding for this project was provided by the National Nanotechnology Infrastructure Network Research Experience for Undergraduates (NNIN REU) Program and the National Science Foundation.

### References:

- [1] K.S. Novoselov, A.K. Geim, S.V. Morozov, D. Jiang, Y. Zhang, S.V. Dubonos, I.V. Grigorieva, A. A. Firsov, “Electric Field Effect in Atomically Thin Carbon Films”, *Science* 306, 666-669 (2004).
- [2] A. Naeemi, J.D. Meindl, “Conductance Modeling for Graphene Nanoribbon (GNR) Interconnects”, *IEEE Electron Device Letters*, Vol. 28, No. 5, May 2007.

# The Diamond Age: Fabrication on Nitrogen-Rich Diamond

David J. Christle

Physics and Mathematics, University of Minnesota-Twin Cities, Minneapolis, MN

**NNIN REU Site: Nanotech @ UCSB, University of California, Santa Barbara, CA**

NNIN REU Principal Investigator(s): Dr. David D. Awschalom, Physics, University of California Santa Barbara

NNIN REU Mentor(s): F. Joseph Heremans, Electrical and Computer Engineering, University of California Santa Barbara

Contact: christle@physics.umn.edu, awsch@physics.ucsb.edu, jheremans@umail.ucsb.edu

## Abstract:

Single-crystal diamond is attractive for use in both electronic and spintronic devices due to its wide 5.5 eV band gap, high thermal conductivity, and lattice defect states such as nitrogen-vacancy centers. These unique properties make diamond ideal for high-power/high-frequency applications, useful as a single-photon source for quantum cryptography, and as two-level system for use in spin-based quantum computation at ambient temperature [1,2]. While current diamond devices rely on polycrystalline diamonds grown by chemical vapor deposition, advances in single-crystal diamond growth make it a feasible alternative to silicon-based devices.

## Experimental Procedure:

In this work, we utilized photolithographic techniques applied to diamond for patterning and deposition of electrical gates for use in the study of a charge-storage effect in diamond. Solutions to challenges in small-sample fabrication are presented. We carried out diamond etching using a focused ion beam system to create micron-sized, free-standing bridges for use as photoexcitation channels of a known depth.

Experiments on nitrogen-rich diamond showed carrier photoexcitation after illumination at energies below the band gap of diamond [3]. A patterned layer of Au was deposited on the diamond surface whereby two Au pads were separated by a channel. We created these “gate” structures with separation gaps of 2  $\mu\text{m}$  to 100  $\mu\text{m}$ . We focussed a 532 nm wavelength (2.3 eV) laser on the sample surface to bridge the gap and apply a voltage across the gate to observe a picoamp current. If we extinguished the laser, removed the source voltage, and subsequently restarted the laser, we observed a picoamp discharge current decaying in a roughly stretched-exponential fashion with a time constant on the order of minutes [4]. The charge carriers decayed to an intermediate energy nitrogen impurity level, and the current flow was dominated by space-charge effects [5]. Samples fabricated in this work were designed to study the effect’s dependence on gap length, focal point, and depth of the excitation channel.

We used Type Ib single-crystal diamond samples measuring 1.5 mm  $\times$  1.5 mm  $\times$  1.0 mm grown by high-temperature, high-pressure methods, with a nitrogen concentration of roughly  $10^{19}$  cm<sup>-3</sup>. Figure 1 is an optical micrograph of a mask for a gate pattern with gaps of 2  $\mu\text{m}$ , 4  $\mu\text{m}$ , 6  $\mu\text{m}$ , and 20  $\mu\text{m}$  that the laser may bridge independently. We designed the gap width at least a factor of two larger than the gap length so that photoexcitation occurred only in a region of constant gate separation even when the focal point depth was changed.

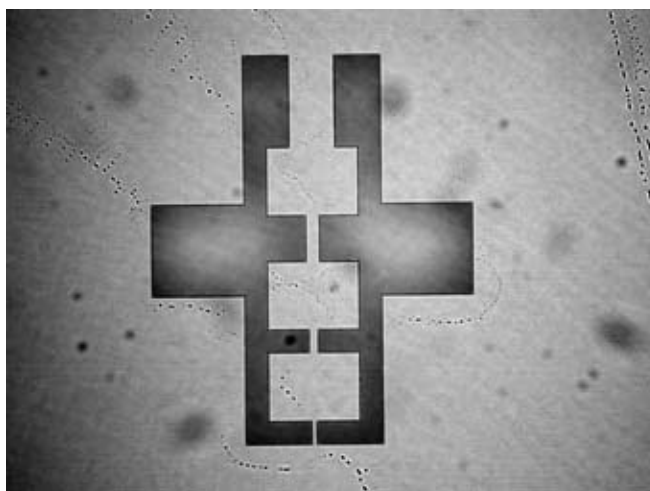


Figure 1: A photolithography mask containing variable gap lengths.

Standard spin-coating techniques produced an uneven buildup of resist at the sample edges, and the unusually small size of the samples in this research meant the entire surface area was dominated by these edge effects. To work around this limitation, we included two additional steps in our spin coating process. Each sample was wax-bound to a glass microscope slide and attached to a photoresist spinner chuck such that the sample was approximately 1 cm off-center. This was done to increase the force felt by the photoresist during spinning.

A second sample was wax-bound adjacent to the first even further from the center of the chuck. The net effect of both steps was the displacement of the photoresist edge buildup from the inner sample to the outer sample. In this fashion, the inner sample contained only one edge bead and a relatively

large surface area of uniform resist coating, while the second sample could be cleaned and reused. Figure 2a shows an optical image of a post-development coplanar waveguide pattern that demonstrates photoresist buildup on only a single edge. Profilometry indicated the SPR955 0.9  $\mu\text{m}$  resist had a nominal 0.7  $\mu\text{m}$  thickness, and we found optimal feature-resolution at a 1.3 second exposure. Finally, we deposited the Ti(50Å)/Au(1500Å) layer by electron-beam-induced deposition.

To study depth dependence of the photoexcitation, we created another design containing 32 independent single-gap gates with 5  $\mu\text{m}$  gap lengths shown in Figure 2b. Through the use of a focused ion beam system, we patterned an 11  $\mu\text{m}$  deep 15  $\mu\text{m} \times 5 \mu\text{m}$  undercut at a 52° tilt from the surface normal on each side of an excitation channel to create a free-standing bridge. Figure 3a shows an SEM micrograph of a completed structure using this process on diamond. Figure 3b shows the same structure rotated 90° and tilted to illustrate the connecting undercuts after severing the bridge. In this etching depth regime, the effective diamond etch rate was 2.4 times slower than Si etching for the same geometry, however this factor was non-linear with depth due to redeposition. By undercutting at different tilt angles, we now controlled the excitation channel depth, paving the way for study of the depth-dependence of the charge-storage effect.

## Conclusions:

We have thus demonstrated a method for reliable structure fabrication on small, single-crystal diamond samples via adjusted lithographic techniques and a focused ion beam procedure, preparing for future work in understanding the physical nature of the charge-storage effect.

## Acknowledgements:

David Christle would like to gratefully acknowledge mentor Joseph Heremans, post-doctoral researcher Dr. Greg Fuchs, and principal investigator Dr. David Awschalom for their generous support and tutelage throughout the program. This work was supported by the NSF, the AFOSR, and the National Nanotechnology Infrastructure Network REU program.

## References:

- [1] D. D. Awschalom, R. Epstein, and R. Hanson, *Sci. Amer* 297, 8 (2007).
- [2] Beverator et al., *Phys. Rev. Lett.* 89, 187901 (2002).
- [3] F. J. Heremans, G. D. Fuchs, C. F. Wang, R. Hanson, and D. D. Awschalom (2008 APS March Meeting, 2008).
- [4] C. G. Van de Walle, *Phys. Rev. B* 53 (1996).
- [5] Dyer et al., *Phil. Mag* 11, 763 (1965).

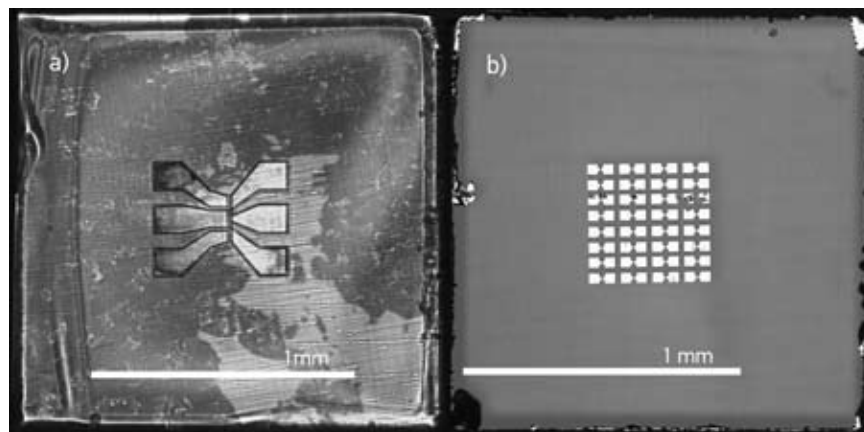


Figure 2: a) An optical image of a sample with developed photoresist.  
b) An optical image showing a gate array before focused ion beam etching.

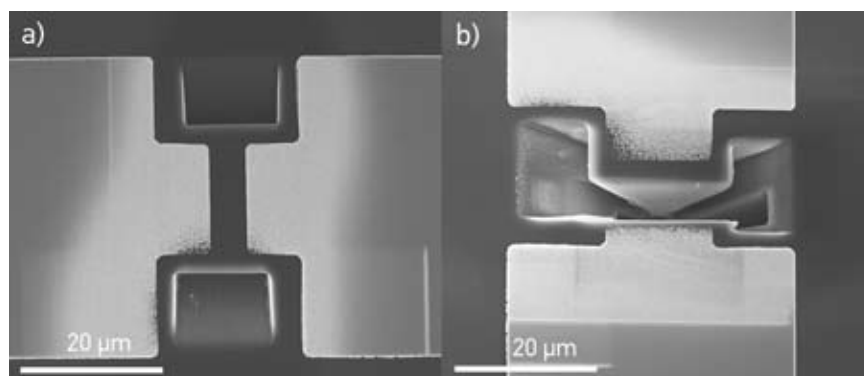


Figure 3: a) An SEM micrograph of a completed free-standing bridge structure.  
b) The same bridge structure after its severance.

# Self-Aligned Germanium TFT Flash Memory

Federico Garcia

Electrical Engineering, Columbia University



**NNIN REU Site: Cornell NanoScale Science and Technology Facility,  
Cornell University, Ithaca, NY**

*NNIN REU Principal Investigator(s): Edwin Kan, Electrical and Computer Engineering, Cornell University*

*NNIN REU Mentor(s): Jaegoo Lee, Electrical and Computer Engineering, Cornell University;*

*Ebenezer Amponsah, Electrical and Computer Engineering, Cornell University*

*Contact: fjj2105@columbia.edu, kan@ece.cornell.edu, jl548@cornell.edu, eka8@cornell.edu*

## Abstract/ Introduction:

In recent years, it has become difficult to scale complementary metal oxide semiconductor (CMOS) technology. There are problems with traditional scaling, such as an increase in leakage currents when the devices become smaller. In order to continue to make more efficient and cost effective devices for a growing flash market, new materials are sought, especially to replace the silicon channel. Incorporating a germanium (Ge) channel is an attractive option since Ge has lower effective mass and a higher hole (4X higher) and electron (2X higher) mobility compared with silicon (Si). Using a Ge channel instead of a Si channel done through e-beam evaporation and chemical mechanical polishing to make the surface smoother, a  $\text{Al}_2\text{O}_3$  tunnel oxide (atomic layer deposition, ALD), Au nanocrystals (e-beam evaporator),  $\text{Al}_2\text{O}_3$  control oxide (ALD), and Cr gate (e-beam evaporator), this thin film transistor device will be compared with a standard Si thin film transistor in terms of IV and CV characteristics. In addition, the self-aligned design will allow us to use ion implantation without a mask, which saves steps in our design process. Ideally, since Ge performs better in PMOS, it will be used only in PMOS on a CMOS platform.

## Experimental Procedure:

First, a mask was used for the alignment marks on the bare silicon wafers. For the resist spinning stage, using P-20 and 1813, we spun at 4000 RPM, 30 seconds; baked at 90°C, 1 minute; used the 5X stepper for exposure; developed using 300 MIF, 90 sec; and postbaked at 115°C 90 sec. Second, we etched the silicon using the Oxford 80-1 using  $\text{SF}_6/\text{O}_2$  at 45 sec. Next, oxide deposition via plasma enhanced chemical vapor deposition (PECVD) for 210 nm, followed by germanium deposition from the electron beam evaporator for 100 nm. We also deposited 20 nm Ge layers on some wafers for the control.

For the 100 nm Ge wafers, chemical mechanical polishing (CMP) was done to try to match the 20 nm layer. The CMP recipe that was used was; 4 psi (back pressure), 15 rpm (table speed), 15 rpm (chuck speed), using P-1000 as the slurry, and a poly pad. These wafers showed a low surface roughness rms = 0.122 nm compared with the non-CMP wafers of 0.224 nm from the atomic force microscope (AFM), shown on Figure 1 and Figure 2.

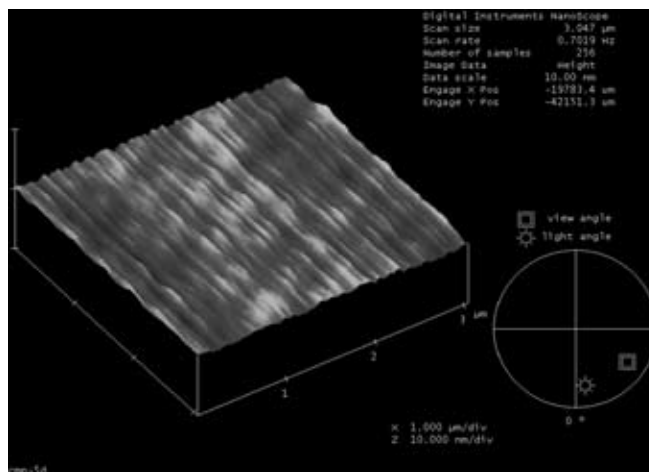
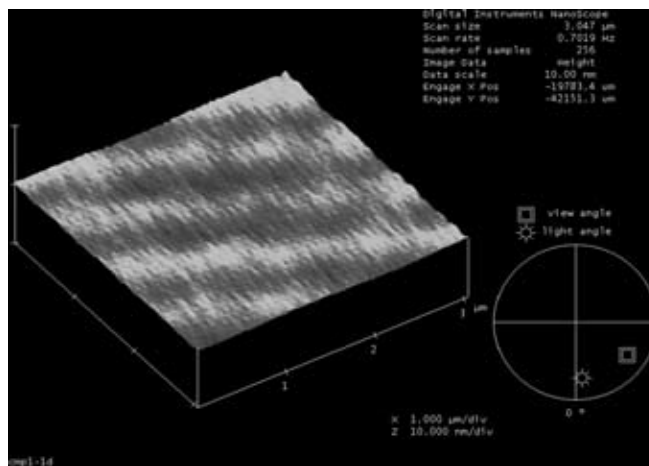


Figure 1, top: AFM. 4psi-15RPM-15RPM; Surface Roughness = 0.122 nm, using Slurry of P-1000 and poly pad.

Figure 2, bottom: AFM of non-CMP wafer.

A second mask was used, for the channel area, similar to the process used for the first mask. This was followed by the Ge etch on the Oxford 80-1 using  $\text{CF}_4$ , LOR spinning and prebake. We used 3000 RPM and tried 45 seconds for spinning, prebaking at  $180^\circ\text{C}$  for 5 min. Then exposed with our last mask for the transistor area, which would enable us to do a lift-off resist process, developed with MIF 300 at 90 seconds on some wafers and 120 s on others, and postbaked at  $115^\circ\text{C}$  for 90 sec.

Next, several splits were done. For all wafers, we deposited  $\text{Al}_2\text{O}_3$  using the ALD for the tunnel oxide for 6.3 nm. Next, gold nanocrystals were deposited on some wafers on the e-beam evaporator of 1.2 nm. This was followed by  $\text{Al}_2\text{O}_3$  deposition for the control oxide of 12.5 nm on some wafers. Other wafers had  $\text{TiDyO}$  as the control using sputtering.

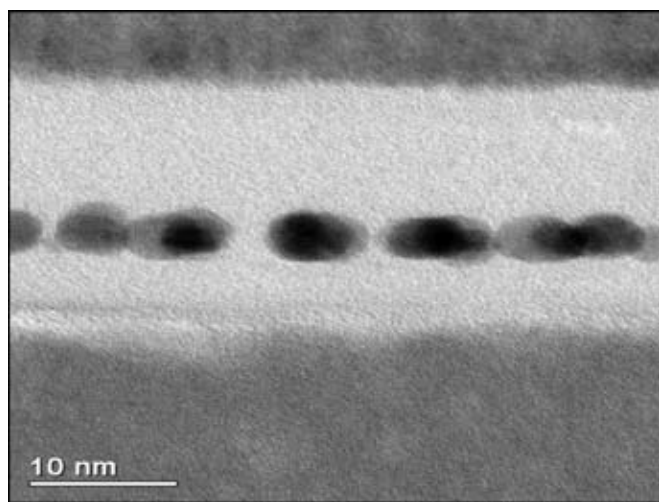


Figure 3: STEM. Bottom to top: germanium channel,  $\text{Al}_2\text{O}_3$ , Au nanocrystals,  $\text{Al}_2\text{O}_3$ , Cr gate.

Lastly, the chromium gate was deposited on the e-beam evaporator for 50 nm. This gate stack can be seen in Fig. 3.

Finally the lift-off process started, dipping the wafers in 1165 for a few hours. In retrospect, the LOR development stage of MIF 300 at 120 seconds was excessive, since it botched the gate deposition. 90 seconds worked better. A picture of this under the scope is seen on Figure 4. Ion implantation was done using the Eaton ion implanter, n-type phosphorous, at  $3 \times 10^{15}/\text{sq.cm}$ . Annealing was done to activate the dopants using the rapid thermal annealer for 1 min,  $450^\circ\text{C}$ , since the furnace tubes may have oxidized the germanium. Lastly, passivation was performed, using the furnace tubes with  $\text{H}_2/\text{Ar}$ ,  $400^\circ\text{C}$  for 30 min.

## Results/ Conclusion:

A few devices were tested with several different combinations of nanocrystals, and control oxides:

1.  $\text{Ge}(20\text{nm})/\text{Al}_2\text{O}_3\text{-tunnel}/\text{Au}/\text{Al}_2\text{O}_3\text{-control}/\text{Cr}$ ,
2.  $\text{Ge}(20\text{nm})/\text{Al}_2\text{O}_3\text{-tunnel}/\text{Al}_2\text{O}_3\text{-control}/\text{Cr}$ ,
3.  $\text{Ge}(20\text{nm})/\text{Al}_2\text{O}_3\text{-tunnel}/\text{Cr}$ .

The results were not ideal. The I-V curves did indeed look like normal transistor I-V curves except the currents were too low. We skipped the annealing of the germanium due to problems and lack of time. This should be noted for future work.

## Future Work:

Annealing was skipped due to the germanium oxidizing. Two theories were given. First, after heating the wafers (right after the germanium deposition), at  $600^\circ\text{C}$  1hr  $\text{N}_2$  ambient, the wafers came out of the furnace tubes still hot, and they came in contact with the air, possibly causing oxidation. The second theory was that the oxide layer under the germanium may have been causing it to oxidize. For future work, a nitride layer may be added under and over the germanium layer. Then annealing can be done, since the nitride will cover both sides of the germanium, and the top nitride layer can be removed. Then the normal procedure outlined here can be followed.

## Acknowledgments:

National Nanotechnology Infrastructure Network Research Experience for Undergraduates (NNIN REU) Program, National Science Foundation, Cornell NanoScale Science & Technology Facility, Intel Foundation, Melanie-Claire Mallison, CNF Staff, Rob Ilic, Judy J. Cha, Sara C. Barron, Edwin Kan, Jaegoo Lee, and Kwame Amponsah.

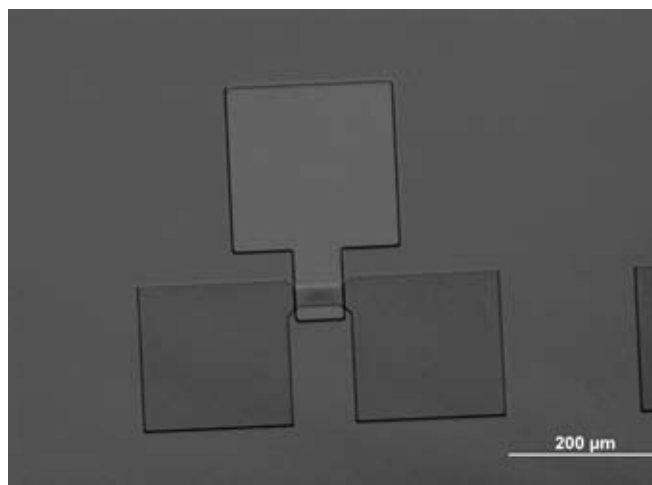


Figure 4: Optical microscope image. Shows the source, drain, gate layout.

# Characterization of Nanoscale Quantum Dots-in-a-Well Infrared Sensors

Jennifer Hou

Molecular and Cellular Biology, Johns Hopkins University

**NNIN REU Site: Nanoscience @ UNM, University of New Mexico, Albuquerque, NM**

NNIN REU Principal Investigator(s): Professor Sanjay Krishna, Electrical and Computer Engr., University of New Mexico

NNIN REU Mentor(s): Rajeev Shenoj, Electrical and Computer Engineering Department, University of New Mexico

Contact: [jhou4@jhu.edu](mailto:jhou4@jhu.edu), [skrishna@chtm.unm.edu](mailto:skrishna@chtm.unm.edu), [rshenoj@ece.unm.edu](mailto:rshenoj@ece.unm.edu)

## Abstract/Introduction:

Infrared detectors have many military, medical, and industrial applications due to their ability to detect radiation in the form of heat. Research groups are striving towards third-generation infrared detectors that have large-area focal plane arrays, improved functionality, and increased operating temperatures [1]. In order to operate at higher temperatures, the dark current (thermally generated electrons) needs to be lowered; then these devices can become more cost-effective by reducing their reliance on expensive cooling equipment.

The innovative quantum dots-in-a-well (DWELL) infrared detector has indium arsenide (InAs) dots, three-dimensionally quantum confined, “embedded in” an  $\text{In}_{0.15}\text{Ga}_{0.85}\text{As}$  well [1]. Electrons in InAs dots can become photoexcited and make intersubband transitions (dot to dot, to well, and to continuum) in the conduction band (Figure 1). DWELL detectors decrease dark current and offer greater “control over the operating wavelength,” where the width of the quantum well can be altered to change energy transitions [1].

The DWELL structure was developed from a single  $\text{In}_{0.15}\text{Ga}_{0.85}\text{As}$  well to a dots-in-a-double well (DDWELL) structure with  $\text{In}_{0.15}\text{Ga}_{0.85}\text{As}/\text{GaAs}$  wells [1] as shown in Figure 1. Less use of indium for the  $\text{In}_{0.15}\text{Ga}_{0.85}\text{As}$  well reduces the strain that was caused by the lattice mismatch between  $\text{In}_{0.15}\text{Ga}_{0.85}\text{As}$  and GaAs, allowing the growth of more stacks and thus more photocurrent absorption. The  $\text{Al}_{0.10}\text{Ga}_{0.90}\text{As}$  barriers located between the asymmetric wells lowered the dark current by blocking the passage of some thermally generated electrons and prohibited electron coupling between active regions. The focus of this project was to optimize the  $\text{Al}_{0.10}\text{Ga}_{0.90}\text{As}$  barriers by characterizing and comparing devices that have 30, 50, and 65 nm  $\text{Al}_{0.10}\text{Ga}_{0.90}\text{As}$  barriers.

## Experimental Procedure:

The characterization parameters investigated were: current-voltage characteristics, spectral response, responsivity, and specific detectivity. Each device—single well with 50 nm barrier, double well with 30, 50, or 65 nm barrier—was individually placed into a cryostat, in which the air was vacuumed from the cavity to avoid condensation and then cooled to a low temperature (i.e. 30, 77K) to reduce the signal from thermally generated electrons.

First, a semiconductor parameter analyzer was used to obtain current-voltage characteristics for the current from both

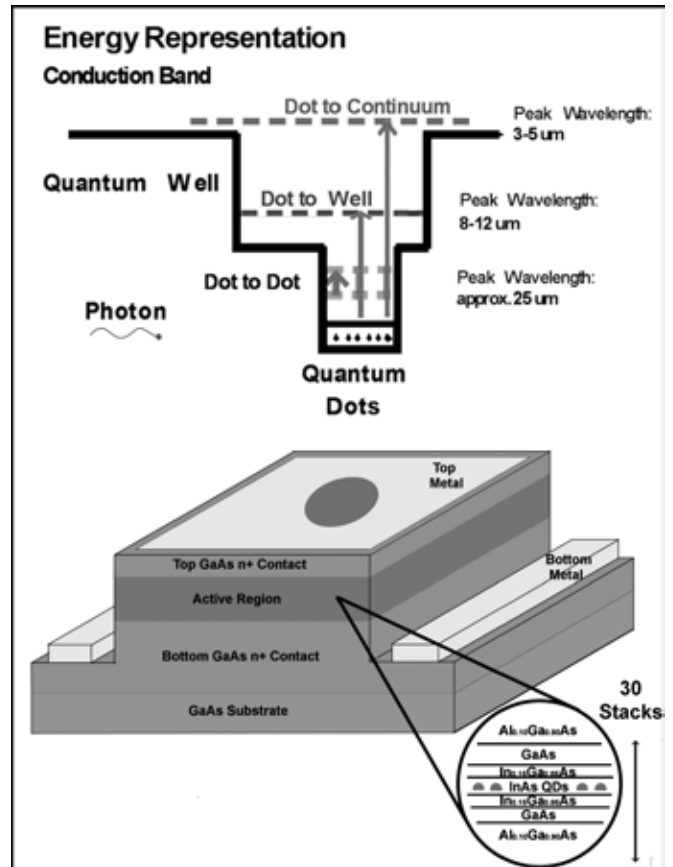


Figure 1: Schematic DWELL energy (at 0V bias) and DDWELL physical representation.

photoexcited and thermally generated electrons. For dark current measurements, a cold shield was used to block any incident light from reaching the device. The temperature of each device was raised from 30°K up to 100°K (150°K for the double well with 65 nm barrier, Sample D) to determine which barrier width was optimal at reducing dark current. Second, the devices’ spectral response at various bias voltages was obtained using a Fourier transform infrared spectrometer (FTIR). Third, responsivity, the signal output per IR power input [2], was used to measure the amount of light absorbed by the detector. For the setup, a blackbody set to a specific temperature (i.e. 527°C) cast an infrared beam which was modulated by a chopper. This frequency was used to trigger

the spectrum analyzer. Also, the current amplifier produced a bias voltage across the top and bottom metal contacts to capture the signal current. Last, specific detectivity or the “normalization of the signal to noise ratio” was calculated to find out the device’s ability with regards to others of various aperture areas or materials [3].

### Results and Conclusions:

At 30K, the dark current for the single well with 50 nm barrier (Sample A) was greater than that of any of the double well structures (Figure 2). As the barrier width increased for the double well, the dark current decreased; the 65 nm barrier had the lowest of these values. At 77K, the dark current increased with temperature for all devices. The single well with 50 nm barrier still had the highest dark current. Also, the dark current values were similar for the double wells with 50 and 65 nm barriers.

Spectral response was measured to determine the highest operating temperatures and to observe the spectral properties of the devices. At 30°K, there was already a greater presence of noise for the single well with 50 nm barrier and double well with 30 nm barrier than for the other devices. Sample D had spectral response peaks of 8.7  $\mu\text{m}$  for -5V and of 6.5  $\mu\text{m}$  for 5V, showing bias-tunability (Figure 3). The device’s spectral response was obtained up to 140°K. The double well with 65 nm barrier was optimal with a peak responsivity of 66 mA/W and a peak detectivity of  $3.1 \times 10^9 \text{ cmHz}^{1/2}/\text{W}$ , taken at a -5V bias and at 77K for an 8.7  $\mu\text{m}$  wavelength (Figure 4).

In conclusion, DDWELL photon detectors retain many qualities (“bias-tunability and multi-color operation”) [4] of the DWELL structure; but they additionally lower strain to permit more stacks and decrease dark current to achieve both higher operating temperatures and detectivity.

### Future Work:

For the advancement of DDWELL photon detectors, the next steps are to reduce strain even more, which will allow for greater photocurrent absorption and to include these devices in focal plane arrays.

### Acknowledgements:

I would like to thank my advisor, Prof. Sanjay Krishna for this profound experience and for his guidance and support. I would like to thank my mentor, Rajeev Shenoj for his encouragement and helpful advice. I would like to thank Prof. Poland. Special thanks to the QDIP group members, to the staff at CHTM, to Stefi Weisburd, and to my family. Last, I deeply thank the National Nanotechnology Infrastructure Network Research Experience for Undergraduates Program and the National Science Foundation for their generous funding.

### References:

- [1] S. Krishna et al, “Quantum Dot Based Infrared Focal Plane Arrays,” Proc. IEEE 95, 1-2, 4, 13 (2007).
- [2] J.D. Vincent, “Fundamentals of Infrared Detector Operation and Testing,” A Wiley-Interscience Publication, 9, 17 (1990).
- [3] Ibid., 9, O.W. P. Wroclawskiej, Materials Science, 133.
- [4] S. Krishna et al, “Quantum Dot Based Infrared Focal Plane Arrays,” Proc. IEEE 95, 1 (2007).

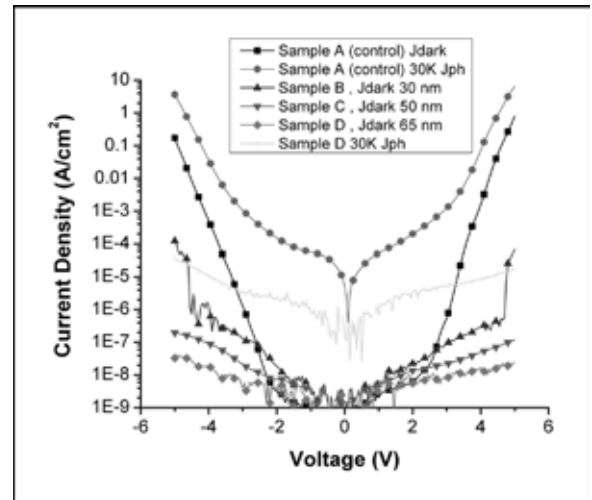


Figure 2: Current density comparison at 30K.

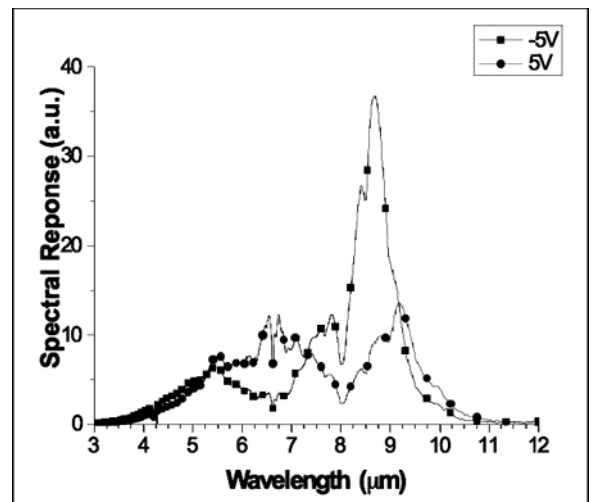


Figure 3: Spectral response for Sample D at 77K.

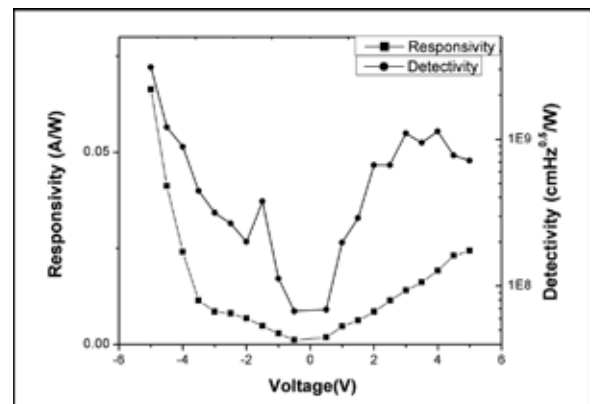


Figure 4: Responsivity and detectivity for Sample D at 77K.

# Assembly and Control of Light-Emitting Nanostructures for Near-Field Imaging

Sunmin Kim

Biological Engineering, Cornell University

**NNIN REU Site: Microelectronics Research Center, University of Texas, Austin, TX**

NNIN REU Principal Investigator(s): Dr. Xiaojing Zhang, Biomedical Engineering, University of Texas at Austin

NNIN REU Mentor(s): Ashwini Gopal, Electrical Engineering, University of Texas at Austin;

Dr. Kazunori Hoshino, Biomedical Engineering, University of Texas at Austin

Contact: sk542@cornell.edu, john.zhang@engr.utexas.edu, ashwinigopal@gmail.com, hoshino@mail.utexas.edu

## Abstract:

A uniform thin film of cadmium selenide quantum dots (CdSe QDs) was self-assembled by using a hydrophobic colloidal suspension. CdSe QDs suspended in hydrophobic solvent were dispensed on a convex water surface. After evaporation of the solvent, the free-floating film can be then used as an “inking pad” for hydrophobic polydimethylsiloxane (PDMS) stamps with various patterns, ranging from 10  $\mu\text{m}$  to 100  $\mu\text{m}$  and be stamped onto flat substrates. Atomic force microscopy (AFM) was used to measure the thickness of each film, which was then correlated to fluorescence intensity of the QDs. To demonstrate the electroluminescence of these particles, an inorganic light emitting diode (LED) was. The well-controlled assembly and stamping technique opens the door for near-field imaging applications with the resolution beyond 10 nm.

## Introduction:

Near-field scanning optical microscopy (NSOM) enables nano-scale topographic measurements as well as optical imaging. This imaging feature requires a miniature light source, such as a fibre tip, that can scan over the surface based on scanning probe technology [1,2]. The size of the light source directly correlates to the imaging resolution. Direct fabrication of nano-scale light source (Nano-LED) on silicon probe has been demonstrated through electrostatic attraction of light-emitting CdSe QDs on the tip [3]. Position control of QDs attachment is critical. Here, we report a technique that would enable the controlled deposition of QD nanoparticles onto the silicon probes by using a uniform, self-assembled film of QDs and micro-contact printing methods. Electroluminescence of stamped films is demonstrated by assembling a LED device.

## Experimental Procedure:

To create the film self-assembly set-up, 30.0ml of DI water was added to a glass Petri<sup>®</sup> dish. A Teflon<sup>®</sup> disk, with an outer diameter of 5 cm, inner diameter of 2 cm, and thickness of 2 mm, was placed in the center, pinning down the water at the edge and forming an upward convex curvature (Figure 1). Specific amounts of CdSe/ZnS core-shell QDs suspended in hexane were added to a 50:50 (v/v) solvent of 1,2-dichloroethane (EDC) and hexane to create the colloidal suspension. This was pipetted onto the water surface. The film was formed after  $\sim$  15 minutes of evaporation. PDMS stamps, fabricated using the rapid prototyping technique, were used to deposit film onto flat, hard substrates, either glass or silicon by placing the stamp down for  $\sim$  30 seconds.

We then fabricated an LED device, through stamping the film onto p-type silicon coated with 10 $\text{\AA}$  of native oxide.

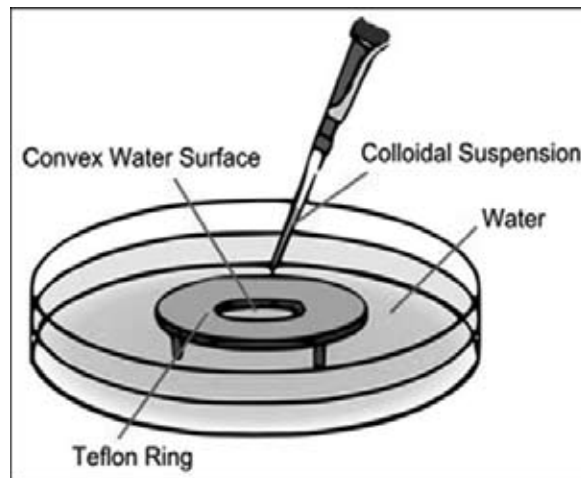


Figure 1: Set-up for quantum dot film self-assembly.

Zinc oxide and tin oxide (400 $\text{\AA}$ ) was co-sputtered to form the electron transport layer. We then deposited 50 $\text{\AA}$  gold and 120 $\text{\AA}$  silver, using electron beam evaporation to form the electron transport layer. Voltage was applied for light emission of the QDs.

## Results and Discussion:

Uniform films of nanoparticles were stamped as 100  $\mu\text{m}$  diameter circles on flat substrates (Figure 2). This was done with QDs of emission wavelengths 560 nm, 580 nm, 600 nm, and 620 nm. Light emissions from the constructed LED devices were observed for QDs with all the expected wavelengths.

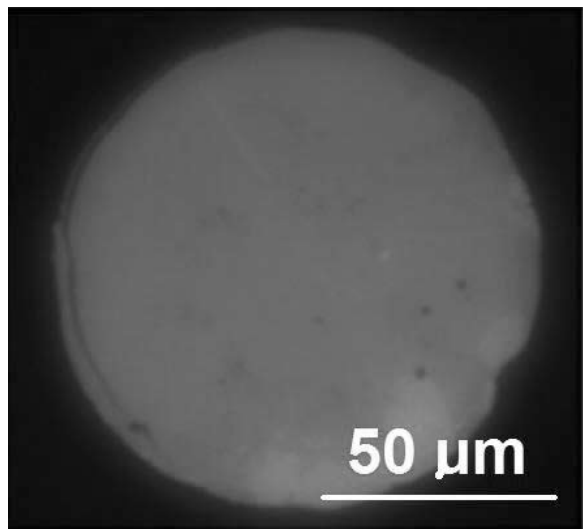


Figure 2: Quantum dot film stamped (580 nm emission wavelength) as 100 μm-diameter circle.

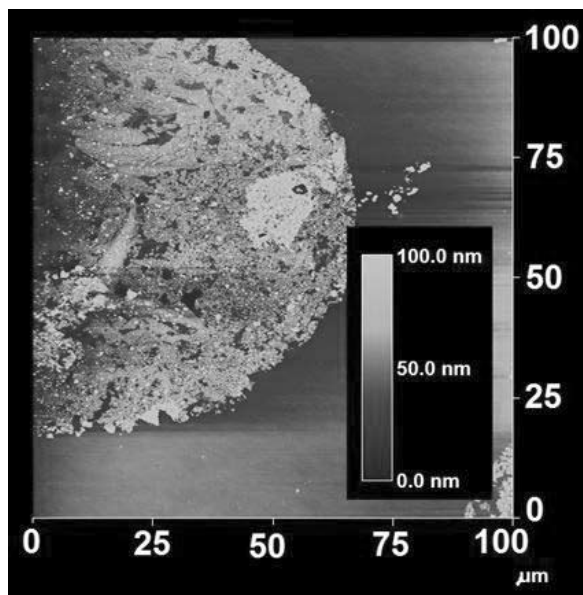


Figure 3: AFM topographic measurement.

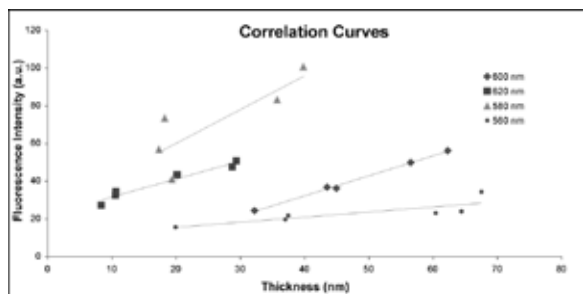


Figure 4: Correlation of thickness of stamped film to its photoluminescence.

The film of nanoparticles is formed due to evaporation, capillary immersion and convective forces. As the hydrophobic solvent begins to evaporate, nanoparticles in the center of water surface is exposed due to the convex shape. Solvent menisci form between individual exposed nanoparticles, and an attractive capillary immersion force collects nanoparticles into densely-packed hexagonal arrays called the nucleus [4]. As the solvent further evaporates, the contact line grows outward radially and convective flow of the solvent attracts nanoparticles from the colloidal suspension to the contact line, where they self-assemble onto the outer edge of the growing nucleus. As the contact line approaches the Teflon ring, where the water is pinned down, meniscus slope angle increases and multilayers are formed [5].

To measure the thickness of these films, stamped films scanned with the AFM (Figure 3). Thickness measurements were then correlated with photoluminescence using Matlab-extracted fluorescent intensity data from the optical micrographs. The plot indicated that there is a positive, linear correlation between film thickness and photoluminescence, especially for the 600 nm and 620 nm nanoparticles (Figure 4).

### Conclusions:

Uniform films consisting of hexagonally-packed array of QDs were self-assembled by dispensing a hydrophobic colloidal suspension on top of a convex water shape. We found that the film thickness and fluorescence intensity had a positive, linear correlation. Electroluminescence of stamped films was successfully demonstrated in an LED device made using this self-assembly and stamping technique. Direct integration of single quantum dot light source onto the scanning probe will have significant impact on molecular scale near-field imaging and sensing.

### Acknowledgements:

I would like to acknowledge Dr. John Zhang (PI), Ashwini Gopal, Dr. Kazunori Hoshino, and the rest of the Zhang Research Group for their support. I would also like to thank my site coordinator, Jean Toll, and the National Nanotechnology Infrastructure Network Research Experience for Undergraduates Program and National Science Foundation for funding.

### References:

- [1] Hecth, B. et.al. "Scanning NF optical microscopy with aperture probes: Fundamentals and applications", J.Chem.Phys. 112:7761-74, 2000.
- [2] Barbara, P.F. et.al. "Characterization of organic thin film materials with near-field scanning optical microscopy (NSOM)." Annu. Rev. Mater. Sci. 29: 433-469, 1999.
- [3] K. Hoshino, et al, "Direct fabrication of nano-scale light emitting diode on Si probe for NF scanning optical microscopy" JMEMS, 17:1, 2008.
- [4] Bresme, F. et al. "Nanoparticles at fluid interfaces." Journal of Physics: Condensed Matter 41: 413101, 2007.
- [5] Dushkin, C. D. et al. "Effect of growth conditions on the structure of 2D latex crystals: Experiment." Coll & Poly Sci 277(10): 914-930, 1999.

# Characterization of Thin-Film Polyamide Nanofiltration Membranes

Vérida Léandre

Physics, North Carolina A&T State University

**NNIN REU Site: Howard Nanoscale Science and Engineering Facility, Howard University, Washington, DC**

NNIN REU Principal Investigator(s): Dr. Kimberly Jones, Department of Civil Engineering, Howard University

NNIN REU Mentor(s): Dr. Malaisamy Ramamoorthy, Department of Civil Engineering, Howard University

Contact: veridlea@umich.edu, kljones@Howard.edu, malaisamy@gmail.com

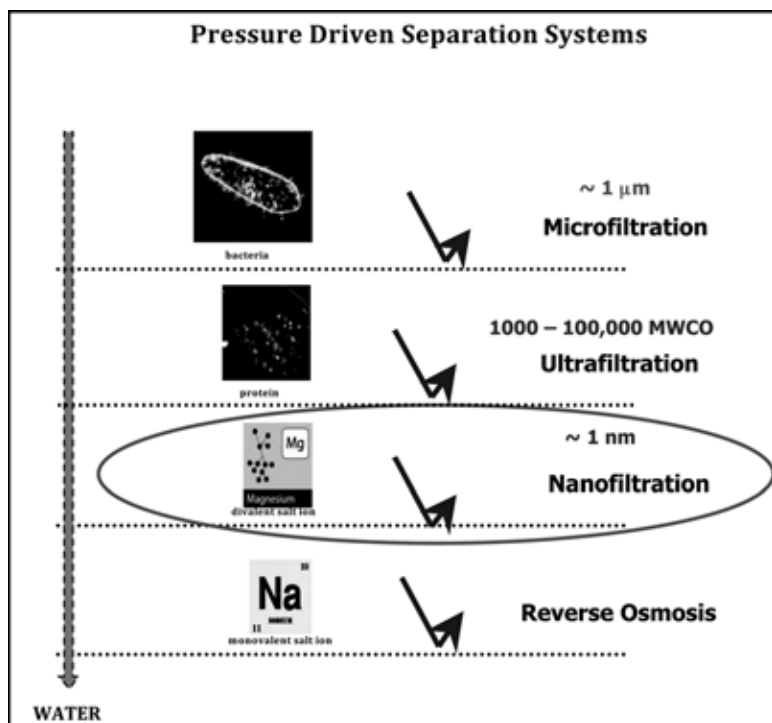


Figure 1: Pressure driven membrane separation systems and the specific particles they can successfully separate from aqueous solutions.

## Background:

Nanotechnology describes the study of matter, usually measuring less than 100 nanometers (nm), on the atomic and molecular scale. The applications of nanotechnology are numerous and far-reaching, ranging from electrical engineering and biology to environmental engineering. An important application of nanotechnology in the field of environmental engineering is water treatment and purification. Thin film polymer composites can be fabricated into membranes that, when modified, have impressive separation qualities/characteristics. Nanofiltration (NF) membranes have a mean pore size of 1 nm. Their separation characteristics lie between ultrafiltration (UF) membranes, which separate suspended solids and solutes with high molecular weight from water and low molecular weight solutes, and reverse osmosis (RO) membranes which reject all ions. Figure 1 depicts pressure driven membrane separation systems and the specific particles they can successfully separate from aqueous solutions. NF membranes are chemically modified using various techniques to increase flux and rejection while

decreasing membrane fouling. Figure 2 illustrates electrostatic deposition, a common membrane modification technique which involves placing bilayers of charged polymers on the membrane's active surface. These charged layers can decrease membrane fouling while increasing monovalent ion rejection. Nanofiltration membranes can filter multivalent salts without any modification, but the purpose of this project is to improve the separation qualities of NF membranes to the level of RO membranes. To assess the success of membrane modification in improving NF membrane filtration, the membranes were characterized using several different techniques: atomic force microscopy, electrokinetic analysis, scanning electron microscopy, and goniometry (contact angle analysis). Characterization of unmodified and modified membranes helps determine which membrane surface features enhance or detract from their membrane separation qualities.

## Methodology:

The membranes used in this experiment were NF270 membranes from Filmtec Corporation. Each membrane was soaked in water for 24 hours, then characterized using several different techniques.

The polyamide thin-film composite that composed the NF membrane was negatively charged, but the polyanions and polycations deposited on the membrane surface during the modification process changed the charge of the membrane surface. An electro-kinetic analyzer (EKA) machine was utilized to monitor the surface charge of the membrane before, during, and after the membrane modification process.

As an electrolyte solution was pumped through the fluid cell containing a membrane, the streaming potential of the surface was measured using electrodes clamped on both sides of the sample. The EKA machine used the streaming potential measurements to calculate the zeta potential of the membrane's active surface, which was directly proportional to the magnitude of the surface charge. The machine simultaneously measured the temperature, pH, and conductivity of the membrane's active surface, and presented these values in graphic or tabular format.

Another method used to characterize membrane surfaces was atomic force microscopy, commonly referred to as AFM. AFM

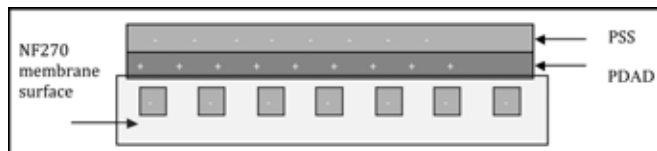


Figure 2: Electrostatic deposition.

uses a high-resolution scanning probe with a resolution 1000x greater than the optical diffraction limit and can magnify matter more than one million times its actual size. Data is gathered when a fine probe attached to cantilever “feels” the sample surface for changes in force along the x-y plane. Different types of probes serve different purposes. Most AFM imaging of NF membranes is performed using sharp silicon probes, but colloid probes can be used for specialized tests such as measuring particle adhesion and other surface characteristics. The NF270 membranes were imaged in several different modes: the cut pieces of membrane were imaged in contact and non-contact mode, and in both air and liquid media.

AFM and EKA testing provide useful information, but a test is needed to determine the hydrophilicity of a membrane’s active surface. Membranes used for water treatment purposes need to be hydrophilic in nature, because water continuously flows around and through these membranes. Hydrophilic membrane surfaces help maintain a high flux and decrease particle adhesion. Goniometry, also known as contact angle analysis, was used to study the interactions between water and membrane surfaces. Static contact angle measurements were taken when the membrane surface was in a fixed position and water was dropped onto it in a controlled manner. A camera and specialized software captured and analyzed the exact angle the water droplet made with the sample surface.

The final mode of characterization used was scanning electron microscopy (SEM). Electron-sample interactions produce electrostatic images that can be read to analyze morphological features of the membrane surface.

## Results:

The various tests performed on the NF270 membranes’ surface provided a great deal of useful information about NF membranes. Electrokinetic analysis showed the charged bilayers of PDAD-MAC and PSS changed the magnitude of the surface charge upon deposition. When PDAD-MAC was deposited on the surface, the negatively charged surface became positively charged. When PSS, a polyanion, was deposited, the magnitude of the membrane’s surface charge was reversed again. AFM proved that as the surface roughness of membranes increases, particle adhesion to the surfaces also increase. Humic particles tend to adhere to rough membrane surfaces more than their smoother counterparts. Goniometric analysis demonstrated the hydrophilic nature of the membrane’s surface. The contact angle measurements of membrane surfaces were all near or less than 30 degrees, which is extremely hydrophilic in nature. Figure 3 shows some results of goniometric analysis. SEM data was inconclusive

Unmodified NF270 Membrane	
Contact Angle (°)	Left Angle (°)
23.31	23.31
22.35	22.35
28.861	28.861
37.825	37.825

Figure 3: Results of goniometric analysis.

because the membrane’s morphological features were too small to be imaged using this technique. Field emission SEM is more commonly used to image NF membranes because the technique is better with imaging objects in the nanoscale range.

## Conclusions:

The purpose of testing and characterizing the NF270 membranes was to compare the separation qualities of modified and unmodified membranes. Modified membranes should have separation characteristics similar to RO membranes which can reject all ions in aqueous solutions. Characterization using AFM, EKA and goniometry showed that the modified NF270 membrane surfaces were less rough and more hydrophilic than the unmodified membranes, indicating that the modified membranes should exhibit increased rejection and decreased fouling when compared to the unmodified membranes.

## Acknowledgements:

I would like to offer special thanks to: Dr. Kimberly Jones, Dr. Malaisamy Ramamoorthy, Mr. James Griffin, Mr. Alain Talla-Nwafo, Ms. Fatou Diagne, Dr. Tina Brower, Dr. Gary Harris, Dr. Peizen Zhou, Dr. William Rose, National Science Foundation, National Nanotechnology Infrastructure Network Research Experience for Undergraduates (NNIN REU) Program, and my family and friends.

## References:

- [1] Afonso, Maria D. “Surface Charge On Loose Nanofiltration Membranes.” *Desalination* 191 (2006): 262-72. 17 June 2008 <[www.elsevier.com/locate/desal](http://www.elsevier.com/locate/desal)>.
- [2] Boussu, K, B VanDerBruggen, A Volodin, and J Snauwert. “Roughness and Hydrophobicity Studies of Nanofiltration Membranes Using Different Modes of AFM.” *Journal of Colloid and Interface Science* 286.2 (2005): 632-38. 19 June 2008.
- [3] Brant, Jonathan A., Kelly M. Johnson, and Amy E. Childress. “Examining The Electrochemical Properties Of A Nanofiltration Membrane With Atomic Force Microscopy.” *Journal of Membrane Science* 276.1 (2006): 286-94. 17 June 2008 <<http://www.sciencedirect.com/science>>.

# Fabrication and Characterization of Nanoscale Light Sources in Diamond

Kathleen Martinick

Department of Chemical and Nuclear Engineering, University of New Mexico

**NNIN REU Site: Center for Nanoscale Systems, Harvard University, Cambridge, MA**

*NNIN REU Principal Investigator(s): Dr. Murray W. McCutcheon, Engineering and Applied Sciences, Harvard University*

*NNIN REU Mentor(s): Prof. Marko Loncar, Department of Engineering and Applied Sciences, Harvard University*

*Contact: kmartini@unm.edu, loncar@seas.harvard.edu, murray@seas.harvard.edu*

## Abstract:

In recent years, the optical properties of diamond have sparked the curiosity of researchers. This interest is due largely to the unique nitrogen-vacancy (NV) centers, which are substitutional defects in the carbon lattice of diamond, consisting of a single nitrogen (N) atom next to a vacancy (V). NV centers are bright emitters of red light, and could be useful for imaging applications or as sources of single photons in optical circuits or computers. In order to control the optical properties of diamond for such applications, nanostructures can be chemically etched into the diamond with reactive ion plasmas. For example, a photonic crystal—a periodic lattice of air holes—could be etched into thin-film diamond to create microcavities where light can be trapped. Moreover, the light emission from an NV center positioned in such a cavity could be significantly enhanced, creating a bright source of single photons.

## Experimental Procedure:

Although diamond is an ideal material for optical applications, it is difficult to etch because of its hardness. Past results using reactive ion etching (RIE) have been reported by several groups [1-3]; however, the etching parameters vary significantly in these reports. For this experiment, an etching protocol for the Unaxis Inductively Coupled Plasma (ICP) etcher was developed and used to etch nanostructures into polycrystalline diamond, thereby demonstrating the feasibility of optically engineering the properties of diamond.

Before etching specific structures into diamond, an etch recipe was created using the ICP. Using 30 standard cubic centimeters (sccm)  $O_2$  as the reactive gas, the chamber pressure, ICP power, and radio frequency (rf) power were varied. Samples were coated with 40-50 nm particles of aluminum oxide powder, which served as a mask so that the etch profile could be characterized using scanning electron microscope (SEM) images. Total etch time was also varied to determine the etch rate using SEM. The parameters that created the best combination of high etch rate and vertical sidewalls were then used to create photonic crystal waveguides in polycrystalline diamond.

To create waveguides in diamond, a double mask technique was used. Firstly, plasma enhanced chemical vapor deposition (PECVD) was used to deposit approximately 90 nm of silicon dioxide ( $SiO_2$ ) on samples which consisted of 160 nm polycrystalline diamond on a 1  $\mu m$  sacrificial layer of silicon dioxide and thick (0.5 mm) silicon substrate.

Electron beam (e-beam) resist was then spin-coated onto the  $SiO_2$  layer, patterned with an Elionix electron-beam writing system using a variety of exposure doses, and developed. The ICP etcher was used to transfer the pattern to the  $SiO_2$ . The

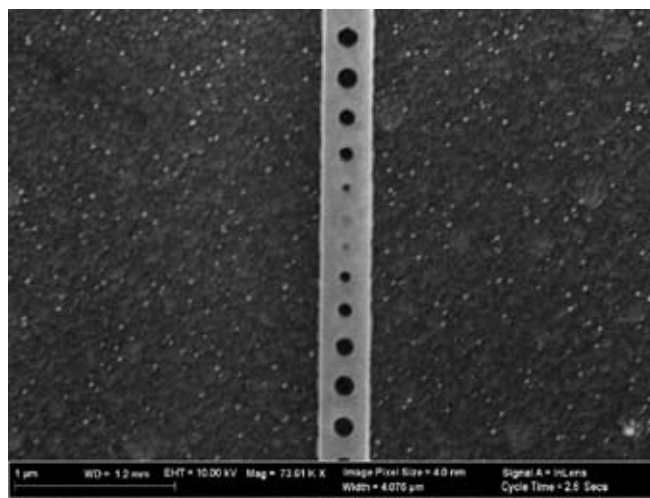


Figure 1: SEM of polycrystalline diamond waveguide with  $SiO_2$  layer.

optimized diamond etch parameters determined in the first stage of the experiment were then used to etch the diamond. Figure 1 shows a waveguide processed through these steps. Between steps, profilometer measurements were used to determine the selectivity of the diamond etch to  $SiO_2$ . Finally, a 5:1 buffered oxide etch (BOE) was used to remove the  $SiO_2$  mask and sacrificial layer. The result was a free-standing photonic crystal.

It was determined that 700 W ICP power with 100 W rf power at a chamber pressure of 10 mTorr produced the most anisotropic (vertical) etch and an etch rate of  $\sim 250$  nm/min (as determined by SEM measurements), and these parameters



Figure 2: Plateaus and nanowires of diamond on silicon. The sidewalls show anisotropic etching.

were used for the fabrication stage. Figure 2 depicts a diamond structure resulting from these etch conditions. During the optimization, an interesting observation was that nanowires of diamond were created as a result of using the aluminum oxide powder mask. Nanowires in diamond have highly interesting applications as directional photon emitters and biosensors [4] and therefore warrant further study.

The e-beam lithography dose exposures ranging from 121 to 145  $\mu\text{C}/\text{cm}^2$  formed appropriately sized lattice air holes in the waveguide. A 70 second etch of the  $\text{SiO}_2$  layer etched completely through the mask, but avoided any isotropic (lateral) etching. For the same reason, a 45 second diamond etch was used. The profilometer measurements taken during these steps suggested a selectivity of diamond to  $\text{SiO}_2$  of 47. Finally, a 10 minute BOE wet etch completely removed the  $\text{SiO}_2$  layers.

### Conclusions and Future Work:

This work shows that the aluminum oxide powder is an effective tool to efficiently characterize etch parameters, as it

successfully protects the masked diamond. The powder could also be used to create diamond nanowires for other purposes.

Since it was possible to etch holes only tens of nanometers in diameter, the double mask method is clearly a successful approach to etching diamond, which was further validated by the high selectivity of diamond to  $\text{SiO}_2$ . From the characterization of ICP diamond etching as well as the fabrication of photonic crystals, it is evident that it is possible to create nanoscale light sources in diamond.

Now that nanoscale structures have been etched into polycrystalline diamond, they must be optically characterized. In the future, the techniques developed in this work can be applied to single crystal diamond, which, because it has less surface roughness and fewer NV centers, is a more attractive platform for creating and manipulating light in the visible spectrum.

### Acknowledgements:

I would like to thank Professor Marko Loncar and Dr. Murray McCutcheon for their help during this project. This work was supported by Harvard University and by the National Science Foundation through the National Nanotechnology Infrastructure Network Undergraduate Research Program. All work was done in the Center for Nanoscale Systems at Harvard University. References:

### References:

- [1] S. J. Pearton, A. Katz, F. Ren, and J.R. Lothian, *Electron. Lett.* 28, 822 (1992).
- [2] W.J. Zhang, X. M. Meng, C. Y. Chan, Y. Wu, I. Bello and S. T. Lee, *Appl. Phys. Lett.* 82, 2622 (2003).
- [3] H. W. Choi, E. Gu, C. Liu, C. Griffin, J. M. Girkin, I. M. Watson, and M. D. Dawson, *J. Vac. Sci. Technol. B* 23(1), 130, (2005).
- [4] Yang et. Al. *Angew. Chem. Int. Ed.* 47, 5183 (2008).

# Ultra-Thin Epitaxial Germanium on Silicon Pillars for Scaled MOSFET Devices

Julie Stiver

Chemical Engineering, University of Massachusetts-Amherst

**NNIN REU Site: Stanford Nanofabrication Facility, Stanford University, Stanford, CA**

NNIN REU Principal Investigator(s): Prof. Yoshio Nishi, Dr. Peter Griffin, Electrical Engineering, Stanford University

NNIN REU Mentor(s): Gaurav Thareja, Electrical Engineering, Stanford University

Contact: jstiver@student.umass.edu, yoshio.nishi@stanford.edu, griffin@stanford.edu, gthareja@stanford.edu

## Abstract:

The vertical surround gate transistor with thin epitaxial germanium (Ge) is a design which allows for the continued scaling of silicon-based metal-oxide semi-conductor field transistors (MOSFETs). Here we report on the optimization of Ge deposition on nano-pillars and the characterization of thin (< 25 nm) Ge using atomic force microscopy (AFM) and ellipsometry. A hydrogen anneal was optimized to maintain pillar structures by raising the pressure to 380 Torr and lowering the temperature at 900°C. Germane partial pressure was high (177 Pa) and temperature during Ge deposition was low (310°C). The results of the characterization study indicate islanding and possible dislocations of the thin Ge layer at thicknesses of only a couple nanometers while thin, strained Ge exists at thicknesses of only a few monolayers (MLs).

## Introduction:

Silicon complementary metal oxide semiconductor (Si CMOS) devices are quickly reaching their physical limit of miniaturization and it is becoming increasingly difficult to enhance their performance through conventional device scaling [1]. Ge channel MOSFETs are attractive because of the high-mobility of both electrons and holes in Ge as compared to Si (2.75 and 4 times respectively) [2]. Ge is also attractive because of its compatibility with the current Si technology.

However, due to the 4.17% lattice mismatch, germanium-on-silicon (GOS) is a particularly challenging case of heteroepitaxy. GOS follows the Stranski-Krastanov (SK) growth mode which is characterized by three stages: pseudomorphic layer-by-layer growth, islanding, and coalescence of islands [3]. For thin, strained GOS, only the first mode is desired. While there is extensive characterization of thicker films in the literature [4], there is still a need for more understanding of thin Ge layers for device applications. This work will report an optimized RP-CVD thin Ge recipe for Si pillars in addition to characterization of ultra thin Ge.

## Experimental Procedure:

The silicon pillars of varying size were defined by optical lithography, cleaned using a standard pre-diffusion clean and immediately loaded into the RP-CVD reactor, taking all precautions to minimize surface oxidation. The GOS-pillar recipe was developed in the Applied Materials Centurion epitaxial system. The Ge characterization on bare Si wafers was done using the ASM Epsilon II single-wafer epitaxial

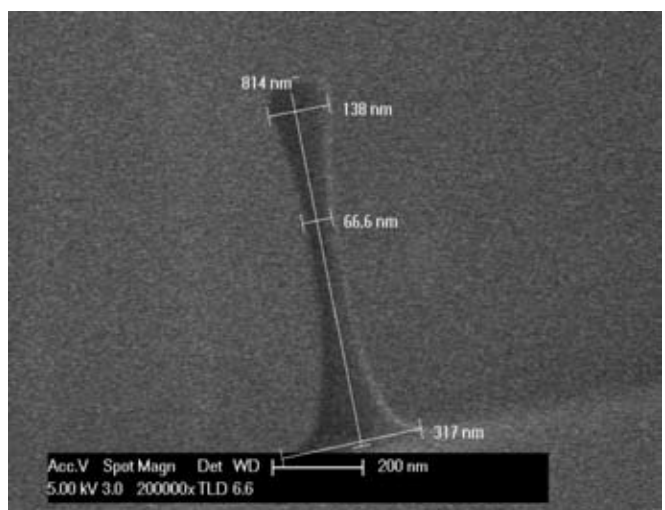
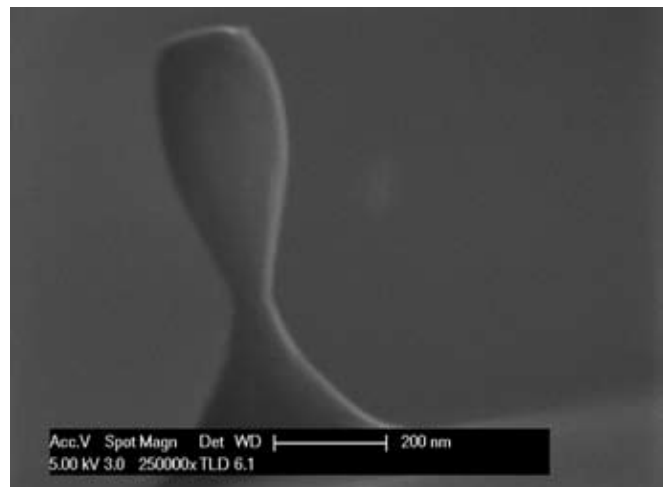


Figure 1, top: Pillar after 900°C, 15 Torr, 1 min anneal.

Figure 2, bottom: Pillar after 900°C, 380 Torr, 1 min anneal.

reactor. The pillar wafers were analyzed by scanning electron microscopy (SEM) to optimize the hydrogen anneal. The bare silicon wafers with epi-Ge were analyzed with AFM and ellipsometry.

## Results and Discussion:

The hydrogen anneal (to remove native oxide and smoothen pillar surface) caused severe necking of all pillars under standard high temperature, low pressure conditions (1100°C/900°C, 15 Torr, 34 slm H<sub>2</sub>) (Figure 1). We found that increasing the pressure to 380 Torr allowed us to keep a sufficiently high temperature of 900°C and pillar structures with diameters of 60 nm or greater survived (Figure 2).

Following the anneal, a Si seed layer (to initialize thin Ge growth) was deposited at 700°C, 15 Torr, 100 sccm dichlorosilane (DCS), and 27 slm H<sub>2</sub>. Ge deposition was done at 310°C, 200 Torr, 40 sccm germane (GeH<sub>4</sub>), and 6 slm H<sub>2</sub>. Finally, a Si cap was deposited at 550°C, 15 Torr, 30 sccm silane (SiH<sub>4</sub>), and 6 slm H<sub>2</sub>.

The first trend realized in the characterization of thin Ge was the thickness of the Ge layer versus the surface roughness (SR) (Figure 3).

SR was low when a few MLs of Ge had been deposited. When thickness exceeded this threshold, it became energetically favorable for islands to form atop the strained bottom layers (illustrated by the dramatic increase in roughness beyond one nanometer). At thicknesses beyond 5 nm, the islands coalesced and surface roughness decreased as dislocations at the interface alleviated misfit strain and islands became shallower with larger diameters. AFM phase images supported these conclusions, but more work must be done to understand and interpret this data.

A growth rate plot (Figure 4) indicated an incubation period during which the first few MLs were deposited followed by linear growth. This indicates that GOS growth occurs at a slower rate than Ge on Ge growth.

## Summary:

One way to increase the speed and performance of modern devices is to include a thin buried Ge layer within the Si channel. High quality strained GOS layers are found at thicknesses of only a few MLs. AFM data indicates severe islanding and possible dislocations of Ge layers as thin as 1 nm. The results of this analysis encourage further investigation into the characterization of ultra-thin germanium. XRD and TEM data will be included in future work. The ensuing processing and completion of these devices will offer an array of new design options for extended scaling and higher levels of functional integration.

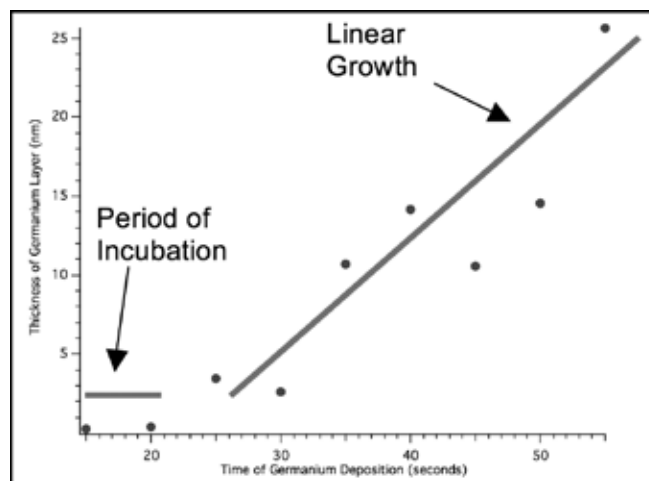
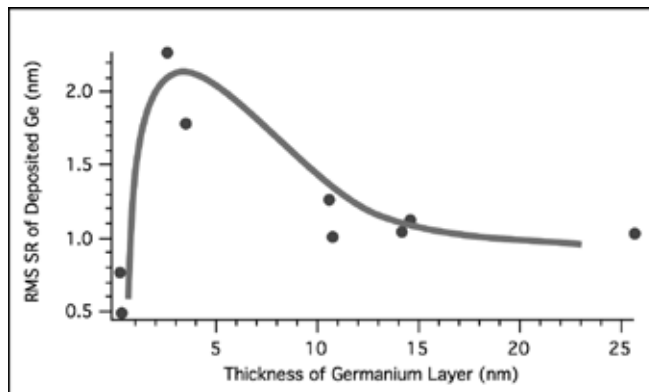


Figure 3, top: Surface roughness vs. thickness trend of thin epi-Ge.

Figure 4, bottom: Growth rate of thin Ge.

## Acknowledgements:

I give the most sincere thanks and appreciation to my mentor, Gaurav Thareja. Thank you also to Dr. Michael Deal, Dr. Peter Griffin, Professor Yoshio Nishi, and the SNF staff. Thank you also to the National Science Foundation and the National Nanotechnology Infrastructure Network Research Experience for Undergraduates Program.

## References:

- [1] D A Muller, T Sorsch, S Moccio, F H Baumann, K Evans-Lutterodt, G Timp, Nature 399, 6738 (1999).
- [2] B Streetman and S Banerjee, Solid State Electronic Devices, Prentice Hall (1998).
- [3] M A Herman, Cryst. Res. Technol. 34, 583 (1999).
- [4] J.Park, M Curtin, C Major, S Bengtson, M Carroll, A Lochtefeld, Electrochem. Solid-State Lett. 10 (11) H313-H316 (2007).

# Characterization of Real-time Drug Release from Engineered Biomedical Coatings

Garrett Swindlehurst

Chemical Engineering , North Carolina State University

**NNIN REU Site: Minnesota Nanotechnology Cluster, University of Minnesota-Twin Cities, Minneapolis, MN**

*NNIN REU Principal Investigator(s): Dr. Greg Haugstad, Institute of Technology Characterization Facility, University of Minnesota*

*NNIN REU Mentor(s): Dr. Jinping Dong, Institute of Technology Characterization Facility, University of Minnesota*

*Contact: grswindl@ncsu.edu, haugs001@umn.edu, dongx033@umn.edu*

## Introduction:

Coronary stents are industrially produced and are a non-invasive alternative to heart bypass surgery. Biomedical thin-film coatings are currently applied to all arterial stents for the release of anti-inflammatory drugs. While drug release from these films is effective, the parameters affecting the release profile are not easily controlled. Nanocopoeia, Inc. of St. Paul, MN, has developed the ElectroNanospray™ process to create advanced composite biomedical coatings of drug and polymer. Previous research has demonstrated that the release profile varies with the process conditions. This suggests that a higher level of controlled drug-release is possible with this process than is currently available. However, the release of drugs from polymeric coatings is non-linear, suggesting complex elution mechanisms that are unknown.

We have characterized the structure and chemical composition of these composite coatings before and during the release process using complimentary high-resolution microscopy methods. The completed characterization work will be used by Nanocopoeia to better understand the release mechanisms of elution. These understandings will then be used to link ElectroNanospray™ parameters to highly-controlled—and predictable—release profiles, thereby allowing the creation of individually-tailored coatings for specific biologic needs.

## Experimental Method:

Composite films of polyisobutylene-polystyrene polymer with 10% (wt/wt) dexamethasone or rapamycin generated on a stainless steel substrate using the ElectroNanospray™ process at 3-12  $\mu\text{m}$  thicknesses were obtained from Nanocopoeia, Inc. These coatings were then analyzed using atomic force microscopy (AFM) and confocal Raman spectroscopy imaging. When combined, these two complementary techniques provide data which can be used to identify drug location and observe the elution from the polymer matrix in real-time.

AFM imaging was chosen for the ability to image the coating surface at high resolution in both air and an aqueous environment. An Agilent Technologies 5500 scanning probe microscope with Witec digital pulsed force mode attachment

was used. Images of topography, cantilever deflection, and tip-sample adhesion were generated to provide varied mechanical property information.

Raman spectroscopy imaging involves the collection of monochromatic light scattered by the sample. Characteristic peaks were chosen based on scans of pure component samples; a 1640-1680  $\text{cm}^{-1}$  peak for C = O functional groups on drug molecules and a stronger 2970-3025  $\text{cm}^{-1}$  peak for aliphatic C-H groups on the copolymer were selected. Scattered Ar-ion laser light was gathered with a Witec Alpha300 R confocal Raman microscope and sent to a spectroscopic detector for each image pixel. The chosen signal peaks were then integrated by the Witec control software to generate a color-contrasted image. This characterization technique allows for spatial resolution of chemical composition and density within the coating.

In-air images were first taken at varying scan sizes and resolutions from 2.5 to 25  $\mu\text{m}$  square and 80  $\times$  80 pixels (Raman) to 512  $\times$  512 pixels (AFM). The samples were then immersed in a phosphate buffer saline (PBS) solution, and time-elapse imaging was similarly conducted in solution at ½ hour, 1, 2, 4, 6, and 24 hours. These images were then qualitatively analyzed for key features and patterns of change which point to observable trends in drug release.

## Results:

Raman images generated from characteristic peaks in solution for dexamethasone samples indicated that the drug was primarily aggregated in vertical columnar domains of increasing diameter, between 2 and 5  $\mu\text{m}$  in size, from 1 to 6.5 hours. Smaller particulate drug aggregates, 500 nm to 1  $\mu\text{m}$  in size, were also observed interspersed between the columnar domains. The visible contrast between the larger aggregates and smaller particles increased over 17 hours, indicating that the drug peak intensity within the large domains decreased. Figure 1 is a characteristic image for the drug peak and Figure 2 is for the polymer peak, with selected peaks intensity indicated by lighter regions. Raman imaging on rapamycin samples has not yet been conducted systematically.

AFM imaging in air on rapamycin samples at  $2.5\ \mu\text{m}$  size showed no characteristic features on the surface, but the phase separation of the block copolymer was evident in the deflection and adhesion images. When placed into solution, large dome-shaped features of low tip adhesion and high deflection (deflection is the slope of the surface,  $dZ/dX$ ) appeared that were not previously evident, indicating that the features were of a different composition than the surface and were protruding. These features are visible in Figure 3. These features increased in number through 2.5 hours, and decreased in size by 25 hours. An image at 25 hours is included as Figure 4; note with comparison to Figure 3. AFM imaging on dexamethasone samples showed no conclusive changes between samples in air and in solution, and no trends in surface changes were observed over time *in situ*.

### Conclusions:

Raman imaging showed that the drug was aggregated in larger micron-sized domains, and that release was primarily due to the decay of these larger features. The decrease in contrast range between columns and particles over time indicates that the relative concentration of drug in the columns was decreasing over time; we believe this to be the main indicator of elution from the columns. The dome-shaped features appearing on the surface of the coating in AFM images are concluded to be the emerging heads of the columns of drug within the coating.

The currently proposed mechanism is a combination of two main transport mechanisms within the coating. Lateral motion of smaller particles within the coating is proposed to be driven by both diffusion and internal stresses. From this motion, particles move to the large columnar domains, and they are subsequently driven to the surface by the concentration gradient in the column. However, further systematic characterization with both techniques is needed to confirm these conclusions. These results demonstrate the power of these complementary techniques for understanding drug release from biomedical coatings.

### Acknowledgments:

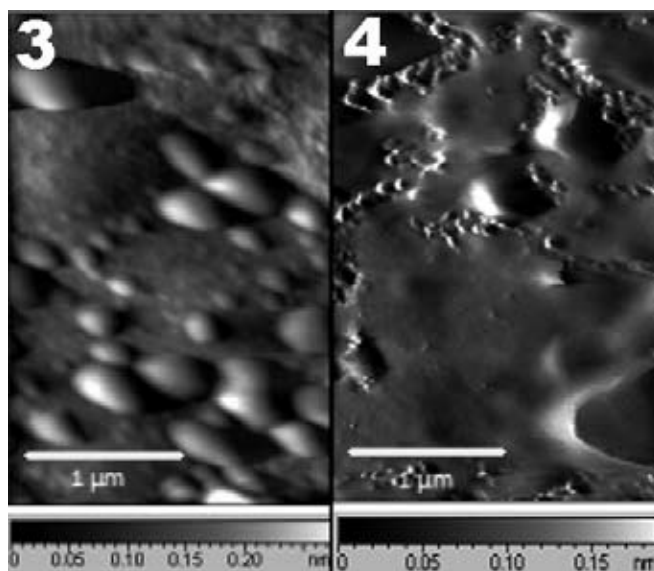
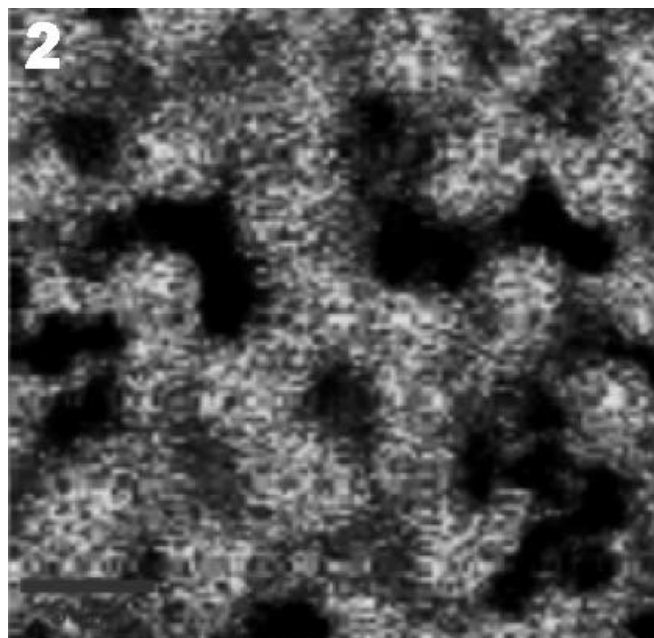
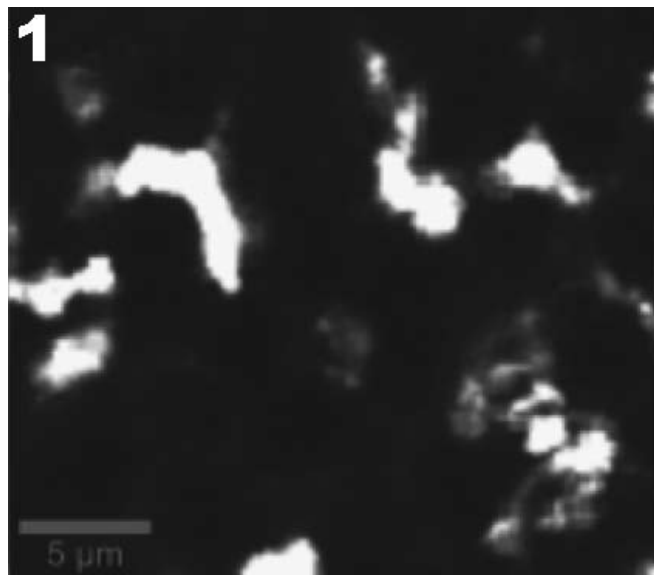
The author would like to thank the NSF and the NNIN REU program for the opportunity and funding for this research, as well as mentors Jinping Dong, Greg Haugstad, John Foley, and Bob Hoerr for their guidance.

Figure 1, top: Drug Raman peak intensity,  
 $25 \times 25\ \mu\text{m}$ , 6.5 hr in PBS.

Figure 2, middle: Polymer Raman peak intensity,  
 $25 \times 25\ \mu\text{m}$ , 6.5 hr in PBS.

Figure 3, bottom left: Deflection AFM image,  
 $5 \times 5\ \mu\text{m}$ , 1 hr in PBS.

Figure 4, bottom right: Deflection AFM image,  
 $5 \times 5\ \mu\text{m}$ , 25 hr in PBS.



# Electron Transfer/Transport in Nanoparticle/Polymer Monolayer Arrays

Tyler Todd

Engineering Physics, Oral Roberts University

**NNIN REU Site: Nanoscience @ UNM, University of New Mexico, Albuquerque, NM**

NNIN REU Principal Investigator(s): Prof. C. Jeffrey Brinker, Chemical and Nuclear Engineering,  
University of New Mexico, Sandia National Laboratories

NNIN REU Mentor(s): Shisheng Xiong, Center for High Technology Materials, Advanced Materials Laboratory,  
University of New Mexico

Contact: dynamite212005@hotmail.com, cjbrink@sandia.gov, s2xiong@gmail.com

## Abstract:

Nanoparticle (NP)/Polymer composites exhibiting advantageous optical, electrical and mechanical properties are of interest and in intensive investigations for a variety of applications. A universal, fast and facile method to prepare robust, freestanding and patternable NP/polymer composites by evaporation-induced self-assembly on a fluid interface has been developed. By transferring the NP/polymer films onto discovery platforms with predeposited interdigitating electrodes, electron transfer at the metallic NP/polymer interfaces and electron transport across the composite films have been studied through a combination of electrical and spectroscopic techniques.

## Introduction:

We studied the localized electron transfer and electron transport characteristics in a composite polymer consisting of a monolayer of monodisperse gold (Au) nanoparticles and poly-(3-hexylthiophene), or P3HT. The ultra thin films that incorporated the Au NPs were successfully created via an interfacial evaporation induced self-assembly (EISA) process. These films were then successfully transferred to the desired substrate, in this case, a discovery platform, which consisted of a series of interdigitated gold electrodes. The discovery platform was then wire-bonded to a carrier, which allowed for bias voltage to be injected through the device. Raman Spectroscopy was then used to measure variances in scattering intensity as an indirect method of detected charge movement across the device.

## Fabrication of Thin Films:

Solutions of P3HT, and Au nanoparticles, in appropriate ratios were dissolved in toluene. One drop of the solution was carefully released over a deionized water surface sitting in a Petri® dish. The solution of P3HT and Au NPs spread out over the surface and a thin film was formed through interfacial evaporation-induced self assembly as shown in Figure 1. The thin film consists of a monolayer of Au NPs spread evenly in a hexagonal close-packed array as shown in Figure 2.

After the toluene evaporated, the thin film was captured on a discovery platform, by submerging the platform under the deionized water and bringing it up though the thin film. The sample was then left to dry undisturbed. Some samples were also thermally annealed to determine if heating would create a better contact between the electrodes and the thin film. It was found that the annealed films showed no significant difference

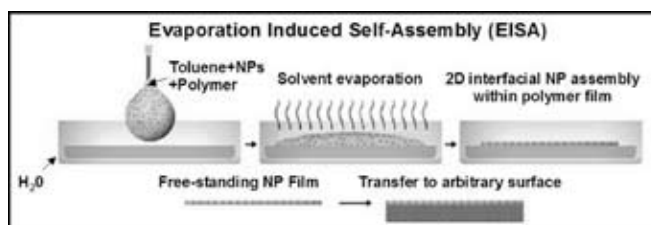


Figure 1: Thin film fabrication via evaporation induced self-assembly.

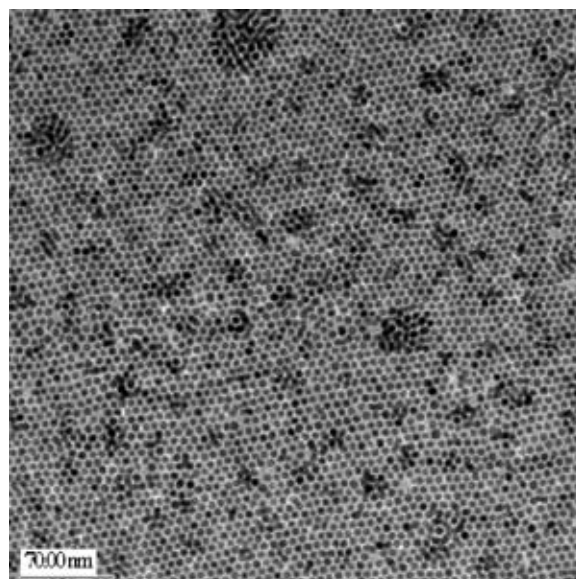


Figure 2: TEM image showing a hexagonal close-packed Au NP/P3HT film.

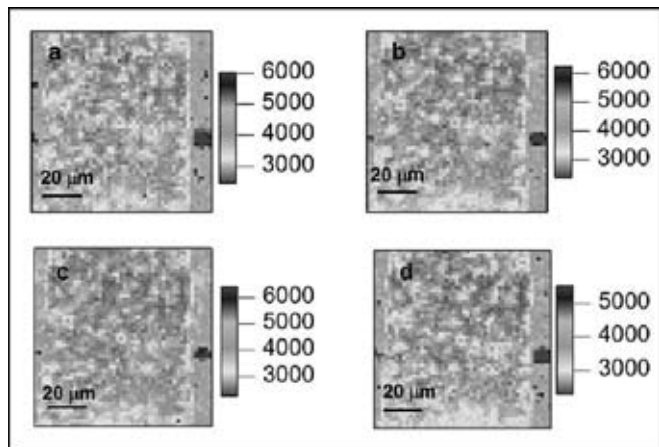


Figure 3:  $C = C$  mode of P3HT/Au monolayer on discovery platform: a) 0 V; b) 50 V; c) 100 V; d) 150 V.

from the other samples. Thin films without Au NPs were also made as a control and comparison.

### Detecting Charge Mobility Across Thin Films:

Four voltages—0 V, 50 V, 100 V and 150 V—were used on the device sample by a function generator and amplifier. A laser of 488 nm generated by an Ar-Kr ion laser head was used to excite the sample. 390  $\mu$ w Raman scattering light was then collected by a sensitive EMCCD. For a single Raman spectrum, acquisition time was  $\sim$  500 ms.

Figure 3 shows the Raman intensity images of the dominant peak,  $C = C$  stretching mode of P3HT on the discovery platform sample under different voltages with excitation 488 nm to understand charge transport. The scan range was set to be 100  $\mu$ m and we selected the region purposely to cross two of the Au electrodes. The intensity drop of these images shown may be due to a photodegradation issue, since the same region exposed to high power intensity laser  $\sim 10^4$  W/cm<sup>2</sup> and air. The features here clearly show two electrodes surrounding a nearby region. Lower intensity regions are indicated as red color and assigned to Au electrode because of the less P3HT in these regions; high intensity region are denoted as blue color and assumed to be between electrodes due to thicker composite layer.

Figure 4 shows the difference images of  $C = C$  mode, which indicate the voltage effect on Raman intensity. The electrode and nanoparticle features are still distinguishable in these difference images. Au electrode regions show positive differences (about 0.2); however, for materials around an

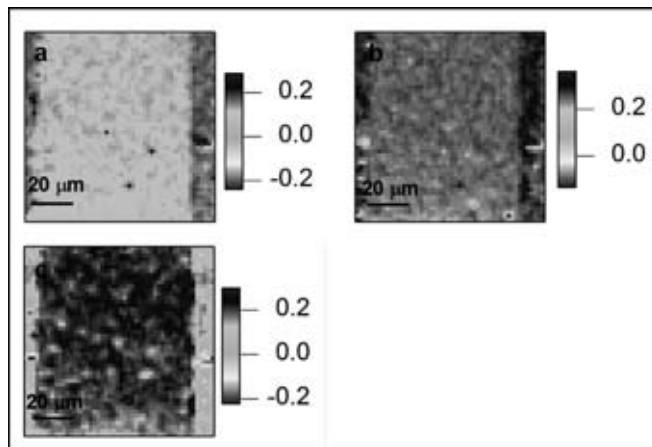


Figure 4: Difference image of  $C = C$  mode: a) 0-50 V; b) 0-100 V; c) 0-150 V.

electrode, they turn to negative and close zero (-0.2-0.1) values at 150 V.

### Results and Future Work:

We were able to successfully view changes in intensity of the  $C = C$  mode of the film indicating that there is some sort of charge movement on the localized level. Although we only had a cursory data set, it seemed that we could conclude that bias-induced chemical changes occurred at the molecule-electrode interface, possibly from charge injection. Also there was no significant charge transfer character that existed in hybrid films as oppose to pure polymer films.

Future things we hope to accomplish are to develop a method to measure current and voltage simultaneously while measuring the Raman scattering effect, determine how size of NPs affects the detection of charge mobility in the composite film, measure the effects on electron mobility when the discovery platform is treated as a FET, and test Raman Scattering at different excitation wavelengths.

### Acknowledgements:

I would like to thank Professor Jeff Brinker and my mentor, Shisheng Xiong, for their help, support and guidance. I would also like to give a special thanks to Yongqian Gao, Felix Jaeckel, Prof. John Grey, Prof. Kevin J. Malloy, the UNM coordinators, the National Nanotechnology Infrastructure Network Research Experience for Undergraduates Program, and the National Science Foundation.

# Development and Optimization of Pulse Plating of Copper Films for MEMS Applications



Merine Zinsou

Electrical Engineering, University of Maryland College Park

**NNIN REU Site: Lurie Nanofabrication Facility, University of Michigan, Ann Arbor, MI**

*NNIN REU Principal Investigator & Mentor: Pilar Herrera-Fierro, Electrical Engr & Computer Sci., University of Michigan*

*Contact: merine@umd.edu, pilarhf@eecs.umich.edu*

## Abstract:

**High-aspect-ratio copper structures are important in the fabrication of heat dissipaters, heat sinks and radio frequency (RF) antennas among many other microelectromechanical systems (MEMS) devices. Electroplating is a preferred technique for coating thick films ( $> 1 \mu\text{m}$ ) on metallic surfaces. The properties of the plated films are improved by the use of pulse plating. In pulse plating, the potential or current is alternated between two different values. The goal of this project is to develop and optimize a process for pulse plating copper on a patterned wafer. The challenge is to plate high aspect ratio, high quality features that are commonly required in the MEMS processes. Forward-reverse cycling enhances film characteristics such as roughness, low stress, uniformity and conformality. The optimum conditions for pulse plating a patterned wafer were determined.**

## Introduction:

The deposition of a metallic coating onto an object is achieved by putting a negative charge on the object (cathode) to be coated and immersing it into a solution (electrolyte) which contains a salt of the metal to be deposited. The metallic ions of the salt carry a positive charge (cations) and are thus attracted to the cathode which provides electrons to reduce the positively charged ions into a metal atom.

Copper plating is the critical step in through-wafer interconnects, which is becoming a promising new alternative for a wide variety of applications such as 3D integrated circuits, MEMS packaging and high frequency applications [1]. Filling of high aspect ratio vias has to be mastered before the technology is available. Bottom-up copper plating into the vias is the critical step to fill through-wafer vias. Other MEMS applications such as heat sinks and RF antennas also require high quality copper films. In the last case the requirements are more stringent, in addition to void free, low stress and highly conformal films the side walls must be very smooth. This can only be achieved by the use of pulse plating [2].

The objective of this work is to develop and optimize a pulse-plating process to be used in this facility.

## Experimental Procedure:

The plating process included: surface preparation, electroplating, photoresist removal and analysis.

**Surface Preparation.** Standard 4" silicon (Si) wafers were seeded with 3000Å of copper by sputtering it over 300-500Å of Cr in a EnerJet sputter-coater. The back of the wafers had been, previously, electrically isolated by depositing a plasma enhanced chemical vapor deposition (PECVD) film of Si-

oxide. The wafers were patterned using 10000Å film of AZ 9260 photoresist. The samples were exposed in a Suss MA6 aligner. After exposure and development the wafers were inspected using an optical microscope and the areas to be plated carefully measured.

**Electrochemistry.** The Pyrex® electrochemical cell, Teflon® lid and electrode holders were leached with diluted sulfuric acid to remove all contaminating ions. The anode material, a (0.027") copper plate 4 × 4" 99.9% pure, prior to use, was degreased with IPA and then etched with ammonium persulfate and soaked in 10% volume sulfuric acid to remove surface oxide, and finally, rinsed with de-ionized (DI) water. The electrolyte was a commercially available plating solution from Enthone Corp., MICROFAB® SC Make-Up and a brightener, MICROFAB SC MD. The cell was kept at 24°C while agitated at 200 rpm. The electrical contact, to the front of the wafer, was done by means of a stainless steel tweezers cut and bent to provide a tight contact. Care was taken to make sure that the electrolyte did not touch the electrical contact.

The DC programmable-pulse power supply used was a Dynatronix® DuPR MicroStar. The in-put variables were:  $I_{\text{fwd}}$ , actual (cathodic) plating current (13 to 43 mA/cm<sup>2</sup>);  $I_{\text{rev}}$ , reverse (anodic) or stripping current (-20 to -63 mA/cm<sup>2</sup>);  $t_{\text{fwd}}$  was the actual plating, ON, time; and  $t_{\text{rev}}$  was the time OFF or the negative pulse duration. The plating was done at constant current. After plating was completed, the samples were removed from the plating bath, and rinsed thoroughly with DI to avoid the appearance of stains on the surface.

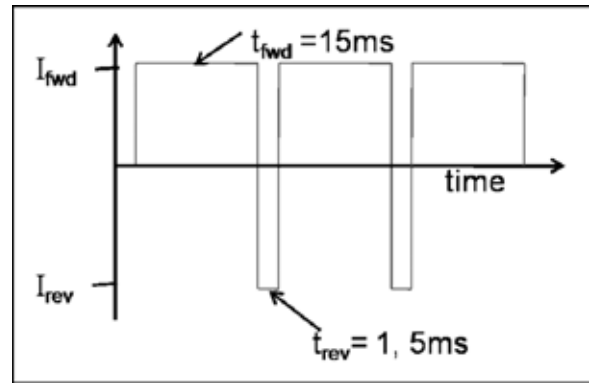
**Post Plating.** Removal of the photoresist was done using PRS 2000. Samples were soaked for 5 min, then thoroughly rinsed and dried. The roughness and thickness were measured in an

HRP-200 KLA-Tencor profilometer. Some samples were also put in a SEM (FEI-Quanta) in order to examine the walls, corners and grain size of the plated features.

**Results:**

In Figure 2 and 3, the conditions were:  $i_{fwd} = 13 \text{ mA/cm}^2$ ;  $t_{fwd} = 15 \text{ ms}$ ;  $i_{rev} = -27 \text{ mA/cm}^2$ ;  $t_{rev} = 1 \text{ ms}$ , plating time 20 min.

In Figure 4, the conditions were:  $i_{fwd} = 17.76 \text{ mA/cm}^2$ ;  $t_{fwd} = 15 \text{ ms}$ ;  $i_{rev} = -26.64 \text{ mA/cm}^2$ ;  $t_{rev} = 1 \text{ ms}$ , plating time 25 min.



**Conclusion and Future Work:**

A process for pulse-plating copper onto a patterned Si wafer was developed. The process deposition rate is  $4000 \text{ \AA/min}$ . The films obtained are uniform, void free and highly conformal. The roughness of the deposited films needs further study. It has been reported in the literature [3] that the roughness of the surface is also due to the seed layer oxidation. This oxide should be removed prior to electroplating to ensure uniformity. The dependence of the brightner and roughness should also be studied.

**Acknowledgements:**

Dr. Pilar Herrera-Fierro, Dr. Sandrine Martin, Matthew Oonk, Edward Tang, Gregory Allion, Trasa Burkhardt and Melanie-Claire Mallison. The National Nanotechnology Infrastructure Network Research Experience for Undergraduates (NNIN REU) Program, NSF, Intel Foundation, fellow REU students at UM, my friends and family.

**References:**

- [1] Dixit P. and Miao J. "Aspect-Ratio-Dependent Copper Electrodposition Technique for Very High Aspect-Ratio Through-Hole Plating", Journal of Electrochemical Society, 153(6) G552-G559 (2006).
- [2] Chandrasekar, M.S., Pushpayanam, M. "Pulse and Pulse Reverse Plating-Conceptual, Advantages and Applications", Electrochimica Acta,53, 3313-3322(2008).
- [3] Jae Jeong, Kim and Soo-Kil Kim. "Optimized Surface Pretreatments for Copper Electroplating." Applied Surface Sci., 183, 311-318, (2001).
- [4] Mordechay, Schlesinger. "Electroplating." September 2002.
- [5] Electrochemistry Encyclopedia. 4 June 2008 <<http://electrochem.cwru.edu/ed/encycl/art-e01-electroplat.htm>>.
- [6] Snyder, Donald. "Choosing and Troubleshooting your Copper Electroplating Process." 2007. PF online. 4 June 2008 <<http://pfonline.com/articles/pfdsnyder01.html>>.

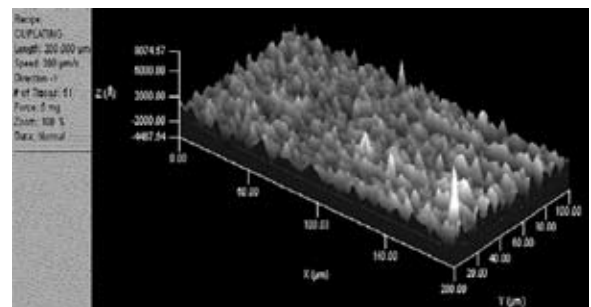
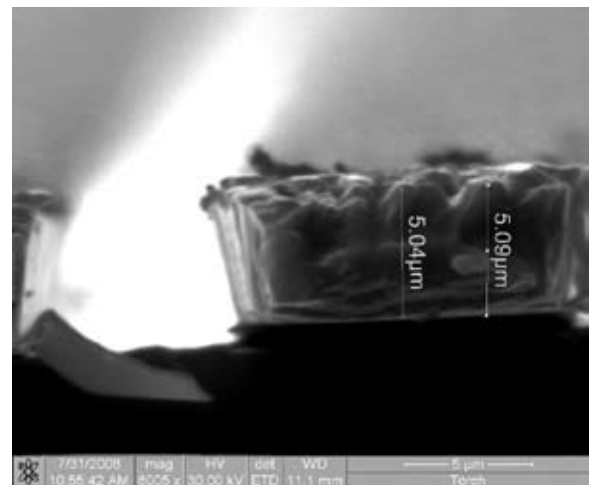
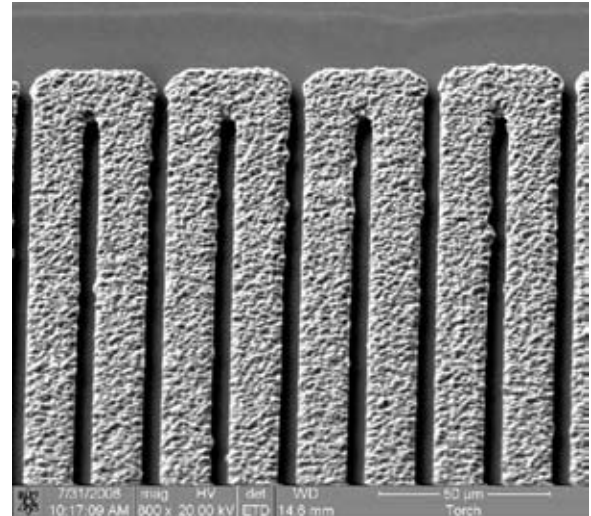


Figure 1, top: Pulse cycle.

Figure 2, upper middle: SEM photo showing conformality.

Figure 3, lower middle: SEM photo showing void free walls.

Figure 4, bottom: Profilometer photo of roughness of the deposited films.

# Clarification of Phase Diagram in a (Zn, Mg)O Pseudo Binary System by Using Ultra-Fine MgO Source Powder

Courtney Bergstein

Chemistry, Carlow University

**NNIN iREU Site: National Institute for Materials Science, Tsukuba, Japan**

*NNIN iREU Principal Investigator(s): Dr. Naoki Ohashi, Optoelectronics Group, National Institute of Materials Science*

*Contact: Bergsteincl@gmail.com, ohashi.naoki@nims.go.jp*

## Abstract:

Zinc and magnesium oxide [(Zn,Mg)O] alloys are appropriate for near ultraviolet (UV) light emitting diodes because of their ability to increase the band gap of ZnO, leading to the tuning of the luminescence wavelength and an increase in the intensity of the light emitted. However, there is no consensus on the solubility limit of MgO in ZnO due to the many difficulties associated with different preparation parameters. This research investigates a small portion of (Zn,Mg)O phase diagram in order to clarify the solubility limit of MgO in ZnO. Grain size measurements, x-ray diffraction measurements, and photoluminescence measurements were used to investigate the composition dependence of lattice parameters as well as energy band gap. All results indicated an increase in the band gap with the increase of concentration and sintering temperature. X-ray diffraction measurements revealed an approximate solubility limit of 18% for samples sintered at 1500°C, 17% for samples sintered at 1400°C, and 15% for samples sintered at 1200°C. Photoluminescence results revealed a solubility limit of approximately 16% for samples sintered at 1400°C. Typical applications are for the use of light-emitting devices.

## Introduction:

ZnO is a promising wide gap semiconductor (3.3 eV) in the field of light-emitting devices because of its large band gap and high exciton binding energy. By alloying ZnO with various concentrations of MgO, the luminescence properties in the visible region can be enhanced [1]. High concentrations of (Zn,Mg)O alloy have been obtained by the technique of pulsed laser deposition (PLD) [2]; however the solubility limit has not been clarified, due to many difficulties in sample preparation—such as the stability of both oxides.

In the present study, we investigated the solubility limit of MgO in ZnO, the lattice constants of unstrained (Zn,Mg)O, as well as some intrinsic properties of (Zn,Mg)O. As MgO concentration and reaction temperature increased, we expected changes in the lattice constants and the intrinsic properties of (Zn,Mg)O. Using this information, a phase diagram will be constructed for this pseudo binary system.

## Experimental Procedure:

Various samples were prepared using a multi-step process. Samples were prepared of different concentrations of MgO from 5 to 20 atomic %. The nanopowders were mixed using the ball milling process and then pelletized using cold isostatic pressure at 100 Mpa. After the powders were pelletized, they were sintered at various temperatures from 800-1500°C for 3 hours to 20 hours for samples of high concentrations. Homogenous and pure ceramic pellets were produced. The ceramic pellets were characterized using various techniques including scanning electron microscope observations (SEM), x-ray diffraction (XRD), and photoluminescence (PL). SEM characterizations were used to define grain boundaries and perform grain size measurements. The ceramic pellet's

crystallographic features, mainly lattice parameters, were determined by x-ray diffraction with copper (Cu) K $\alpha$  radiation using silicon (Si) standard powder. Luminescence properties of the samples were characterized with photoluminescence using a pulsed laser at 266 nm. All characterizations were performed at room temperature. Calculations were then performed to determine solubility limit in terms of luminescence properties (energy band gap) and lattice parameters (a and c).

## Results:

SEM grain size measurements indicated an increase in grain size as temperature increased, but a decrease in grain size as concentration increased. XRD results showed that

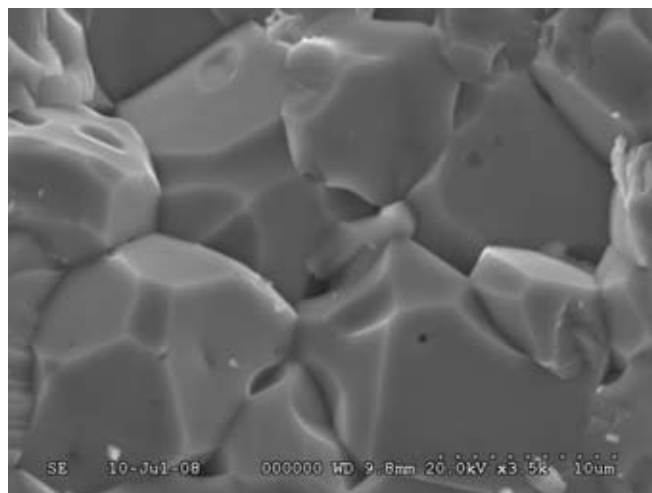


Figure 1: SEM image of 15% (Mg,Zn)O at 1400°C.  
Average grain size = 7.095 µm.

as concentration and temperature increased, diffraction angle decreased (refer to Figure 1). Using the data obtained from XRD, lattice parameters were calculated. The lattice parameter,  $a$ , increased as concentration and sintering temperature increased and the lattice parameter,  $c$ , decreased as concentration and sintering temperatures increased.

According to Vegard's Law, the plot (Figure 2) shows that the samples with a concentration of 20% MgO did not diffuse into the ZnO lattice. The estimated solubility limit of MgO was 15% for samples prepared at temperatures of 1200°C, 17% at 1400°C, and 18% at 1500°C.

Using the photoluminescence data, the band gap was calculated for all samples. A blue shift of the luminescence occurred with the increase of MgO concentration and reaction temp. Photoluminescence data showed that the band gap had increased to approximately 3.6 eV. As the concentration increased, the band gap should have increased linearly.

Using this linear relationship, it can be determined that the MgO solubility limit was approximately 16% for samples sintered at 1400°C (Figure 3). These limits are approximations as the actual chemical composition is likely to be different from nominal composition, due to ZnO evaporation during the sintering process.

### Conclusions:

A preliminary phase diagram for a pseudo-binary MgO-ZnO system was constructed, as seen in Figure 4. As MgO concentration increased, reaction temperature had to be increased to ensure full diffusivity into the ZnO lattice. By alloying ZnO with MgO, the band gap increased from 3.3 eV to 3.62 eV, causing a blue shift of the luminescence. This allowed for tuning of the luminescence wavelength, making the (Zn,Mg)O alloy a good material for LEDs.

### Future Work:

Future work includes performing chemical composition analysis of the samples to determine the actual composition as ZnO can evaporate during the sintering process. The peak photoluminescence wavelengths need to be determined with accuracy. The samples need to be sintered a high temperatures and then annealed at lower temperatures to determine the solubility limit associated with lower reaction temperatures.

### Acknowledgements:

The National Nanotechnology Infrastructure Network iREU Program, National Science Foundation, and the National Institute of Materials Science. I want to give a special thanks to Dr. Naoki Ohashi.

### References:

- [1] Chawla, S., et al; "Synthesis and optical properties of ZnO/MgO nanocomposite"; Journal of Alloys and Compounds, 459,457-460 (2007).
- [2] Zhuang, L, et al; "Microstructure and optical properties of Mg<sub>x</sub>Zn<sub>1-x</sub>O thin films by means of pulsed laser deposition"; Computational Materials Science (2006).

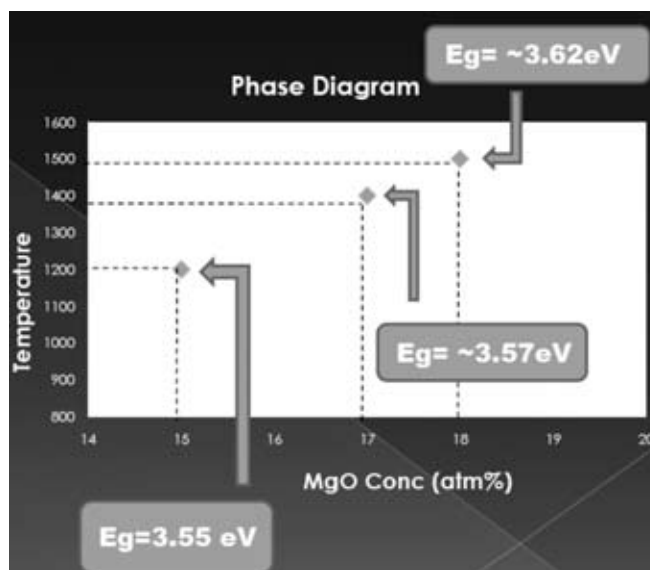
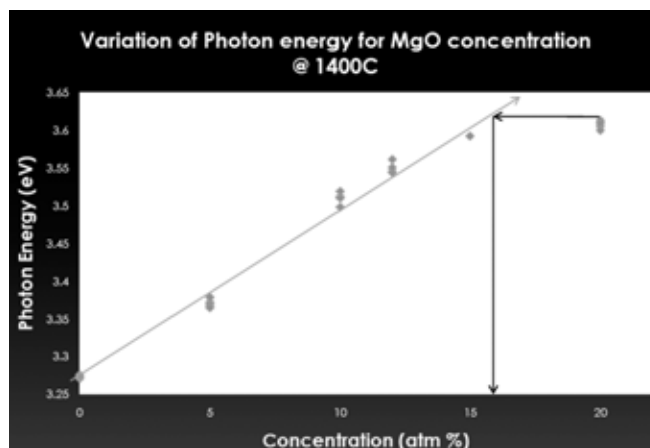
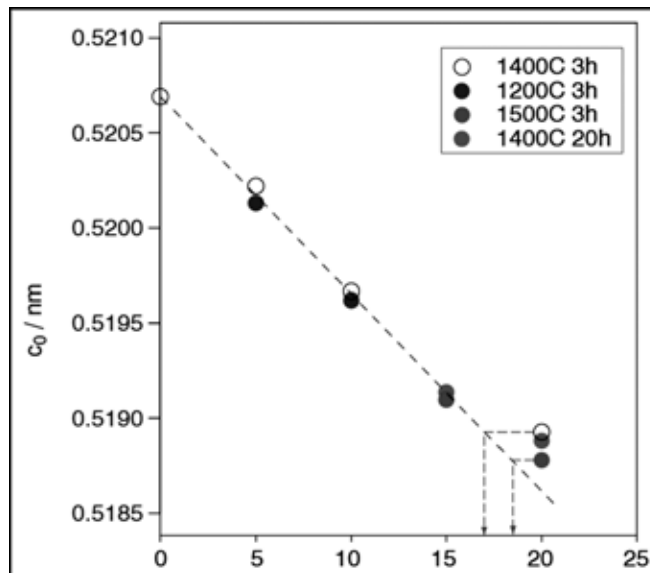


Figure 2, top: Plot of the change of lattice parameters with sintering temperature and increasing concentration.

Figure 3, middle: Graph showing the variation of photon energy with increasing MgO concentration.

Figure 4, bottom: Section of a phase diagram for an (Zn,Mg)O pseudo-binary system.

# Insulated Polythiophene: Self-Threaded Conjugated Polymer via Alkyl Chain Straps

Ryan M. Harrison

Biomedical Engineering, Johns Hopkins University

**NNIN iREU Site: National Institute for Materials Science, Tsukuba, Ibaraki, Japan**

NNIN iREU Principal Investigator(s): Dr. Masayuki Takeuchi, Macromolecules Group

NNIN iREU Mentor(s): Dr. Kazunori Sugiyasu, Macromolecules Group

Contact: rharrison@jhu.edu, Takeuchi.Masayuki@nims.go.jp, Sugiyasu.Kazunori@nims.go.jp

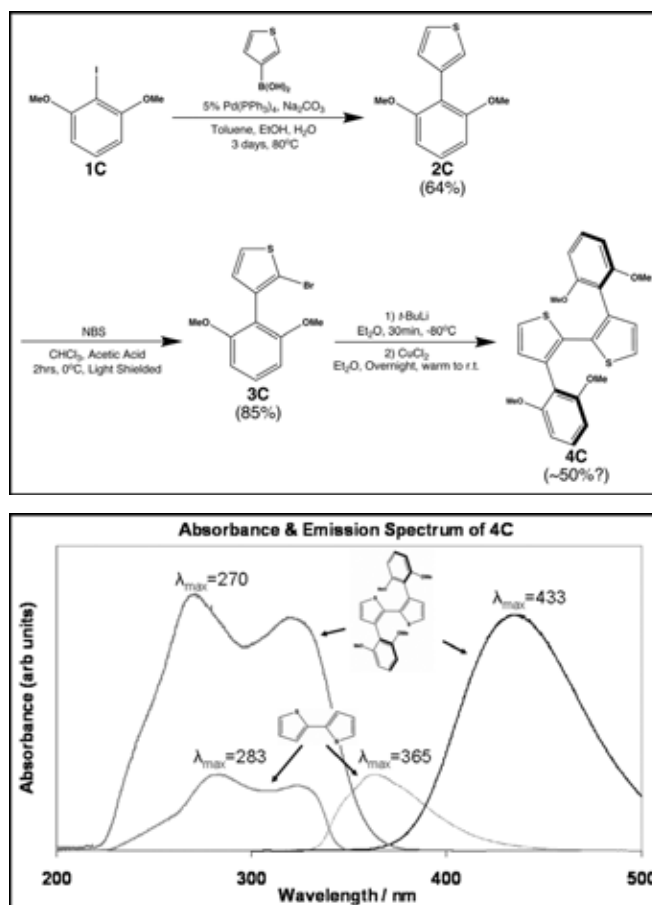
## Introduction:

Polythiophenes are a popular class of organic conducting polymers, known for their environmental stability, conductivity [1], fluorescence and electroluminescent properties [2]. Conducting polymers, such as polythiophenes, have enormous potential in both static and dynamic applications, ranging from field-effect transistors and diodes to chemical sensors [3]. Many applications require the use of conducting polymers in the solid phase, which presents a painful trade off between high and low density deposition. High density deposition allows for easier charge injection as well as greater overall charge density, luminescence and conductivity. Unfortunately, inter-molecular interactions between uninsulated conducting polymers in the solid phase result in imprecise band gap control (mainly due to  $\pi$ - $\pi$  stacking), crosstalk between threads, and quenching (lower fluorescent and electroluminescent quantum yield). While low density deposition can often alleviate these problems, it is often impractical. By inhibiting undesired inter-molecular interactions, insulated conducting polymers offer a solution; ideally, allowing for high density deposition with better band gap control and little/no loss in quantum yield [4]. In this study, we seek to develop an intramolecular bi-thiophene rotaxane with minimal degradation of the conductive, fluorescent and electroluminescent properties of bi-thiophene. The intramolecular bi-thiophene rotaxane must also be suitable for polymerization and use in the solid phase.

## Results:

A bi-thiophene control compound (Scheme 1) was synthesized to both elucidate the effect of covalently attached benzene on bi-thiophene, but also to verify core components of our synthetic approach, namely Suzuki coupling [5,6] and thiophene homo-coupling. Compounds **2C** and **3C** were easily synthesized with moderate to good yield; **4C** required the optimization via multiple reaction conditions, with both a  $n$ -BuLi/ZnCl/CuCl<sub>2</sub> and  $n$ -BuLi/Fe(acac)<sub>2</sub> reaction resulting in 0% yield. A  $t$ -BuLi/CuCl<sub>2</sub> reaction was eventually arrived at, resulting in ~50% yield.

Optical characterization via UV-Vis spectroscopy (Figure 1) revealed that control compound **4C** had over twice the peak absorbance of bi-thiophene as well as double the Stokes shift.



Scheme 1, top: Synthetic pathway for bi-thiophene control compound.

Figure 1, bottom: UV-Vis spectra for bi-thiophene control compound **4C** and bi-thiophene. Bi-thiophene absorbance/emission spectra in orange and aqua respectively; **4C** absorbance/emission spectra in red and blue respectively. Note the increased absorbance and Stokes shift of **4C** versus bi-thiophene.

The increased absorbance could be attributed to a change in thiophene's electron density due to the attached benzene. The increase in Stokes shift was likely due to the increase in the number of degrees of freedom between **4C** and bi-thiophene (more rotation/vibration states in which to dissipate energy).

Synthesis of the intramolecular bi-thiophene rotaxane followed the same basic approach as the bi-thiophene control compound (Scheme 2), with reactions proceeding with similar yields. The cyclization reaction was particularly challenging, requiring optimization across a variety of reactors; the highest yield being 20% via discrete feed semi-batch reactor (portion wise). For comparison, a batch reactor under the same reaction conditions achieved a 6.5% yield. The bromination reaction (**6R/3C**) for the intramolecular rotaxane was unsuccessful (Figure 2). Noting that deuterium was not visible on  $H^1$ -NMR, we elucidated lithiation site specificity via *t*-BuLi lithiation and deuterated methanol quenching. This test revealed no selectivity between the two  $\alpha$ -positions on the thiophene group, ruling out the possibility of selective coupling via direct lithiation. The final coupling reaction remains elusive.

### Conclusions and Future Directions:

This study reveals that the synthesis of a bi-thiophene intramolecular rotaxane (**7R**) is plausible; however, without the complete synthesis of the intramolecular bi-thiophene rotaxane, comparison to bi-thiophene and the synthetically successful bi-thiophene control compound **4C** is impossible. We will continue working on completing the coupling of **7R**, and then proceed to optical characterization. If favorable (minimal degradation of the fluorescent and electroluminescent

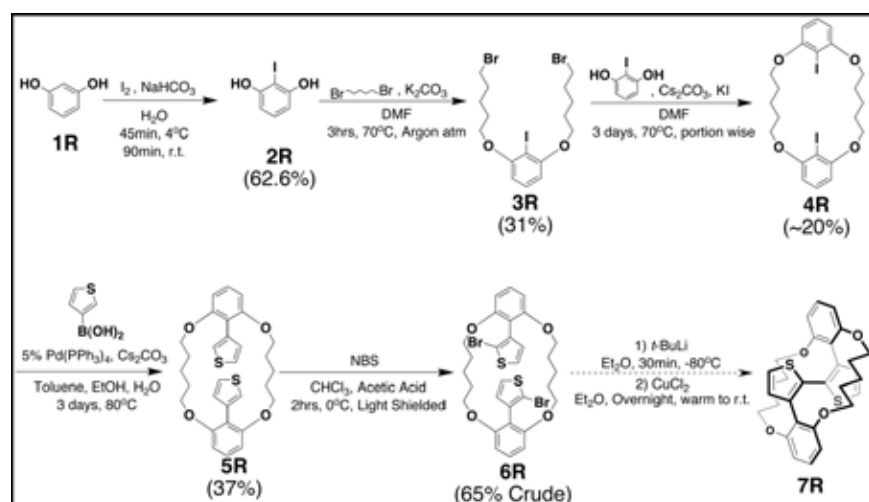
properties of bi-thiophene) polymerization, bulk property and solid-state studies will ensue.

### Acknowledgements:

I would like to thank the Macromolecules Group and NIMS for their generous hosting. On both a personal and professional level, living and working in Japan was an amazing experience. Research funded by the National Nanotechnology Infrastructure Network Research Experience for Undergraduates Program and National Science Foundation.

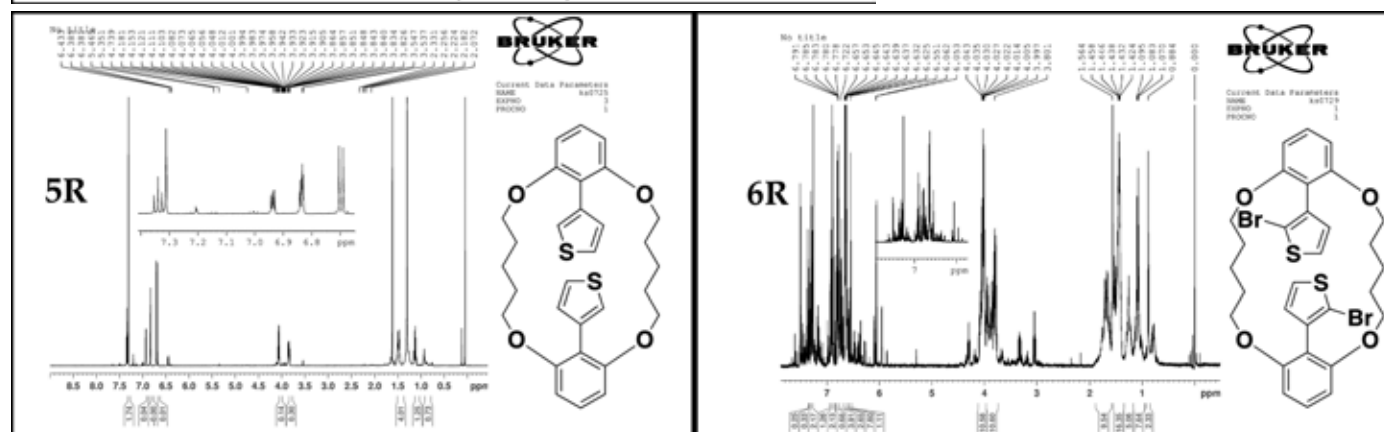
### References:

- [1] Marsella MJ, S.T., Designing Conducting Polymer-Based Sensors: Selective Ionochromic Response in Crown Ether Containing Polythiophenes. *J. Am. Chem. Soc.*, 1993. 115: p. 12214012215.
- [2] McCullough, R.D., The Chemistry of Conducting Polythiophenes. *Adv. Mater.*, 1998. 10(2): p. 93-116.
- [3] V. Martina, L. Pigani, F. Terzi, A. Ulrici, C. Zanardi, R. Seeber, Development of an electronic tongue based on a PEDOT-modified voltammetric sensor. *A&B Chemistry*, 2007. 387(6): p. 2101-2110.
- [4] M. Frampton, L. Harry, Insulated Molecular Wires. 2007. p. 1028-1064.
- [5] Barder TE, W.S., Martinelli JR, Buchwaldk SL, Catalysts for Suzuki-Miyaura Coupling Processes: Scope and Studies of the Effect of Ligand Structure. *J. Am. Chem. Soc.*, 2005. 127: p. 4685-4696.
- [6] Bedford R, Butts CP, Holder D, The Suzuki coupling of aryl chlorides in TBAB-water mixtures. *Chem. Commun.*, 2003: p. 466-467.



Scheme 2, left: Synthetic pathway for intramolecular bi-thiophene rotaxane.

Figure 2, below:  $H^1$ -NMR spectra of **5R** and **6R** using the same brominating reaction and workup as  $2C \rightarrow 3C$ . Note that **5R/6R** and **2C/3C** are identical on TLC.



# Fabrication and Characterization of Cu-WO<sub>3</sub>-Pt and Pt-WO<sub>3</sub>-Pt Switching Devices

Rehan Kapadia

BSEE, University of Texas at Austin; EECS Department, University of California, Berkeley

**NNIN iREU Site: Jülich Forschungszentrum, Jülich, Germany**

NNIN iREU Principal Investigator(s): Dr. Carsten Kuegeler, Institut für Festkörperforschung (IFF), Jülich Forschungszentrum

NNIN iREU Mentor(s): Robert Weng, Institut für Festkörperforschung (IFF), Jülich Forschungszentrum

Contact: kapadia.rehan@gmail.com, c.kuegeler@fz-juelich.de, r.weng@fz-juelich.de

## Abstract/Introduction:

Due to fundamental barriers that prevent further scaling of metal oxide semiconductor (MOS) field effect transistor technology, novel devices are sought as the foundation for next generation memories and processors [1]. Resistive random access memory (RRAM) offers a promising solution to further scaling of memory technology. The building block of RRAM is a device that has multiple resistance states that can be reached depending on the history of current or voltage application.

Metal-insulator-metal (MIM) structures with transition metal oxide (TMO) insulators are typically used to implement resistive switching devices [2]. The specific structures studied in this paper are copper-tungsten oxide-platinum (Cu-WO<sub>3</sub>-Pt) and platinum-tungsten oxide-platinum (Pt-WO<sub>3</sub>-Pt). The devices were characterized in the virgin state through capacitance-voltage (CV), current-time (It), and current-voltage (IV) curves. A constant voltage forming method was used to induce repeatable resistive switching behavior. Stable bipolar and unipolar switching was observed in devices with Cu top electrodes and Pt top electrodes respectively.

## Experimental Procedure:

The devices (Figure 1) were fabricated on sputtered 100 nm Pt substrates with a Pt/ZrO<sub>x</sub>/SiO<sub>2</sub>/Si structure. 60 nm of WO<sub>3</sub> was deposited using a WO<sub>3</sub> target in an oxygen atmosphere at

1 mbar. Both Cu and Pt top electrodes were deposited using a Cu and Pt target, respectively. 100 nm of each was sputtered in an inert environment of argon at  $\sim 1 \times 10^{-3}$  mbar. The top electrodes were patterned using a shadow mask with circular openings of diameter 100 nm and 200 nm. However, the exact dimensions of the electrodes are uncertain due to shadowing.

A Keithley 2611 System SourceMeter was used for IV and It characterization of the chips. CV measurements were carried out using a 100 mA 10 KHz signal superimposed on a DC sweep from -1V to +1V. The capacitance was extracted by modeling the resulting data by a capacitor in parallel with a resistor. After a constant voltage forming step, a voltage sweep was used to switch the devices between multiple resistance states. For certain devices, millisecond constant voltage pulses were used to change resistance state of the device.

## Results:

The IV curves of the pristine devices showed asymmetric behavior with respect to positive and negative bias for both types of devices (Pt and Cu top electrode). This was expected, due to the difference in the interface between the top electrode and bottom electrode because of fabrication methods. However, the value of the leakage current could not be reliably extracted from the IV curve due to time dependent current sources such as dielectric relaxation. The leakage current at

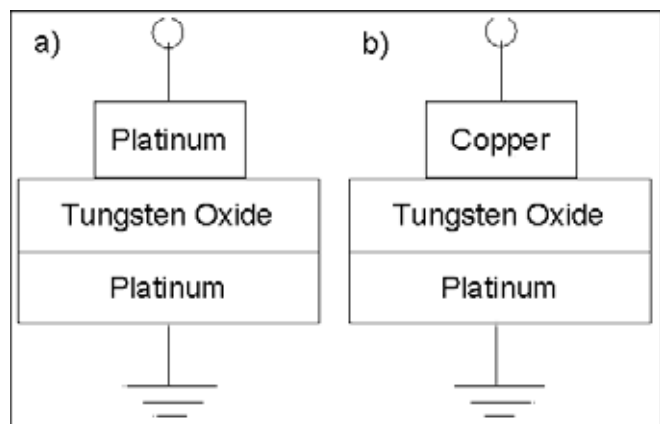


Figure 1: Cross sectional view of device structure.

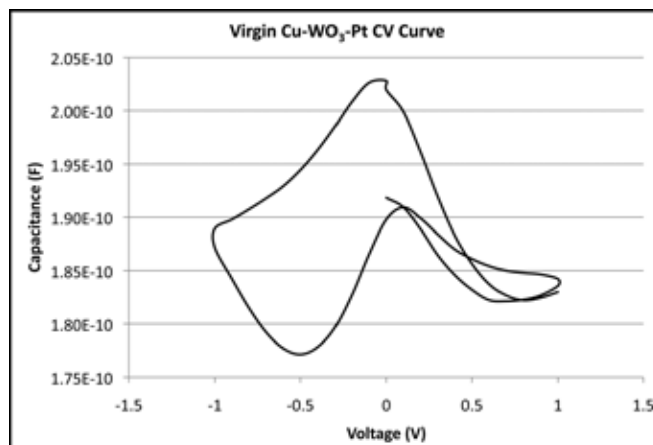


Figure 2: CV curve of devices with copper top electrodes.

0.1 V, obtained from  $I_t$  curves, was  $\sim 10^{-7}$  A for devices with Cu top electrodes, and  $\sim 10^{-9}$  A for Pt top electrodes.

CV curves of the Cu-WO<sub>3</sub>-Pt devices (Figure 2) exhibited significant hysteresis, while Pt-WO<sub>3</sub>-Pt (not shown) CV curves exhibited essentially none. It should be noted that multiple sweeps from -1 V to 1 V starting and ending at 0 V resulted in similar capacitance values. This could be attributed to copper ion diffusion into and out of the WO<sub>3</sub> film [2]. Since Pt does not diffuse appreciably, no significant hysteresis was observed for Pt-WO<sub>3</sub>-Pt devices.

Forming was carried out on the Cu-WO<sub>3</sub>-Pt devices using +3 V with current compliances of 0.1 mA and 1 mA. The time required for a device to form ( $t_f$ ) was a parameter of considerable interest since it is an indicator of the amount of electric stress the dielectric must undergo before repeatable resistive switching is observed. In a sample of 8 identical devices, formed in succession, under exactly the same conditions,  $t_f$  ranged from 48s to 2367s. Devices also had  $t_f$ 's of 62s, 104s, 216s, 362s, 422s, and 1550s. Since these devices were on the same chip, in an area of less than 0.25 cm<sup>2</sup>, and were tested in a timespan of under four hours, these changes are thought to be due to microstructural variations. Elucidating the cause of the  $t_f$  variation would require materials investigation beyond the scope of this REU project.

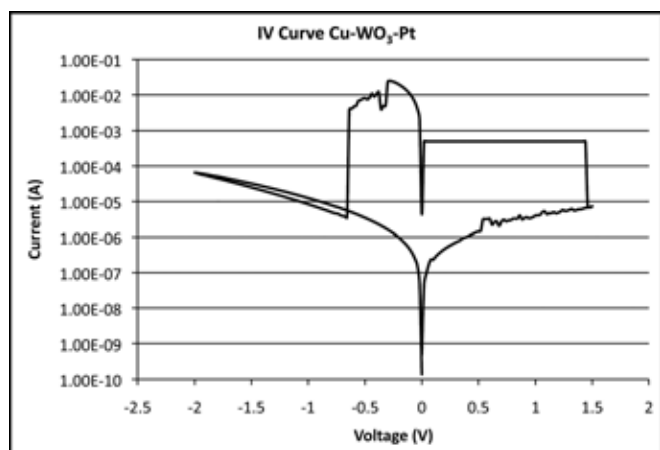


Figure 3: Bipolar switching curve for devices with copper top electrodes.

The bipolar switching for the Cu-WO<sub>3</sub>-Pt (Figure 3) device was obtained after a forming at +3 V with a compliance of 0.5 mA. After forming, repeatable on/off switching occurred at +0.9 V and -0.6 V. The *On* state resistance was measured to be on the order of 10 Ω, and the *off* state resistance was on the order of 10<sup>5</sup> Ω. Both states were stable for at least 10 minutes. It is believed this switching arose due to formation of a copper channel between the top and bottom electrode [2].

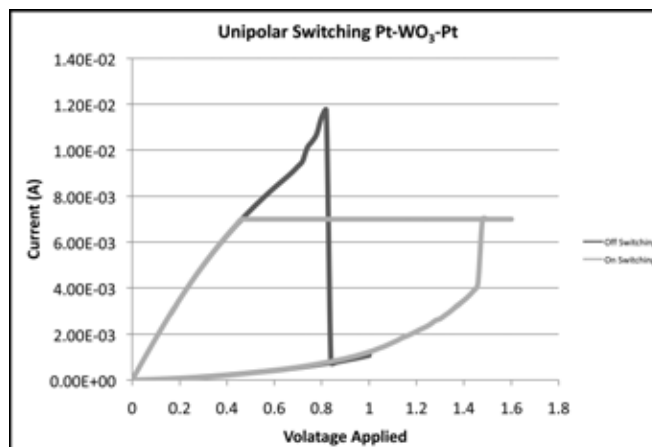


Figure 4: Unipolar switching curve for devices with platinum top electrodes.

The unipolar switching observed for the Pt-WO<sub>3</sub>-Pt (Figure 4) device was obtained after 800 seconds of -3 V bias, followed by 1 second of -4 V bias with a compliance current of -1 mA. Figure 4 shows the device switching on at 1.5 V and switching off at 0.85 V with 12 mA current.

## Conclusions:

Cu-WO<sub>3</sub>-Pt and Pt-WO<sub>3</sub>-Pt MIM structures were fabricated, electrically characterized, formed, and switched. The results showed repeatable bipolar switching between stable 10 Ω and 10<sup>5</sup> Ω states with a Cu top electrode. Repeatable unipolar switching was also observed in a Pt-WO<sub>3</sub>-Pt device structure. Further work is required to determine possible mechanisms for the unipolar switching behavior.

## Acknowledgments:

I wish to thank the the NSF, IREE, the NNIN iREU Program, and the Forschungszentrum Jülich for the opportunity to pursue this research. This research would not have been possible without the time and effort spent to organize the iREU by Dr. Lynn Rathbun and my hosts in Germany, Herr Dr. Prof. Rainer Waser and Dr. Carsten Kügeler. I also wish to thank Robert Weng, Rohit Soni, and Dr. Doo Seok Jeong for their guidance and support.

## References:

- [1] Vogel, E. M. Technology and metrology of new electronic materials and devices. *Nature Nanotech.* 2, 25–32 (2007).
- [2] Waser, R. & Aono, M. Nanoionics-based resistive switching memories. *Nature Mater.* 6, 833–840 (2007).

# Fabrication of Stacked Quantum Dot Diodes and Related Nanostructures and Their Transport Properties

Brian Lambson

Electrical Engineering and Computer Science, UC Berkeley

**NNIN iREU Site: National Institute for Materials Science, Tsukuba, Japan**

*NNIN iREU Principal Investigator(s): Takeshi Noda, Quantum Dot Research Ctr, National Institute for Materials Science*

*NNIN iREU Mentor(s): Hiroyuki Sakaki, Toyota Technological Institute and the National Institute for Materials Science*

*Contact: lambson@eecs.berkeley.edu, noda.takeshi@nims.go.jp, h-sakaki@toyota-ti.ac.jp*

## Abstract:

One way to make a quantum dot intermediate band solar cell (QD-IBSC) is to embed indium arsenide (InAs) quantum dot stacks inside an ordinary solar cell. Embedded QD stacks serve as generation and recombination centers as well as scattering centers in the QD-IBSC, altering the photocarrier transport characteristics of the device. In our work, we studied the photocurrent induced by above-bandgap photons in a 5-period InAs/GaAs QD stack, InGaAs/GaAs superlattice, and undoped gallium arsenide (GaAs) system. Our measurements showed that the efficiency of photocurrent generation was not significantly reduced in the QD sample. We suggest that the influence of the quantum dots on transport was limited due to the relative thinness of the QD region and the de-localization of trapped holes and electrons in the intermediate band. A strain-free quantum dot diode with a thicker active region needs to be studied in the future to determine whether or not the effects of embedded QDs on photocarrier transport are in fact negligible.

## Introduction:

The intermediate band solar cell (IBSC) has the potential to achieve higher energy conversion efficiency than many alternative photovoltaic conversion devices [1]. The IBSC is characterized by the presence of an allowed energy band within what would otherwise be the forbidden energy gap of a conventional semiconductor material. Sub-bandgap photons that normally pass through the material can then be absorbed in two transitions: valence band (VB) to intermediate band (IB) followed by IB to conduction band (CB). High-energy photons are absorbed as usual, by the VB to CB transition.

Engineering a device with the energy band structure proscribed by IBSC theory has proved challenging. One oft-studied possibility is the quantum dot intermediate band solar cell (QD-IBSC). In this structure, embedded quantum dots confine electrons such that discrete energy levels are attained below the CB of the bulk material. If the dots are stacked directly on top of one another, periodicity in the direction of stacking results in the formation of an IB.

One major advantage of the QD-IBSC is controllability. By manipulating the size and spacing of the quantum dots, one can adjust the position and bandwidth of the IB, respectively. Likewise, one can position the Fermi level as needed using modulated doping techniques. InAs/GaAs quantum dots have been the most widely studied for the QD-IBSC due to a desirable band structure and convenient growth methods [2].

As research on the QD-IBSC presses forward, we investigated effects of InAs/GaAs QD stacks on carrier transport. We were particularly interested in whether or not the scattering

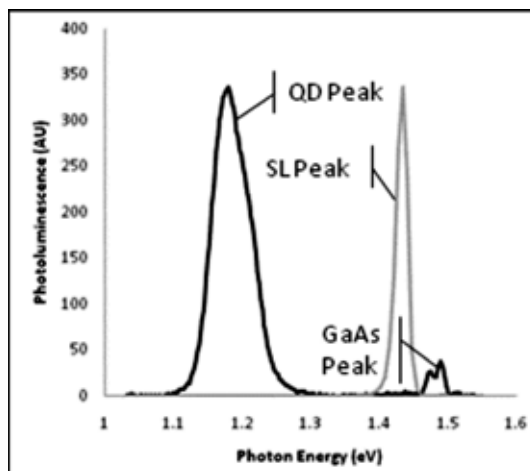


Figure 1: Photoluminescence spectra showing QD, SL, and GaAs ground state energies.

and/or trapping rates of carriers were increased as the result of embedded quantum dots. These effects suppress the photocurrent and solar efficiency of the device and can be used to address the limitations of the QD-IBSC as a model for the ideal IBSC.

## Experimental Procedure:

First, a wafer containing five periods of alternating InAs QD layers and  $\delta$ -doped GaAs capping layers was prepared by molecular beam epitaxy. The quantum dots were self-

assembled by the Stranski-Krastanow method. Next, an InGaAs/GaAs SL sample was grown by incorporating the same amount of In as that for the QD wafer; note here that the strain in InGaAs is reduced so that its growth remains in layer-by-layer mode rather than forming QDs. Last, an undoped GaAs sample with the same dimensions as the QD and SL samples was prepared. The photoluminescence spectra for the three samples is shown in Figure 1.

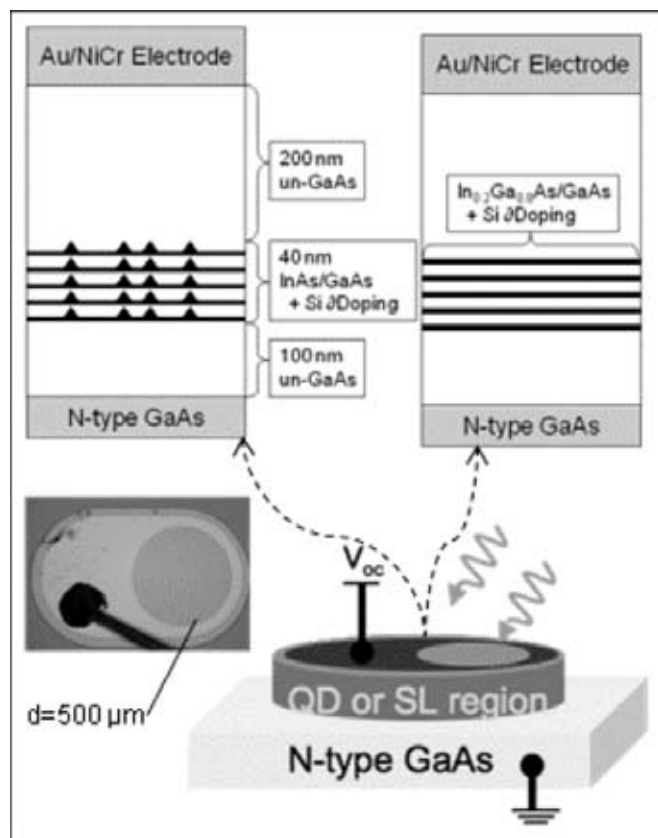


Figure 2: Comparison of QD and SL sample structure (top) and Schottky photodiode diagram (bottom).

These wafers were processed to make Schottky diodes, as shown in Figure 2. For this purpose, transparent Au/NiCr electrodes were patterned via metal liftoff and used as an etch mask for the diode structure. A thicker electrode, patterned to leave a transparent window, capped the device. Current-voltage characteristics of these three devices were measured at room temperature under dark conditions and under 808 nm, 635 nm, and 532 nm laser illumination. Photons with energies well above the GaAs bandgap energy were used for illumination because the generation of carriers by sub-bandgap excitation was negligible. Based on the current-voltage measurements, we evaluated the photocurrent efficiency of the device—the photocurrent per unit flux of incident photons.

### Results and Conclusions:

The photocurrent efficiency results are shown in Figure 3. Our key finding was that the photocurrent efficiency was not

lower in the QD sample than the SL and un-GaAs samples. This was contrary to our expectation; QD systems tend to reduce the mobility of photocarriers by disturbing the crystal periodicity and increase recombination by trapping electrons and holes in close proximity. To address the contradiction of our expectation, we suggest that: (1) the average mobility, taking into account the mobility and thickness of the intrinsic GaAs region, may not vary measurably between samples; and that (2) if the sub-band energy levels of the QD stacks are coupled and an electric field is present, electrons and holes drift to opposite ends of the stack where they have a low probability of recombining.

### Future Work:

Future work should focus on determining the extent to which our surprising result can be generalized. The systematic measurement of photocurrent and radiative recombination under various bias voltages is important short-term work to assess whether or not recombination in the QD stacks is influenced by the magnitude of the built-in electric field. Fabricating and testing larger QD stacks, using strain-free systems, is a long-term goal.

### Acknowledgements:

We would like to thank the National Institute for Materials Science, the National Nanotechnology Infrastructure Network iREU Program, and the National Science Foundation for supporting this project.

### References:

- [1] A. Luque and A. Marti, "Increasing the Efficiency of Ideal Solar Cells by Photon Induced Transitions at Intermediate Levels," *Phys. Rev. Letters*, vol. 78, pp. 5014-5017, 1997.
- [2] A. Marti et. al., "Novel Semiconductor Solar Cell Structures: The Quantum Dot Intermediate Band Solar Cell," *Thin Solid Films*, pp. 638-644, 2006.

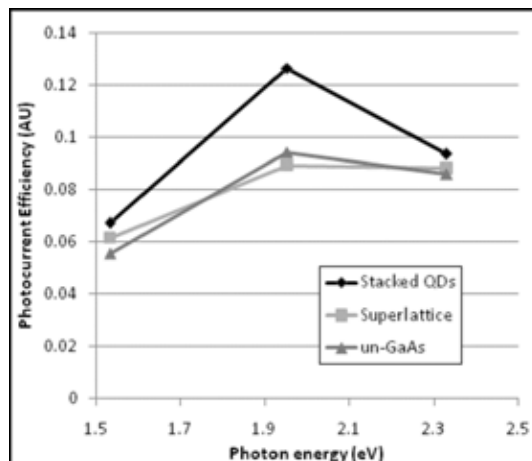


Figure 3: Photocurrent efficiency using 808 nm, 635 nm, and 532 nm laser excitation.

# Adatom Displacement Using the Scanning Tunneling Microscope

Alexander V. Luce

Engineering Physics, The University of Arizona, Tucson, AZ

**NNIN iREU Site: National Institute for Materials Science, Tsukuba, Japan**

*NNIN iREU Principal Investigator(s): Dr. Daisuke Fujita, Managing Director, Adv. Nano Characterization Center, NIMS*

*NNIN iREU Mentor(s): Dr. Keisuke Sagisaka, Advanced Scanning Probe Microscopy Group, NIMS*

*Contact: aluce@email.arizona.edu, FUJITA.Daisuke@nims.go.jp, SAGISAKA.Keisuke@nims.go.jp*

## Abstract:

**Tunneling electrons in a scanning tunneling microscope were used to displace silicon (Si) adatoms on a Si(111)  $7 \times 7$  surface at 78K. The displacement was observed to occur using both positive and negative bias voltages. Five topography levels of the displaced adatom were observed, each corresponding to a different configuration of Si adatoms in the half unit cell directly beneath the microscope tip.**

## Introduction:

The scanning tunneling microscope (STM) is a powerful tool for nanoscale characterization and manipulation of individual atoms on both metallic and semiconducting surfaces. The STM can accurately probe the atomic structure of various conductive surfaces [1]. The Si(111)  $7 \times 7$  surface reconstruction was the first semiconductor surface imaged with atomic resolution by STM [2]. Atomic scale manipulation experiments have shown that specific Si adatoms on the bare Si(111)  $7 \times 7$  surface can be reversibly laterally displaced under the influence of both tunneling and field emitted electrons [3]. Stipe et al. reported that the center silicon adatom in both the faulted half (FH) and unfaulted half (UFH) of the unit cell can be displaced to a neighboring metastable threefold site (T4 site) with a sample bias above +2.0 V. This phenomenon has been touted as the basis for a single atom switch [5].

## Experimental Procedure:

In this paper, we report new findings on the adatom displacement phenomenon by observing the Si(111)  $7 \times 7$  surface with low temperature STM. Unlike previous experiments, the displacement can be induced with both positive and negative voltage pulses applied with respect to the sample. Figure 1(A) shows an STM image of the Si(111)  $7 \times 7$  surface at 78K. The dimer-adatom-stacking-fault (DAS) structure is visible, a single unit cell is highlighted, and the scan voltage of -1.0 V highlights the contrast between the FH and UFH unit cell. A schematic of the surface layer is shown in Figure 1(B). In the top adatom layer, there are six Si atoms in “corner” sites and six Si atoms in “center” sites, each of these atoms lies on a T4 site of the “rest atom” layer underneath the surface. Positive and negative voltage pulses above approximately +2.0 V or below -2.0 V cause a transfer of the center site adatom to a neighboring metastable T4 site, as shown in Figure 2. Stipe et al. studied this phenomenon and found that at temperatures below 175K, voltage pulses above +2.0 V induce a single adatom transfer or return in the

half unit cell of the ( $7 \times 7$ ) structure, with the displacement probability in the FH being 100 times greater than the UFH. Furthermore, the transfer and return rate of the adatom depends on sample bias, tunneling current, temperature, and excitation is not localized beneath the STM tip. Our experiments on the Si (111)  $7 \times 7$  surface were consistent with these observations, but with the exception that the adatom displacement could be induced by applying negative voltage pulses.

Experiments were performed in an ultrahigh vacuum STM with base pressure of approximately  $5 \times 10^{-9}$  Pa, operating at 78K. The samples used were n-type Si(111), phosphorus doped, with a resistance of 0.01  $\Omega$  cm. The surface was cleaned by flashing to a temperature of 1200K, followed by an annealing step to produce the  $7 \times 7$  reconstruction. Electrochemically etched tungsten tips were used for imaging. Topographical images were typically scanned with a sample bias of  $\pm 1.0$  to 1.5 volts and 0.2 nA tunneling current.

The frequency of the adatom displacement was measured by positioning the STM tip above a selected center atom in the FH. The bias voltage was increased to a predetermined value, and the z position (tip height above surface) of the STM tip was measured as a function of time. This produces a frequency trace corresponding to the measured local density of electronic states (LDOS) directly underneath the tip. Figure 2 presents a series of z-height traces as a function of time when the bias voltage was increased to +2.0, 2.6, and 3.0 volts respectively. During the time of increased tip-sample bias, the z position of the tip fluctuates between several height states, each corresponding to a transfer of adatoms among metastable sites within the half unit-cell. Observation of the tip height during the voltage pulse reveals five distinct height steps, denoted by lines a, b, c, d, and e in Figure 3.

Previous experiments have analyzed the mechanics between only the two topographic states corresponding to a “single hop” or the z position of a center adatom in the “normal” position, and in the “vacancy” position [3]. However, we have

observed the underlying mechanics to be further complicated given the five possible z-height positions measured. As shown in Figure 4, these steps correspond to (a) the center adatom in its “normal” position, (b) an “adatom vacancy” underneath formed underneath the tip, (c) contrast enhancement due to a “single hop” of a neighboring center atom in the same half unit cell into an adjacent T4 site, (d) contrast enhancement due to a “double hop” of the other two center adatoms into the adjacent T4 sites, and (e) a “depressed adatom” where a decrease in topographic contrast is observed when an adatom vacancy is created in the adjacent UFH unit cell. It is worth noting that the local electronic structure and surface potential of the depressed adatom differ from those on a clean surface [4,6].

### Results and Conclusions:

In summary, adatom displacement experiments using on the clean Si(111)  $7 \times 7$  surface have been performed using the STM. These experiments proved that center adatom displacement in the faulted half unit cell is possible at both positive and negative sample bias voltages. Additionally, five distinct topographic states have been observed for bias voltages above +2.0 V while the STM tip is placed directly above a center adatom in the faulted half unit cell. Future work will focus on a detailed understanding of the physical mechanism for the adatom displacement phenomenon and the resulting changes in the electronic structure of the Si(111)  $7 \times 7$  surface.

### Acknowledgements:

Support of this research from NSF award OISE-0727552 to the NNIN through the International Research Experience for Students Program, and the National Institute of Materials Science is gratefully acknowledged.

### References:

- [1] G. Binnig, H. Rohrer, C. Gerber, and E. Weibel, Physical Review Letters 49, 57 (1982).
- [2] G. Binnig, H. Rohrer, C. Gerber, and E. Weibel, Physical Review Letters 50, 120 (1983).
- [3] B. C. Stipe, M. A. Rezaei, and W. Ho, Phys.Rev.Letts 79, 4397 (1997).
- [4] K. Sagisaka and D. Fujita, Physical Review B (Condensed Matter and Materials Physics) 77, 205301 (2008).
- [5] B. C. Stipe, M. A. Rezaei, and W. Ho, Science 279, 1907 (1998).
- [6] An in-depth discussion on the electronic structure of the depressed adatom will be provided in a separate paper.

Figure 3, right, middle: Z-height trace of the STM tip height over a center adatom in the faulted half of a unit cell showing evidence of five topographical states. The levels correspond to: adatom vacancy (A), depressed adatom (B), normal position (C), single hop (D), and double hop (E).

Figure 4, right, bottom: STM images of the five possible topographic states of the center atom in the faulted half unit cell denoted by black arrow. These correspond to: (a) normal position, (b) adatom vacancy, (c) single hop, (d) double hop, and (e) depressed adatom.

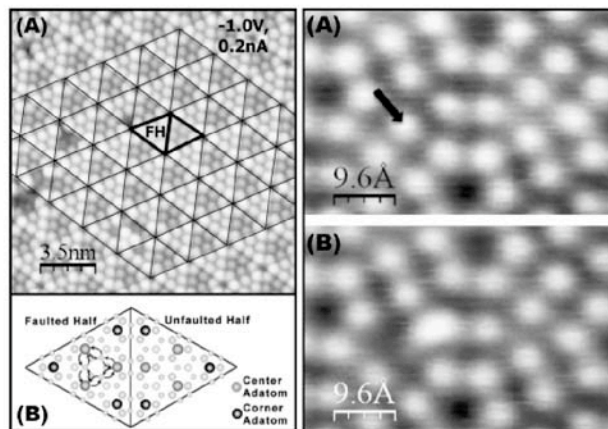
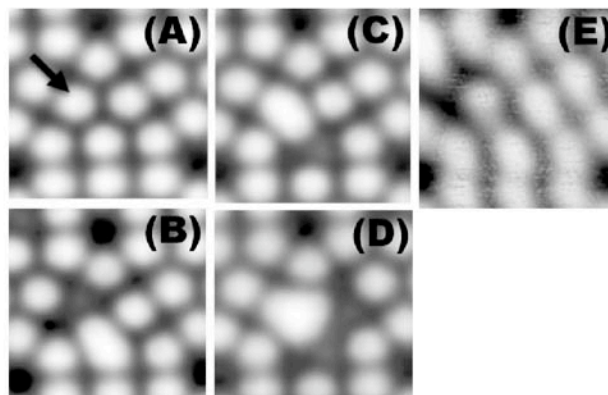
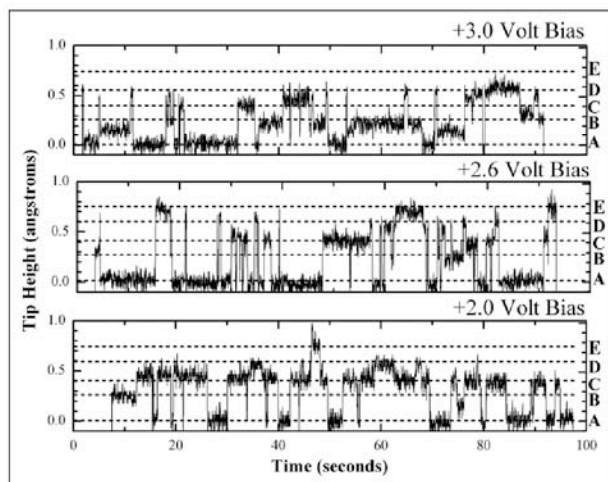


Figure 1, left: (a) STM image of Si(111)  $7 \times 7$  surface at 78 K. (b) Schematic of DAS model of Si(111)  $7 \times 7$  surface showing detail of center adatom displacement between neighboring T4 sites, adapted from Sagisaka et al.

Figure 2, right: (a) STM image of Si(111) at 78K showing  $7 \times 7$  unit cell. The tip is positioned above the denoted adatom and the bias voltage increased until a change in z position is observed. (b) Rescan over same area shows the center adatom has been displaced to a neighboring metastable T4 site.



# Dual Micro Contact Printing of Proteins to Control Neuronal Adhesion and Outgrowth

Alice MacQueen

Biology and Biochemistry, University of Virginia

**NNIN iREU Site: Jülich Forschungszentrum, Jülich, Germany**

NNIN iREU Principal Investigator(s): Prof. Andreas Offenhäuser, Inst. for Bio & NanoSystems 2, Forschungszentrum Jülich

NNIN iREU Mentor(s): Dr. Kristin E. Michael, Institute for Bio and NanoSystems 2, Forschungszentrum Jülich

Contact: e. alicem@virginia.edu, a.offenhaeuser@fz-juelich.de, k.michael@fz-juelich.de

## Introduction:

*In vitro* neuronal networks are inherently complex systems. Simplified networks could benefit applications such as cell-based biosensors, neuroelectronic circuits, and neurological implants while also addressing fundamental biological questions. Previously, we have employed geometric control of network formation by printing a protein grid of poly-D-lysine (PDL) and extracellular matrix gel (ECM) on a non-adhesive glass background. Although cells adhered to the pattern and formed various circuit types (linear connections, feedback loops, and branching/converging pathways), complex connectivity patterns still formed [1]. Here, we focused on creating more intricate patterns by; (i) dual-stamping of two different proteins [2], and (ii) nanostructured gradient patterns [3]. For dual-stamping, PDL “nodes” were printed to promote cell body adhesion, and aligned lines of laminin (LN) were printed to induce axon extension. After three days of neuron culture, neurons and protein patterns were immunofluorescently labeled and imaged. Line pattern type influenced neuron adhesion and axon extension, with a closer spaced pattern appearing optimal. Neurons also preferred lines of 1  $\mu\text{m}$  width in comparison to gradients.

## Experimental Procedure:

Two stamp combinations were used for dual-printing (Figure 1). Stamps were created from a silicon master (dual-printing from standard photolithography, nanopattern from ebeam lithography) by baking polydimethylsiloxane (PDMS, Sylgard 184, Dow Corning) on top (60°C, overnight). 1 cm<sup>2</sup> stamps were cut out, cleaned in ethanol, and dried (argon). Stamps were immersed in SDS (7.5%, 10 min), dried, rinsed (MilliQ H<sub>2</sub>O), redried, and immersed in protein solutions for 20 minutes. For nodal stamps, a mixture of the fluorescent protein TRITC (10  $\mu\text{g}/\text{ml}$ ) and PDL (10  $\mu\text{g}/\text{ml}$ ) in Gey’s Balanced Salt Solution (GBSS) was adsorbed. For lines, a LN solution (20  $\mu\text{g}/\text{ml}$ ) or LN/PDL solution (20  $\mu\text{g}/\text{ml}$  LN and 5  $\mu\text{g}/\text{ml}$  PDL) was adsorbed. The stamps were then rinsed, dried, and stamped on a flamed glass substrate using a fine placer (20 min, 10g pressure) in quick succession to give aligned, dual-stamped substrates (Figure 1). Nanoprinting stamps were immersed in FITC-PDL (10  $\mu\text{g}/\text{ml}$ ) and ECM (10  $\mu\text{g}/\text{ml}$ ) mixture (Sigma). Stamped substrates were left overnight in petri dishes (pre-coated with PDL) containing Gentamycin (10  $\mu\text{g}/\text{ml}$ ). Primary embryonic rat cortical neurons were plated (50,000 cells/plate) and cultured for

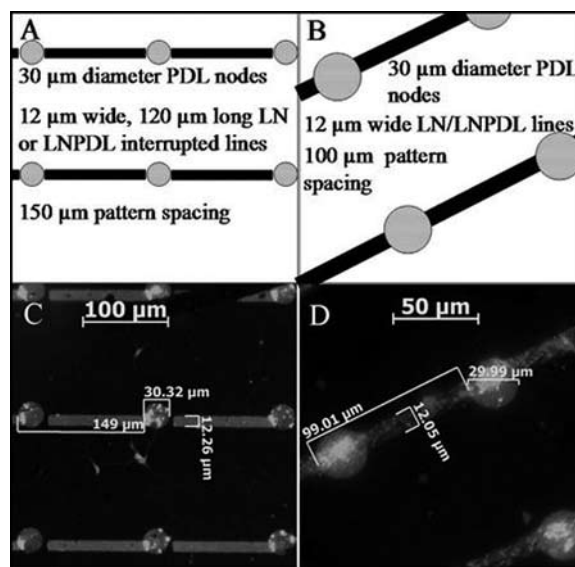


Figure 1: Dual-printed micropatterns, shown as: A. 150  $\mu\text{m}$  schematic; B. 100  $\mu\text{m}$  schematic; C. 150  $\mu\text{m}$  printed pattern; D. 100  $\mu\text{m}$  printed pattern.

three days before fixing and immunofluorescently labeling for either Tau1 (axons, Chemicon), Map2 (dendrites, Chemicon) and LN (Abcam) or MAP2 and  $\beta$ -tubulin (Sigma). Imaging was completed with a Zeiss Apotome fluorescence microscope with AxioVisionRel [4].

## Results:

For dual-patterned substrates, neuron cell bodies and neurites were typically restrained to the pattern for both protein mixtures on the 100  $\mu\text{m}$  patterns (Figure 2). For the 150  $\mu\text{m}$  patterns, those axons relatively restricted to the pattern were still noticeably less constrained by the lines than the 100  $\mu\text{m}$  spaced patterns.

Cell body locations were counted (Figure 4A) as one measure of neuron adhesion to the protein pattern, ideally on PDL nodes. This cell body-to-node specific adhesion occurred for the majority of cells only on 100  $\mu\text{m}$  line LN patterns with PDL nodes. For LN/PDL patterns, more than half of the cells on the pattern adhered to the LN/PDL lines, randomizing their position. This position is not ideal for applications such as in neuroelectronic circuits with electrode arrays. The majority of cells on the 150  $\mu\text{m}$  patterns adhered to the

unstamped background. PDL contamination of the background due to stamp sagging or from pre-coated PDL petri dishes could be partly responsible.

Axon locations were also recorded as a meter of line guidance (Figure 4B). 150  $\mu\text{m}$  lines had more axons unconstrained or only slightly constrained by the lines. The axons on 100  $\mu\text{m}$  lines of LN were guided best by these lines, which also correlated with typical axon length [3]. Studies [2] have suggested that a pattern in which neurons cross from a different substrate onto LN gives the best restriction to LN. Perhaps an interrupted line pattern, without overlap of LN and PDL, would give better guidance by LN.

For nanopatterned gradient substrates, neurons were fluorescently-labeled to monitor all neurite projections along the patterns (Figure 3). Preliminary experiments completed here showed that neurites preferred 1  $\mu\text{m}$  line widths over all other gradients or lines provided by the pattern.

### Conclusions:

Both the cell body adherence and line guidance were significantly better for the 100  $\mu\text{m}$  spaced patterns than for 150  $\mu\text{m}$  lines. LNPDL randomized the cell body location across the protein pattern, as cells would adhere equally to the PDL printed as a line or node. Of the few options tested, the 100  $\mu\text{m}$  spaced pattern with LN lines would seem best for limiting locations of cell body attachment.

### Future Work:

Future work could involve basic stamp redesign to optimize neuron growth and differentiation on these patterns, such as making narrower lines to prevent cell body adhesion, larger nodes to contain all dendrites, and shorter pattern spacings such as 80  $\mu\text{m}$  [3] to match typical axon length. Other adhesion proteins, such as L1, NCAM, or tenascin C could also be substituted.

### Acknowledgements:

Many thanks to Dr. Kristin Michael and Prof. Andreas Offenhäuser for their guidance, Julie Nucci for giving us the tools to 'survive' in Germany, and to the NNIN, NSF, and FZJ for funding this work.

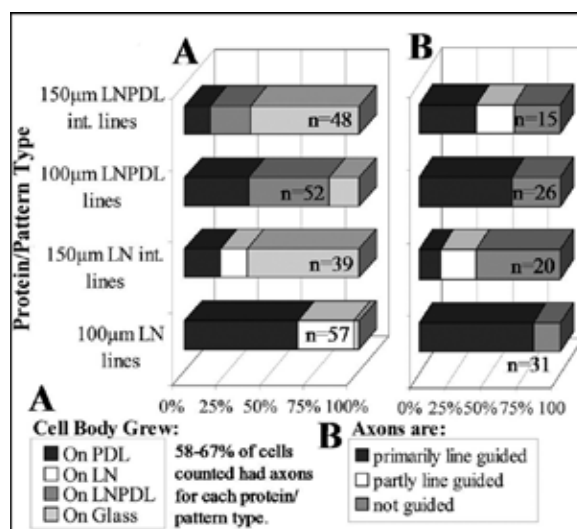
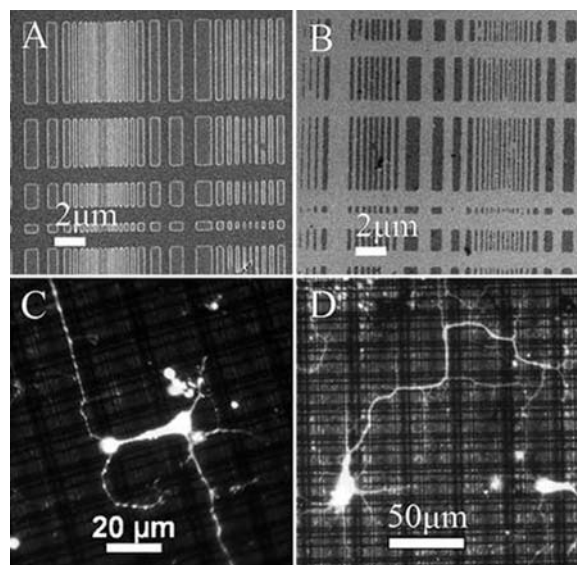
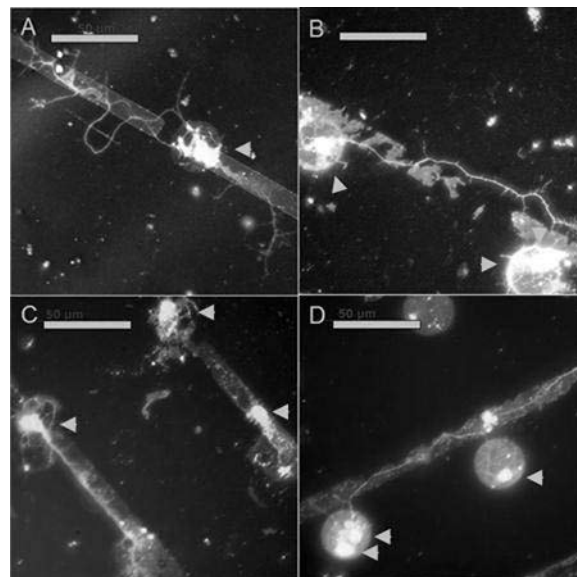
### References:

- [1] Vogt, A.; Brewer, G.; Offenhausser, A. "Connectivity Patterns in Neuronal Networks of Experimentally Defined Geometry"; *Tissue Engineering*, 11(11-12), 1757-1767 (2005).
- [2] Esch, T.; Lemmon, V.; Banker, G. "Local Presentation of Substrate Molecules Directs Axon Specification by Cultured Hippocampal Neurons"; *Journal of Neuroscience*, 19(15), 6417-6426 (1999).
- [3] Dertinger, S.; Jiang, X.; Li, Z.; Murthy, V.; Whitesides, G. "Gradients of substrate-bound laminin orient axonal specification of neurons"; *PNAS*, Vol. 99, 12542-12547 (2002).

Figure 2, top: Neurons cultured on: A. 150  $\mu\text{m}$  LN interrupted lines; B. 150  $\mu\text{m}$  LNPDL interrupted lines; C. 100  $\mu\text{m}$  LN lines; D. 100  $\mu\text{m}$  LNPDL lines. 50  $\mu\text{m}$  scale bar.

Figure 3, middle: Preliminary nanocontact printing of axon guidance protein gradient. A. Stamp SEM image. B. printed PDL-ECM. C. and D. Neurons growing on nanopatterned PDL-ECM.

Figure 4, bottom: Quantification of Pattern Resilience A. Cell body-to-PDL node location; B. LN and LNPDL-to-axon location.



# Highly Symmetric GaAs/AlGaAs Quantum Dots on (111)A GaAs Using Droplet Epitaxy

Brian McSkimming

Electrical Engineering and Mathematics, University at Buffalo, State University of New York

**NNIN iREU Site: National Institute of Material Sciences, Tsukuba, Japan**

NNIN iREU Principal Investigator and Mentor: Dr. Takaaki Mano, Quantum Dot Research Center,

National Institute of Material Sciences, Tsukuba, Japan

Contact: mcskimming@gmail.com, MANO.Takaaki@nims.go.jp

## Abstract:

We report the successful growth of highly symmetric GaAs/AlGaAs quantum dots (QDs) on the (111)A surface of a GaAs substrate using modified droplet epitaxy. A growth recipe was optimized in order to attain samples with small, low density QDs as well as small, high density QDs and those parameters are reported here. The QD samples were characterized with macro and micro photoluminescence to determine their optical properties as well as possible size distributions.

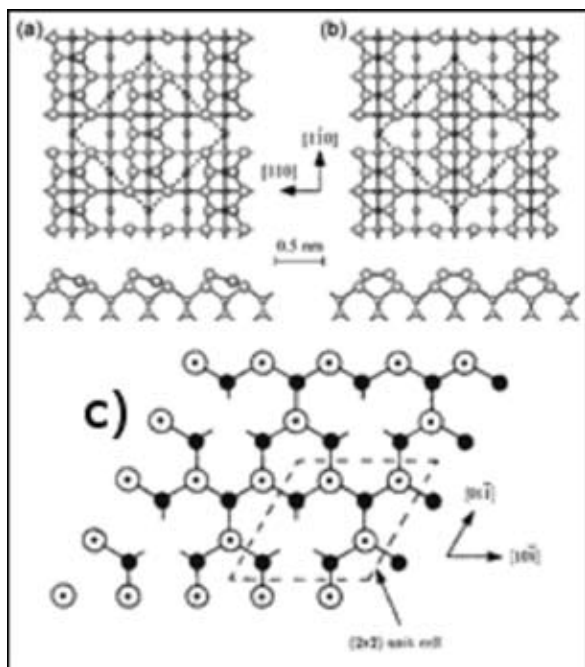


Figure 1: (a) & (b) GaAs (100) surface reconstruction; (c) GaAs (111)A surface reconstruction.

## Introduction:

As the semiconductor industry continues to progress towards new and novel devices and structures the quantum dot (QD) continues to assert itself as one of the more promising and flexible nanostructures. One example of this flexibility is demonstrated in the capability of the QD to emit not only single photons, but an entangled photon pair. To date, entangled photon emission has been coaxed out of QDs through the use of external electric and/or magnetic fields as the fine structure splitting of the QD energy levels

otherwise results in a lack of photon energy degeneracy. In order to eliminate this fine structure splitting, we utilized the following techniques: 1) QD growth using modified droplet epitaxy as opposed to Stranski-Krastanov (SK) growth which eliminates strain inherent and necessary in SK growth; and 2) QD growth on (111)A GaAs as opposed to the more standard (100) GaAs substrate with the expectation that the three-fold symmetry of the (111)A surface reconstruction as opposed to the two-fold symmetry of the (100) surface reconstruction will enforce greater symmetry and reduced anisotropy in the QDs themselves (Figure 1).

## Experimental Procedure:

All of our samples were grown in a standard Riber molecular beam epitaxy (MBE) machine and characterized using atomic force microscopy (AFM) measurements to determine size and density/distribution, and photoluminescence measurements to determine the sample's emission spectrum. In order to be able to test and characterize individual QDs, it was necessary to grow our sample with a density lower than  $10^9$  QDs/cm<sup>2</sup>, something that had not been published before utilizing the (111)A substrate. Further, in order to achieve what was believed to be optimum emission spectra, we desired the QDs to have a width of approximately 30-40 nm and a height of less than 4 nm.

All QD samples were grown utilizing a technique known as modified droplet epitaxy (MDE), in which gallium (Ga) is first deposited on the substrate alone, forming Ga droplets on the substrate surface, and then arsenic (As) is introduced into the growth chamber crystallizing the Ga droplets into GaAs QDs. It is these Ga droplets which we initially optimized for density and droplet size through a variance of three growth parameters, namely substrate temperature ( $T_s$ ), Ga deposition rate and total amount of Ga deposited. Ga droplet samples

were grown in three stages, each varying one of our growth parameters. The  $T_c$  was varied from 200°C through 500°C in increments of 100°C, while the deposition rate and deposition amount were held constant at 0.1 monolayer (ML)/s and 2 ML respectively. The second set of Ga droplet growths varied the deposition rate with growths at 0.1 ML/s, 0.05 ML/s and 0.01 ML/s while holding  $T_c$  constant at the optimized temperature and holding the deposition amount at 2 ML. Our third set of growths varied the deposition amount (2 ML, 0.1 ML and 0.05 ML) while holding the other two parameters constant.

Once we had achieved our desired density and size distribution we then grew crystallized GaAs samples with both low and high QD densities in order to measure the optical emission properties of our samples through photoluminescence. Macro photoluminescence was utilized to determine the emission spectrum of the overall quantum dot sample. From the sample's emission spectrum, there could be some estimations made with regard to quality and size of the quantum dots within the sample. Micro photoluminescence would then be used to characterize and determine the properties of individual nanostructures with specific attention paid towards attempting to determine the fine structure splitting of the quantum dot's energy levels.

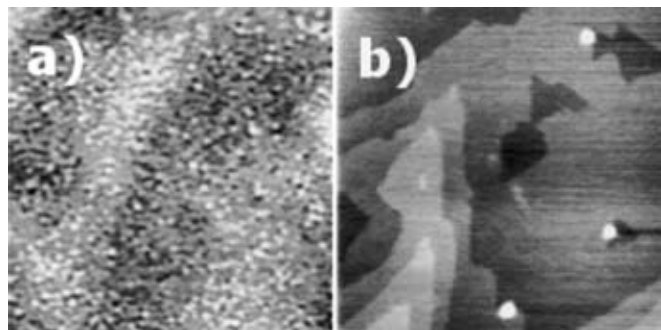


Figure 2: (a) Non-optimized Ga droplet sample; (b) Optimized Ga droplet sample.

## Results and Conclusions:

Substrate temperature ( $T_c$ ) and deposition rate had the greatest effect on droplet density reducing it from  $2.8 \times 10^{11} \text{ cm}^{-2}$  (with  $T_c$  of 200°C and deposition rate of 0.1 ML/s) to  $7.1 \times 10^8 \text{ cm}^{-2}$  (with  $T_c$  of 500°C and deposition rate of 0.01 ML/s). The droplet size was able to be reduced from a maximum size distribution with a mean of  $\sim 100.0 \text{ nm}$  wide by 21.8 nm high to a distribution with mean of 43.9 nm wide by 4.14 nm high. This reduction corresponds to a total volume decrease of more than a factor of ten. These drastic reductions in droplet density and size distribution can be seen in Figure 2. Macro photoluminescence results from one of the low density QD samples demonstrate something which was initially unexpected (Figure 3), that being a double peak in the optical emission spectrum. This double peak suggests that there is a certain point at which small Ga droplets coalesce into larger droplets, thus creating a vacancy in the photoluminescence

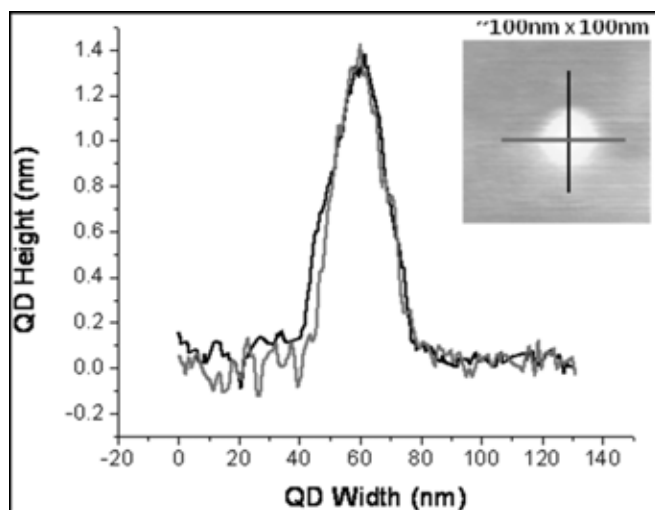
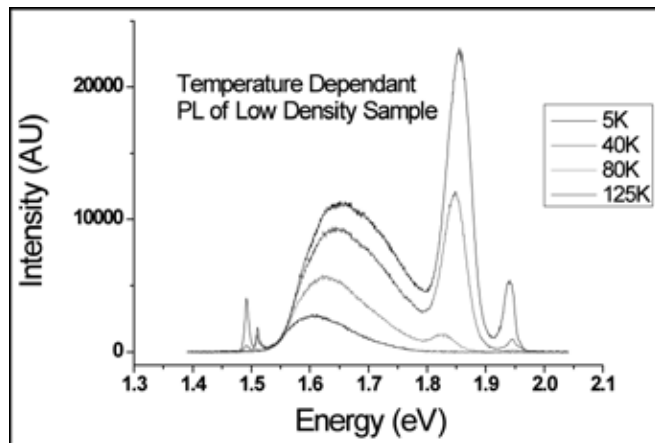


Figure 3, top: Cross-sectional profile of a single QD taken from two different orthogonal directions and overlaid on top of each other.

Figure 4, bottom: Temperature dependent photoluminescence emission of a low-density quantum dot sample.

plot where the emission from these mid-sized QDs would appear. The QDs grown demonstrate the isotropy and symmetry that we desired, as can be seen in Figure 4 where a cross-sectional profile was taken of the AFM image across two orthogonal directions.

## Future Work:

Future work will include additional micro photoluminescence characterization intended to verify the emission of entangled photons from these QDs, as well as detailed characterization of the properties of these QDs.

## Acknowledgements:

Many thanks to the National Nanotechnology Infrastructure Network for providing this opportunity, NSF for funding and to Japan's National Institute for Materials Science for everything.

# Development of AlGaN/GaN HEMT Technology for Highest Frequency Operation

William J. Roman

Biomedical Engineering, Electrical Engineering, University of Rhode Island

**NNIN iREU Site: Jülich Forschungszentrum, Jülich, Germany**

*NNIN iREU Principal Investigator: Dr.-Ing Michel Marso, Institut für Bio- und Nanosysteme (IBN-1), Jülich Forschungszentrum*

*NNIN iREU Mentor: Benjamin Strang, Institut für Bio- und Nanosysteme (IBN-1), Jülich Forschungszentrum*

*Contact: roman.will@gmail.com, m.marso@fz-juelich.de, b.strang@fz-juelich.de*

## Abstract:

The ever increasing demand for high power, high frequency, and high temperature devices has prompted much research into AlGaN/GaN high electron mobility transistors (HEMTs) because of their high breakdown voltage and excellent electron transit properties. Optimized AlGaN/GaN HEMTs promise to play a pivotal role in next generation mobile phone base stations, radar, mixers, oscillators, and attenuators in both commercial and military applications. This work characterizes the performance of AlGaN/GaN HEMTs on SiC in relation to source-gate spacing. Development of HEMT technology is explored utilizing T-gates and optimized ohmic contacts for improving the high frequency operation of future HEMT generations.

## Introduction:

Gallium nitride (GaN) HEMTs excel over competing technology for high power, high frequency applications. GaN HEMTs have an order of magnitude higher power density and higher efficiency over silicon (Si) and gallium arsenide (GaAs) transistors, allowing a ten time size reduction for the same output power, while simultaneously saving material cost. The wide band gap (3.4 eV) allows for rugged high-voltage, high-temperature application extensively covering both commercial and military markets [1].

AlGaN/GaN HEMTs with varying source-gate spacing were fabricated using a standard technology process developed in our lab. HEMTs were characterized by their DC, I-V, C-V characteristics, Hall measurements, and high frequency (HF) measurements. A hydrogen silsesquioxane (HSQ)/polymethyl methacrylate (PMMA) T-Gate process was then developed to increase the  $f_t$  and  $f_{max}$  of the next generation HEMTs. Ohmic contacts with improved morphology and line edge definition after annealing were also investigated.

## Experimental Procedure:

Transistors were fabricated on a semi-insulating silicon carbide (SiC) substrate (Figure 1) with a layer stack grown by metal-organic-vapor-phase-epitaxy (MOVPE). Transistor fabrication began with mesa isolation performed by argon sputtering followed by ohmic contact and Schottky gate metallization. Ohmic contacts consisted of Ti/Al/Ni/Au metallization from bottom to top with a respective layer thickness of 35/200/40/100 nm. Schottky gate metallization was Ni/Au with thickness 25/100 nm with 170 nm gate length. Contact pads to the source, gate, and drain consisted of Cr/Au

Source	Gate	Drain
GaN		3 nm
AlGaN		20 nm
GaN		3 $\mu$ m
SiC		380 $\mu$ m

Figure 1: AlGaN/GaN HEMT layers.

with respective thickness 20/400 nm. Contact resistance was 0.68  $\Omega$ •mm and the sheet resistance was 422  $\Omega$  per square, determined by transmission line measurements.

T-Gate processes can be categorized in one-step and in two step-processes. In the latter, the gate foot is defined separately from the gate head. This approach was chosen for investigation utilizing HSQ and PMMA as e-beam resists. HSQ was used for the gate foot because of its availability and high resolution, while a PMMA tri-layer (200K/200K/950K) was chosen for the gate head.

E-beam markers maintaining a better morphology and line edge definition were investigated to automate T-gate alignment without any undesired offsets from source or drain. In this manner, the introduction of an additional marker layer could be circumvented. Ti/Al/Mo/Au metallurgy was tested as an alternative to the standard contact metallurgy of Ti/Al/Ni/Au.

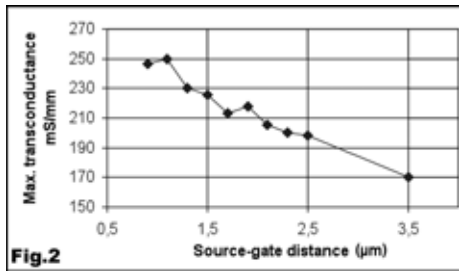


Figure 2: Maximum transconductance.

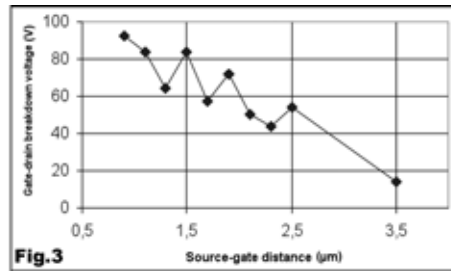


Figure 3:  $V_{gd, breakdown}$ .

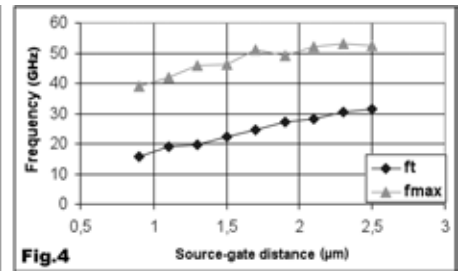


Figure 4: Maximum transit frequency ( $f_t$ ) and maximum frequency of oscillation ( $f_{max}$ ).

## Results:

In the transistor experiment, source resistance  $R_s$ , was decreased by aligning the gate closer to the source during the gate fabrication process step. As intended, the external transconductance  $g_{m,ext}$  increased with a decreasing source resistance (Figure 2).

Moving the gate from the drain towards the source increases gate-drain distance simultaneously. For a HEMT, the largest potential difference can be found between the gate and the drain if a common bias point is considered. In this way an increased source-gate distance lowers the gate-drain breakdown voltage  $V_{gd, breakdown}$  (Figure 3).

Both results, extracted from DC measurement data, showed an improvement of the device regarding  $g_{m,ext}$  and the  $V_{gd, breakdown}$ . Cut-off frequency,  $f_t$ , increases inversely with gate-source capacitance,  $C_{gs}$ , and proportionally with  $g_{m,ext}$ . However, high frequency measurements do not exhibit an increase in  $f_t$  despite the lowered source resistance and higher  $g_{m,ext}$  (Figure 4). The reason for the decrease of both operating frequencies with a lowered source-gate distance is believed to result from more  $C_{gs}$  than  $g_{m,ext}$  increase.

A reproducible two-step e-beam T-Gate process was successfully developed (Figure 5) with HSQ/PMMA. An excellent gate foot width of 90 nm was achieved with experiments yielding good results down to 40nm. Future work will consist of gate recess etching in order to keep a reasonable aspect ratio of the HEMT gate structure.

/Al/Mo/Au based ohmic contacts yielded better morphology and line edge definition after annealing than our previously optimized Ti/Al/Ni/Au contacts. In comparison to optimized contacts, Ti/Al/Mo/Au contacts had double the contact resistance ( $R_c = 1.2 \Omega/mm$ ) and resulted in an order of magnitude higher contact resistivity of about  $\rho_c = 3.82 \cdot 10^{-5} \Omega \cdot cm^2$ , indicating that more investigation of layer properties would be needed to lower resistance.

## Conclusion:

Analysis of standard technology fabricated transistors with varying source-gate distances was performed to establish a starting point of further investigations. A HSQ/PMMA T-Gate process was successfully developed for next generation AlGaIn/GaN HEMTs. Currently, the T-Gate process step is being integrated into the standard HEMT process with a gate recess etch, and gate dimension optimization to reduce  $C_{gs}$  and improve  $f_t$  will follow soon thereafter. To allow automated e-beam T-Gate alignment, Ti/Al/Mo/Au e-beam markers with lower resistivity will also be further investigated.

## Acknowledgements:

I would like to express my gratitude to the IREE, NSF, NNIN iREU Program, and to the Jülich Forschungszentrum for their funding and facilities. I am especially thankful to program coordinator Dr. Lynn Rathbun for developing an unparalleled international research experience program that has taught me so much. I would also like to express my appreciation to Dr. Michel Marso and Benjamin Strang for inclusion in their research and to the III-V and Nitrides Group and the Cleanroom Staff for their guidance and welcoming.

## References:

- [1] Mishra et al, "AlGaIn/GaN HEMTs-An Overview of Device Operation and Applications," Proceedings of the IEEE, vol. 90, pp.1022-1031, June 2002.

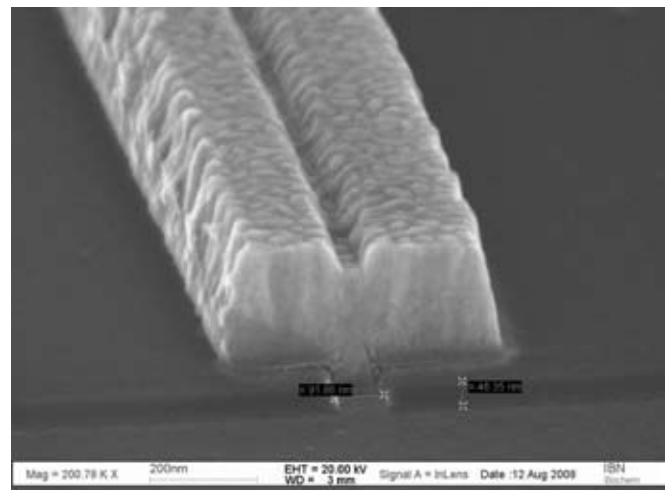


Figure 5: T-Gate with 90 nm gate foot width, 46 nm gate foot height, 250 nm gate head height, and 490 nm gate head width.

# INDEX

## 2008 NNIN REU Reports by Site

Cornell University .....	24, 30, 48, 74, 94, 98, 104, 116, 122, 126, 132
Georgia Institute of Technology .....	8, 10, 16, 112, 128
Harvard University .....	42, 90, 118, 124, 140
Howard University .....	2, 72, 80, 138
Pennsylvania State University .....	58, 68, 82, 96, 120
Stanford University .....	4, 28, 62, 76, 78, 88, 142
University of California, Santa Barbara .....	22, 40, 44, 46, 52, 110, 114, 130
University of Michigan, Ann Arbor .....	12, 32, 54, 64, 66, 86, 106, 148
University of Minnesota-Twin Cities .....	36, 70, 92, 102, 144
University of New Mexico .....	18, 20, 100, 134, 146
University of Texas at Austin .....	6, 14, 38, 50, 60, 136
University of Washington .....	26, 34, 56, 108

## 2008 iREU Reports by Country

Germany .....	154, 160, 164
Japan .....	150, 152, 156, 158, 162

## A

<b>Abreu, Andrew U.</b> .....	<b>2</b>
Adibi, Ali .....	10
Aggarwal, Gagan .....	92
<b>Akouala, Christer</b> .....	<b>66</b>
<b>Allaf, Sophia M.</b> .....	<b>4</b>
<b>Allen, Noah</b> .....	<b>126</b>
Amponsah, Ebenezer .....	132
<b>Ancukiewicz, Damian</b> .....	<b>100</b>
Anderson, David .....	94
<b>Aristizabal, Katherine</b> .....	<b>38</b>
Awschalom, David D. ....	130

## B

Baker, Chad .....	38
Barron, Sara .....	74
Batt, Carl .....	24
Beardslee, Luke A. ....	16
<b>Beasten, Amy</b> .....	<b>68</b>
<b>Beernink, Molly</b> .....	<b>70</b>
Benz, Lauren .....	42
<b>Bergstein, Courtney</b> .....	<b>150</b>
Bordonaro, Garry .....	126

## C

Bowers, John .....	114
Boyd, Erin .....	118
Brand, Oliver .....	16
Brinker, C. Jeffrey .....	146
<b>Brooks, Jason</b> .....	<b>128</b>
Broz, Margaret .....	92
Burek, Gregory .....	52

Caldorera-Moore, Mary .....	6
Campbell, Stephen A. ....	92
<b>Caraway, Jennifer</b> .....	<b>50</b>
Cassidy, Maja .....	90
<b>Cha, Elizabeth</b> .....	<b>6</b>
<b>Chang, Wendi</b> .....	<b>72</b>
Chen, Hui-Wen .....	114
Chen, Jiayu .....	100
<b>Christle, David J.</b> .....	<b>130</b>
Cobb-Sullivan, Janet .....	112
Cohen, Itai .....	122
<b>Connolly, Allison</b> .....	<b>8</b>
Connor, Stephen .....	4, 28

## D

<b>Connors, Megan</b> .....	<b>52</b>
<b>Cote, Alissa</b> .....	<b>40</b>
Craighead, Harold .....	98
Cross, Josh .....	98
Cruz, Samantha .....	110
Cui, Yi .....	4, 28

Dauskardt, Reinhold .....	76
Demirel, Melik .....	82
DenBaars, Steven P. ....	110
<b>Deshazer, Garron</b> .....	<b>116</b>
Dodabalapur, Ananth .....	60
Dong, Jinping .....	144
Dutta, Soumya .....	60

## E

<b>Edwards, Ryan</b> .....	<b>10</b>
<b>Elias, Christina</b> .....	<b>42</b>

## F

Fedorov, Andrei G. .... 8  
**Foley, Justin** ..... 102  
**Fonseca, José** ..... 74  
Friend, Cynthia M. .... 42  
Fujita, Daisuke ..... 158  
Fung, Wayne ..... 54  
Fygenson, Deborah ..... 22

## G

**Garcia, Federico** ..... 132  
Gerbode, Sharon ..... 122  
Ginger, David S. .... 84  
**Goldman, Rachel S.** ..... 66  
**González, Sergio Oberlín** . 118  
Gopal, Ashwini ..... 136  
Gopinath, Anand ..... 102  
Gottfried, David ..... 112  
**Graham, Brielle** ..... 104  
Gregoire, John ..... 74  
**Grice, Sarah** ..... 94  
Griffin, James ..... 80  
Griffin, Peter ..... 88, 142  
**Guevarra, Jose** ..... 12  
Guo, L. Jay ..... 32

## H

**Habimana-Griffin, LeMoyne** . 76  
Hall, Ruth ..... 26  
Han, Songi ..... 40  
Haque, Aman ..... 96  
Harris, Gary L. .... 2, 72, 80  
**Harrison, Ryan M.** ..... 152  
Hart, A. John ..... 86  
**Hartsfield, Tom** ..... 78  
Haubrich, Jan ..... 42  
Haugstad, Greg ..... 144  
Heremans, F. Joseph ..... 130  
Herrera-Fierro, Pilar ..... 148  
Herskowitz, Lawrence ..... 20  
Hickner, Michael A. .... 68  
Hight-Huf, Nick ..... 46  
Hinke, Jonathon ..... 102  
**Holmberg, Angela L.** ..... 14  
Hoshino, Kazunori ..... 136  
**Hothur, Pradeep** ..... 16

**Hou, Jennifer** ..... 134  
Howe, Roger ..... 78  
Hsu, Chih-Peng ..... 56  
Hsu, Ching-Mei ..... 4, 28  
Hu, Yong-Sheng ..... 44

## I

Im, Hyungsoon ..... 36

## J

Jain, Ravi ..... 100  
**Jakus, Adam** ..... 18  
Jawerth, Louise ..... 124  
**Jewell, Jason** ..... 106  
Jin, Yu ..... 66  
**Jolaoso, Oluwatosin** ..... 80  
Jones, Kimberly ..... 138  
Jung, Taeil ..... 64  
**Journey, Patrick** ..... 20

## K

Kan, Edwin ..... 132  
Kant, Rishi ..... 78  
**Kapadia, Rehan** ..... 154  
**Keefer, Derek** ..... 120  
Kennedy, Matthew ..... 24  
**Kim, Sunmin** ..... 136  
Kim, Taek Soo ..... 76  
**Kiser, Jillian** ..... 122  
Koch, Steven ..... 20  
**Koehler, Sarah** ..... 96  
Korgel, Brian A. .... 14  
Krishna, Sanjay ..... 134  
Ku, Pei-Cheng ..... 64  
Kügeler, Carsten ..... 154  
Kurabayashi, Katsuo ..... 12  
Kurdak, Cagliyan ..... 66

## L

**Lambson, Brian** ..... 156  
**Latunde, Olaronke** ..... 44  
**Léandre, Vérida** ..... 138  
Lee, Jaegoo ..... 132

**Lee, Jaime** ..... 54  
Lee, Yong ..... 38  
**Lehman, Jessica** ..... 56  
Li, Fan ..... 70  
Li, Xingde ..... 108  
**Li, Yu** ..... 46  
Lin, Albert ..... 62  
Lingwood, Mark ..... 40  
Lipson, Michal ..... 104  
Liptak, Richard ..... 102  
Loncar, Marko ..... 140  
**Lowman, Jill** ..... 82  
Lucas, Brandon D. .... 32  
**Luce, Alexander V.** ..... 158  
Lui, Clarissa ..... 24  
Lu, Wei ..... 54

## M

**MacQueen, Alice** ..... 160  
Mallick, Shrestha ..... 78  
**Malyutin, Andrey** ..... 84  
Mamishhev, Alexander ..... 56  
Mano, Takaaki ..... 162  
Manoharan, Mohan ..... 96  
Marcus, Charles ..... 90  
Marso, -Ing Michel ..... 164  
**Martinick, Kathleen** ..... 140  
McCutcheon, Murray W. .... 140  
McFarland, Eric ..... 44  
**McSkimming, Brian** ..... 162  
Meacham, J. Mark ..... 8  
Memon, Tosifa ..... 18  
**Meng, Alice F.** ..... 108  
Michael, Kristin E. .... 160  
**Moebius, Michael** ..... 86  
Mohney, Suzanne ..... 58  
Moran-Mirabal, Jose ..... 30  
Moskovits, Martin ..... 46  
Murali, Raghunath ..... 128

## N

Neufeld, Carl ..... 110  
Nishi, Yoshio ..... 88, 142  
Noda, Takeshi ..... 156  
Nothorn, Denis ..... 106

## O

O'Neill, Patrick ..... 22  
Offenhäuser, Andreas ..... 160  
Oh, Jaesong ..... 102  
Oh, Sang-Hyun ..... 36  
Ohashi, Naoki ..... 150  
**Osgood-Jacobs, Logan ..... 48**  
Osinski, Marek ..... 18  
**Ott, Joshua ..... 98**  
**Ouyang, Jiaomin ..... 88**  
**Owusu-Boamah, Yaw ..... 58**

## P

**Padmaraju, Kishore ..... 22**  
**Pak, Taemee ..... 24**  
Patil, Nishant ..... 62  
Patrick-Boardley, Nefertiti ..... 2  
Petrina, Stephanie ..... 68  
**Points, Micah S. .... 110**  
Poitras, Carl ..... 104  
Provine, J. .... 78

## R

Ramamoorthy, Malaisamy .... 138  
Rasch, Michael R. .... 14  
**Reeves, Daniel ..... 90**  
**Reeves, Victoria ..... 124**  
Reid, Obadiah G. .... 84  
Rey, Diego ..... 24  
Rodwell, Mark ..... 52  
**Roman, William J. .... 164**  
Roy, Krishnendu ..... 6  
**Rudisill, Stephen ..... 92**  
Ruoff, Rodney S. .... 50

## S

Sagisaka, Keisuke ..... 158  
Sakaki, Hiroyuki ..... 156  
Sankar, Krishnaprasad ..... 18  
Sarpawari, Karthik ..... 58  
**Schmidt, Laurel ..... 26**  
**Scofield, Adam ..... 112**  
**Sengupta, Trisha ..... 28**  
Shenoi, Rajeev ..... 134  
Shi, Li ..... 38

Shtein, Max ..... 106  
**Shutler, Alisha ..... 114**  
**Simmons, Rachel ..... 30**  
Solgaard, Olav ..... 78  
Song, Juho ..... 48  
Southworth, Darren ..... 98  
Steen, Paul ..... 94  
Stein, Andreas ..... 70  
Stelick, Scott ..... 24  
Stewart, Derek ..... 116  
**Stiver, Julie ..... 142**  
Stoller, Meryl ..... 50  
Strang, Benjamin ..... 164  
Stroock, Abraham ..... 48  
Sugiyasu, Kazunori ..... 152  
**Swain, Arun ..... 60**  
**Swindlehurst, Garrett ..... 144**

## T

Takeuchi, Masayuki ..... 152  
Tang, Mary ..... 4, 28  
Tawfick, Sameh ..... 86  
Taylor, Crawford ..... 72  
Tendulkar, Mihir ..... 88  
Tennant, Donald ..... 126  
**Teran, Alan S. .... 62**  
**Tesfaslassie, Isaias ..... 32**  
Thareja, Gaurav ..... 142  
Thomas, Wendy ..... 34  
**Todd, Tyler ..... 146**  
Traxler, Beth ..... 26  
Trodahl, Halvar ..... 118  
Truxal, Steven ..... 12

## V

van Dover, R. Bruce ..... 74

## W

Walker, Larry ..... 30  
Wang, Hui ..... 82  
Wang, Li ..... 100  
**Weber, Steven ..... 64**  
Weitz, David A. .... 124  
Weng, Robert ..... 154

Westervelt, Robert M. .... 118  
Whitfield, Matt ..... 34  
Wong, H.-S. Philip ..... 62  
**Woods, Suron ..... 34**  
Wu, Yicong ..... 108

## X

Xiong, Shisheng ..... 146  
Xu, XiuMei ..... 94

## Y

Yang, Yinxiao ..... 128  
Yegnanarayanan, Siva ..... 10  
**Yoon, Justine Soo Yun ..... 36**

## Z

Zhang, Xiaojing ..... 136  
Zhu, Jun ..... 120  
**Zinsou, Merine ..... 148**  
Zou, Ke ..... 120

**The 2008 NNIN REU  
Research Accomplishments  
were formatted by  
Ms. Melanie-Claire Mallison,  
NNIN REU Program Assistant.  
She welcomes your comments  
at [mallison@cnf.cornell.edu](mailto:mallison@cnf.cornell.edu).**

**The reports are also online in  
PDF, at: [http://www.nnin.org/  
nnin\\_2008reu.html](http://www.nnin.org/nnin_2008reu.html)**